NUREG/CR-5674
SAND91-7058

Evaluation of Behavior and the Radial Shear Strength of a Reinforced Concrete Containment Structure

Prepared by
H. P. Walther

Department of Civil Engineering
University of Illinois

Sandia National Laboratories
Operated by
Sandia Corporation

Prepared for
U.S. Nuclear Regulatory Commission

AVAILABILITY NOTICE

Availability of Reference Materials Cited in NRC Publications

Most documents cited in NRC publications will be available from one of the following sources:

1. The NRC Public Document Room, 2120 L Street, NW., Lower Level, Washington, DC 20555

2. The Superintendent of Documents, U.S. Government Printing Office, P.O. Box 37082, Washington, DC 20013-7082

3. The National Technical Information Service, Springfield, VA 22161

Although the listing that follows represents the majority of documents cited in NRC publications, it is not intended to be exhaustive.

Referenced documents available for inspection and copying for a fee from the NRC Public Document Room include NRC correspondence and internal NRC memoranda; NRC bulletins, circulars, information notices, inspection and investigation notices; licensee event reports; vendor reports and correspondence; Commission papers; and applicant and licensee documents and correspondence.

The following documents in the NUREG series are available for purchase from the GPO Sales Program: formal NRC staff and contractor reports, NRC-sponsored conference proceedings, international agreement reports, grant publications, and NRC booklets and brochures. Also available are regulatory guides, NRC regulations in the *Code of Federal Regulations*, and *Nuclear Regulatory Commission Issuances*.

Documents available from the National Technical Information Service include NUREG-series reports and technical reports prepared by other Federal agencies and reports prepared by the Atomic Energy Commission, forerunner agency to the Nuclear Regulatory Commission.

Documents available from public and special technical libraries include all open literature items, such as books, journal articles, and transactions. *Federal Register* notices, Federal and State legislation, and congressional reports can usually be obtained from these libraries.

Documents such as theses, dissertations, foreign reports and translations, and non-NRC conference proceedings are available for purchase from the organization sponsoring the publication cited.

Single copies of NRC draft reports are available free, to the extent of supply, upon written request to the Office of Administration, Distribution and Mail Services Section, U.S. Nuclear Regulatory Commission, Washington, DC 20555.

Copies of industry codes and standards used in a substantive manner in the NRC regulatory process are maintained at the NRC Library, 7920 Norfolk Avenue, Bethesda, Maryland, for use by the public. Codes and standards are usually copyrighted and may be purchased from the originating organization or, if they are American National Standards, from the American National Standards Institute, 1430 Broadway, New York, NY 10018.

NUREG/CR-5674
SAND91-7058
R1, RD

Evaluation of Behavior and the Radial Shear Strength of a Reinforced Concrete Containment Structure

Manuscript Completed: December 1991
Date Published: January 1992

Prepared by
H. P. Walther

Department of Civil Engineering
University of Illinois
Urbana, IL 61801

Under Contract to:
Sandia National Laboratories
Albuquerque, NM 87185

Prepared for
Division of Engineering
Office of Nuclear Regulatory Research
U.S. Nuclear Regulatory Commission
Washington, DC 20555
NRC FIN A1401

Abstract

This study is on the behavior and strength of the 1/6-scale reinforced concrete containment model tested at Sandia National Laboratories. The containment model was pressurized to more than three times its design pressure until a tear in the liner terminated the test. Deformation data from the model test was used to interpret behavior and to estimate the internal forces at the wall-basemat connection. Analytical models were developed for radial-expansion response and for the wall and basemat interaction. A possible mode of structural failure of containments subjected to high pressures is by radial-shear failure at the wall-basemat connection. Although the containment model showed no sign that such a failure was imminent when the test was stopped, if it had been possible to increase the internal pressure an abrupt shear failure was possible. A method based on the compressive force due to flexure at the wall-base was developed to evaluate the radial shear strength of the 1/6-scale containment model. Using the developed methodology, an estimate is made of the pressure that would initiate a shear failure at the wall-basemat junction of the model. This estimate is based on a projection of the observed strength of similar 1/12-scale wall-basemat connections, which have failed in shear.

Table of Contents

Table of Contents (cont.)

List of Tables

List of Figures

List of Figures (cont.)

List of Notation

a	depth of equivalent uniform stress block in concrete
a/d	shear-span ratio
A_d	area of diagonal reinforcement
A_g	gross section area
A_h	area of circumferential reinforcement
A_s	area of steel in a unit section
A_{tr}	area of transformed section
A_v	area of vertical reinforcement
C_a	unit force in concrete based on actual strains
C_c	unit force in concrete
C_{cb}	unit compressive radial force carried by concrete in the basemat
C_f	compressive force due to flexure
C_m	unit force in concrete estimated from measured strain data
D_b	flexural rigidity for the basemat
E_{base}	elastic modulus for the basemat
E_c	Young's modulus for concrete
E_{hoop}	elastic modulus for the shell wall in the hoop direction
E_s	Young's modulus for steel
E_{vert}	elastic modulus for the shell wall in the vertical direction
f'_c	compressive strength of concrete
f_{sd}	stress in diagonal reinforcement
f_{sh}	stress in circumferential reinforcement
f_t	effective tensile strength of concrete
f_{vy}	yield strength of shear reinforcement
f_y	yield strength of reinforcement
$f_{yt,eff}$	effective yield strength of the liner
F	unit force in studs
h	wall thickness
H	total cylinder wall height
I_{cr}	moment of inertia of cracked section
I_{gross}	moment of inertia of gross section
K_c	cracked-section stiffness
K_u	apparent stiffness before cracking
m_o	unit plastic moment capacity
M	bending moment
M_a	moment based on actual strains
M_m	moment based on measured strain data
M/Vd	shear-span ratio
n	modular ratio (E_s/E_c)
n	number of effective bars crossing a potential shear crack
n_o	unit plastic hoop force capacity
N_h	unit hoop force in the wall
N_u	force acting on section (tension negative)
N_v	vertical unit force in the wall
p	internal pressure
p	distance to plastic centroid from the wall exterior
P_C	C-model limit pressure
P_d	design pressure
P_{design}	design pressure
P_{ult}	ultimate sustained pressure
P_y	pressure required to yield circumferential reinforcement

List of Notation (cont.)

Q	unit radial shear force acting at the wall-base
R	cylinder radius
$R_{flexural}$	ratio of flexural stiffness before and after cracking
R_i	inner radius of the wall
s_d	spacing of diagonal bars
s_h	spacing of circumferential bars
s_v	spacing of vertical bars
t	thickness of the cylindrical wall
t_c	concrete thickness
t_l	liner thickness
T_a	force in steel based on actual strains
T_m	force in steel estimated from measured strain data
T_s	vertical component of force in the steel
T_{sb}	unit tensile radial force carried by reinforcement in the basemat
v_c	nominal shear strength of concrete
v_s	nominal shear strength of reinforcement
v_u	nominal (total) shear strength
V_{cw}	unit shear force carried by concrete in the wall
V_{gross}	shear force at the wall-base determined from an elastic fixed-base model based on gross sections
V_{sw}	unit shear force carried by shear reinforcement in the wall
V_{total}	total unit shear strength estimated by the C-model
W	weight of the cylinder wall and dome
α	inclination of reinforcement from the vertical
β	ratio of uniform stress block depth to neutral axis depth
δ	assumed virtual radial deflection
ε_a	actual strain
ε_c	maximum concrete strain at extreme compression fiber
ε_d	strain in diagonal reinforcing bars
ε_h	circumferential strain
ε_m	measured strain
ε_o	strain at maximum compressive stress of concrete
ε_o	initial compressive strain due to dead load
ε_u	ultimate compressive strain of concrete
ε_v	vertical strain
ε_y	reinforcement yield strain
θ	inclination of a potential shear crack from the vertical
μ	coefficient of friction
ν	Poisson's ratio
ρ	ratio of total area of reinforcement to gross section area
ρ_h	circumferential reinforcement ratio
ρ_v	shear reinforcement ratio
σ_n	stress normal to a section (tension positive)
ϕ_{cr}	cracked section curvature

List of Abbreviations

ACI	American Concrete Institute
ASME	American Society of Mechanical Engineers
BWR	Boiling Water Reactor
c.o.v.	coefficient of variation
CTL	Construction Technology Laboratories, Skokie, IL
F	Fahrenheit
Fig.	Figure
ft	foot
HPT	High Pressure Test
ILRT	Integrated Leak Rate Test
in.	inch
kip	one thousand pounds
ksi	kips per square inch
lb	pound
LWR	Light Water Reactor
mm	millimeter
No.	Reinforcing bar diameter in one-eighth inch units
psi	pounds per square inch
psig	pounds per square inch gage pressure
PWR	Pressurized Water Reactor
ref	reference
RH	Relative humidity
S&WE	Stone and Webster Engineering Co., Boston, MA
SIT	Structural Integrity Test
SNL	Sandia National Laboratories

Acknowledgments

Support for this research was provided by Sandia National Laboratories under contract 63-5261. The generous assistance of W. A. von Riesemann, D. B. Clauss, D. S. Horschel, M. B. Parks, and J. R. Weatherby of Sandia Labs is appreciated. This work was a part of the Containment Integrity Programs conducted at Sandia Labs and sponsored by the Nuclear Regulatory Commission. The continued assistance of J. F. Costello at the N. R. C. is acknowledged.

The project was directed by Mete A. Sozen, Professor of Civil Engineering, University of Illinois, Urbana. His unselfish guidance is gratefully appreciated. The author wishes to thank W. J. Hall, A. R. Robinson, S. L. Wood, and C. P. Siess, faculty at the Univ. of Ill., for their suggestions and contributions to this manuscript. Thanks are due also to fellow students, J. Bonacci, M. Eberhard, and J. Dragovich, for sharing their engineering knowledge and to D. Bever for her secretarial assistance.

EXECUTIVE SUMMARY

In this report the behavior of a 1/6-scale reinforced concrete containment model subjected to overpressurization is described and an evaluation of the radial shear strength at the wall-basemat connection is presented.

Containment buildings are important for the safe operation of nuclear power reactors because they are the last engineered barrier to prevent the release of radioactive material that might be released to the environment. In the unlikely event of a severe accident, containment buildings may be subjected to temperature and pressure loadings far exceeding the loads for which they were designed.

The U. S. Nuclear Regulatory Commission has sponsored a series of programs to develop test-validated methods for predicting the response of light water reactor containment buildings to loadings beyond the design basis. At Sandia National Laboratories, experiments on scale models of containment buildings subjected to internal pressures have generated data that could be used to evaluate analytical methods for predicting the performance of these structures. At present, four 1/32-scale steel containments, one 1/8-scale steel containment, and one 1/6-scale reinforced concrete containment have been tested. The test of the reinforced concrete containment is the subject of this report.

Containment Model and Tests

The reinforced concrete containment model was configured as a domed cylindrical shell fixed to a circular base. The model was developed to resemble the general features of U.S. PWR containments and was designed and built according to the same code standards as full-size prototypes. Overall dimensions were 25 ft wide by 37 ft tall. The cylindrical shell had an inside radius of 11 ft with a 9.75-in. wall thickness. A steel liner was attached by headed studs to the inside surface of the structure to provide a leak-tight barrier to internal pressure. The liner attached to the wall and basemat was 1/16-in. thick and the liner attached to the dome was 1/12-in. thick. The shell wall was provided with eight layers of 1/2-in. diameter reinforcing bars: reinforcement ratios were 2.2% in the horizontal (hoop) direction and 1.2% in the vertical direction. The containment design pressure was 46 psig. More than 1200 channels of instrumentation, including strain gages, displacement transducers, and other sensors, monitored the containment model response.

A series of internal pressurization tests were conducted in July 1987. During the first test, a structural integrity test, pressure was slowly increased in steps to 53 psig (1.15 times design pressure) and then released. Later, a high pressure test was conducted in which pressure was slowly increased to 145 psig when failure of the liner occurred and the pressurization system could no longer sustain pressure. Post-test examination revealed a 21 in. vertical tear in the liner near one of the penetrations. This was the major source of leakage; there were numerous other small tears.

Background

Numerous reports and papers have been written on the construction and instrumentation of the model, on material properties, on the experimental results, and on pretest and posttest analyses. Several nuclear power research and regulatory organizations, including Sandia, participated in "round-robin" pretest analyses to predict the model response and mode of failure. After the test these organizations made revisions/refinements to their analyses to compare test data to results of posttest calculations. Although the containment model failed by liner tearing, eight of the ten pretest analyses identified radial-shear failure at the junction of the wall and basemat as the likely mode of failure.

Summary of Behavior

As internal pressure in the containment was increased, the data indicated that the cylindrical wall cracked and yielded in both hoop and vertical directions. By the end of the pressure tests there was overall yielding (more that 1% strain) in the hoop direction but not in the vertical direction. The containment design pressure was 46 psig. Cracking of the wall occurred at 20 psig, initial yielding in the hoop direction occurred at 110 psig, and overall hoop direction yielding began at 130 psig. Initial yielding in the vertical direction began at 125 psig. The test was stopped at 145 psig as pressure could not be sustained due to tears in the liner.

Deformation of the 40-in. thick by 25-ft dia. basemat was negligible at pressures less than 75 psig. The basemat cracked at 75 psig and began to uplift, reaching a maximum upward displacement at the edge of 3/8 in. at the end of the test. The response of the basemat was found to influence the history of radial shear and meridional bending moment at the base of the wall.

Evaluation of Radial Shear Strength

Strain data were used to estimate the internal forces at the wall-basemat junction. At the maximum test pressure (145 psig), the unit forces, expressed as average stress on the gross wall section, were estimated to have been 920 psi ($11.7\sqrt{f'_c}$) axial tension and 450 psi ($5.7\sqrt{f'_c}$) radial shear. Concurrently, the base of the wall had yielded in flexure. This combination of vertical tension, moment, and radial shear is beyond the range of stresses at failure of other wall-basemat connections that have been tested.

The strength of reinforced concrete subjected to radial shear, bending, and tensile stresses (as found at the wall-basemat connection) is not well known. Estimates of the shear strength of reinforced concrete sections must be based strictly on the results of experiments. A literature survey to identify experiments of reinforced concrete members subjected to stress conditions at failure similar to those in the containment model found no test data that could be used directly to guide an estimate of the shear strength of the 1/6-scale containment. The Central Institute of the Electric Power Industry, Japan, conducted tests on 1/12-scale, 45° sectors, of a wall and basemat

connection. Data from these tests were found to provide the only rough means by which a strength estimate of the Sandia containment model could be made.

To provide an intelligible connection between the data from the containment test and data from simulated wall-basemat connections, a procedure for estimating the radial shear capacity from the compression force in flexure was defined. This procedure was applied to the 1/6-scale containment and to the 1/12-scale wall-basemat connection experiments. Through the calculation procedure, stress conditions at failure in simulated 1/12-scale connections are compared with stresses postulated to exist in the 1/6-scale model. At an internal pressure of 185 psig the stress conditions in the Sandia model would be similar to the stress conditions at failure of one of the 1/12-scale connections. Because the Sandia containment had not failed in radial shear at 145 psig, the maximum test pressure achieved, there is a 40 psig uncertainty in the implied 185 psig failure pressure. There is no other experimental data that could be used to support this rough estimate of radial shear capacity.

Conclusions

An interpretation of the containment model structural behavior from the test data is presented. This will aid in future assessments of analytical methods to predict the response of the 1/6-scale model. The most effective way to compare results of calculations with results of experiments is by identifying qualitative and quantitative similarities in predicted and measured response.

This research highlights the lack of experimental data necessary to estimate the shear strength at the wall-base of a typical reinforced concrete containment structure. The evaluation of behavior and strength of the 1/6-scale containment model has shown that the results of this test could be used to guide lower-bound estimates of radial shear strength.

The wall-basemat connection resisted large vertical tension and radial shear stresses at a section which had yielded in flexure. Prior to this test, given this (presumed) severe internal stress state and the limited experimental data on which to base a judgment on the integrity of this connection, the estimate of the potential for a failure at 145 psig internal pressure would be quite high. Although the strength of the wall-basemat connection is presently unknown, the analysis of the test data presented herein has shown that the connection capacity is greater that what one would have estimated before the test.

1. INTRODUCTION

In this report the behavior of a 1/6-scale reinforced concrete containment structure subjected to internal pressure is described and an evaluation of the radial shear strength at the wall-basemat connection is presented. The U. S. Nuclear Regulatory Commission has initiated a set of programs to develop test validated methods for predicting the performance of Light-Water Reactor (LWR) containment buildings subjected to pressure loadings beyond the design basis. Experiments at Sandia National Laboratories (SNL) on scale models of containment buildings have generated data that can be used to evaluate analytical methods for predicting the response and mode of failure of these structures. These experiments are a part of the Containment Integrity Programs [Ref. 1.1]. To date, four 1/32-scale steel containments, one 1/8-scale steel containment, and one 1/6-scale reinforced concrete containment have been tested by internal pressurization. Data from the test of the 1/6-scale reinforced concrete containment (Fig 1.1), subjected to a series of pressurization tests in July 1987, provides the basis for this work.

Containment buildings are important for the safe operation of nuclear reactors because they are the last engineered barrier to contain radioactive material that might be released to the environment. The pressurization test of the 1/6-scale reinforced concrete containment was discontinued when a large tear and several smaller tears developed in the liner allowing leakage. At the time the test was stopped, there were no indications of gross structural failure. If the liner had not torn greater pressures would have been sustained and another mode of failure might have been activated.

The results of a series of pretest analyses [Ref. 1.2] on the containment model indicated that one possible mode of structural failure was by radial-shear failure near the wall-basemat connection. Radial-shear failure results from failure of the concrete at the wall-base due to the combination of meridional bending, vertical tension, and radial shear. Radial shear stresses are transverse to the cylindrical wall and are oriented along a radius defining the wall surface. During internal pressurization radial shear stresses are greatest at the wall-basemat connection because of the difference in the radial-expansion stiffness of the wall and basemat. Although the containment showed no sign that a radial-shear failure was imminent, an abrupt shear failure might have occurred at a higher pressure level. For this reason, the radial shear strength at the wall-basemat connection is of concern and is evaluated herein.

1.1 Description of Work

Little is known about the strength of reinforced concrete structures subjected to the combined effects of shear, bending, and tension across a critical section. A survey of experimental research identified three series of tests of wall-basemat connections of containment structures. Only one set of these tests had loading conditions resembling the stress state at the wall-base of a whole containment structure.

Strain and displacement data gathered during the 1/6-scale containment model overpressurization test was analyzed to evaluate the behavior of the

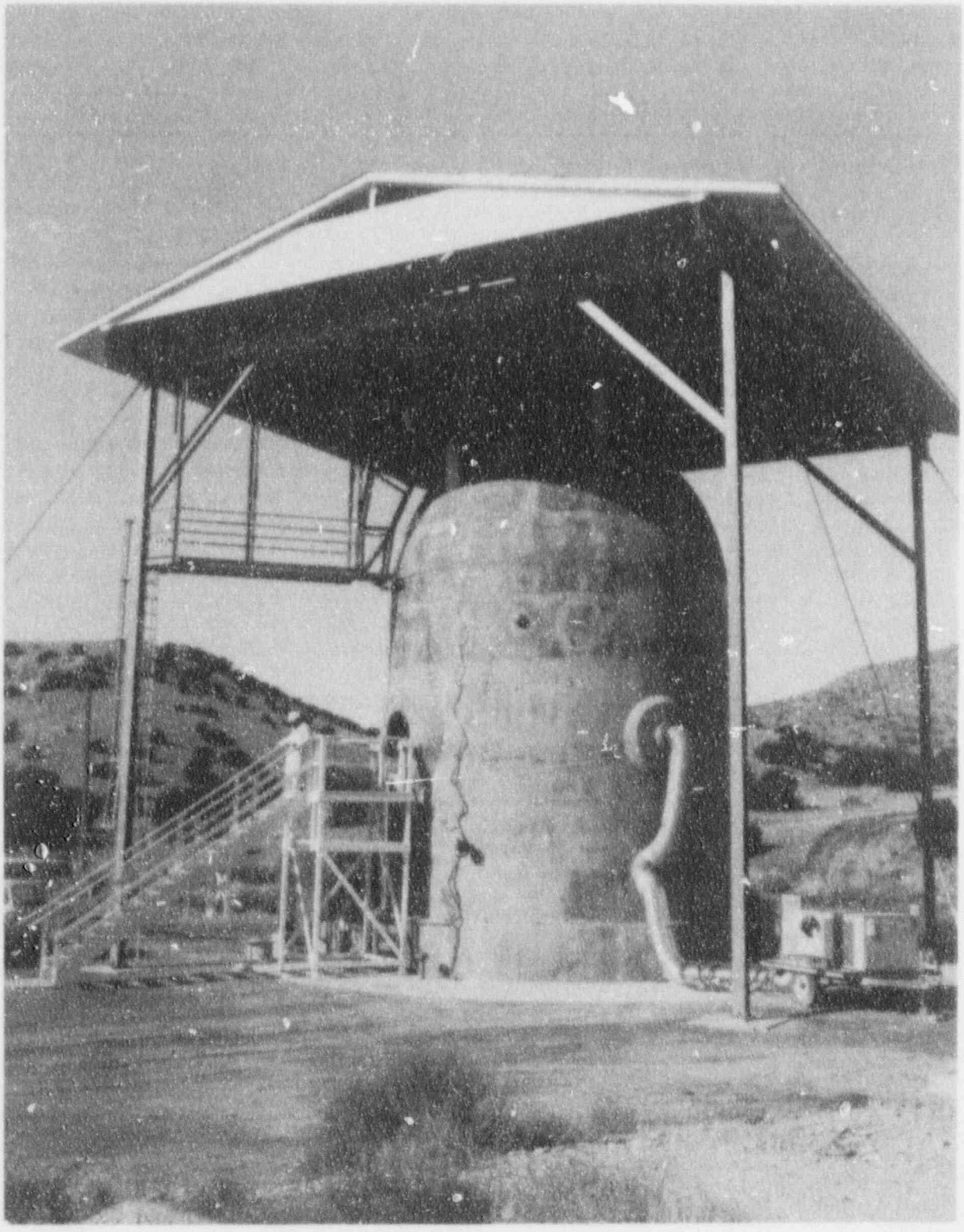

Fig. 1.1 1/6-Scale Reinforced Concrete Containment Model Tested at Sandia National Laboratories

structure. It was determined that the combination of radial-shear, moment, and vertical tension at the wall-base at the maximum test pressure was beyond the range of stresses at failure of other wall-basemat connections that have been tested. Estimates of the strength of reinforced concrete sections in shear must be based strictly on the results of the limited number of experiments. This research highlights the inadequacy of the database of experience to guide confident estimates of the shear strength of wall-basemat connections. An estimate of the shear strength at the wall-base of a typical reinforced concrete containment structure could be made at present with a low degree of confidence.

1.2 Outline of Report

Chapter 2 provides a description of the configuration and material properties of the 1/6-scale reinforced concrete containment tested at Sandia. An outline of the pressurization tests and a description of the instrumentation is presented in Chapter 3. The data obtained from Sandia required alignment, as described in Chapter 3, in order that plots of test pressure versus response from both the structural integrity and high pressure tests might represent what would have been measured by one continuous loading.

A discussion of measured response is presented in Chapter 4. Plots of representative data are shown and interpretations of behavior indicated by the plots are offered. An analytical model to assess the credibility of the measurements is described in Chapter 5. A study of the effects of cracking on measured response data is discussed. With the aid of analysis, it is shown that the basemat participated in the overall response and affected the internal force history at the wall-basemat junction.

Techniques for estimating the meridional bending moment and radial shear force at the base of the wall from strain gage data are described in Chapter 6. Present methods for evaluating shear strength and a literature survey of comparable experimental research are described in Chapter 7. A procedure for evaluating shear strength of wall-basemat connections, based on the compressive force in flexure, is then developed. The amount of uncertainty in estimates of shear strength is indicated at the end of Chapter 7.

2. DESCRIPTION OF TEST STRUCTURE

The 1/6-scale reinforced concrete containment model (Fig. 2.1) was designed and built to the American Society of Mechanical Engineers (ASME) code [Ref. 2.4] by United Engineers and Constructors, Inc. The containment was modeled to resemble a typical Light Water Reactor (LWR) reinforced concrete containment building. Construction began in December 1985, with the placement of the basemat, and was completed in June 1986.

In this chapter the containment model design and configuration is described and the data on material properties obtained from tests of reinforcement, liner, and concrete samples is presented. In the latter part of this chapter a detailed description of the concrete cylinder sample data is included. Strength of the sample cylinders increased with curing time to six months and later decreased. A literature survey was performed to establish a precedence for this decrease with age in measured concrete strength. Additional information on the model design and construction and on the reinforcement and liner materials is available in references 2.1 to 2.3.

2.1 Containment Model Design

2.1.1 Configuration

The containment model was configured as a domed cylindrical shell fixed to a circular base, Figure 2.1. Overall dimensions were 25 ft wide by 37 ft tall. The cylindrical shell had an inside radius of 11 ft with a 9.75 in. wall thickness. The dome thickness was 7 in. and the basemat thickness was 40 in. A steel liner was attached to the inside surface of the reinforced concrete shell to provide a leak-tight barrier to internal pressure. Operable equipment hatches and personnel airlocks were provided at 90 degree intervals at mid-height on the cylinder wall. The model rested atop a steel-reinforced "mudmat" measuring 41 ft in diameter and 6 in. thick.

The shell wall was reinforced by eight layers of No. 4 diameter reinforcing bars (Fig. 2.2). Two layers of reinforcement were oriented vertically, four layers were oriented around the circumference, and two layers of seismic reinforcement were oriented 45 degrees to horizontal and were orthogonal to each other. The liner was secured to the wall by 1/2-in. and 3/4-in.-long steel studs welded to the outside of the liner plate and embedded in concrete. The eight layers of No. 4 bars continued into the dome and were anchored in the basemat. Reinforcement ratios (excluding the liner) in the wall, dome, and basemat are indicated in Figure 2.3. Details on the basemat reinforcement and additional reinforcement at the wall-basemat connection are described in Section 3.3.

2.1.2 Design Basis

The design of the containment model conforms to the provisions of the ASME Boiler and Pressure Vessel Code, Division III, for nuclear power plants and components [Ref. 2.4]. The design accident pressure was 46 psig internal pressure. The fundamental design function of containment structures is to prevent or delay the release of radioactivity to the environment after an

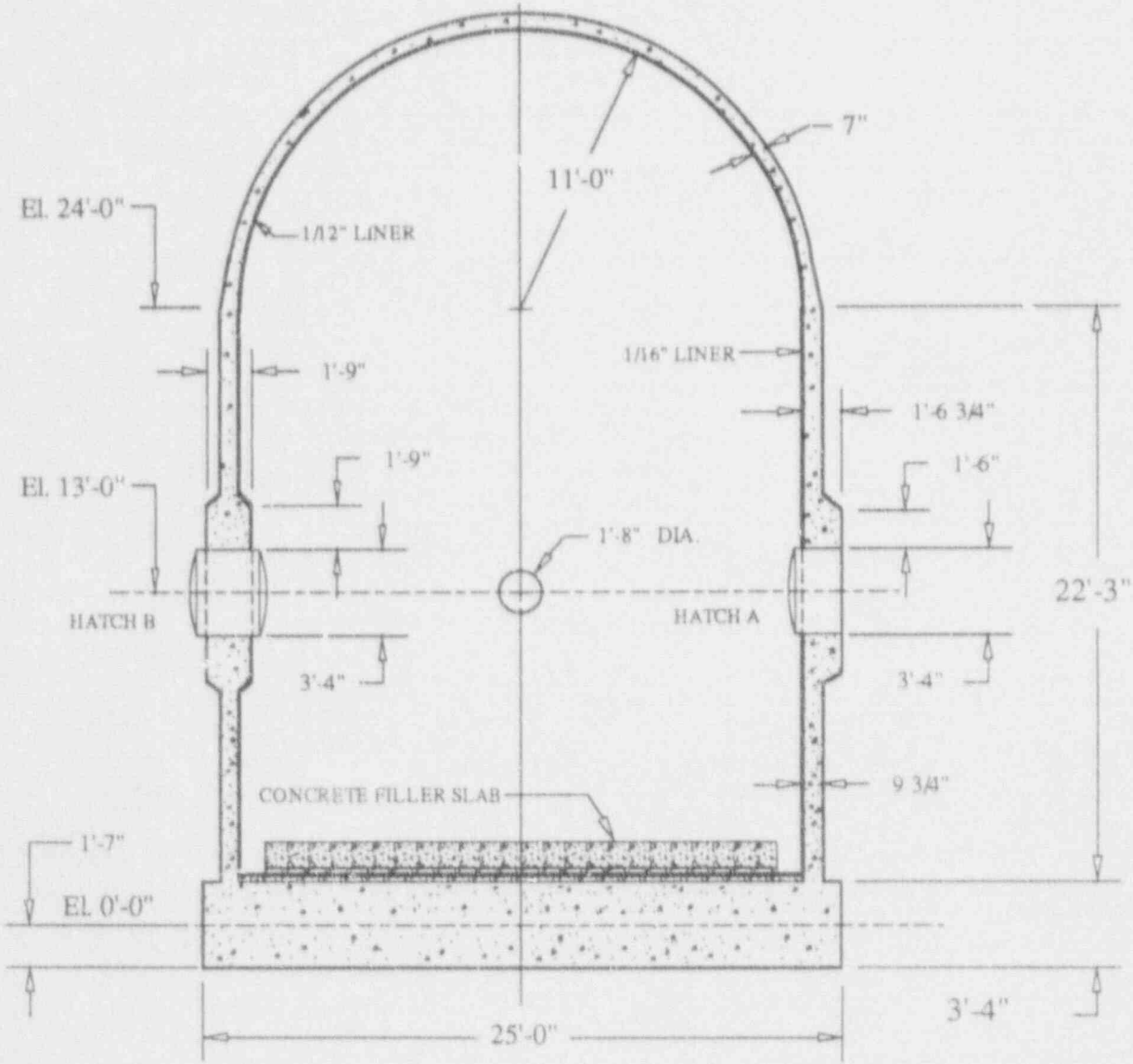

Fig. 2.1 Overall Dimensions of Containment Model

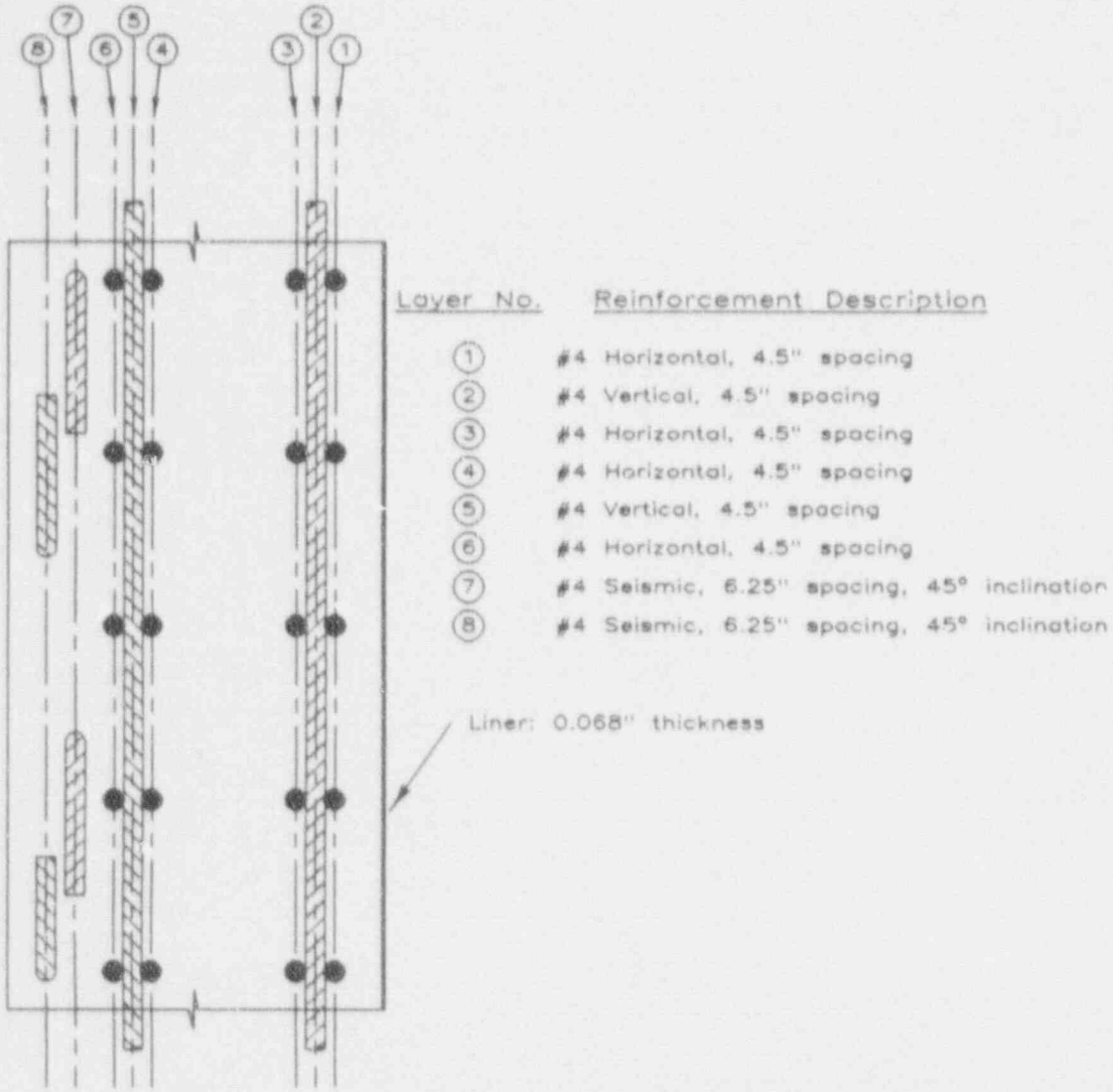

Fig. 2.2 Cylinder Wall Elevation with Typical Reinforcement Distribution

accident in which radioactive materials are released to the containment. The steel liner is, in essence, the containing element and the reinforced concrete shell provides support. A failure of the containment, therefore, is any event that would lead to the inability of the liner to perform its function. The focus of this report is on the strength of the reinforced concrete structure and its ability to provide support and to maintain the integrity of the liner.

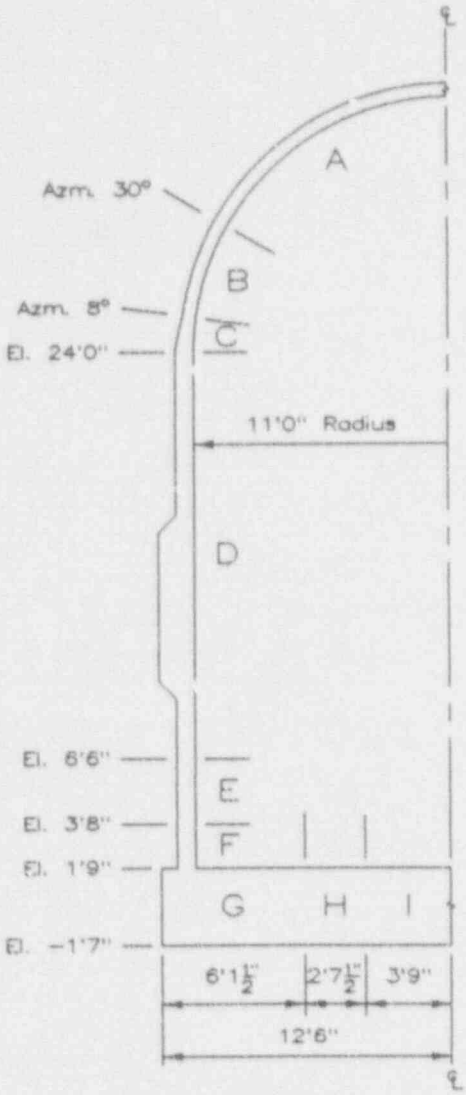

Net Reinforcement Ratio

Dome	A	B	C
ρ_ϕ meridional	0.0148	0.0175	0.0124
ρ_θ circumferential	0.0143	0.0173	0.0215

Wall	D	E	F
ρ_v vertical	0.0124	0.0225	0.0271
ρ_h hoop	0.0215	0.0215	0.0215

Basemat	G	H	I
ρ_r radial	0.0045	0.0058	0.0040
ρ_θ circumferential	0.0046	0.0053	0.0040

Fig. 2.3 Net Reinforcement Ratios (excluding liner)

2.2 Material Properties

2.2.1 Reinforcing Steel

The reinforcing steel used for construction of the containment model consisted of deformed bar sizes No. 3, No. 4, No. 5, No. 6, and some imported 6 mm (0.24 in.) diameter bars. Tensile strength tests were performed on samples of all bar sizes except for the No. 6 bars. Four samples of each bar size of the 6 mm, No. 3, and No. 5 bars were tested and twenty samples of the No. 4 bar were tested. The No. 4 bars represent a majority of the reinforcing steel provided for the containment model. The mean yield strength and fracture strength for these bars were 64 ksi and 102 ksi, respectively. Strength statistics for all bars tested are summarized in Table 2.1. A representative stress strain curve for a No. 4 bar is shown in Figure 2.4. Further details on the results of tests on reinforcing steel were reported in reference 2.3.

Table 2.1 Reinforcing Bar Tensile Strength

Bar Size	No. Samples	Mean Yield Load lb	Mean Maximum Load lb	Yield Strength psi	Ultimate Strength psi
6mm	4	3340 (60)*	4330 (70)	76,200	98,800
No. 3	4	7160 (130)	11020 (190)	65,100	100,200
No. 4	20	12730 (280)	20440 (380)	63,600	102,200
No. 5	4	21240 (310)	32850 (300)	68,500	106,000

*Numbers in parenthesis indicate the standard deviation in lbs.

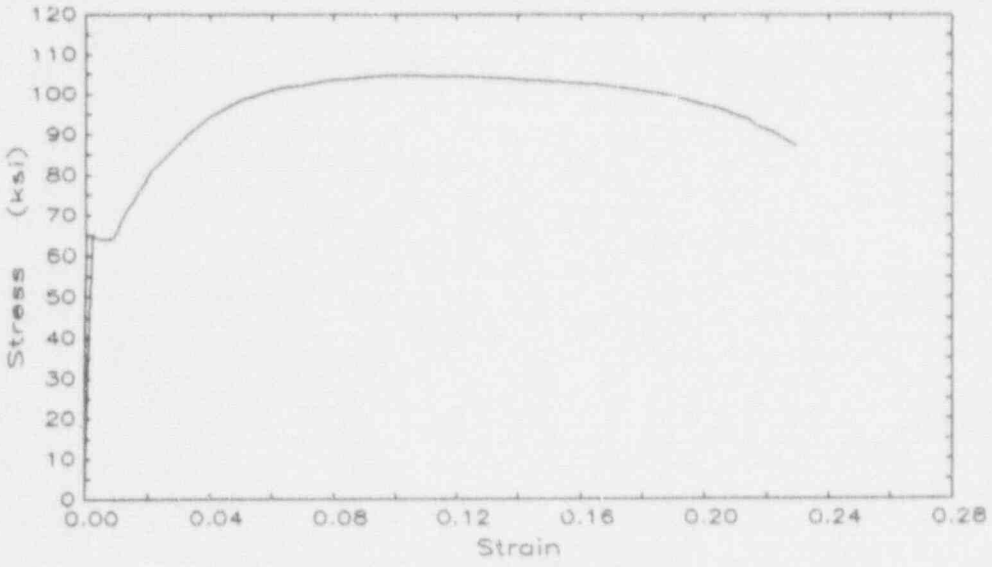

Fig. 2.4 Typical Stress-Strain Curve for No. 4 Reinforcing Bar [Ref. 2.3]

2.2.2 Liner Steel

The containment model was provided with a steel liner attached to the inside surface of the concrete shell. The nominal liner thicknesses of the liner plate attached to the cylinder wall and to the basemat was 1/16 in. and the liner plate attached to the dome was 1/12 in. Actual liner thicknesses for the wall and dome material were 0.068 in. and 0.090 in., r ectively. Four samples of each liner thickness were tested for uniaxi sile strength. Half of the samples were tested in their rolling dire nd half were tested transverse to thei rolling direction. Mean yie trength and fracture strength for the liner placed on the cylinder wall ar basemat were 2250 ksi and 70 ksi, respectively. The rolling direction and o tation did not significantly influence the tests. A summary of strength statistics for the liner material is presented in Table 2.2. A representative stress strain curve for the liner is shown in Figure 2.5. Further details on the results of additional chemical, metallurgical, and mechanical tests on liner material were reported in reference 2.3.

Table 2.2 Liner Material Tensile Strength

Thickness	No. Samples	Mean Yield Strength ksi	Mean Ultimate Strength ksi
0.068 in. RD*	2	50.2	69.7
0.068 in. TD	2	49.4	70.6
0.090 in. RD	2	50.7	69.8
0.090 in. TD	2	52.4	69.6

* RD: Tested in liner rolling direction.
TD: Tested transverse to rolling direction.

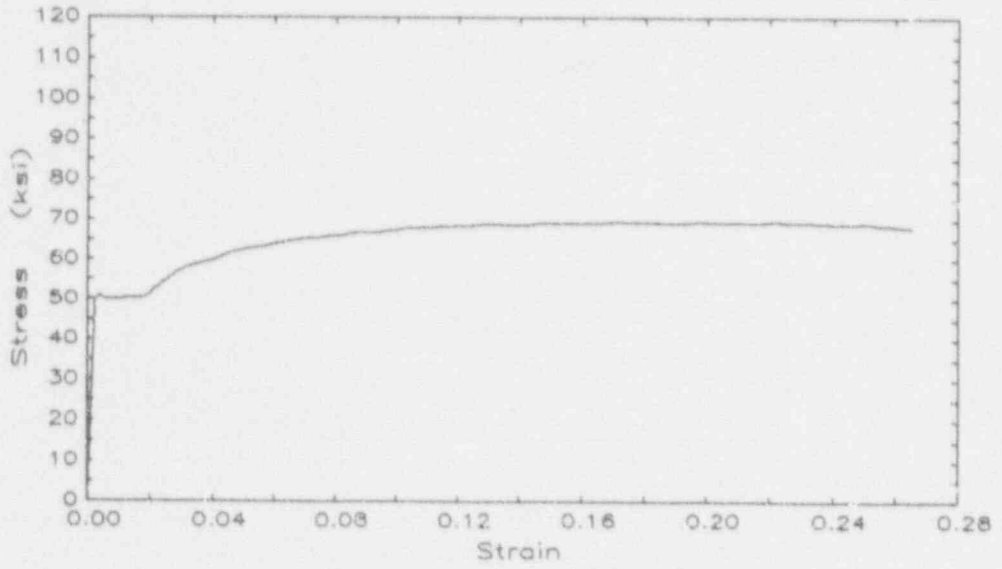

Fig. 2.5 Typical Stress-Strain Curve for 0.068-in. Liner [Ref. 2.3]

2.2.3 Concrete

The concrete supplied for the containment model was composed of normal weight aggregates having a nominal maximum size of 3/8 in. The net water/cement ratio was 0.53. The slump of concrete placed in the wall was approximately eight inches. The slump of concrete placed in the base and dome was slightly less. All concrete was placed in a sequence of eleven lifts. The first lift, forming the basemat, was placed December 13, 1985. The second through final lifts, forming the wall and dome, were placed March 13 through May 15, 1986 [Ref. 2.1].

Approximately nine to eleven standard size (6 by 12 in.) cylinder samples were cast with each lift and later tested for uniaxial compressive strength, for split cylinder tensile strength, and for direct tensile strength. At

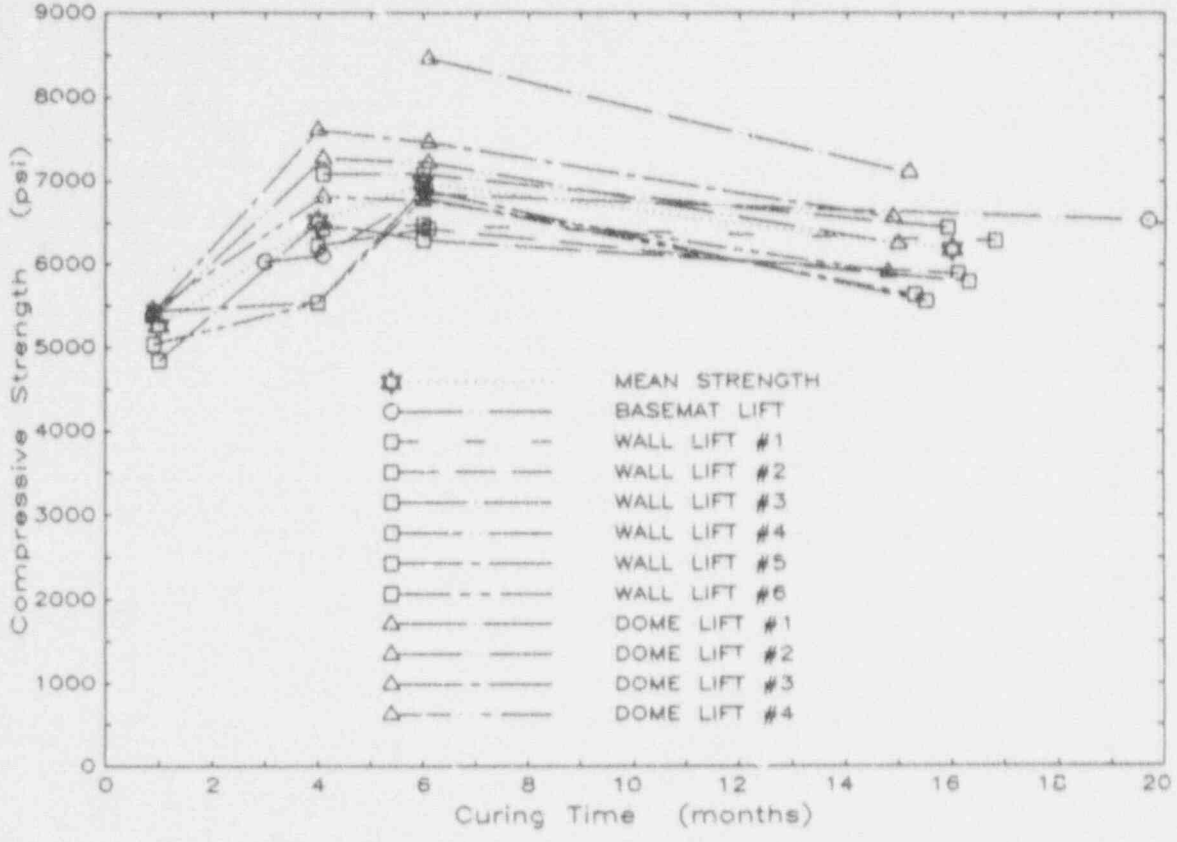

Fig. 2.6 Uniaxial Compressive Strength of Concrete Cylinder Samples

least 30 of the total 109* concrete samples cast were initially cured in a water tank for the first two to four months. Curing conditions for the other samples is not known.

Cylinders were tested at ages of one, four, and six months, and at the containment pressurization. At this time the samples from the wall and dome lifts had aged 15-17 months and those from the basemat had aged 20 months. Data for the uniaxial compression, split cylinder tension, and direct tension tests are shown in Figures 2.6 through 2.8, respectively. Each point in the figures represents the test of one cylinder per lift. Straight lines connect data from the same lift and track the strength development over time. Figure 2.6 indicates that the compressive strength of the cylinder samples increased with age up to six months but decreased at sixteen months. The variation of strength with time follows the same pattern for the tensile strength tests (Fig. 2.7, 2.8).

---

* An independent testing lab cast and tested approximately 443 additional cylinders for compressive and split-cylinder tensile strength. These tests conformed to ASTM specifications and were the basis for quality control and acceptance of each batch of concrete. These tests were made on cylinders which had aged primarily 28 days or less. Further information on these tests is available from the staff at SNL. The data from the concrete tests reported herein are from tests conducted at Sandia by their technicians.

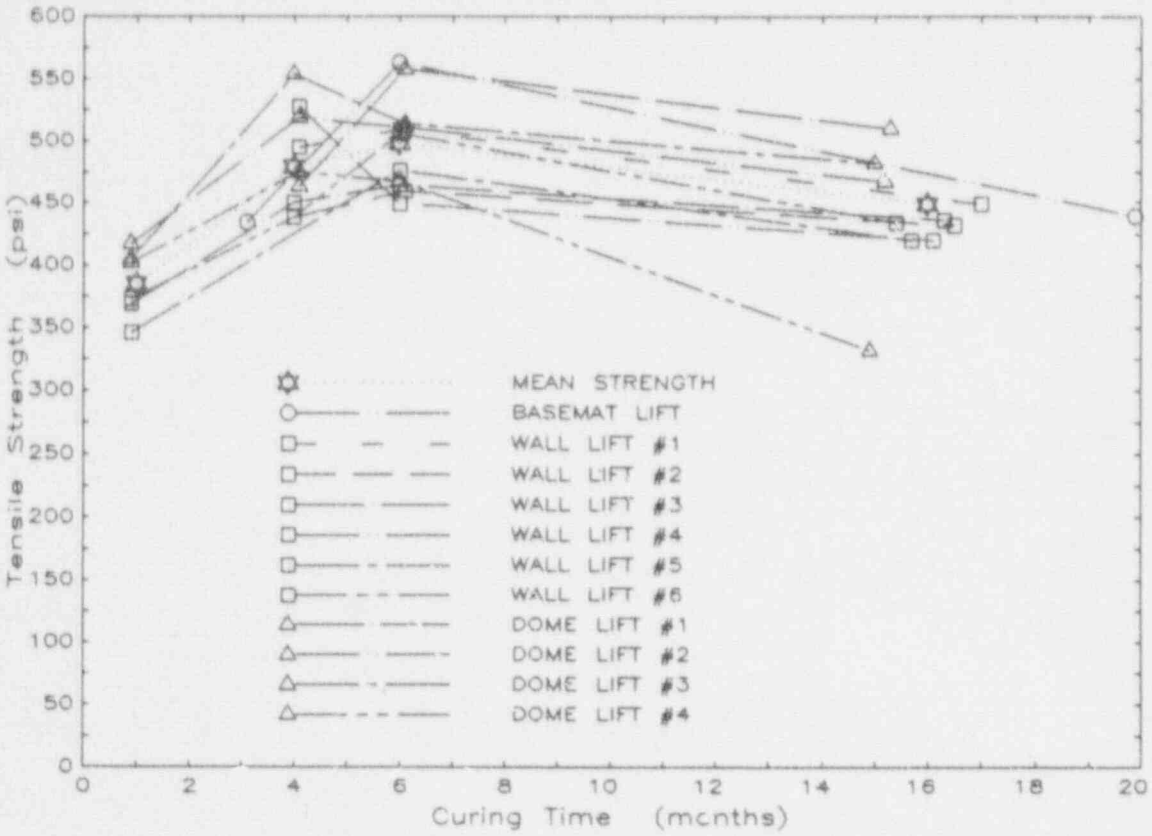

Fig. 2.7 Split-Cylinder Tensile Strength of Concrete Cylinder Samples

The technician responsible for the cylinder sample tests made comments regarding the validity of the strength data obtained from each cylinder sample test.* His comments suggest that of the 42 samples tested in compression one sample may be discarded because it did not fail prior to reaching the testing machine capacity. All of the 38 samples in the split cylinder tensile test appear valid based on the test procedure. Of the 29 direct tensio. tests only eleven may be considered to represent an estimate of direct tensile strength. Most of the other "dog-bone" shaped specimens failed due to pull out of the anchorage prior to cracking within the necked-down region.

Mean values for compressive and split cylinder tensile strength are calculated at curing ages of one, four, six, and sixteen months (Table 2.3). These values are shown on the strength development curves (Fig. 2.6, 2.7). Mean values for direct tensile strength are not calculated because of the paucity of good data. An indication of the concrete quality is the coefficient of variation (c.o.v.) associated with the mean sample strength. This cannot be estimated from the data because only one cylinder from each lift was tested at a particular age.

---

* M. McNamee, "1/6-Scale Containment Model Concrete Cylinder Strength Test Reports," Sandia National Labs, Albuquerque, March 1986 - August 1987.

Table 2.3 Compressive and Split-Cylinder Strength of Concrete Samples

Curing Age	Compressive Strength		Split-Cylinder Tensile Strength	
	sample number	psi	sample number	psi
28 days	6	5260	6	385
4 months	10	6520	10	479
6 months	11	6980	11	498
at test date	11	6180	11	449

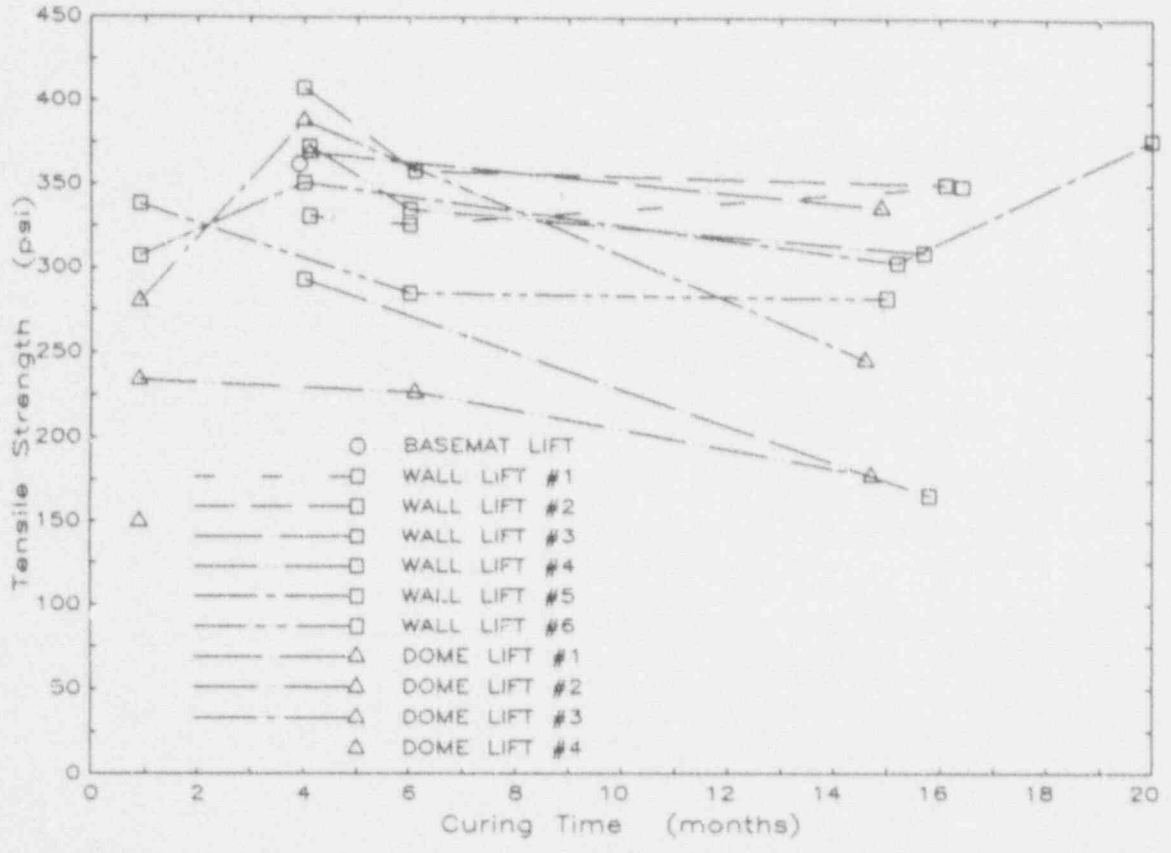

Fig. 2.8 Direct Tensile Strength of Concrete Cylinder Samples

It should be noted that the strength indicated by the concrete sample tests is not necessarily the same as that in the test structure. Casting and curing conditions were different. However, it is convenient to have an index value for concrete strength for projections to be made about the shear strength of the cylinder walls. The estimate of the compressive strength of cylinder samples at the time of the containment model pressurization is 6200 psi. The corresponding estimate for split cylinder tensile strength is 450 psi. Unless otherwise specified, throughout this document the value used for the compressive strength of concrete, indicated by f'_c, is 6200 psi.

2.2.4 Change in Concrete Strength with Age

Measured strength for concrete cylinder samples from the containment model increased for the first six months and then decreased. It is customarily assumed that, barring unusual curing conditions and/or mix, concrete compressive strength is likely to increase with time or to remain at the same level. The trend in measured compressive strength raises doubt about the strength of the cylinder samples at the time of the containment model test. It is uncertain whether the mean cylinder strength at the time of testing ought to be represented by the maximum strength (7000 psi) measured in cylinders aged six months, or by the decreased strength (6200 psi) measured in cylinders aged approximately sixteen months. A literature search was performed to determine if there was precedence for this decrease in strength with age.

2.2.4.1 Previous Research on Curing

Results of research on the influence of curing on concrete strength indicate that certain curing conditions have a marked effect. Klieger [Ref. 2.5] investigated the effect of various mixing and curing temperatures on compressive and flexural (unreinforced beam) strength. Price [Ref. 2.6] summarized numerous conditions (including materials and mix proportions, curing, accelerators, rate of load, and deterioration) influencing concrete strength. His research was aimed at understanding to what extent a value assigned to the 28-day strength of 6 by 12 in. control cylinders is representative of the compressive strength of the in-place structure. Neither Price nor Klieger address specifically the variation of strength with time and its likely causes. This topic is of particular importance because in a construction atmosphere where a limited number of control cylinders are cast and tested at intervals, a false confidence in concrete strength can arise as a result of early tests if that concrete is later subjected to curing conditions that may cause strength to decline.

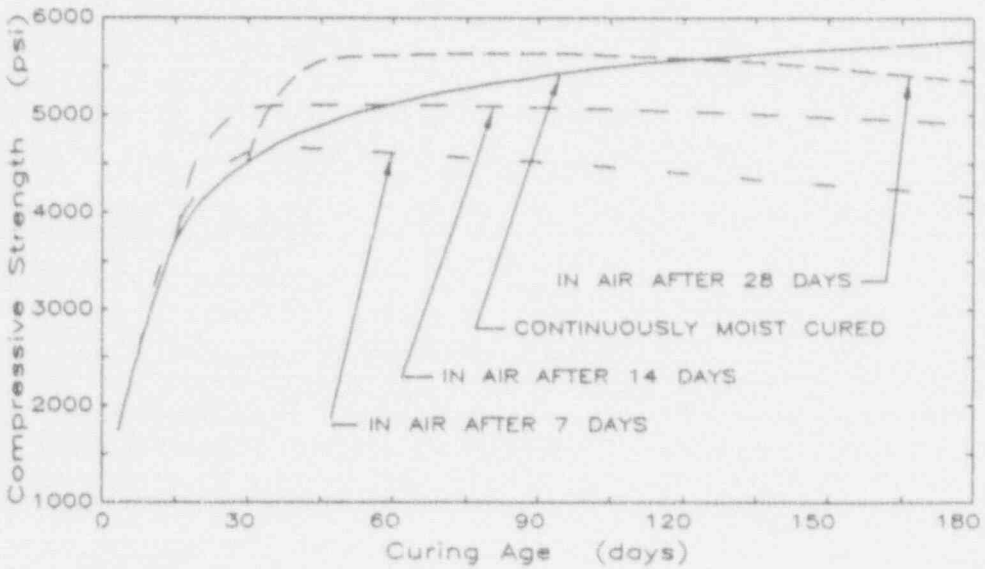

Fig. 2.9 Effect of Air Drying After Initial Moist Curing on Concrete Strength Gain with Age [Data from Ref. 2.6]

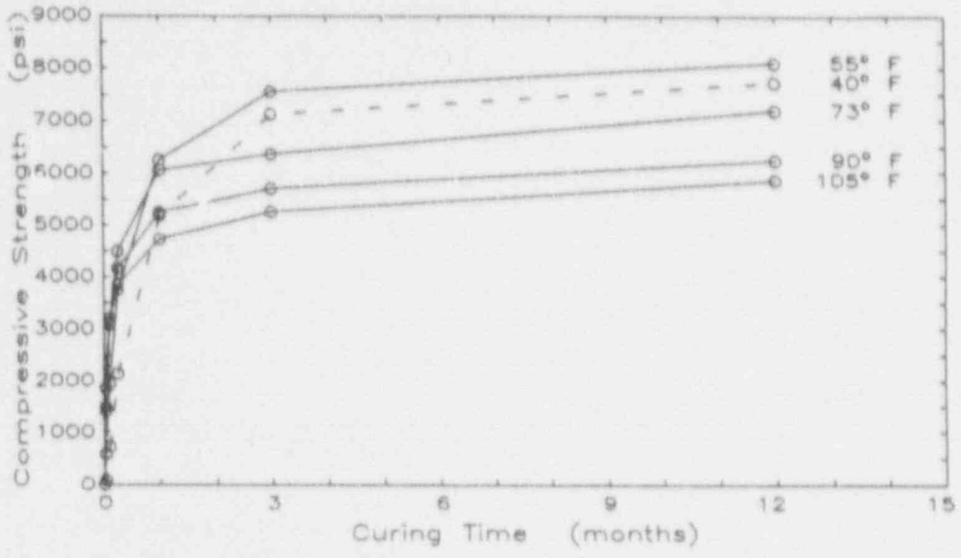

Fig. 2.10a Effect of Moist Curing on Concrete Strength Gain
[Data from Ref. 2.5]

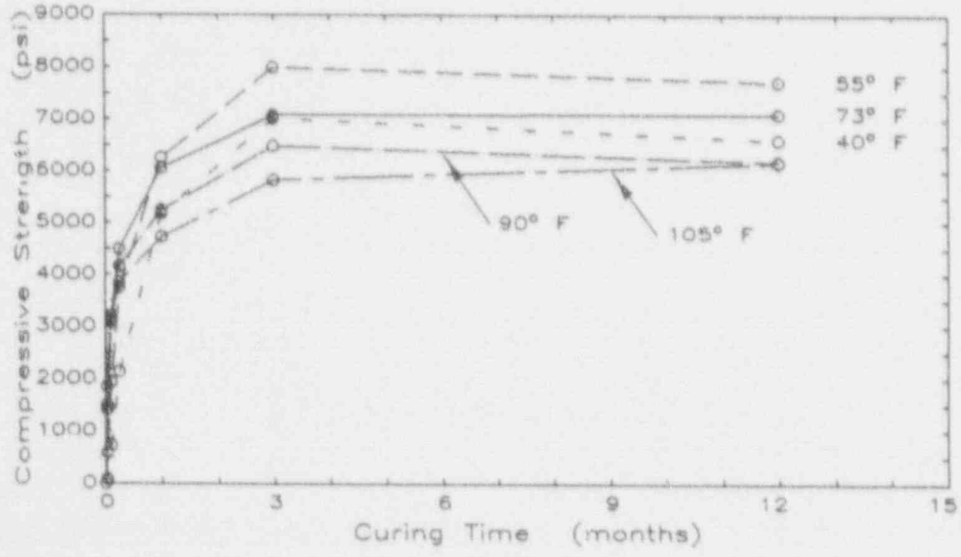

Fig. 2.10b Effect of Dry Curing on Concrete Strength Gain
[Data from Ref. 2.5]

Data from Price (Fig. 2.9) indicate that the strength of cylinders cured moist at 70°F over a six month interval continues to increase. Cylinders from the same batch that were initially moist cured for 7, 14, or 28 days and then exposed to laboratory air showed first an increase in strength after exposure, followed by a decrease in strength for the remainder of the six months. Klieger provides data from six inch modified cubes which exhibited a similar rise and decline in strength when cured initially moist and then dried. In Figure 2.10a data is shown from five groups of cubes cured at 100% relative humidity (RH) over a year at temperatures ranging from 40°F to 105°F the first 28 days and thereafter at 73°F. In Figure 2.10b data are shown for

five groups of cubes cured under the same conditions the first 28 days but thereafter at 50% RH and 73°F. These concrete samples cured moist for 28 days and then dried had a greater strength at three months than companion samples kept continuously moist. However, the strength of concrete that was dried was less at twelve months than at three months.

2.2.4.2 Other Relevant Strength Data

The variation of concrete strength with time has been measured in other construction and research projects where the influence of curing condition was not an issue. A comparison is shown in Figure 2.11 of the mean compressive strength of the 1/6-scale containment model cylinder samples to cylinders cast during the construction of a reinforced concrete tall building [Ref. 2.8] and to cylinders cast during a University of Illinois research project on column strength [Ref. 2.7]. It is interesting to note how the mean cylinder strengths at one, four, six and sixteen months for the containment model compare (Fig. 2.11). Russell and Corley [Ref. 2.8] report strength variation over time for five different design strength mixes used to construct Water Tower Place, Chicago. Each plotted point (Fig. 2.11) represents the mean of eight cylinders from the same batch. All cylinders were cured moist for seven days after which some were cured, "within a sheath of copper foil to simulate moisture conditions in large columns," while the others were stored at 50% RH and 73°F. Richart and Brown [Ref. 2.7], in the third series of their comprehensive column strength study, examined, among other variables, the influence of moist and laboratory air storage on the strength of 153 short columns. All cylinder samples from the test columns were cured moist at room temperature for the first two months. For the subsequent twelve months half were exposed to laboratory air while the others were kept moist. Each plotted point (Fig. 2.11) for the 3500 and 5000 psi design mixes represents the mean of approximately 50 sample cylinders. Straight lines are drawn in the figure to connect the two and fourteen month mean values to track similar batches and curing conditions. They are not meant to imply that strength development with time was linear.

2.2.4.3 Conclusion on Concrete Strength

The conventional wisdom that concrete strength increases with time or remains the same applies strictly to concrete cured continuously moist. The influence of moisture availability has not been emphasized in the technical literature [Ref. 2.5, 2.8] and this may explain the popular concept that concrete strength increases steadily during the early life of the structure.

The data presented in Figures 2.9 to 2.11 represent concrete mixes of normal proportions and typical design strengths. There were differences in curing, identified above, between concretes that have been cured moist and those that have been dried after moist curing. Despite these differences, except for long-term moist curing, none of the curing regimes can be classified as nontypical. Moist curing of concrete samples for up to a year, as was done by Klieger [Ref. 2.5], is highly unusual since it is seldom done for a civil engineering structure. Comparing the strength of the containment model sample cylinder with the evidence presented, it is concluded that the compressive strength of the concrete samples tested at the time of test, 6200 psi, is appropriate. There is no evidence to suggest that the result at 16 months was due to sampling procedure or improper materials.

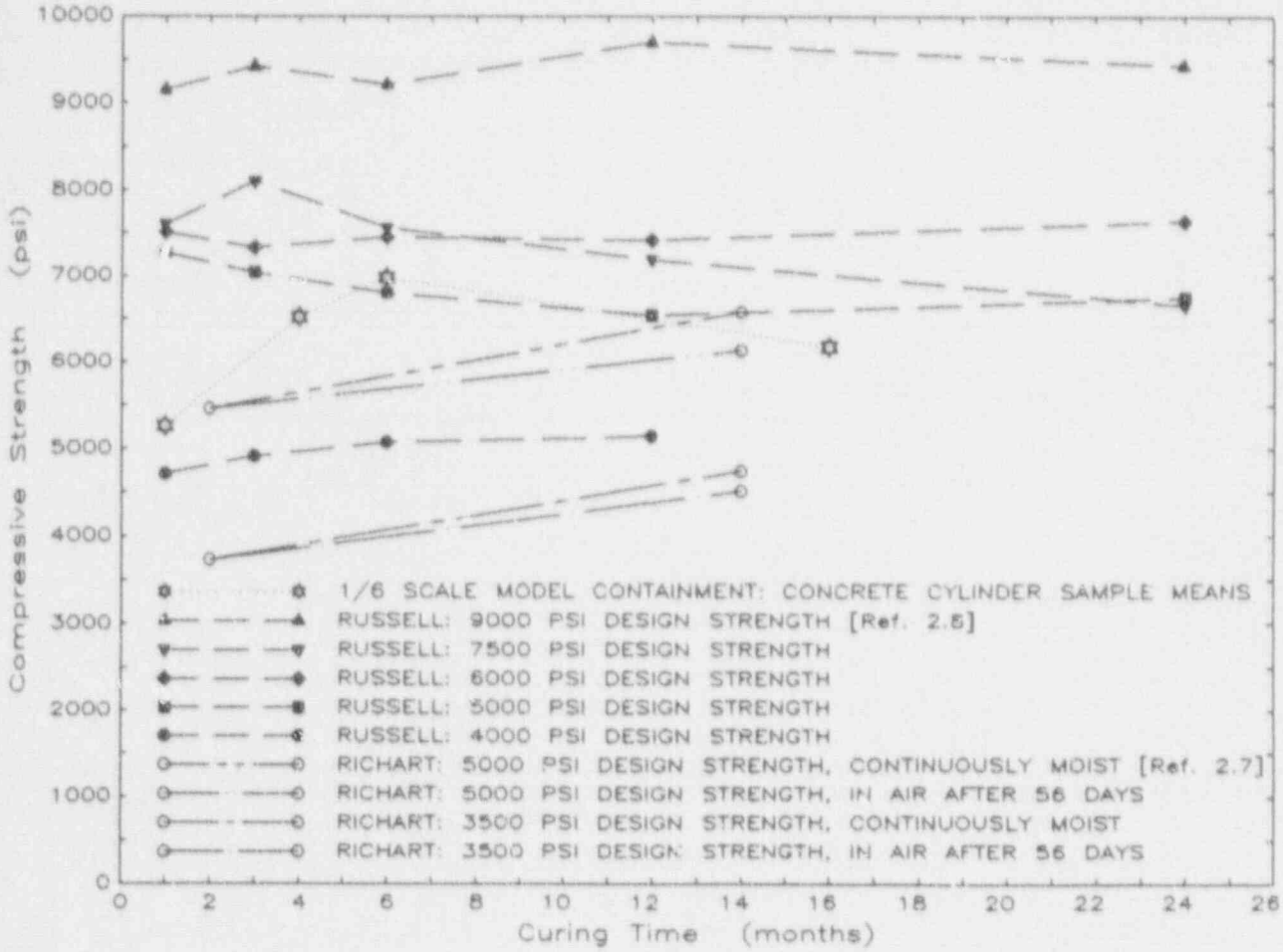

Fig. 2.11 Data from Several Concrete Compressive Strength Gain Tests

3. TESTS AND INSTRUMENTATION

A primary purpose for the construction and testing of the containment model was to generate data that could be used to validate numerical methods for predicting the performance of LWR reinforced concrete containment structures during severe accidents. The containment model was subjected to a series of internal pressurization tests in July 1987. During these tests approximately 1100 strain gages and displacement transducers were used to monitor the response.

In this chapter a general description is presented of the pressurization tests and instrumentation of the containment model. Details are provided on the instrumentation at the wall-basemat connection. Strain and displacement values measured during each pressure test were recorded independently. Because the gage readings were re-zeroed before each test, a procedure was developed to align the data so that a continuous record of structural response could be identified with each gage. The alignment includes the effects of the Structural Integrity Test (SIT) loading with the structural response measured during the High Pressure Test (HPT). This alignment procedure is described at the end of this chapter and is illustrated with example plots of representative data. Further details on the tests and instrumentation are available in references 2.2 and 3.1.

3.1 Pressurization Tests

The containment model was subjected to a series of pressure loadings during July 1987 (Table 3.1). The model response was recorded by strain and displacement gages during the first test, the SIT, and during the final test, the HPT. The SIT required two attempts as described in Section 3.1.1. The intervening loadings were conducted to perform leak rate tests on the containment model and on one of the equipment hatches. Strain and displacement data were not collected during these leakage tests.

3.1.1 Structural Integrity Test

The SIT was conducted during July 6-10, 1987 according to procedures in article CC-6000 of the ASME code [Ref. 2.4]. The containment was pressurized by dry air in 4-5 psig pressure steps to 53 psig, or 115% of design pressure. Crack mapping was performed at six locations about the exterior of the structure just before the test, at the completion of the test, and at six pressure steps during the test. The SIT pressurization schedule, including crack mapping and data scan intervals, is summarized in Table 3.2.

At the first SIT attempt (July 6), pressure was increased to 12 psig and several of the gage readings appeared inconsistent with the load level. The test was stopped and pressure was released so that a bad connector on one of the data acquisition units could be replaced. The SIT was subsequently restarted on the morning of July 8 and all transducer readings were rerecorded. On the second attempt the SIT proceeded without interruptions until the final unloading on July 9. Five additional data scans were taken the following day after the structure was unloaded. The total elapsed time with the structure under pressure was approximately 36 hours.

Table 3.1 Complete Pressurization Schedule*

Date (all 1987)	Test Name	Strains and Displacements Recorded	Pressure Range	Test Description
July 6-10	Structural Integrity Test (SIT)	yes	0 ~ 53 ~ 0 psig	slowly increasing and decreasing over 36 hours
July 11-13	Integrated Leak Rate Test (ILRT)	no	46 psig	held at constant pressure 50 hours
July 13	ILRT with 0.137 in. orifice	no	56.4 ~ 53.6 psig	slow leak allowed over 4 hours
July 14	Equipment Hatch B Unseating	no	53 psig	held at constant pressure half day
July 15-16	ILRT with 0.070-in. orifice	no	57.1 ~ 51.4 psig	slow leak allowed over 22 hours
July 28-29	High Pressure Test (HPT)	yes	0 ~ 145 psig	slowly increasing over 32 hours until termination due to excessive leakage

*Data summarized from:

D. S. Horschel, "Quick Look Report on the Low Pressure Testing of a 1/6-Scale Reinforced Concrete Containment Building," Sandia National Laboratories, Albuquerque, New Mexico, July 1987.

D. S. Horschel, "High Pressure Test Briefing," Sandia National Laboratories, Albuquerque, New Mexico, August, 1987.

3.1.2 Leakage Tests

Four separate leakage tests were conducted after the SIT. For each test the containment model was held at about a constant pressure level while leakage out of the containment was measured. Three of these tests were conducted as Integrated Leak Rate Tests (ILRTs) while the fourth was an equipment hatch unseating test. The first ILRT was conducted over a 50-hour period with the internal containment pressure maintained at 46 psig. Two other ILRTs were conducted over a 4 or 22-hour period with small diameter orifices installed so that pressurized air within the containment was allowed to pass through them. During these tests the air within the containment was pressurized to approximately 57 psia and was then allowed to escape (Ambient

Table 3.2 Structural Integrity Test Pressurization Levels

Date	Data Scan	Pressure Level	Crack Mapping Number
July 6, 1987			1
July 8, 1987	1	-0.05 psig	
	2	5.33	
	3	12.31	2
	4	16.44	
	5	20.51	
	6	20.46	3
	7	20.47	
	8	27.05	
	9	34.69	
	10	34.53	4
	11	34.53	
	12	39.70	
	13	45.90	
	14	45.65	5
	15	45.62	
	16	50.10	
	17	53.47	
	18	53.29	6
	19	53.21	
July 8	20	50.49	
July 9	21	46.14	
	22a	46.13	7
	22b	44.97	
	23	38.98	
	24	33.99	
	25	33.96	
	26	26.83	
	27	21.88	
	28	21.90	
	29	16.69	
	30	11.74	
	31	11.77	
	32	5.05	
July 9	33	0.02	
July 10	34	-0.04	
	35	-0.02	
	36	-0.02	
	37	0.02	
	38	0.02	8

Table 3.3 High Pressure Test Pressurization Levels

Date	Data Scan	Pressure Level	Track Displacement Scan
July 28, 1987	1	9.89 psig	
	2	19.55	
	3	29.57	
	4	39.42	
	5	49.16	2
	6	54.50	
	7	59.57	3
	8	64.20	
	9	69.32	4
	10	74.16	
	11	80.16	5
	12	85.61	
	13	90.58	6
	14	95.69	7
July 29	15	100.92	8
	16	103.25	
	17	106.11	
	18	108.31	9
	19	111.08	
	20	113.24	10
	21	117.83	11
	22	120.92	12
	23	123.28	
	24	122.97	
	25	125.82	13
	26	125.60	
	27	127.84	
	28	130.19	14
	29	132.53	
	30	135.33	15
	31	134.42	
	32	138.35	
	33	140.16	16
	34	142.63	
	35	145.78	17
	36	142.52	
	37	0.22	18

pressure was approximately 12 psia). The pressure-unseating seals for equipment hatch B were tested over a half day with the internal containment pressure at 53 psig and the pressure within hatch B at 70 psig. A complete list of the pressurization tests is included in Table 3.1. Between each of the four leakage tests the pressure within the containment was maintained at approximately 46 psig.

3.1.3 High Pressure Test

The HPT was conducted on July 28-29, 1987. Nitrogen gas was introduced into the containment model initially in 10 psig steps up to 50 psig, and then in 5 psig steps up to the first sign of nonlinear structure response, which occurred at about 100 psig. Pressure was increased in 2-3 psig steps above 100 psig until the excessive gas leakage out of the containment terminated the test. The first indication of a leak occurred at approximately 125 psig [Ref. 3.1], when, based on acoustic measurements,* it appeared that there was leakage in the vicinity of Equipment Hatch B. Pressurization continued and additional leakage was noticed at 138 psig in the vicinity of Equipment Hatch A. The maximum pressure sustained was 145 psig. At this pressure the rate of leakage exceeded the rate at which gas could be delivered to the containment. The HPT pressurization schedule and data scan intervals are included in Table 3.3. The time elapsed with the structure under pressure was approximately 32 hours.

3.2 Instrumentation

More than 1200 data channels from gage instruments recorded the model response during the SIT and HPT [Ref. 2.2]. Data was recorded at discrete pressure steps for a total of 76 data scans during the two load cycles. Discrete and track mounted displacement transducers and inclinometers, or slope sensors, recorded the overall response. Many more sensors recorded local response. These included strain gages attached to the reinforcement, to the liner, or embedded within the concrete, and thermocouples attached to the liner or embedded within the concrete. A summary of the types and number of gages is included in Table 3.4.

Five pressure gages, which measured either gage pressure or absolute pressure, were provided at various locations within the model. Gage pressure data from gage P3, channel number 2, is used throughout this study as the reference pressure. The sections that follow give details for those sensors that provided the data on which the remaining chapters of this report are based: the reinforcement strain gages, the displacement transducers, and the track measurement system.

3.2.1 Reinforcement Strain Gages

A total of 297 strain gages were attached to reinforcement bars at various locations throughout the containment model and were oriented along the bar

---

* Acoustic sensors were placed near the equipment hatches and around the wall-basemat junction. These sensors could detect both steady-state noise, due to leakage, and impulse noises caused by concrete cracking.

Table 3.4 Instrumentation Summary

Gage type	No. Channels SIT data	No. Channels HPT data	No. Channels SIT and HPT data
Bonded rebar	29	29	29
Displacement	98	109	98
Embedment	17	17	17
Pressure	5	5	5
Rosette gage	483	483	483
Single gage	38	41	36
Strip gage	71	91	71
Track Mounted Displacement	0	18	0
T-Rosette	0	8	0
Thermocouple	72	73	72
Welded rebar	294	294	294
Total	1107	1168	1105

axis. Of these, 29 gages were bonded to reinforcement and 258 gages were welded directly to reinforcement. The only other weldable gages were 36 gages attached to the liner at the wall-basemat junction. The weldable gages were capable of measuring 6 to 7 percent strain according to tests conducted at Sandia [Ref. 2.2]. This is much greater than the strain that any of the bars in the containment experienced in the tests.

3.2.2 Displacement Transducers

A total of 109 displacement transducers recorded radial and vertical displacements of the wall and dome, basemat uplift, concrete crack opening, displacements of the equipment hatches and of a personnel airlock, and movement of the steel access structure inside the containment model. Radial displacements were measured by 26 transducers attached to the interior wall and connected by a thin wire to a ten-inch diameter vertical steel pipe at the center of the model. This central column was anchored to the containment floor and continued to elevation 19 ft 7 in. In this report it is assumed to provide a stationary point of reference. Twelve vertical displacement gages were attached to the inside wall surface at various elevations and were connected by thin vertical wires to the containment floor. Because these gages were attached to the floor and because it was observed during testing that the basemat lifted off its foundation, these gages were an indicator only of average vertical wall strain. The locations of the radial and vertical displacement gages attached to the wall are presented in Figure 3.1. Three displacement gages were provided about the exterior of the basemat (Fig. 3.6) at the 12 ft 6 in. radius, where the edge of the basemat meets the mudmat foundation. These gages indicated the uplift of the basemat. A fourth uplift gage was attached to the end of an arm cantilevered from the central column and recorded the vertical floor displacement at an 11 ft radius. Ten gages recorded the displacement of the dome normal to its surface. Eight gages added prior to the HPT monitored concrete crack opening across cracks incurred by the previous loadings. Five gages recorded relative displacements of the central column and the steel access structure. The remaining 44 gages recorded displacements of various parts of the equipment hatches and of one of the two personnel airlocks.

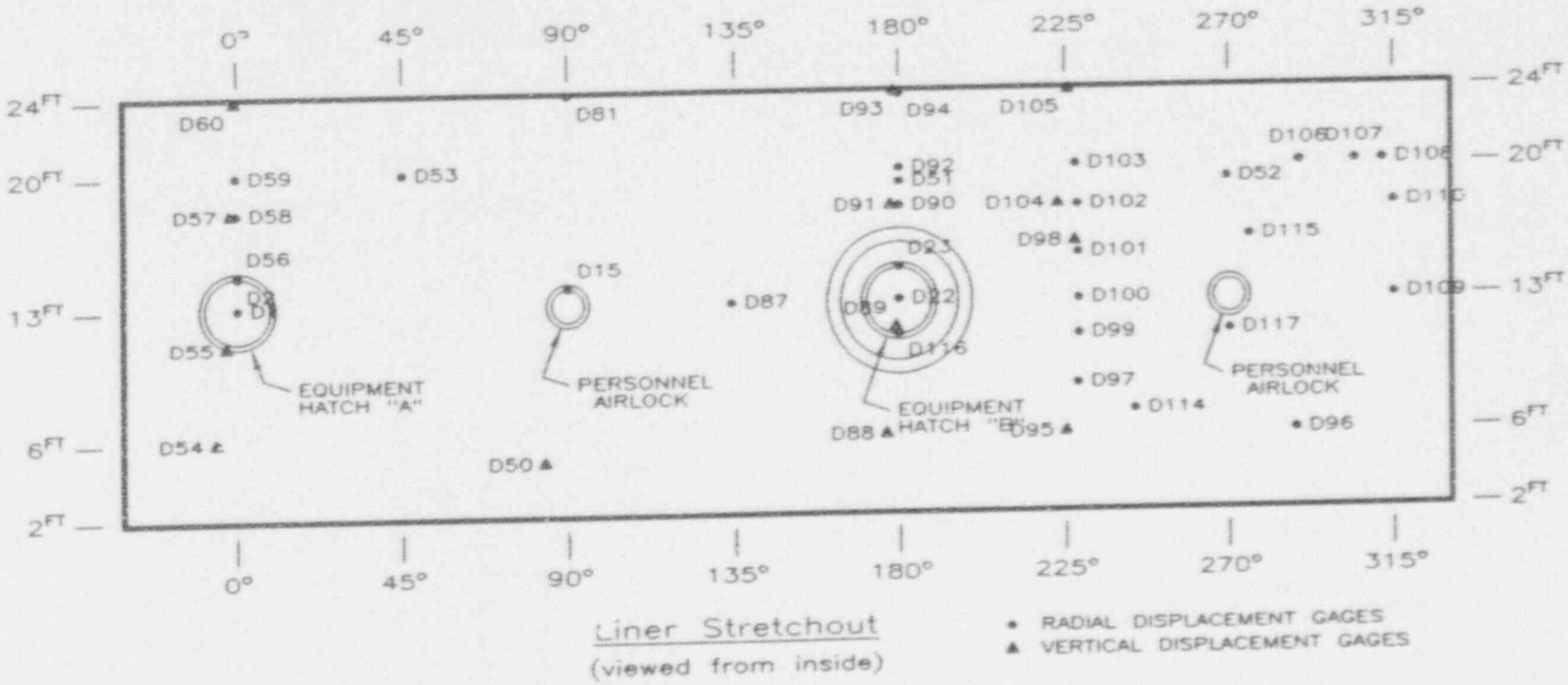

Fig. 3.1 Location of Radial and Vertical Displacement Gages on Cylinder Wall

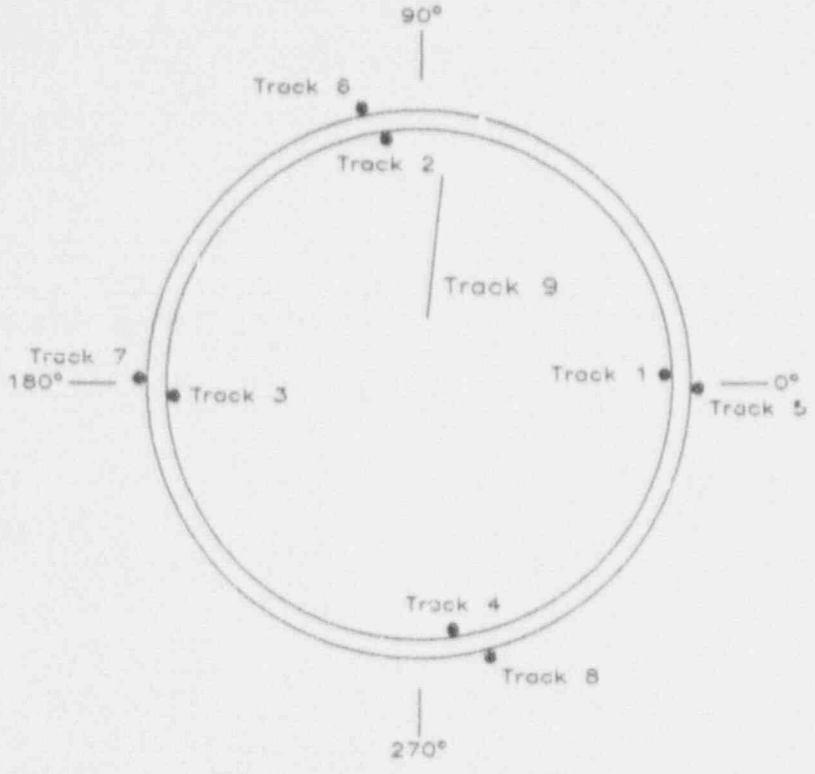

Containment Model Plan

Track	Location	Azimuth	Measurement Range			Elevation/Radius
1	Interior	2°	31.6	~	98.1 inches	elev.
2	Interior	98°	29.4	~	287.3	elev.
3	Interior	183°	31.6	~	97.6	elev.
4	Interior	278°	29.8	~	288.1	elev
5	Exterior	359°	26.0	~	100.0	elev.
6	Exterior	102°	27.3	~	268.3	elev.
7	Exterior	179°	28.1	~	101.6	elev.
8	Exterior	285°	26.2	~	267.1	elev.
9	Interior	84°	33.5	~	108.9	radius

Fig. 3.2 Location of Track Mounted Displacement Gages

3.2.3 Track Measurement System

Displacement transducers were mounted on horizontal or vertical fixed tracks and were able to move along the tracks to record a displacement profile (Fig. 3.2). The track measurement system recorded the response at 17 data scans during the HPT (Table 3.3). Eight of these tracks were oriented vertically allowing transducers to measure the radial displacement of the wall. Four tracks were located on the interior of the wall, four were located on the exterior, and the tracks were spaced at ninety degree intervals around the circumference. A ninth track was oriented horizontally along the containment floor. The track projected radially from the central column and measured the basemat uplift. Each track was provided with two displacement gages. One gage was oriented perpendicular to the track and mounted on a sliding truck. This gage measured the displacement from the truck to a roller that followed

the contour of the wall or floor. A second gage measured the distance along the track to the location of the sliding truck. The truck was powered by a system of cables and a motor fixed at the track end.

3.3 Gages at Critical Locations

Gages located within the basemat and at the junction of the wall and basemat are of a special interest because they provide the evidence needed to make an interpretation of the containment model behavior at this location. Reinforcement bars at these locations were heavily instrumented with strain gages.

3.3.1 Wall-Basemat Connection Detail

The eight principal layers of No. 4 reinforcement bars in the containment wall (Fig. 2.2) are supplemented at the wall-basemat junction by reinforcement provided to increase the radial shear and meridional bending capacity at this location (Fig. 3.3 - 3.5). An additional layer of vertical No. 6 bars (layer 10) is provided near the inside wall surface at 4.5-in. spacing to increase the meridional moment capacity. These bars are anchored by a 90 degree bend within the basemat and continue to elevation 6 ft 6 in. (Fig. 3.6). A layer of inclined No. 4 bars (layer 11) oriented at 45 degrees to a horizontal radius is provided at 4.5-in. spacing for added radial shear capacity. This layer extends diagonally to the bottom of the basemat and continues up the wall to elevation 3 ft 8 in. (Fig. 3.6). No. 3 diameter stirrups are also provided at the junction for added shear capacity. Of the eight principal layers of wall reinforcement, the two layers of vertical bars (layers 2 and 5) are anchored in the basemat by a 90 degree bend and the two layers of seismic bars (layers 7 and 8) continue into the basemat but are not hooked. The four layers of hoop reinforcement (layers 1, 3, 4, and 6) terminate within the wall at the top of the basemat.

Strain gages were installed on the vertical, seismic, hoop, inclined, and stirrup reinforcement in the wall-basemat junction region, mainly at three locations about the model: at 90, 210, and 330 degree azimuths. Figures 3.3, 3.4, and 3.5 illustrate the locations of strain gages at each of the three slices. Because the number of gages at the 90 degree azimuth slice (Fig. 3.3) are more numerous than at other locations, they provide the primary source of data used in subsequent chapters for behavioral interpretations. A total of 37 strain gages were installed on reinforcement at the 90 degree azimuth, 13 gages at the 210 degree azimuth, and 21 gages at the 330 degree azimuth.

3.3.2 Basemat Gages

The 40-in. thick basemat was provided with two sets of layers of reinforcement, at the top and at the bottom of the slab, connected by No. 3 ties. The bottom reinforcement consisted of No. 6 bars placed in two layers of orthogonal bars. The top reinforcement consisted of No. 5 bars placed in one layer of radially oriented bars atop a layer of concentric circular bars. The top radial bars at the center of the basemat are replaced by two orthogonal layers of parallel bars to alleviate congestion of reinforcement.

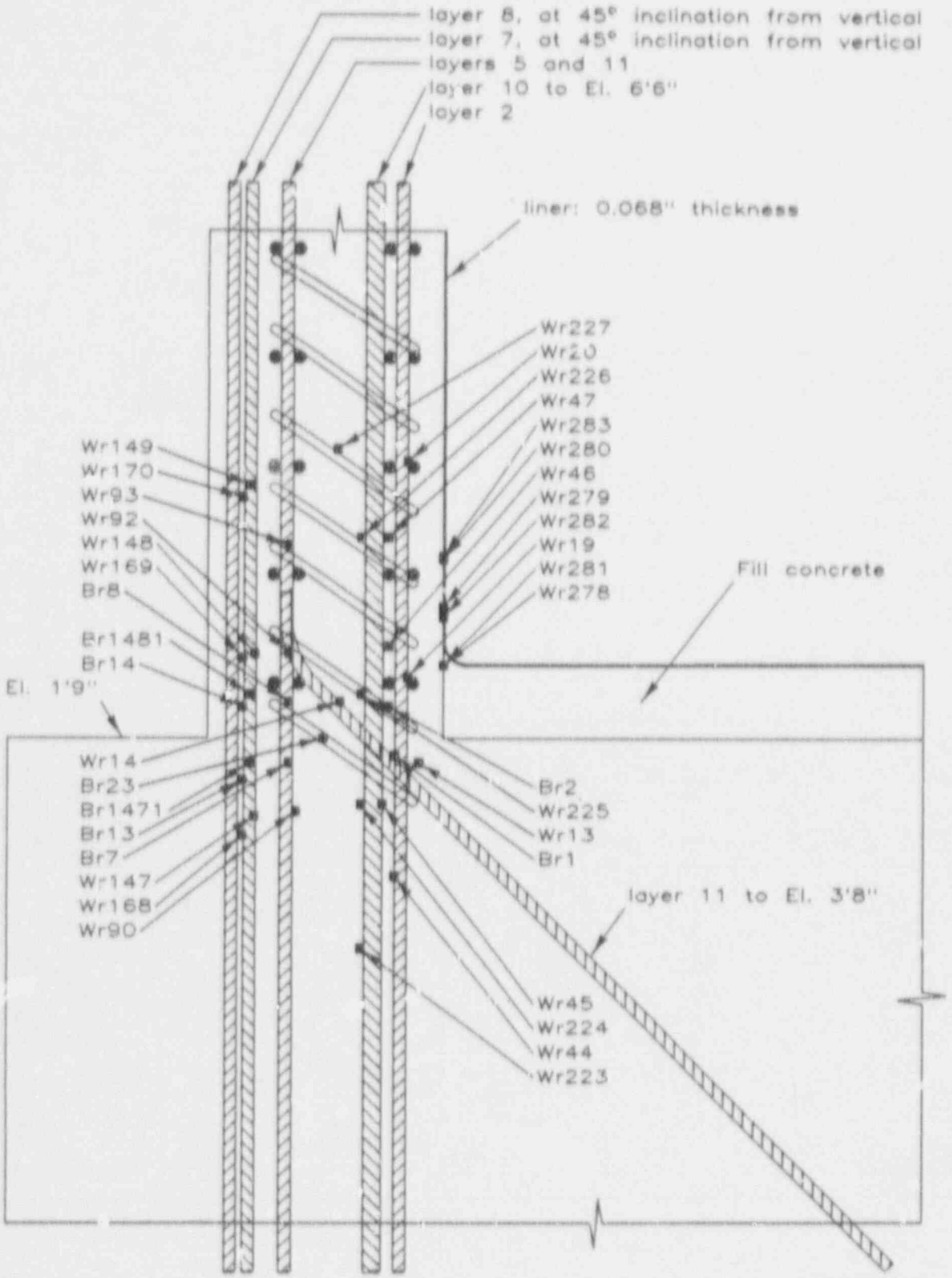

Fig. 3.3 Location of Gages at Wall-Basemat Junction at Azimuth 90 Degrees

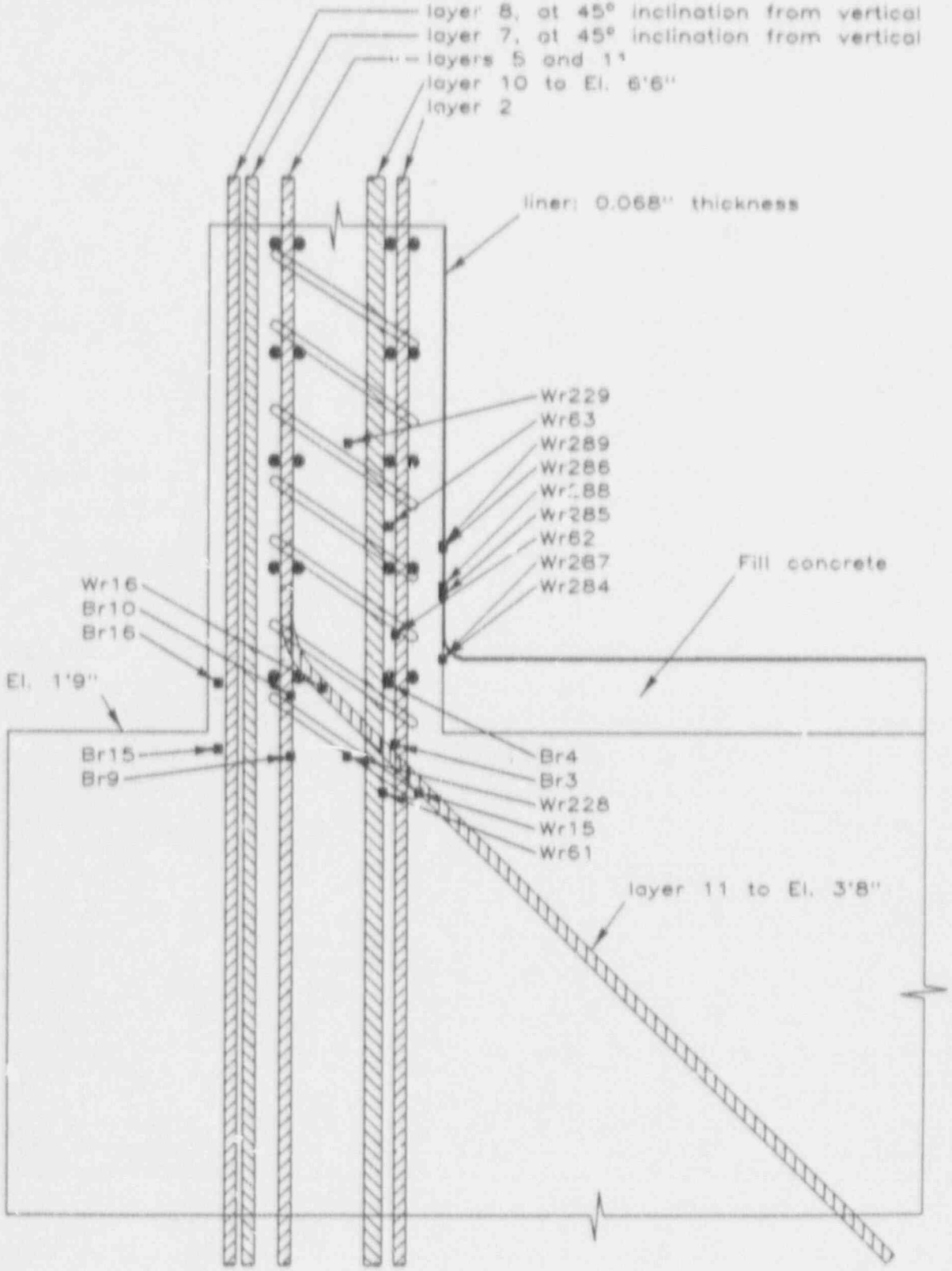

Fig. 3.4 Location of Cages at Wall-Basemat Junction at Azimuth 210 Degrees

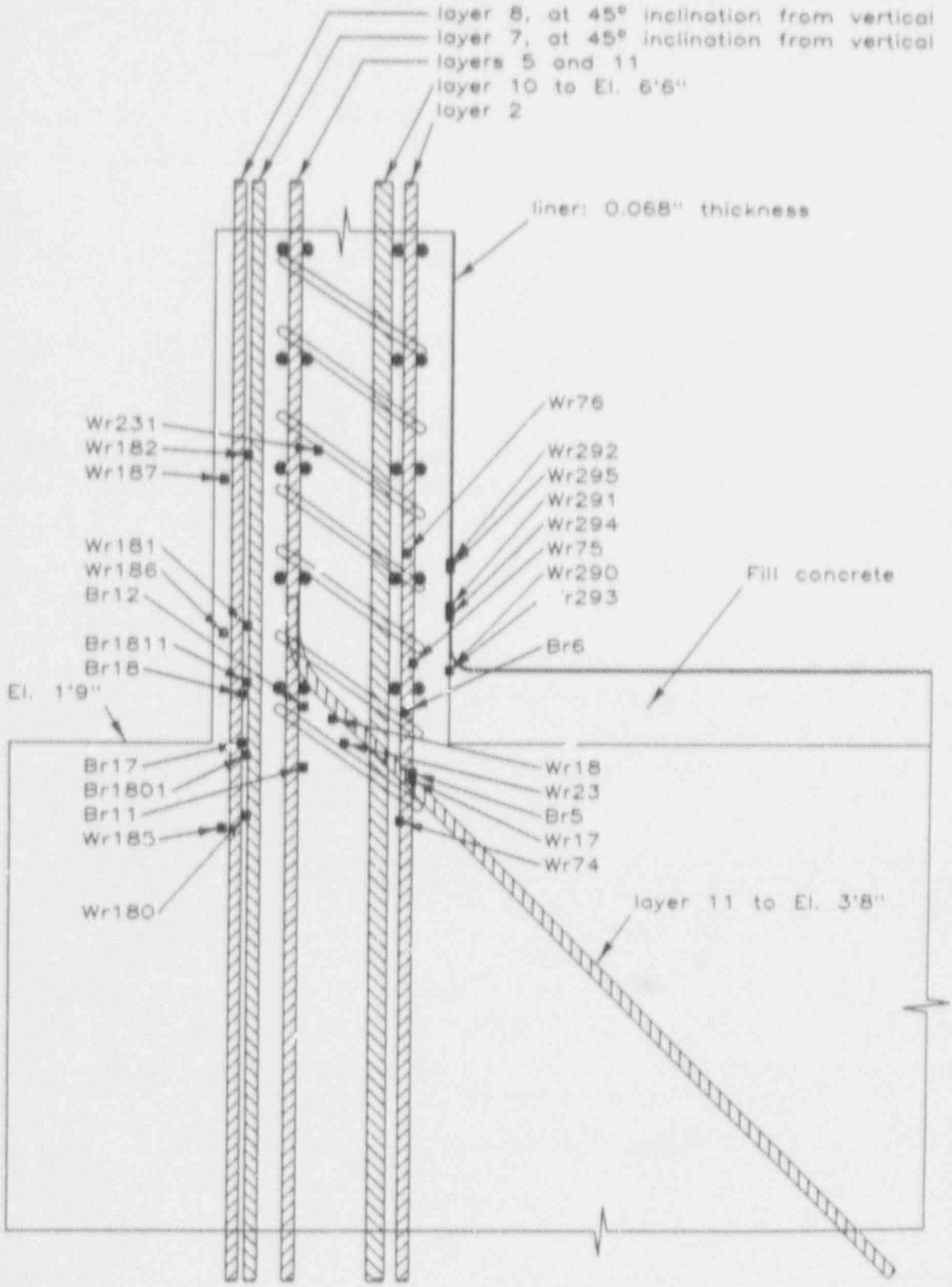

Fig. 3.5 Location of Gages at Wall-Basemat Junction at Azimuth 330 Degrees

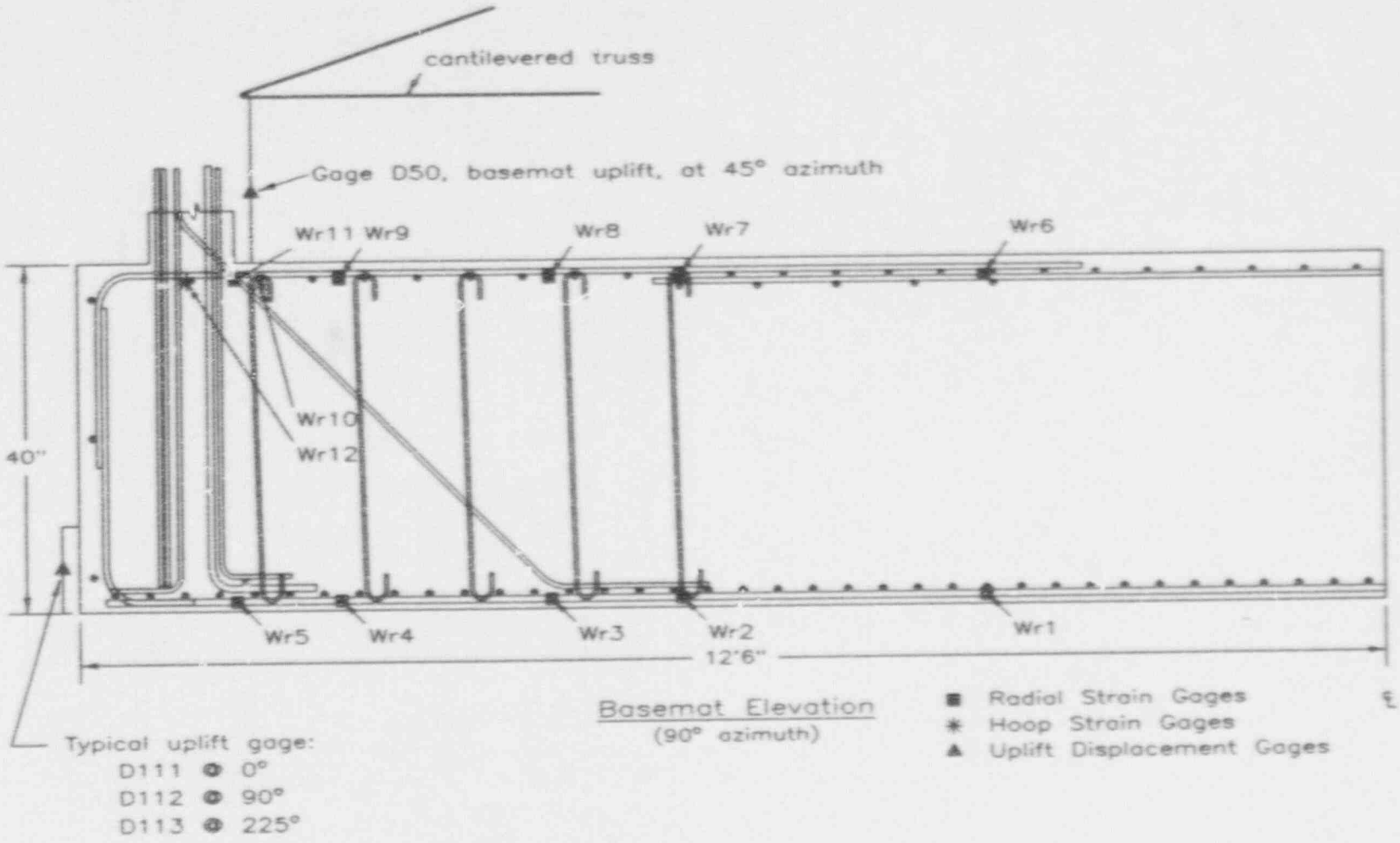

Fig. 3.6 Basemat Elevation at Azimuth 90 Degrees

Five strain gages were installed on a radially oriented top bar and five analogous gages on a straight bottom bar, located directly below it, at the 90 degree azimuth (Fig. 3.6). Although the bottom basemat bar is placed within an orthogonal grid, the particular bar on which the five strain gages were installed passes through the basemat center. Two strain gages were installed on two circumferential bars at the top of the basemat (Fig. 3.6).

3.4 Data Adjustment

Adjustments were made to the strain and displacement data (excluding track-mounted displacement data) obtained from Sandia. These adjustments were made to correct the apparent zero point of each gage and so that the effects of previous loadings would be included in data measured during the HPT. The adjustments to correct the apparent zero point for both SIT and HPT data effectively shift the origin of each gage slightly so that the trend in data for the first three data scans in each test appears to emanate from zero. Because the gage readings were re-zeroed before each test a shift in the measured HPT data is required to account for irreversible displacements incurred during prior loadings. The unloading history of SIT data is the basis for the permanent displacement set that occurred during that loading. Although the containment model was subjected to pressurizations (Table 3.1) after the SIT and before the HPT, these loaded the model to approximately the same or lower internal pressure than the maximum SIT pressure. The effect of these loadings on additional irreversible displacements is assumed to be negligible.

Three adjustments were made to measured data to determine the origin, the SIT end point, and the HPT initial point for each gage. The best method to determine the necessary adjustments is to produce plots of as-measured data and judge for each gage the relevant shifts required to make the data reflect the sequence of loadings. Due to the large number of data involved an automated procedure was developed and is described in the following paragraphs. Approximately 5 percent of the gage data were, however, adjusted individually because the curve-fitting operations employed did not represent well the measured values.

3.4.1 Adjustment of Initial Gage Readings

The data values for most strain and displacement gages were not based on an absolute zero point before the SIT. All SIT data obtained from SNL were shifted so that the initial loading curve begins at a zero gage reading.

The initial point of the SIT and of the HPT was determined through a linear least-squares regression of response quantity with respect to test pressure. In the accompanying figures of pressure versus response (Fig. 3.7 - 3.9), pressure values were plotted as ordinates and displacements or strain values as abscissae. This was done for comparison with figures derived from other structural engineering experiments in which displacement was the controlled load. In all calculations test pressure was regarded as the independent quantity, regardless of its position on the figures.

The regression calculation used three data points from data scans 2, 3, and 4, which correspond to pressures of 5.33, 12.31, and 16.44 psig, respectively

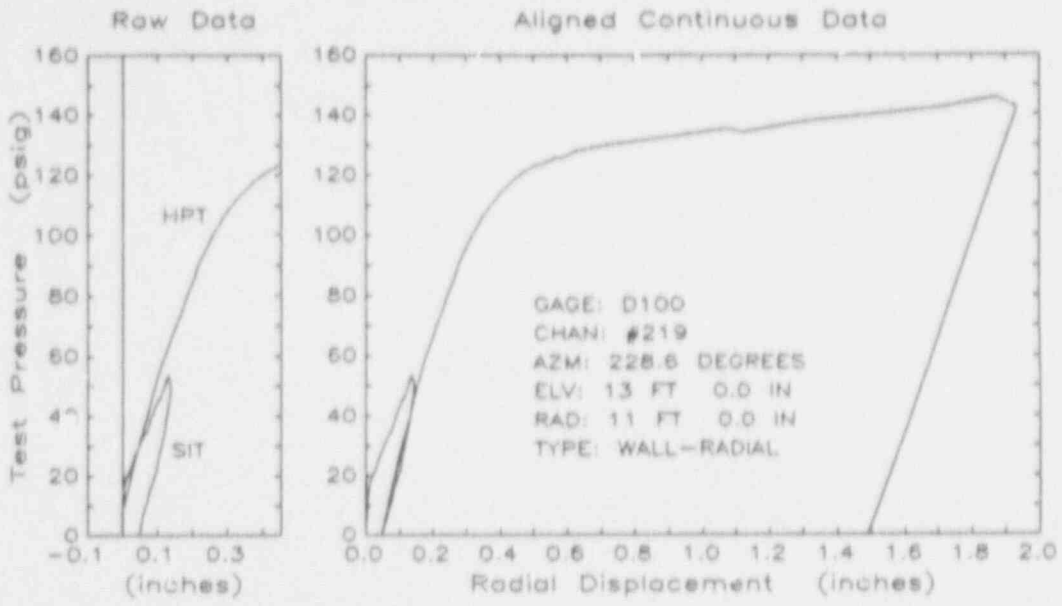

Fig. 3.7 Raw Data and Aligned Data for Gage D100

(Table 3.2). These three points represented model behavior before cracking (Section 4.1), in the realm where response was expected to be approximately linearly related to test pressure. Data scan no. 1 at a test pressure of zero was disregarded as it would have influenced the calculation. The response level at zero pressure was determined from the regression line and all SIT data points were arithmetically shifted so that this initial point was zero. In most cases the initial point determined through the regression was different from the response value at data scan no. 1. After shifting the SIT data all gage readings from data scan no. 1 (Table 3.2) were deleted from the modified data set and replaced with zeros.

3.4.2 SIT End Point

When the SIT and HPT data were examined concurrently, test values of displacement or strain were lower for equal load pressures during the HPT than during the SIT (Fig. 3.7 - 3.9). To correct this anomaly the end point of the SIT was determined and each channel of HPT data was adjusted so that the reloading data begins from this end point.

The SIT end point was found through a polynomial least-squares approximation of the unloading curve. The eight data points shown in Table 3.5 were selected for the regression calculation. For each data channel polynomials of first through fourth order were considered to suit the amount of nonlinearity in the data. The highest order polynomial was selected which resulted in a positive or zero curvature (change in incremental pressure with respect to response) at zero load pressure. Some of the gage measurements exhibited a fairly linear unloading curve. For these gages a straight line provided the best fit to data. Most of the unloading curves were nonlinear and required a second or third order curve to fit the data and result in a positive curvature at zero pressure. A few of the gages exhibited a highly nonlinear unloading curve and required a fourth order curve to produce a good

Table 3.5 Data Scans Used in Calculation to Determine SIT End Point

Data Scan No.	Pressure	Data Scan No.	Pressure
22B	44.97 psig	28	21.88 psig
23	38.98	29	16.69
25	33.96	31	11.77
26	26.83	32	5.05

fit to the data. Polynomials of higher order were not considered because the goal was to find a smooth curve which approximated the gage readings rather than to find a curve (of seventh order) which passed through the eight data points exactly. The value of the regression curve at zero pressure was defined as the end point to the SIT.

The SIT data set included six data scans after unloading at zero pressure (data scans 33 through 38, Table 3.2). Displacement or strain measurements were not uniquely defined at this pressure since they tended to oscillate. Therefore, none of the data values from the last six SIT data scans were used in the alignment procedure and were consequently discarded from behavioral interpretations.

3.4.3 HPT Initial Point

Before conducting the HPT (post-SIT) the gage readings were reset by SNL staff to zero. Examination of several channels of HPT data indicated that the initial point was different from zero. All HPT data were subsequently shifted so that the initial point coincided with the end point of the SIT unloading curve.

Linear regression was performed for the HPT data in the same manner as for the SIT data. The first three data values from data scans 1, 2, and 3, corresponding to test pressures of 9.89, 19.55, and 29.57 psig, respectively (Table 3.3), were used. The initial point for the HPT data was determined from the regression line at zero pressure.

Since a data scan was not performed at zero pressure immediately prior to the HPT it is difficult to estimate from what prestrained state the model began its deformation with the final pressurization. If the amount of adjustment to each channel had been recorded when the gage readings were reset, before the HPT, then this would have served as the HPT origin correction. Lacking channel adjustment values, the only way to view the HPT data was to correct it so that its initial point coincided with the SIT end point projected from the unloading curve.

3.4.4 Examples

Two displacement gages and one reinforcement strain gage illustrate the data alignment procedure (Fig. 3.7 - 3.9). One displacement gage recorded radial displacement at mid-height on the cylinder wall and the other displacement gage recorded the vertical displacement of the dome apex. The strain gage was attached to a vertical reinforcing bar located at mid-height on the

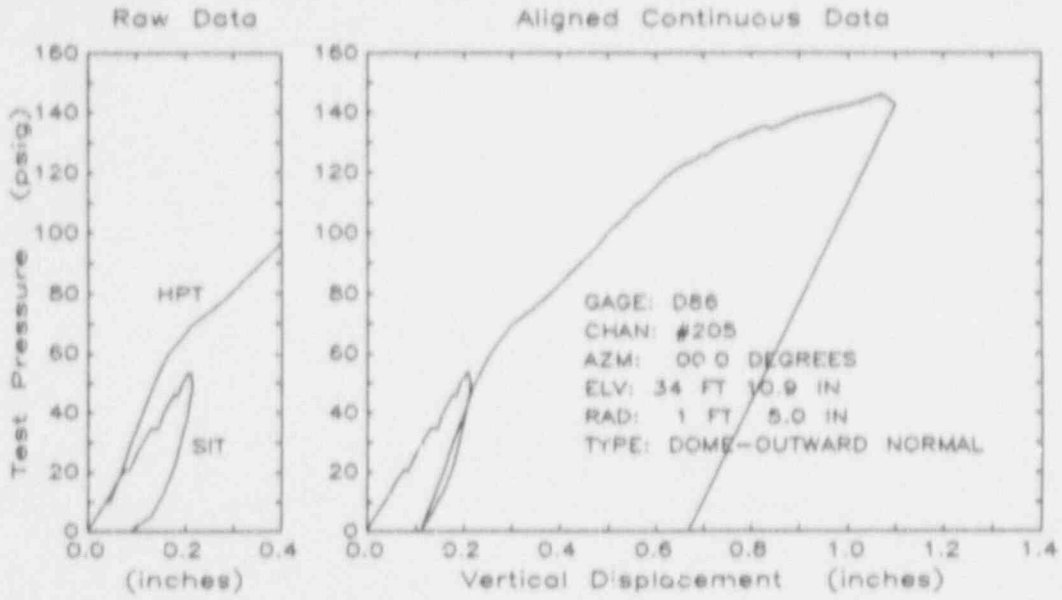

Fig. 3.8 Raw Data and Aligned Data for Gage D86

cylinder wall. Each of Figures 3.7 - 3.9 has two plots of data. The left plot shows the raw data recorded during the SIT and the HPT while the right plot shows the data modified according to the described alignment procedure. A summary of adjustments to data values for these three gages is presented in Table 3.6.

Table 3.6 Summary of Adjustments to Raw Data for Selected Gages

Gage	Measurement Type	Radius	Azimuth	Elevation	Adjustments to Raw Data SIT	HPT
D100	Radial displ. mid-ht. cyl. wall	11'	225°	13'	+0.005	+0.060
D86	Vertical displ. dome apex	0	---	35'	-0.001	+0.086
Wr263	Vertical % strain, reinf. layer 5 wall mid-ht.	11' 6"	45°	13' 5"	+0.001	+0.017

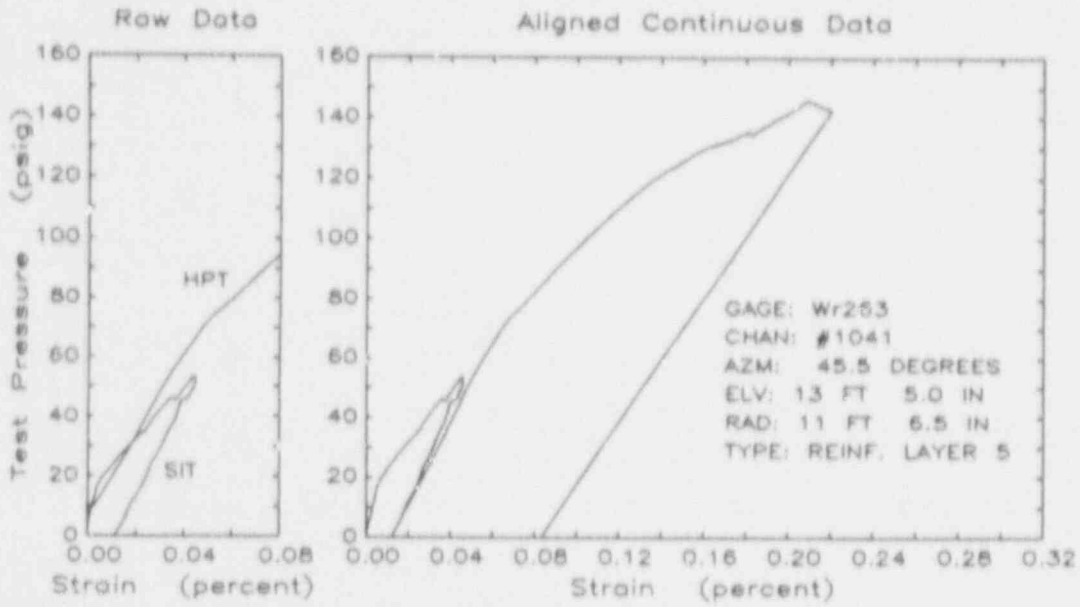

Fig. 3.9 Raw Data and Aligned Data for Gage Wr263

4. MEASURED RESPONSE

Representative data from the SIT and HPT pressure loadings are presented in this chapter. This data forms the basis for inferences on structural behavior which follow. Response behaviors are outlined for the wall, the basemat, and the wall-basemat interaction.

Except for track mounted displacement data (Section 3.2.3), for which only HPT data is available, all plots of pressure versus response will consider the two pressurization cycles as one continuous loading. Only continuous data (Section 3.4) is presented.

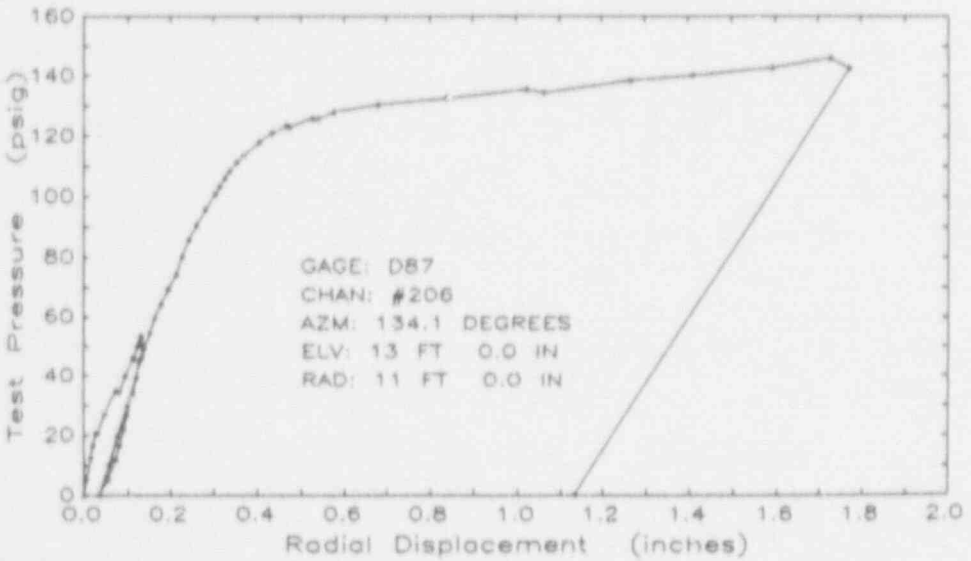

Fig. 4.1 Radial Displacement at Cylinder Mid-Height

4.1 Wall Response

4.1.1 Hoop Direction Response Data

Figure 4.1 is a plot of internal pressure versus radial displacement. The data are from gage D87 located at mid-height on the cylinder wall at azimuth 134 degrees (Fig. 3.1). The gage was mid-way between equipment hatch B and one of the personnel airlocks. The change in slope in the plotted data at 20 psig is attributed to concrete cracking. Yielding in the hoop direction begins at approximately 110 psig and by 130 psig overall yielding is complete. The test was stopped at 145 psig because of leakage, but one may note the significant post-yielding stiffness measured at the end of the test. The plotted data suggest that, had the liner not leaked, the cylinder wall could have withstood greater pressure with a correspondingly greater radial displacement.

4.1.2 Meridional Direction Response Data

In Figure 4.2 data are shown from vertical displacement gage D105 located at the top of the cylinder wall at azimuth 226 degrees (Fig. 3.1). This gage was connected by a thin wire to the basemat floor for a gage length of

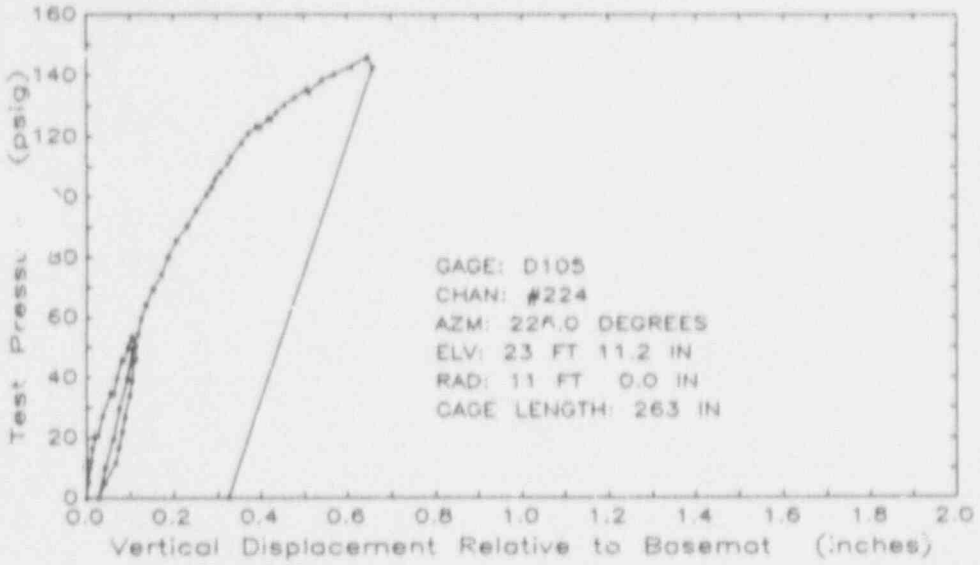

Fig. 4.2 Vertical Displacement at Top of Cylinder Wall

approximately 263 in. Because the vertical displacement transducers mounted on the wall recorded displacement relative to the containment floor (Section 3.2.2), data from gage D105 indicates average vertical wall strain. The plotted data show perceptible changes in slope at 20, 65, and 125 psig. The slope change at 20 psig is attributed to concrete cracking. The change in slope at 125 psig is attributed to the initiation of vertical yielding of the wall. An explanation for the slope change at 65 psig or for the general nonlinear response in the range 20 to 110 psig, as compared with the linear radial displacement response in this range (Fig. 4.1), cannot be offered solely from data observations. Average vertical strain does not show an overall yielding response at the end of the test as was observed in the hoop direction response (Fig. 4.1).

4.1.3 Displacement Track Data

(a) Wall Elevation Profile

Radial displacement data from displacement track 2 are presented in Figure 4.3. Track 2 was located on the interior of the model at azimuth 98 degrees and recorded a radial displacement profile of the wall between elevations 2 ft 5 in. and 23 ft 11 in. (Fig. 3.2). Eight of the 17 track gage data scans (Table 3.3) at nominal pressures of 60, 80, 100, 120, 130, 135, 140, and 145 psig are included in the figure. Approximately 300 pairs of elevation-displacement data were recorded for each scan at an average vertical spacing of 1.7 in. The initiation of overall hoop direction yielding observed at 130 psig (Fig. 4.1) is shown dramatically in Figure 4.3. The deflection of the wall at its mid-section, between elevations 7 ft and 19 ft, appears as an "unrestricted ballooning." At 120 psig the radial deflection of the mid-section was approximately 0.3 in., whereas at 145 psig the deflection was approximately 1.6 in. The restraint provided by the dome and basemat is evident. The wall profile data indicate that the radial deflection at the maximum test pressure was approximately 0.4 in. at the springline and approximately 0.1 in. at the base of the wall.

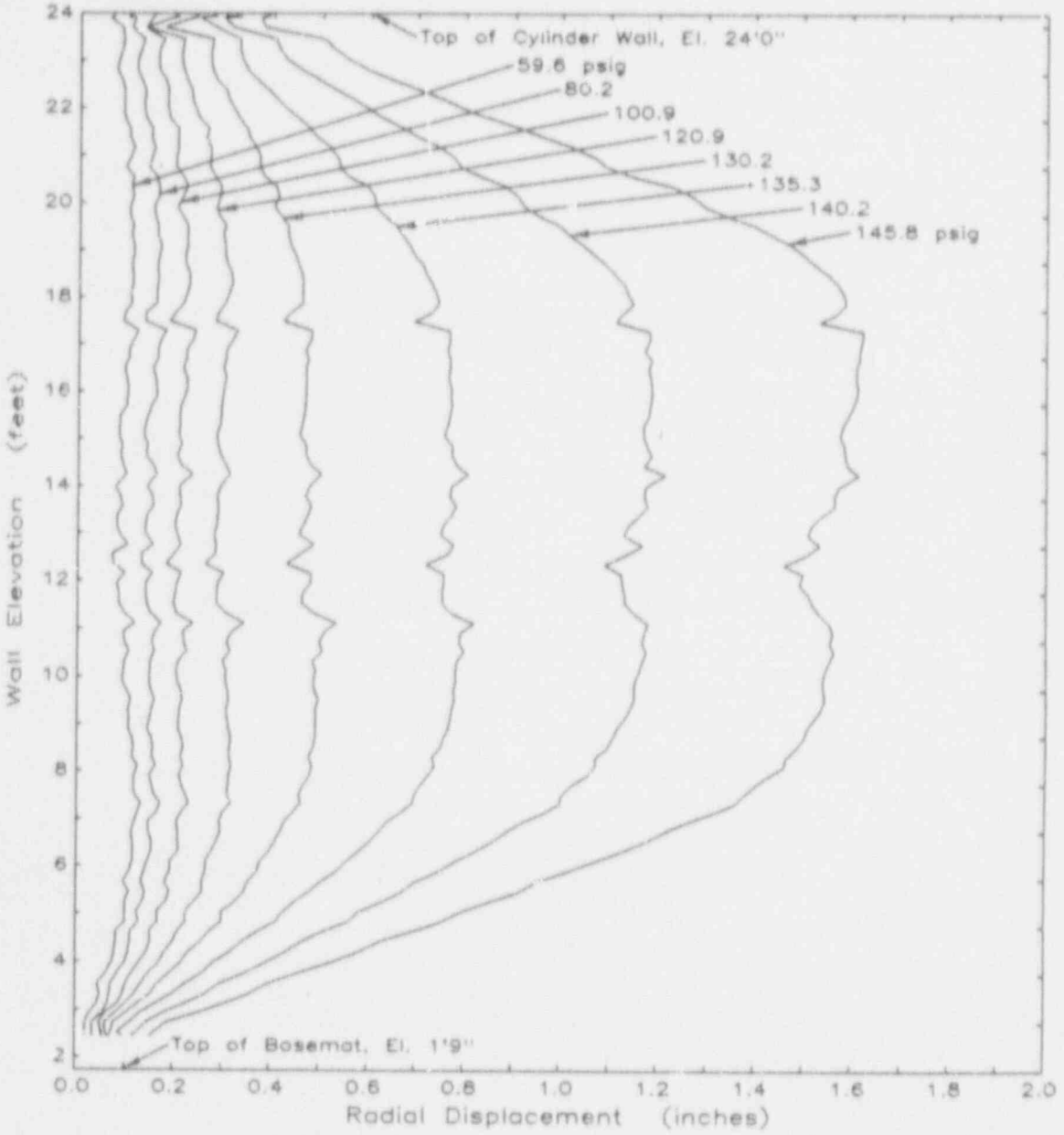

Fig. 4.3 Cylinder Wall Profile Data from Displacement Track 2

(b) Rotation at Base of Wall

A detail plot of radial displacement data from track 2 is presented in Figure 4.4. Shown are data at elevations below 5 ft for 16 data scans between pressures 49.2 psig and 145.8 psig. The top of the basemat was at elevation 1 ft 9 in., but the lowest elevation at which the track measurement system could record a radial displacement was 2 ft 5 in. Approximately 25 pairs of elevation-displacement data are represented by each line in the plot. The plotted lines are nearly linear suggesting that their slope migh. be an indicator of the rotation of the wall at its base. A linear least-squares fit to the data in Figure 4.4 was performed and the calculated slope, or wi il

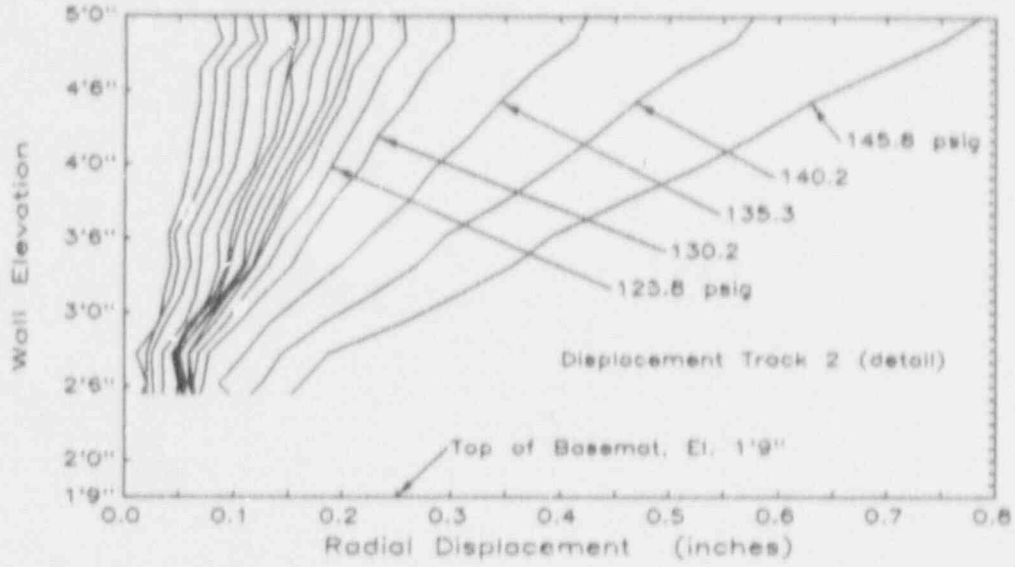

Fig. 4.4 Wall Profile at Base of Cylinder Wall

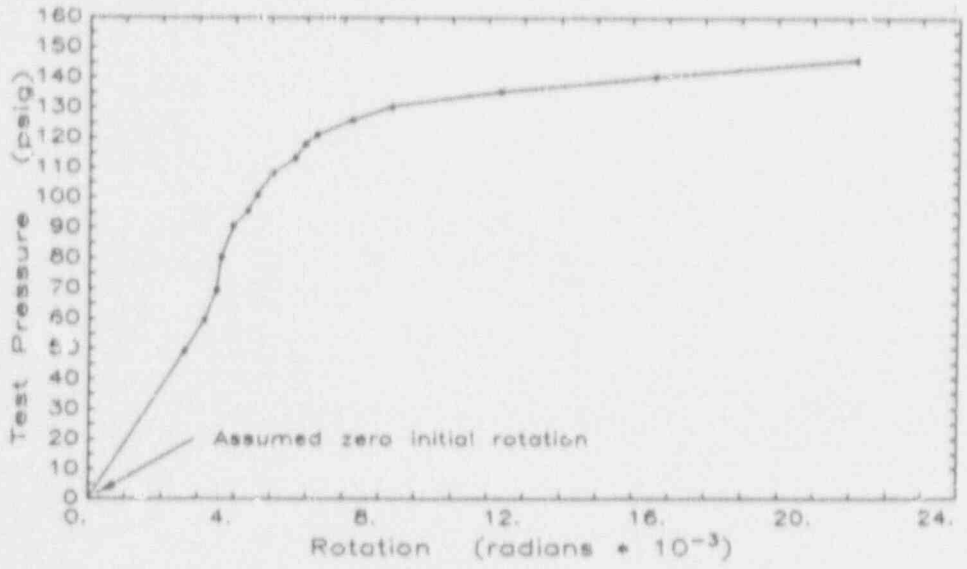

Fig. 4.5 Calculated Rotation at Base of Cylinder Wall

rotation, is presented in Figure 4.5. It was assumed that before loading the wall and the displacement track were parallel. The calculated rotations suggest that the base of the wall yielded in flexure at 120 psig. The rate at which the wall rotated with pressure was initially constant up to 70 psig. The rate of rotation between 70 and 110 psig was not as great as it was before 70 psig. These observations are representative of calculated wall rotation from any of tracks 1 to 8 as the data are remarkably identical. An explanation for the observed rotation history is included in section 5.3.

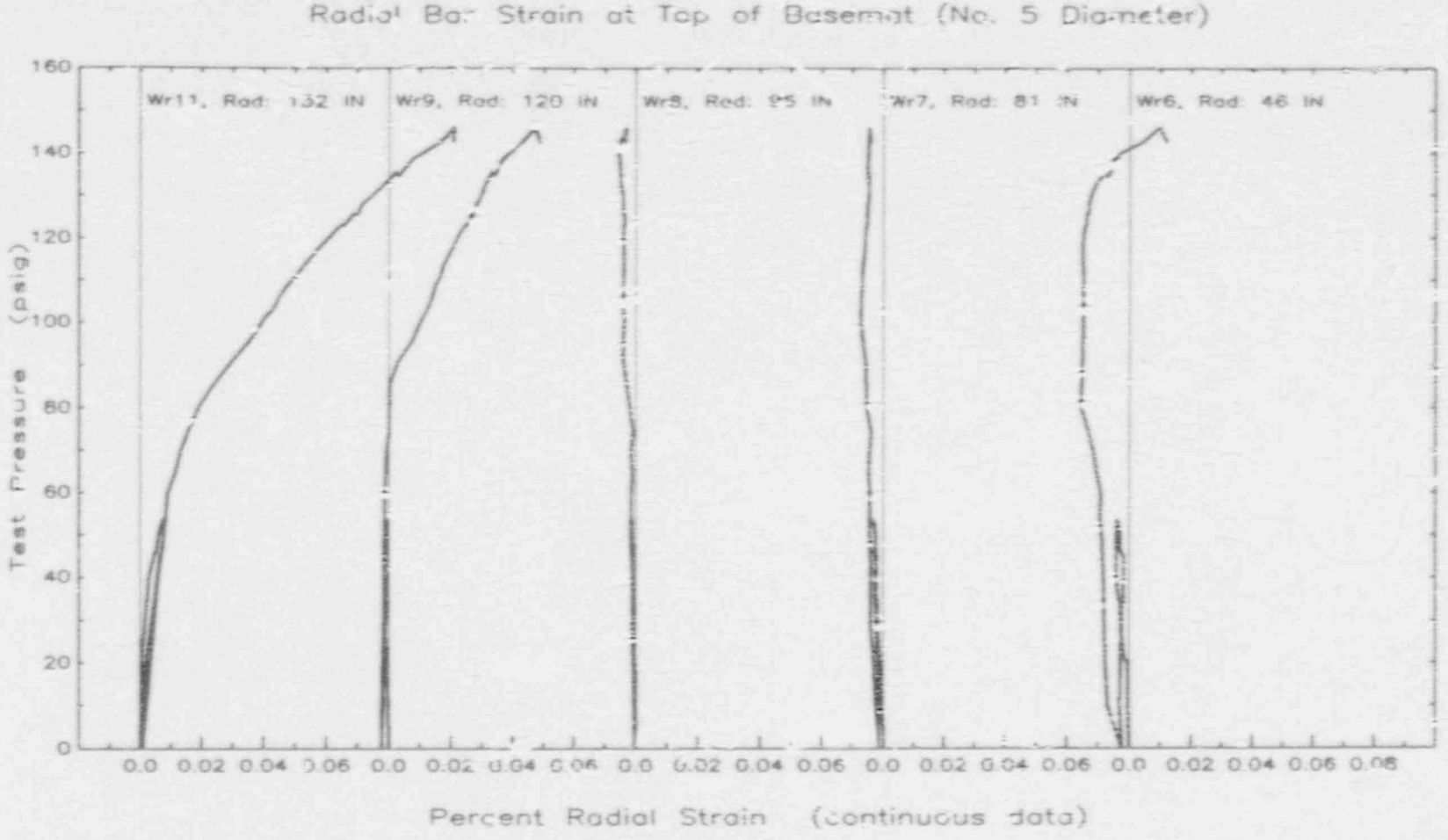

Fig. 4.6 Reinforcement Strain at Top of Basemat

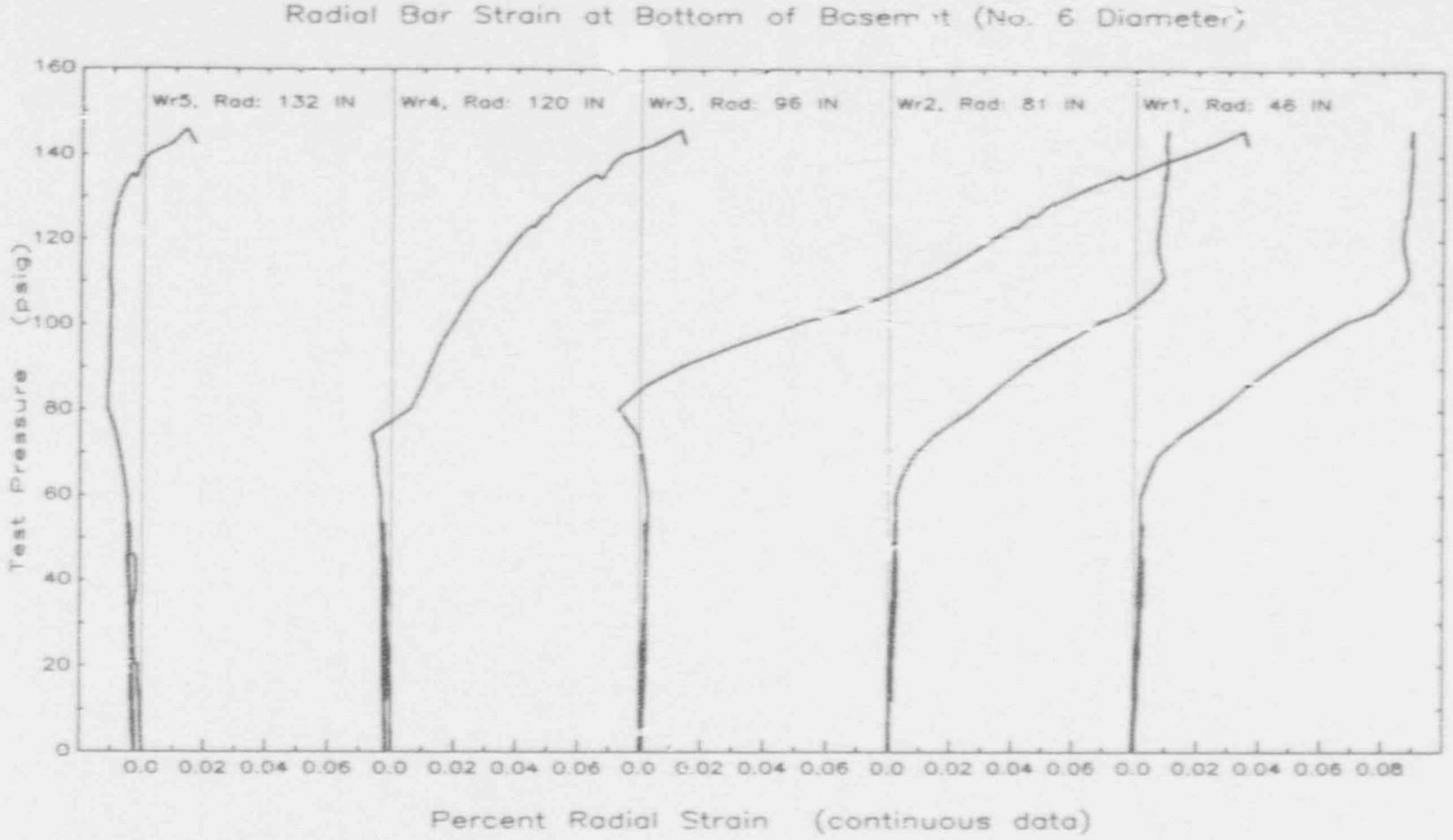

Fig. 4.7 Reinforcement Strain at Bottom of Basemat

4.2 Basemat Response

4.2.1 Radial Strain Data

Data from ten strain gages attached to one top and one bottom basemat reinforcing bar are presented in Figures 4.6 and 4.7. The data shown in the five plots in each of the figures are from gages installed on the same radially oriented bar at radii of 46, 81, 96, 120, and 132 in. Strain measured by all ten gages was less than 0.0001 for pressures less than 75 psig indicating that the basemat was essentially inert below this pressure level. The maximum strain recorded by these gages at the end of the test (by gage Wr3 on the bottom bar at radius 96 in. (Fig. 4.7)) was 0.0019 in tension. This is slightly less than the expected yield strain (0.0022) for reinforcement.

4.2.2 Basemat Extension

The radial extension of the basemat was estimated from strains measured on one top and one bottom basemat radial-oriented bar. The extension was calculated by integrating, along a radius, the strain data shown in Figures 4.6 and 4.7. The results of the calculation are presented in Figure 4.8. The calculated extension of the basemat at the maximum test pressure was 0.02 in. at the top and 0.14 in. at the bottom of the slab. The calculation assumed zero strain at the center of the basemat and linearly varying strain between each of the gage locations. No direct measurement of the basemat radial extension is available for comparison.

4.2.3 Basemat Uplift

The radial strain gages placed on a bottom basemat reinforcing bar were located directly below similar gages on a top bar (Fig. 3.6). An estimate of curvature within the basemat may be derived from the difference in readings in a pair of gages at equal radii. These estimates of curvature were used to calculate basemat uplift at the 11-ft radius, at the junction of the wall with the basemat. In the calculation zero curvature was assumed at the center of the basemat and the curvature was assumed to vary linearly between each of the gage locations. Results of this calculation are presented in Figure 4.9. Also shown in the figure is a direct measurement of basemat uplift provided by data from displacement gage D50. That gage was located in the interior of the containment at a 11-ft radius and measured displacement of the floor relative to a truss cantilevered from the central reference column (Fig. 3.6). The qualitative and quantitative agreement between the two curves (Fig. 4.9) provides confidence for the use of strains measured on the basemat reinforcement.

4.3 Response at the Wall-Basemat Junction

In the preceding two sections, representative data were presented to summarize the overall kinematic response of the containment model. In this section, measured strains are related qualitatively to flexure and shear forces at the junction of the wall and basemat. In Chapter 6, techniques are described for using these strain data quantitatively to estimate the internal forces transmitted from the wall to the basemat.

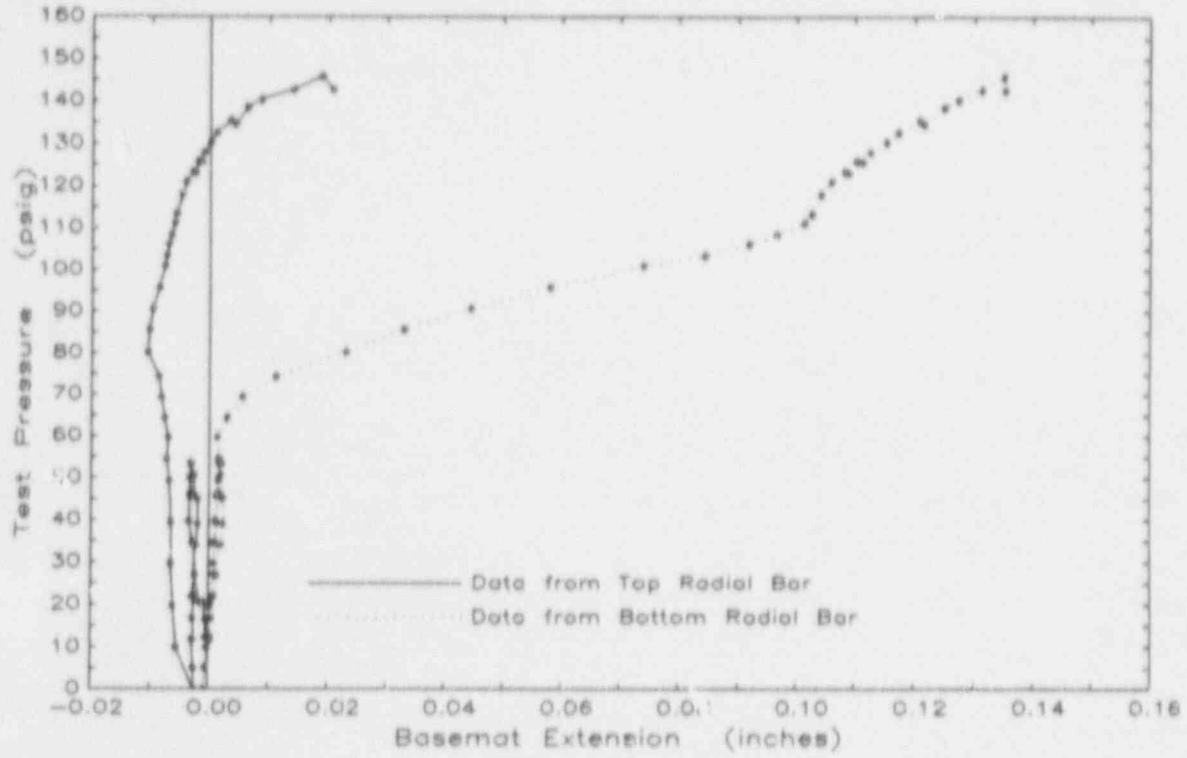

Fig. 4.8 Basemat Extension at 11 Ft Radius

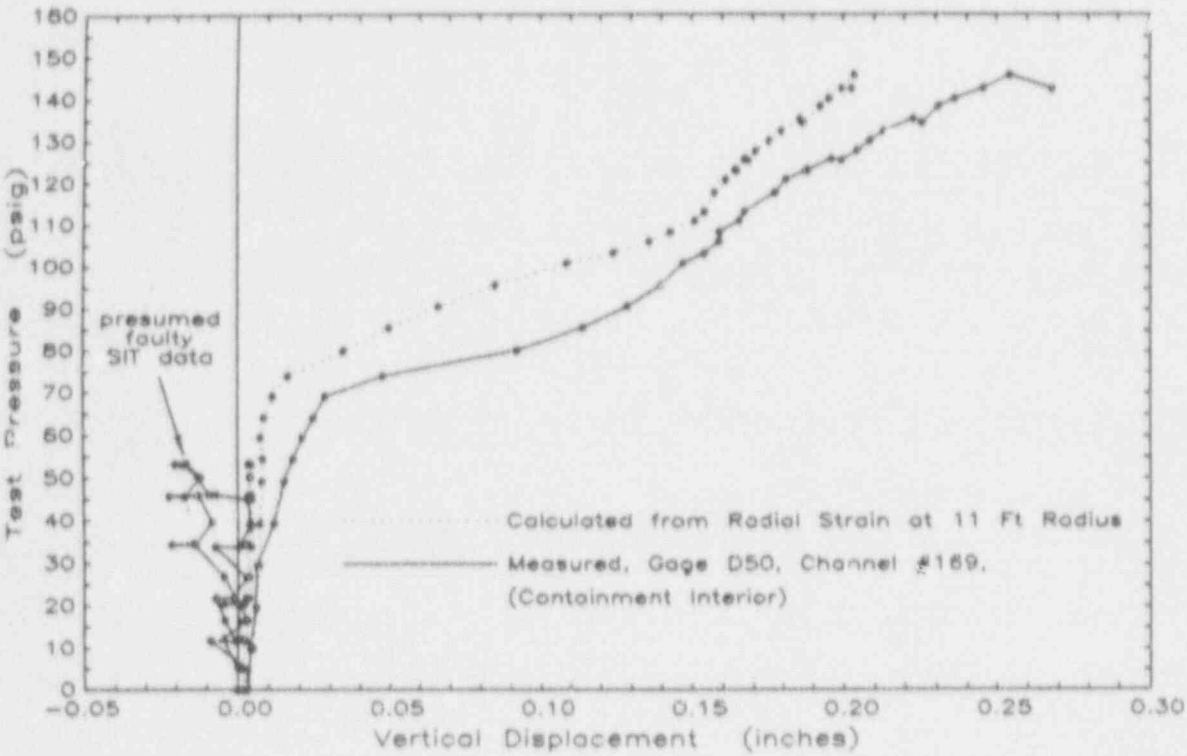

Fig. 4.9 Basemat Uplift

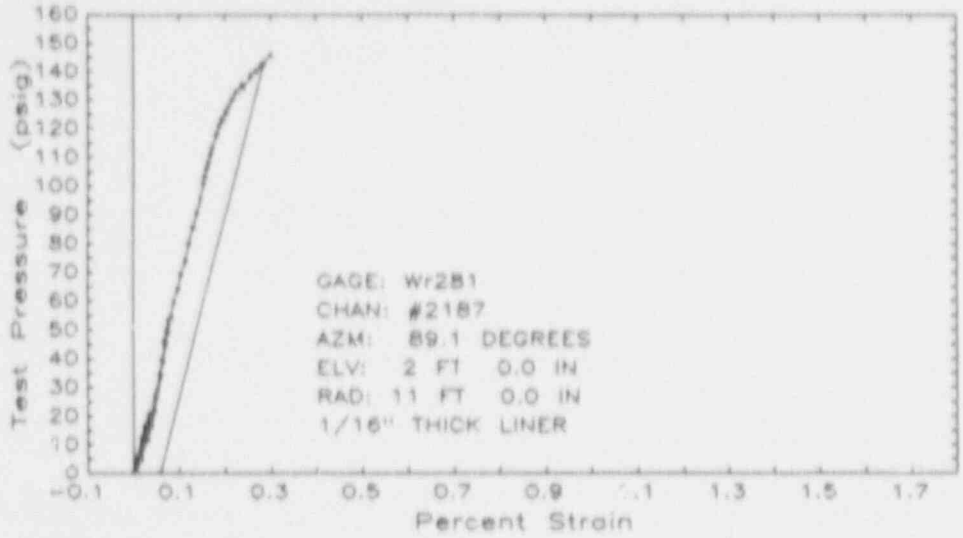

Fig. 4.10 Vertical Strain on Liner

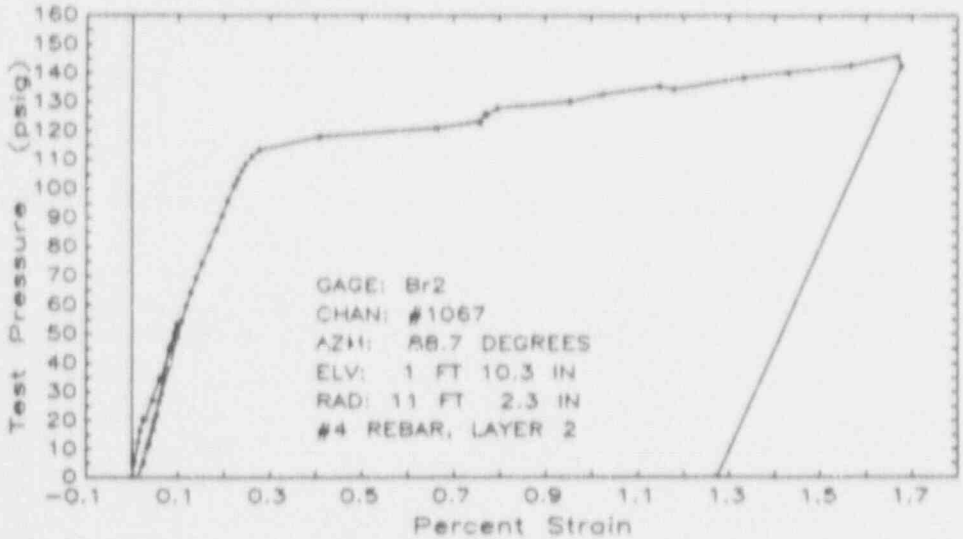

Fig. 4.11 Strain on Vertical Reinforcement Layer 2

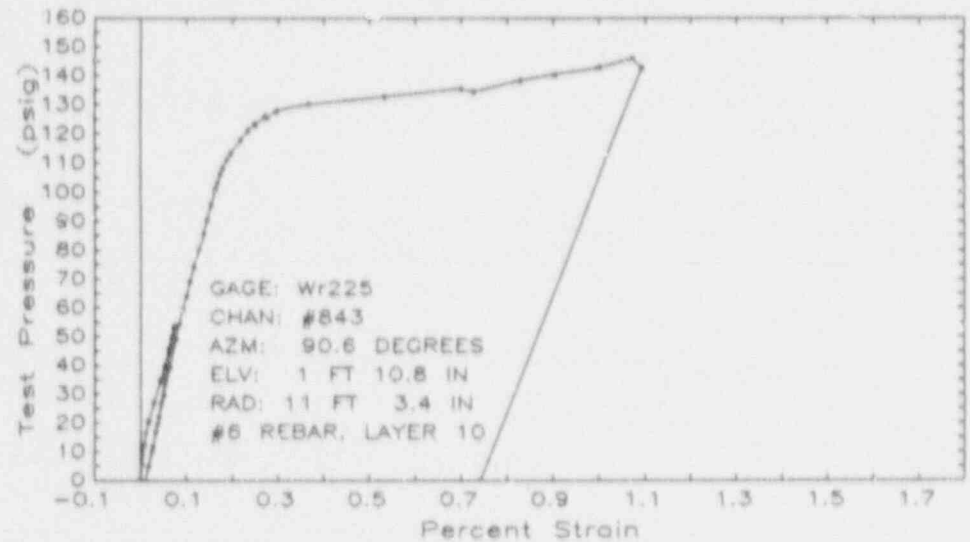

Fig. 4.12 Strain on Vertical Reinforcement Layer 10

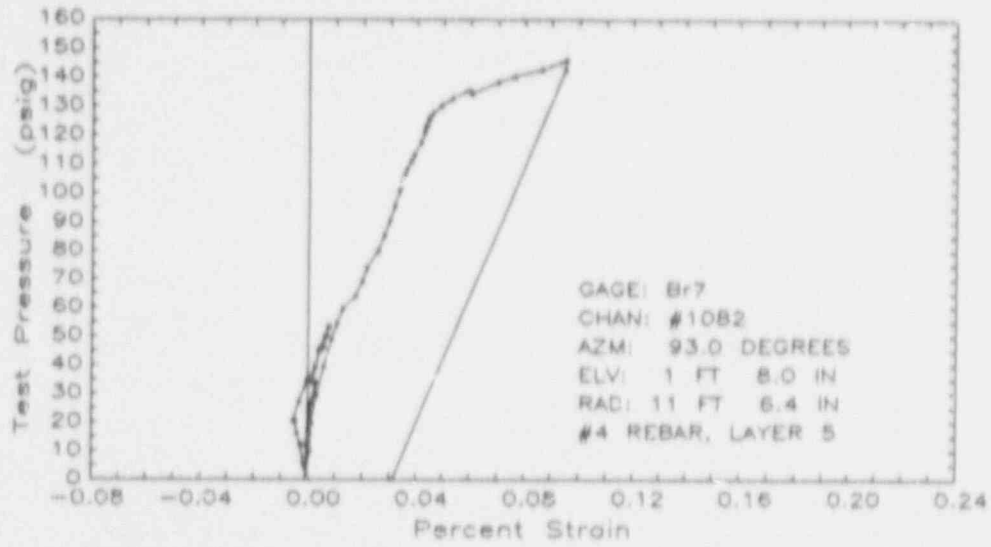

Fig. 4.13 Strain on Vertical Reinforcement Layer 5

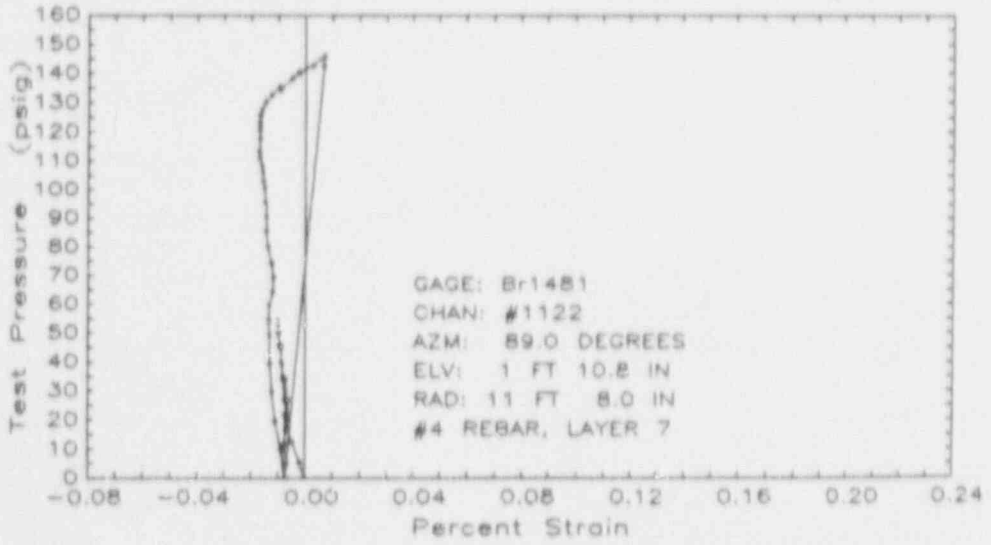

Fig. 4.14 Strain on Seismic Reinforcement Layer 7

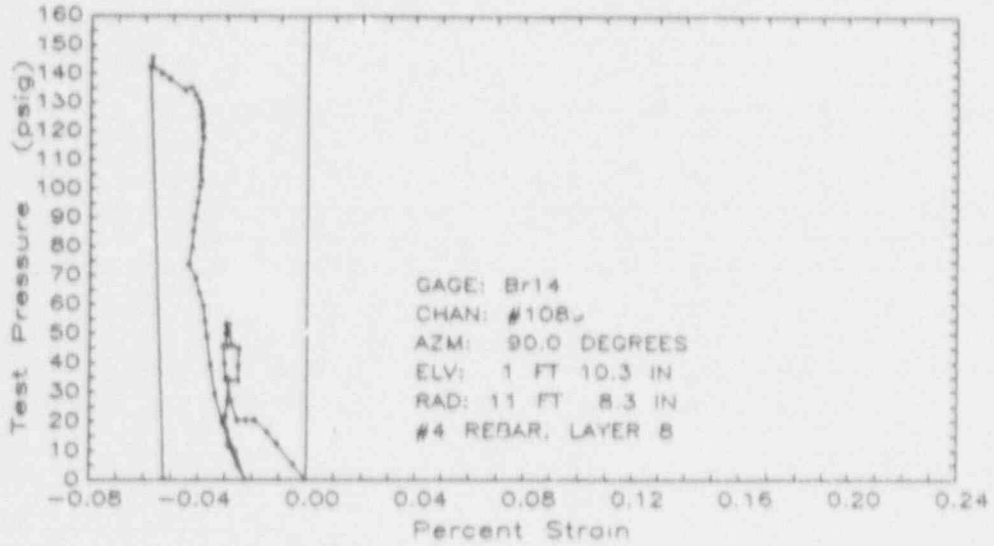

Fig. 4.15 Strain on Seismic Reinforcement Layer 8

A series of eight plots of data from gages located at azimuth 90 degrees at the wall-basemat junction are presented in Figures 4.10 to 4.17. The data are from gages Wr281, Br2, Wr225, Br7, Br1481, Br14, Wr14, and Br23, which are identified in Figure 3.3. Data from these gages provide a complete set of strain measurements through the wall thickness for each of the reinforcing bars and the liner at this junction.

A series of bar charts of data from these gages at pressures of 20.5, 106.1, and 145.8 psig is presented in Figure 4.18. In the figure, no adjustments were made to data from gages that measured strain on reinforcement inclined from the vertical.

4.3.1 Wall Base Flexure

Strains measured on vertical reinforcing bars indicate the wall fiber strain at depths into the wall coinciding with the expected locations of the gaged bars. Shown in Figures 4.10 to 4.15 are data from six strain gages: mounted on the liner and oriented vertically, on vertical reinforcement layers 2, 10, and 5, and on seismic reinforcement layers 7 and 8 (oriented 45 degrees from vertical and perpendicular to a radius). The plots are ordered by depth within the wall, from interior to exterior. Data from these gages together indicate the flexure and vertical forces at the base of the wall. None of these gages were on bars oriented to develop strain perpendicular to the wall surface. Referring only to Figures 4.10 to 4.15, and Figure 4.18 the following observations are offered:

1. For the combined SIT and HPT tests, strains measured near the interior of the wall were tensile and strains measured near the exterior of the wall were compressive.

2. The gages measuring only tensile strains (Fig. 4.10 - 4.12) indicated cracking of concrete at a pressure of approximately 20 psig: the rate of strain increase with pressure was greater above 20 psig for each gage. Strains measured on the liner by gage Wr281 (Fig. 4.10) do not exhibit the effect of concrete cracking as significantly as do strains measured on vertical reinforcement layers 2 and 10 (Fig. 4.11, 4.12).

3. Gages on layers 2 and 10 (Fig. 4.11, 4.12) indicated yielding at approximately 115 psig while yielding of the liner (Fig. 4.10) was not recorded until 130 psig.

4. Gages on the liner and layers 2, 10, and 5 (Fig. 4.11 - 4.13) showed a nearly linear strain increase with pressure between pressures of 20 and 115 psig.

5. Gages on layers 7 and 8 (Fig. 4.14, 4.15) recorded compressive strains, which were small in magnitude compared with the maximum tensile strains recorded by gages on layers 2 and 10 (Fig. 4.11, 4.12). The maximum recorded compressive strain was approximately 0.0006 (Fig. 4.15) while tensile strains greater than one percent were recorded by gages on layers 2 and 10.

6. Gage Br7 on layer 5 (Fig. 4.13) responded initially in compression up to a pressure of 20 psig. Above 20 psig the direction of the response became tensile.

7. Gage Br1481 on layer 7 (Fig. 4.14) responded in compression throughout the test and shifted at the end of the test, at pressures above 140 psig, to record tensile strains.

8. The neutral axis at 20.5 psig was near the center of the wall, inside of gage Br7 on layer 5 (Fig. 4.18) at a depth of less than 6.5 in.

9. When gage Br7 began to record tensile strain, the neutral axis shifted to between reinforcement layers 5 and 7 (Fig. 4.18) at a depth between 6.5 and 8 in.

10. By the end of the test the neutral axis shifted to between layers 7 and 8 (Fig. 4.18) leaving the exterior 1.0 to 1.75 inches in compression.

The flexural behavior of the wall may be summarized by stating that the data identify distinct stages of uncracked and cracked behavior. The response after cracking increased linearly with pressure up to the pressure that initiated yielding of the inside vertical bars, layers 2 and 10. The location of the neutral axis shifted with increases in pressure from near the center of the wall to within 1.0 to 1.75 in. of the exterior of the wall at the end of the test.

4.3.2 Wall Base Shear

The No. 4 diameter diagonal dowels (layer 11) and No. 3 diameter stirrups placed at the base of the wall were provided primarily to enhance the wall capacity to transmit shear to the basemat. Shown in Figures 4.16 and 4.17 are data from strain gage Wr14 installed on a diagonal dowel and from gage Br23 on a stirrup. Observations on the plotted data include the following:

1. Concrete cracking was sensed by gages Wr14 and Br23 between 16 and 20 psig; the rate of strain increase with pressure was greater above 20 psig for both of the gages.

2. At 80 psig the rate of strain increase in the diagonal bar slowed down while the stirrup stopped straining further.

3. At 120 psig the rate of strain of the diagonal bar increased and the stirrup again developed additional strain. Between 80 and 120 psig the strain recorded by gage Br23 on the stirrup was essentially constant.

4. The diagonal bar (Fig. 4.16) reached its expected yield strain (0.22 percent strain) at 135 psig yet the rate of strain increase for both it and the stirrup decreased above 135 psig.

The diagonal dowel was oriented radially at 45 degrees to the horizontal and the stirrup was oriented radially at approximately 40 degrees to the horizontal. These bars have both radial and vertical components. Strains

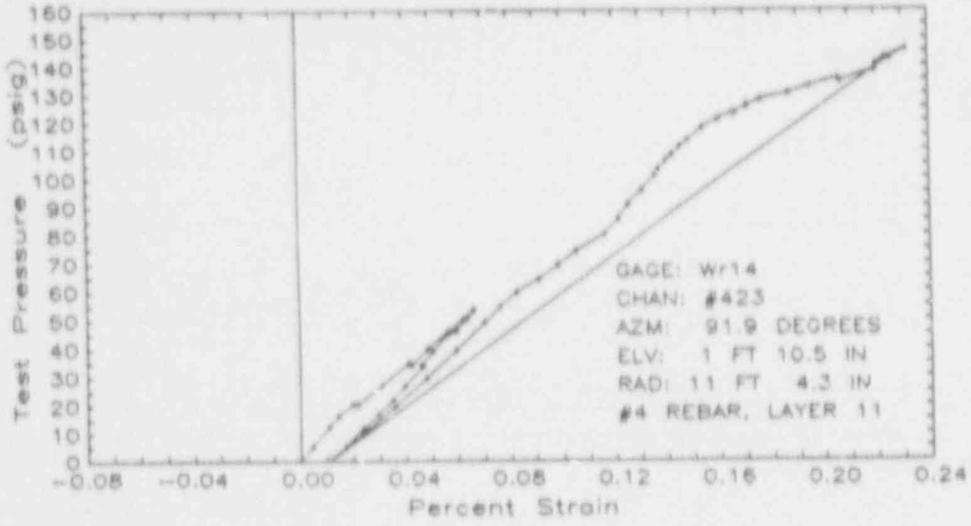

Fig. 4.16 Diagonal Dowel Strain

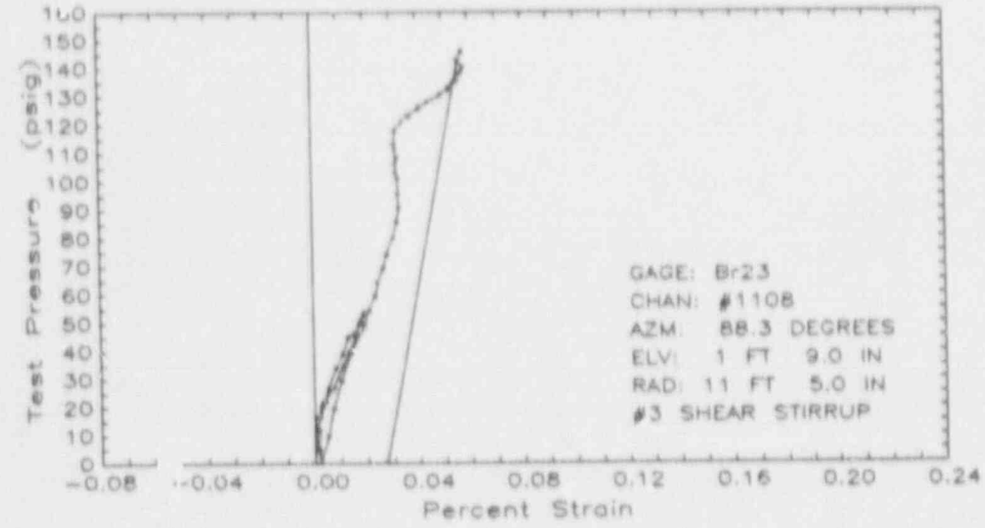

Fig. 4.17 Diagonal Stirrup Strain

measured on them would be expected to respond to vertical and radial deformations due to vertical force, meridional moment, and radial shear. The strain histories in Figures 4.16 and 4.17 are markedly different from the strain history of any of the vertical or seismic reinforcing bars or the liner (Fig. 4.10 - 4.15). The difference is assumed to be due to the influence of shear. The reduction in the strain rate for the shear reinforcement that occurred at 80 psig or for the events observed at 120 and 135 psig can not be explained solely from data observations nor can they be related directly to the flexural response of the wall.

At pressures greater than 135 psig the stirrup stops developing additional strain (Fig. 4.17). This may be due to slippage. Or this may be due to the inclination of the stirrups. They were hooked around the interior and

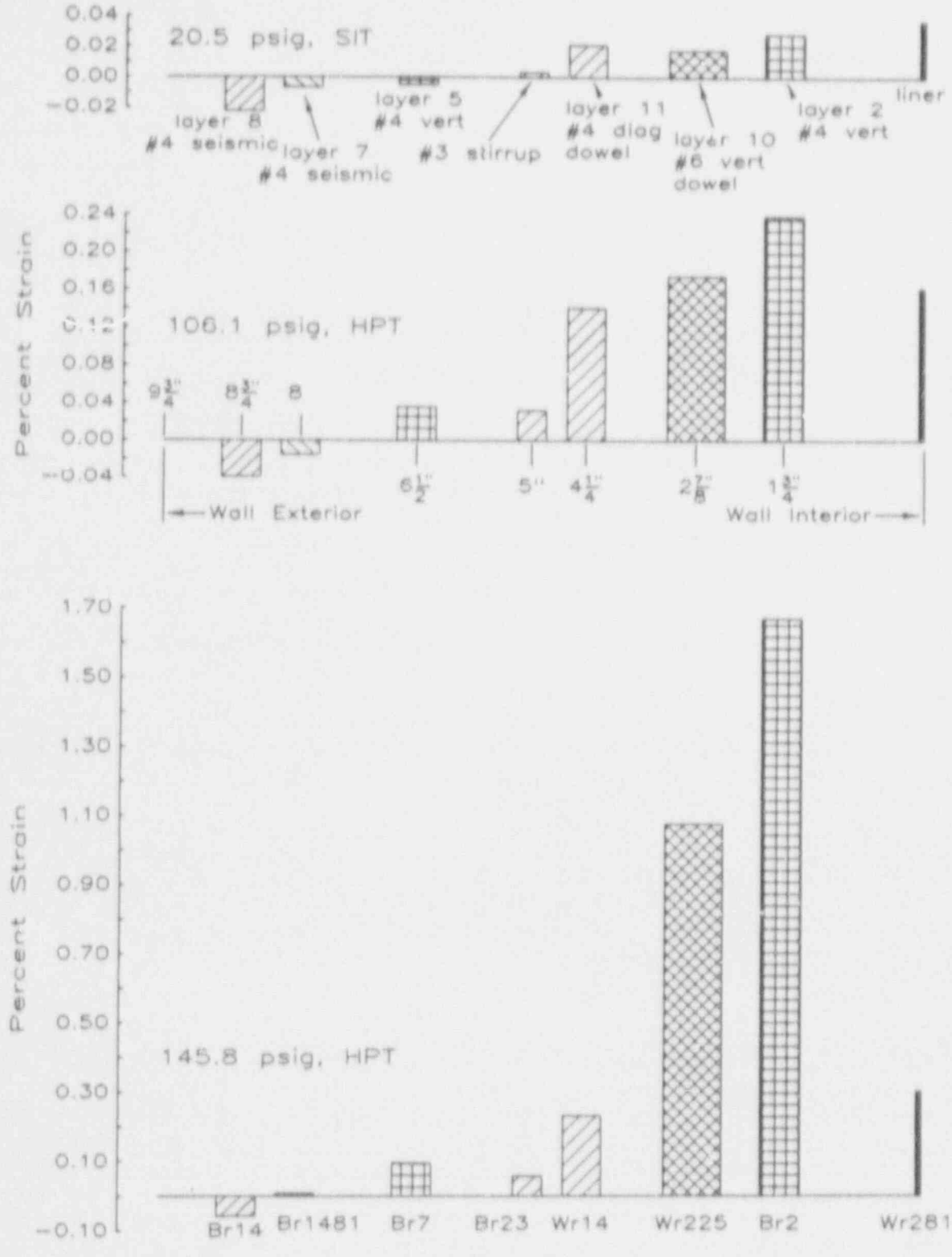

Fig. 4.18 Illustration of Shifting Neutral Axis

exterior vertical reinforcement, layers 2 and 5 (Fig. 3.3). As the wall deformed in flexure the interior surface was in tension and the exterior surface was in compression. An outward rotation of the wall, therefore, could have produced a relative decrease in the distance between the locations on the vertical reinforcement on which the stirrups were hooked. Had the stirrups been horizontal or inclined downward rather than upward this conjecture could not be offered.

4.4 Summary of Measured Response

The data presented indicate that the wall cracked and yielded in both hoop and vertical directions and that by the end of the test overall yielding occurred in the hoop direction but not in the vertical direction. Cracking of the wall occurred at 20 psig, initiation of hoop direction yielding occurred at 110 psig, and overall hoop yielding began at 130 psig. Yielding in the vertical direction did not begin until 125 psig. Plots of pressure versus deformation data indicate that the response of the wall was fairly linear in the pressure ranges between cracking and yielding.

Deformation of the basemat was negligible at pressures less than 75 psig. The basemat showed signs of cracking at 75 psig followed by uplift at the edge of the slab. The cracking and uplift of the basemat at 75 psig cannot be identified with affecting the response of the wall in the hoop or vertical directions at the cylinder wall mid-section (Fig. 4.1, 4.2).

Data at the wall-basemat junction indicate that, while responding in flexure, the wall exhibited cracking at 20 psig and yielding at 120 psig. Between flexural cracking and yielding, measured vertical strain on reinforcement layers 2 and 10 and the liner increased linearly with pressure. Vertical strains measured on reinforcement layers 5, 7, and 8 were small in magnitude compared with the inside vertical strains. This suggests that the bending moment at the base of the wall increased linearly with pressure in this range. Strains measured on shear reinforcement indicate cracking at 20 psig, a slow-down in the rate of response at 80 psig, and an increase in the rate of response at 120 psig. The shear reinforcement slowed again in the rate of response at 135 psig just as the inclined reinforcement layer 11 began to yield.

The interrelation of response events for the basemat and for the wall-basemat junction is discussed in detail in Chapter 6. Observations offered here on the causal effects on structural response are given only as a preliminary perspective. The slow-down in the rate of increase with pressure of shear reinforcement strain at 80 psig appears to be due to the increase in flexibility caused by concrete cracking in the basemat. Vertical strains in the base of the wall showed no deviation in response with basemat cracking as might be expected. Vertical wall strain is indicative of bending moment, which is expected to decrease with a decrease in the stiffness of the wall fixity to the basemat. The increase in the rate of strain of shear reinforcement and the initiation of flexural yielding at 120 psig appear correlated, although the relation implied does not follow what would be expected from mechanics. As the wall yields in flexure the flexibility of the wall-basemat connection would increase. An elastic analysis of a cylindrical shell wall subjected to internal pressure would show that the

radial shear force at the wall-base decreases as the rotational restraint decreases. This means that a slow-down in the rate of strain increase of shear reinforcement is more likely after flexural yielding. The slow-down in straining of shear reinforcement at 135 psig occurs just as one of the shear reinforcement bars reaches its expected yield strain rather than at 120 psig when flexural yielding occurred. Other events, which cannot be determined from the measured data alone, affected this slow-down by restraining the base of the wall from deflecting radially and preventing the shear reinforcement from straining further.

5. EVALUATION OF OVERALL RESPONSE

In this chapter a framework for evaluating the overall response of the containment model is described. In the following sections it is shown that it is possible to understand the response with simple methods of analysis and that the measured response values are credible.

In Section 5.1 "benchmarks" in hoop direction (radial expansion) response of the shell wall are defined via membrane analysis. The benchmarks relate to specific events in calculated wall response. They identify turning points in behavior such as concrete cracking or the yielding of a layer of reinforcement. In Section 5.2 a study of the response before and after cracking at various regions of the structure is presented. This section illustrates the relative changes in stiffness caused by cracking in the wall and in the basemat. In Section 5.3 an axisymmetric nonlinear analysis of the junction of the wall and basemat is described. This section gives some understanding to anomalies in the load history of shear and moment at the base of the wall, indicated in Section 4.4.

The structural analyses described in this chapter serve fundamentally distinct purposes. The first analysis model (membrane analysis, Section 5.1) is used to verify the data: to establish credibility in the measurements. It is reasonable to expect that the radial-expansion response of the cylindrical shell wall is like that of a membrane. The calculation of such response is straightforward and uncertainties attributed to the proportions or strengths of the materials composing the wall are minimal (Section 2.2). Therefore, differences between measured and calculated response indicators can be attributed more to errors in measurement than to errors in analytical modeling. The second analysis model (axisymmetric nonlinear analysis, Section 5.3) is used to aid the interpretation of behavior from measured data. The wall and basemat interaction is complicated: attempts to interpret their behavior exclusively from data leave several questions unanswered (Section 4.4). One tool to assist behavioral interpretations is an analytical model composed of structural elements for each of which the load response is known. As the parameters for each element are varied, the calculated response of the aggregate model can be compared with the measured response of the wall and basemat. Favorable comparisons provide a basis for explaining the behavior at the wall-basemat junction. This second type of analysis is based on the premise that while the real structure is complex and its response to load is complicated or not understood, the mathematical model of the structure is controlled, allowing for a straightforward interpretation of its behavior.

5.1 Hoop Response Benchmarks

A force-deformation relation for a structure composed of several elements might illustrate distinct stages in behavior brought about by changes in the response of its constituent elements. For example, the yielding of a reinforcement layer in a reinforced concrete structure could effect a change in the slope of plotted force-deformation data. These changes in state, from one stage in behavior to another, are defined herein as benchmarks. Knowing the behavior of a structure and the proportions and strengths of its composite parts, it is possible to calculate these benchmarks and establish

a one-to-one correspondence between the results of calculation and points of experimental data.

Plots of load-deformation data presented in Chapter 4 imply that the response of the containment model was monitored continuously. Although only 76 data scans at discrete pressure values (Tables 3.2, 3.3) were made, it is justifiable to interpolate response between readings and to connect data points on a plot with a continuous line. Comparison of data with calculated response to determine the reliability of the measurements must be conducted efficiently. The model selected for the analysis should be capable of representing expected response trends yet should not be so detailed that more information about the response is generated by the calculation than was measured during the experiment. Shell membrane theory, integrated with a rationalization of the stress strain characteristics of the various elements composing the wall, is selected as being appropriate for the analysis. The concrete, liner, and reinforcement layers are evaluated in turn for their contribution to the load carrying ability of the wall with regard to effecting a change in the slope of plotted force-deformation data. Hoop response calculations are made at these benchmarks. Unlike the measured data, interpolation between calculated benchmarks is ill advised because the benchmarks are defined at changes from one behavior stage to the next and response between each benchmark may not be linear. A finite element analysis with incremental loading was not considered for the analysis because it is believed that greater accuracy at pressure levels coincident with the benchmarks would not be afforded. The goal was to select an analysis method that minimizes modeling error so that credibility in the measurements could be established.

After a brief outline of general features of the analysis, the benchmarks in radial expansion of the cylindrical shell wall are defined. These benchmarks identify changes in the calculated response of the membrane analysis model and relate to the response of the actual wall at events defined by hoop-stress cracking, yielding of the liner, and yielding of circumferential and diagonal reinforcement. Comparisons of data with calculated response, for hoop strain and for radial displacement, near the mid-height of the cylinder wall confirm the credibility of the measurements.

5.1.1 Membrane Analysis Model

In membrane analysis it is assumed that the shell behaves as a two-dimensional curved membrane that may carry stresses only within the plane of the shell. It is assumed that these stresses do not vary through the shell thickness, that stresses normal to the shell surface are negligible, and that deflections of the membrane are small in relation to the thickness. These assumptions preclude the ability of the membrane to carry moment or to transmit shear forces having a component normal to the surface of the shell. Stress resultants, such as hoop force in a cylindrical shell, are calculated simply as the product of membrane stress and shell thickness.

Hoop force and vertical force act within the plane of a cylinder wall in directions indicated in Figure 5.1. Neglecting dead load and considering only load due to internal pressure, the resultant hoop force and vertical force are determined as $N_h = pR$ and $N_v = pR^2 / (2R + t)$, respectively, where p signifies internal pressure, R the internal radius of the cylinder,

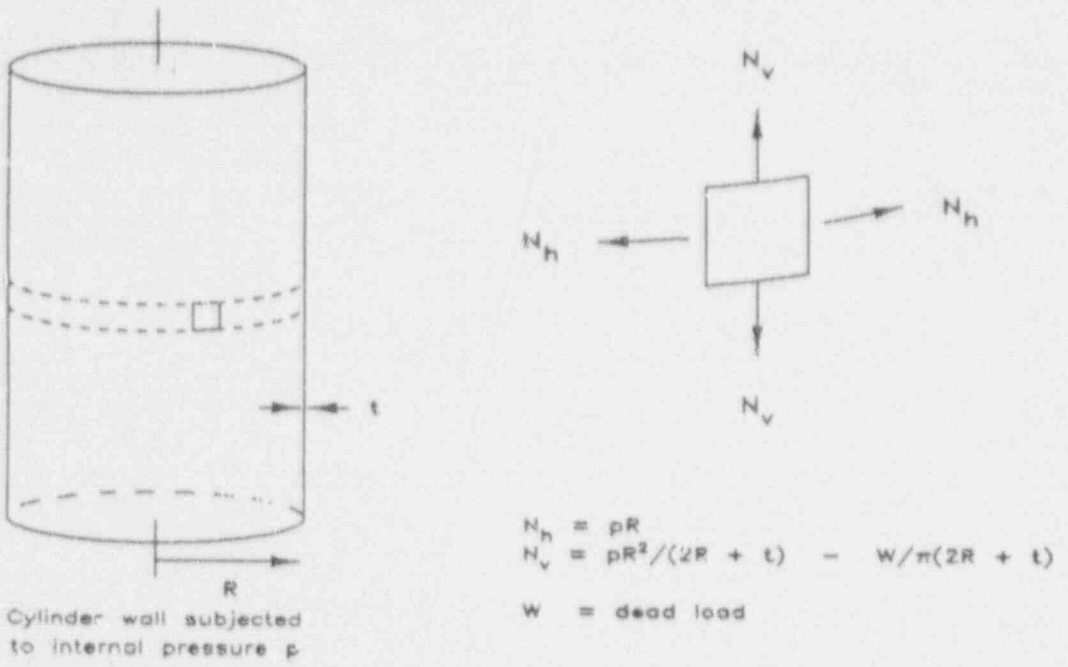

Fig. 5.1 Notation of Internal Forces in Membrane Analysis

and t its thickness. In-plane shear stress is zero because the geometry and applied load are axisymmetric. Including dead load in the analysis adds a constant vertical stress equal to the weight of all portions of the structure above a particular section divided by the circumferential area of that section. At the cylinder mid-height the combination of dead load and internal pressure render net vertical force zero at a pressure of approximately 3 psig. The weight of the dome is approximately 70 kips and the weight of the wall is approximately 8.7 kips per foot in height. This suggests that dead load may be ignored without loss in accuracy in vertical force calculations.

In the following sections membrane theory is applied to the cylindrical shell for the calculation of hoop and vertical forces in the shell wall. The analysis is assumed to apply to the "free-field" response of the wall in areas not affected by the penetrations, the dome, or the basemat. Values for elastic constants of various elements composing the wall are assumed so that pressure equilibrium may be determined for each hoop strain defining the benchmark. For all calculations Poisson's ratio for intact concrete is assumed to be zero and reinforcing bars carry stress only along their axis. Determination of internal pressure for a particular hoop strain must, therefore, consider vertical force in addition to hoop force because of cross-axis coupling caused by the diagonal reinforcement and the liner (Fig. 5.2). Values of hoop strain, radial displacement, and internal pressure for the benchmarks are tabulated in Table 5.1. Radial displacement was calculated from hoop strain at the 132-in. inner wall radius.

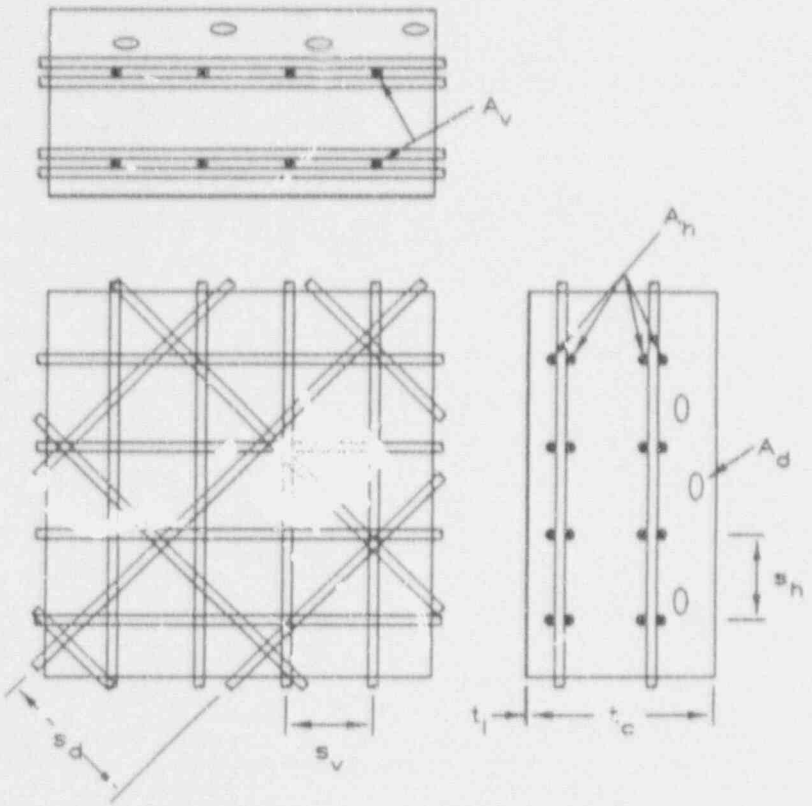

t_c	9.75	in.	Thickness of concrete
t_l	0.068	in.	Thickness of liner
A_h	0.80	in.^{2}	Area of circumferential reinforcement
A_v	0.40	in.^{2}	Area of vertical reinforcement
A_d	0.20	in.^{2}	Area of diagonal reinforcement
s_h	4.5	in.	Spacing of circumferential reinforcement
s_v	4.5	in.	Spacing of vertical reinforcement
s_d	6.25	in.	Spacing of diagonal reinforcement

Not Shown:

R_i	132.	in.	Inner radius of wall
A_{tr}	11.60	in.^{2}	Transformed section area in circumferential direction. (modular ratio = 8.05)

Fig. 5.2 Dimensions and Geometry of a Wall Section

5.1.2 Hoop-Stress Cracking

Hoop-stress cracking of concrete, resulting in vertically oriented cracks, is defined when the stress in concrete reaches its effective tensile strength, f_t. Strain at hoop cracking is determined by $\varepsilon_h = f_t/E_c$ where E_c is Young's modulus for concrete. This is a simplification of the phenomena leading to tensile cracking of concrete. The effective tensile strength of concrete is generally determined from tensile tests whereas Young's modulus is generally determined from a compression test of a concrete cylinder sample. The relationship between stress and strain at strains less than ε_h is likely to be nonlinear. The uncertainty in estimating ε_h could be greater than 100% of the calculated value. Since the strain at cracking is quite small compared with hoop strains at other benchmarks (Table 5.1), inaccuracies in its

Table 5.1 Hoop Response Benchmarks

Defined Event	Hoop Strain	Radial Displacement (inches)	Pressure (psig)
Concrete hoop cracking	0.00007	0.0092	22.0
Yielding of the liner	0.0015	0.20	97.5
Yielding of circumferential reinforcement	0.0022	0.29	127.
Yielding of diagonal reinforcement	0.0029	0.39	131.

determination for comparison with measured data are trivial. The assumed value for effective tensile strength of concrete is 250 psi ($3.2\sqrt{f'_c}$). The value for concrete modulus is taken as 3.6×10^6 psi (see below). Internal pressure at hoop cracking is determined by $p = A_{tr}\, f_t / R_i$ where A_{tr} is the area of a transformed section, per unit height, and R_i is the inner radius of the wall. The dimensions and geometry of a wall section are summarized in Figure 5.2. The calculated pressure corresponding to hoop-stress cracking is 22 psig.

Tensile strength was indicated by split cylinder tests (Fig. 2.7) to be approximately 450 psi ($5.7\sqrt{f'_c}$). Restraint presented by reinforcement hinders free shrinkage. Including the liner, the circumferential reinforcement ratio amounts to 2.9 percent. If the average restrained shrinkage strain of the containment model was 0.0003 through the section, a reduction of 200 psi in the effective tensile strength to the assumed value, 250 psi, is credible. Tensile strength determined by standard split cylinder tests is expected to be higher than the effective tensile strength of concrete in a structure [Ref. 5.1].

The value taken for Young's modulus for concrete represents the secant modulus for data from eleven compression tests of sample cylinders [Ref. 2.2]. Typically this value is calculated from $E_c = 57000\sqrt{f'_c}$ [Ref. 5.2] for normal weight concrete, resulting in 4.4×10^6 psi for $f'_c = 6000$ psi. The lower value used in the calculation is justifiable because it is based on cylinder tests of the same concrete mix and because the modulus in tension is not expected to exceed the value in compression. Young's modulus for steel is taken as the customary value, 29×10^6 psi.

5.1.3 Yielding of the Liner

Yielding of the liner is defined when stresses in the liner satisfy von Mises's yield criterion [Ref. 5.3]. The uniaxial yield strength of the liner is taken as 50.2 ksi (Table 2.2). Poisson's ratio is assumed to be 0.3. The liner is assumed to be in a state of plane stress with an assumption that vertical strain is half the hoop strain. This assumption was originally hypothesized from the ratio of vertical to circumferential in-plane force. Vertical and radial displacement data shown in Figures 4.1 and 4.2 when converted to vertical and hoop strains, confirm the assumed ratio of vertical

strain to hoop strain.* These assumptions with Hooke's law allow calculation of hoop strain to be 0.00154† and effective liner yield strength in the hoop direction to be 56.5 ksi. With the assumption that vertical strain is half the circumferential strain, strain in the diagonal bars may be determined by:

$$\varepsilon_d = 0.5\ (\varepsilon_h + \varepsilon_v) \tag{5.1}$$

where ε_h = circumferential strain
ε_v = vertical strain and
ε_d = strain in diagonal reinforcing bars.

Internal pressure at onset of liner yielding is determined from the following equation:

$$p = \frac{\left(\frac{A_h\ f_{sh}}{s_h} + \frac{A_d\ f_{sd}}{s_c} + t_\ell\ f_{y\ell,eff} \right)}{R_i} \tag{5.2}$$

where A_h = total circumferential bar area over spacing s_h
s_h = spacing of circumferential bars
A_d = area of one diagonal (seismic) bar
s_d = spacing of diagonal bars (measured perpendicular to bar axis)
t_ℓ = liner thickness
f_{sh} = stress in circumferential reinforcement ($E_s\ \varepsilon_h$)
f_{sd} = stress in diagonal reinforcement ($E_s\ \varepsilon_d$)
$f_{y\ell,eff}$ = effective yield strength of the steel liner, 56.5 ksi and
R_i = inner wall radius.

The calculated pressure corresponding to yielding of the liner is 97.5 psig.

5.1.4 Yielding of Circumferential Reinforcement

Yielding of circumferential reinforcement is defined when stress in the bars reaches the mean yield strength for a No. 4 bar, 64 ksi (Table 2.1). Elastic components of strain in the liner are assumed unchanged from those at yielding, implying that liner hoop stress is maintained at its effective yield stress ($f_{y\ell,eff}$ = 56.5 ksi). Strain hardening is not considered because the liner strains at this benchmark are small. Hoop strain is determined by

---

* Average hoop strain in the cylinder wall may be obtained from the radial displacement data in Figure 4.1 by dividing the measured values by the radius to the mid-surface of the wall, 137 inches. Average vertical strain is obtained from the data in Figure 4.2 by dividing by the 263-in. gage length for gage D105. The average hoop and vertical strains at 95 psig are: 0.002 and 0.001 respectively.

† The hoop strain value is obtained by solving simultaneously the plane stress equations of Hooke's Law, $\varepsilon_h = (\sigma_h - \nu\sigma_v) / E$ and $\varepsilon_v = (\sigma_v - \nu\sigma_h) / E$, with the von Mieses's yield criterion, $(\sigma_{yield})^2 = \sigma_h^2 - \sigma_h\sigma_v + \sigma_v^2$, and the assumed relation between vertical and hoop strain, $\varepsilon_v = \frac{1}{2}\ \varepsilon_h$.

$\varepsilon_h = f_y/E_s$ to be 0.0022, where f_y is the reinforcement yield strength. Strain in diagonal reinforcement is determined from Equation (5.1) under the assumption that vertical strain is half the hoop strain. Internal pressure at the onset of circumferential reinforcement yielding is determined from:

$$p = \frac{\left(\frac{A_h \ f_y}{s_h} + \frac{A_d \ f_{sd}}{s_d} + t_f \ f_{yf,eff} \right)}{R_i} \qquad (5.3)$$

The calculated pressure at yielding of circumferential reinforcement is 127 psig.

5.1.5 Yielding of Diagonal Reinforcement

Assumptions identical to yielding of circumferential reinforcement apply to define yielding of diagonal reinforcing bars. Hoop stress in the liner is assumed unchanged from yielding. The magnitude of the hoop and vertical strains is within the observed yield plateau in tension tests of liner samples (Fig. 2.5). Strain hardening did not occur in the tension tests before 2 percent strain. Stress in circumferential reinforcement is assumed unchanged from yielding. Strain in diagonal reinforcement is determined from $\varepsilon_d = f_y/E_s$ to be equal to the yield strain of circumferential reinforcement, 0.0022. The overall yielding response of the cylinder wall is not possible before diagonal reinforcement yielding, and was not indicated by data to occur before 130 psig. It is therefore reasonable to continue the assumption that vertical strain is half the hoop strain and calculate hoop strain, by Equation (5.1), to be 0.0029. Internal pressure at onset of diagonal reinforcement yielding is determined from:

$$p = \frac{\left(\frac{A_h \ f_y}{s_h} + \frac{A_d \ f_y}{s_d} + t_f \ f_{yf,eff} \right)}{R_i} \qquad (5.4)$$

The calculated pressure at yielding of diagonal reinforcement is 131 psig.

5.1.6 Comparison of Benchmarks and Data

Calculated benchmarks (Table 5.1) and measured data are compared in Figures 5.3 and 5.4 Data from four strain gages (Br19, Br22, Br24, and Br25) on circumferential reinforcement near the mid-height of the cylinder wall are shown in Figure 5.3. Calculated hoop strains are converted to radial displacement at the inner radius of the wall (132 in.), and are compared in Figure 5.4 to radial displacement data from four gages (D58, D90, D102, and D110) at elevation 18 ft. Except for one case (radial displacement, gage D102), the calculated benchmarks compare well with the measurements. This provides credibility to the measurements, implying that gages located about the containment recorded an accurate response history to the pressurization tests.

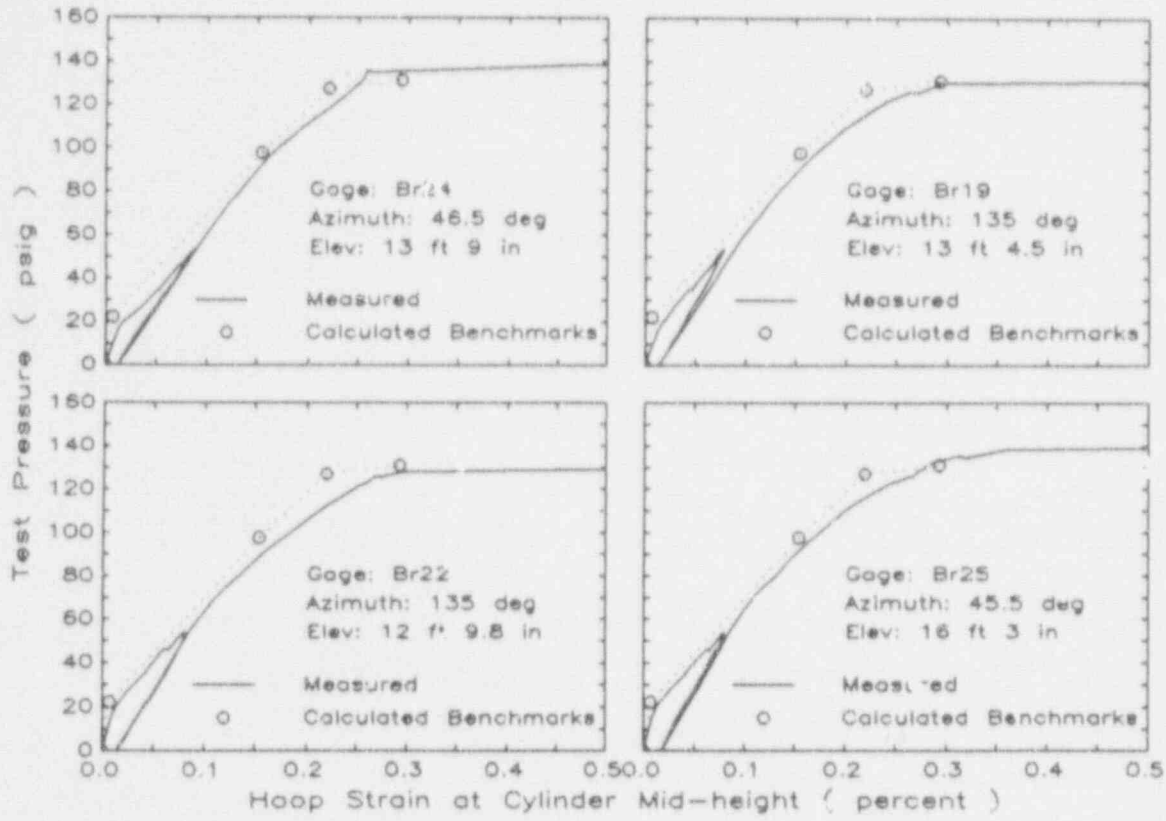

Fig. 5.3 Comparison of Hoop Strain at Cylinder Mid-Height to Benchmarks

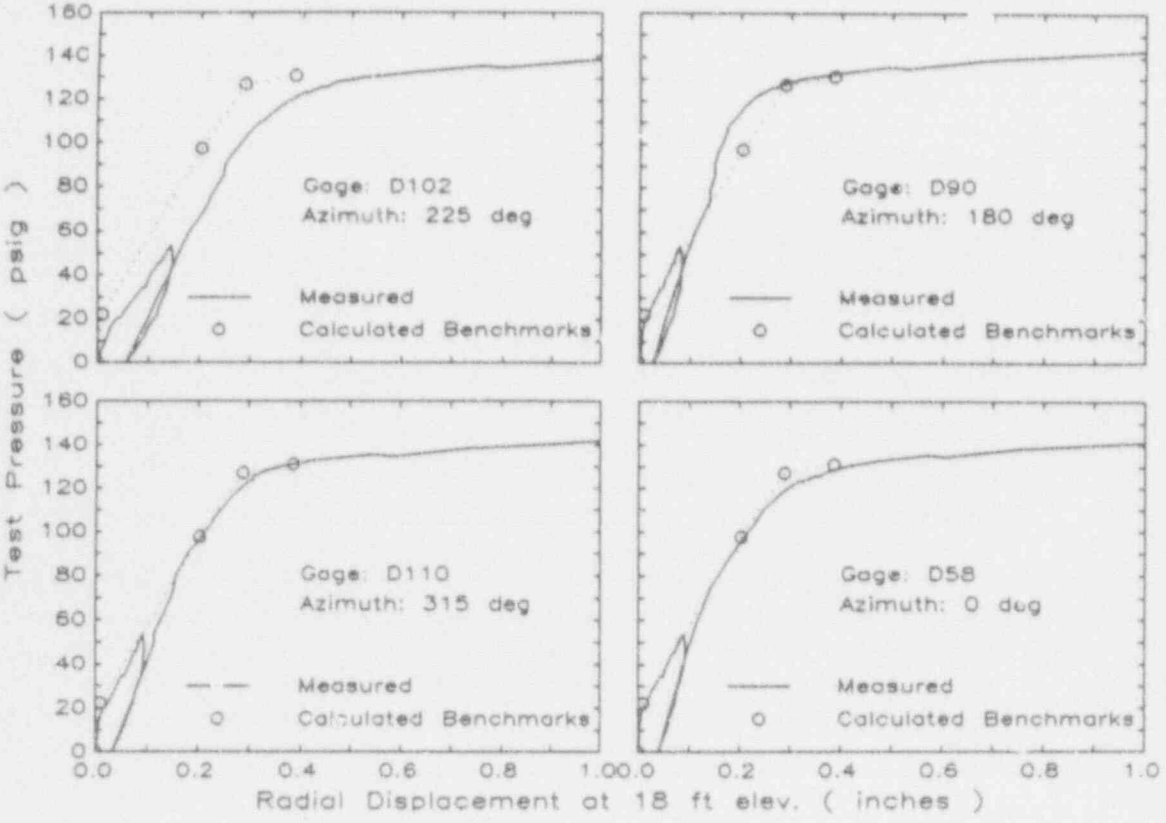

Fig. 5.4 Comparison of Mid-Height Radial Displacement to Benchmarks

5.2 Comparison of Measured Response Before and After Concrete Cracking

In this section the relative changes in apparent stiffness caused by concrete cracking in the wall and basemat are quantified. This data is necessary to establish a basis for estimating the effects of cracking on calculated response. The data is used in the nonlinear analysis model in Section 5.3 to guide selections of model parameters at various stages in behavior.

The slopes of lines connecting measured data on a plot with internal pressure along the vertical axis (Fig. 4.1, 4.2) indicate a response stiffness. Changes in slope at 20 psig in data plots, presented in Chapter 4, of gages that responded to membrane or bending stresses in the wall (Fig. 4.1, 4.2, 4.10 - 4.17) are attributed to concrete cracking. Cracking in the basemat is attributed similarly to changes in slope at 70 psig in data from strain gages on reinforcing bars there (Fig. 4.6 - 4.9). To quantify the effects of cracking on overall response a study of strain and displacement data was made to determine trends in the change in apparent stiffness due to cracking. A total of 213 plots of displacement gages, bonded strain gages, and welded strain gages were considered. Gages on the dome or those that recorded the deformation of hatches or their surrounding areas were excluded from this study. Each data plot was examined to determine a ratio of apparent stiffness before and after cracking. The data were separated, by gage location, into three groups according to whether the likely effect a gage had responded to was membrane behavior of the cylinder wall, bending at the base of the wall, or basemat bending and uplift. The definitions used and manner in which the ratio values were determined are outlined below. Results of this study suggest that there was a measurable difference in the effect of cracking on wall stiffness responding as a membrane or in bending, and on the basemat stiffness in bending.

5.2.1 Definition of Stiffness Terms

The slope of a line passing through the origin and the curve of plotted data at a distinct pressure level is referred to as the "apparent stiffness" at that pressure. Apparent stiffness is defined here as a secant stiffness and is not representative of an incremental stiffness. The apparent stiffness at 20 psig is defined as the "apparent stiffness before cracking." This value is identical with initial tangent stiffness for most of the gages since, in general, a linear response was measured in the pressure range 0 to 20 psig during the SIT. The "cracked-section apparent stiffness" is defined here as the apparent stiffness at approximately 115 psig, or at the pressure at which a gage first sensed yielding, whichever was less. Some of the gages on reinforcement sensed yielding at pressures less than 115 psig. For these gages, cracked-section apparent stiffness is determined at the initiation of yielding. These stiffness definitions are illustrated in Figure 5.5 on a plot of data from gage Wr152, which was located on seismic reinforcement layer 7 near the mid-height of the cylinder wall.

The pressure levels used to define apparent stiffness were carefully selected to include, to the greatest extent possible, the influence of concrete cracking on gage measurements. The reasons supporting the selection of the two stiffness terms may be illustrated by reference to Figure 5.6. The figure shows an idealized plot of applied load versus deformation for a section of reinforced concrete. It gives a symbolic illustration of the

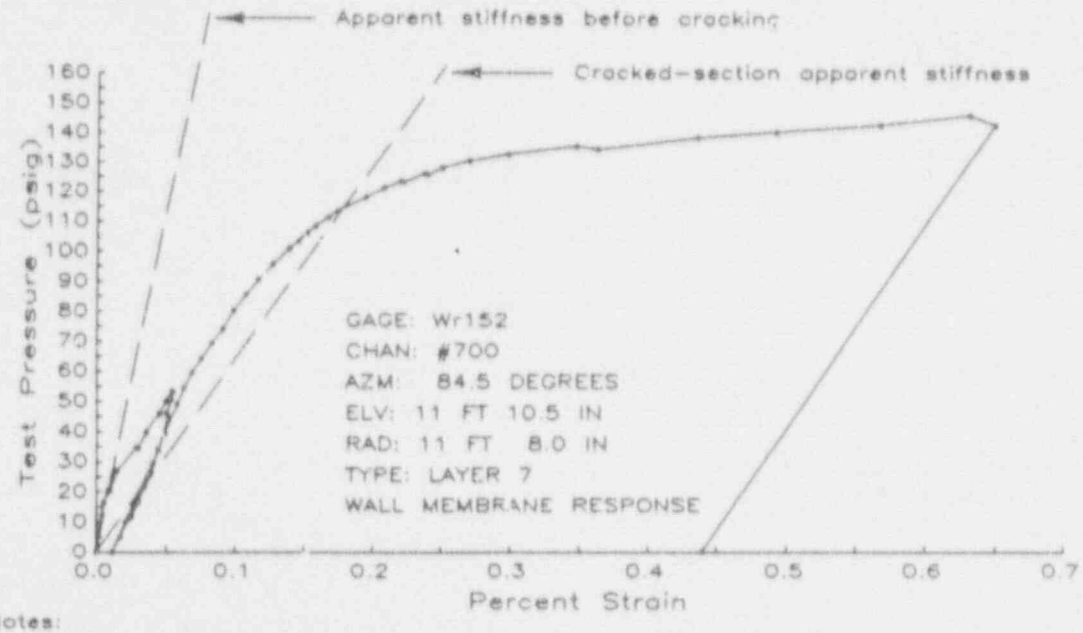

Notes:

1) Apparent stiffness before cracking and initial stiffness are essentially the same.
2) The slope of the line indicated by cracked-section apparent stiffness and the slope of the unloading curve are approximately equal.

Fig. 5.5 Illustration of Apparent Stiffness Definitions

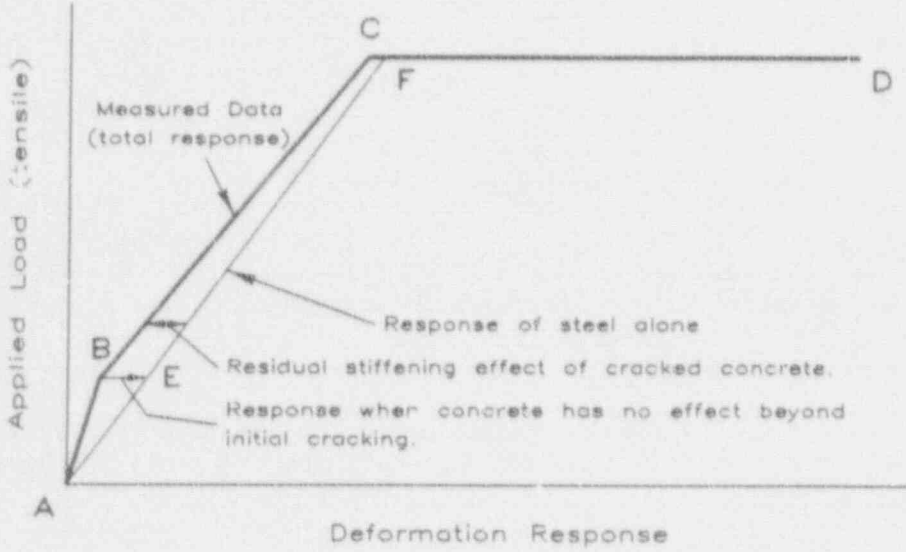

Fig. 5.6 Illustration of the Effect of Concrete Cracking on Measured Data

effect of cracking on measured data. The portion of the plot shown is in the region where the load produces tensile strains within the reinforced concrete. Line A-B-C-D in the plot may be identified with the measured deformation or total response of the structural section due to an applied load. The line defined by points A-E-F-D represents the deformation of reinforcing steel under the assumption that the concrete carries no load and

adds no stiffness to the structure. Under these assumptions the concrete merely retains the steel in its place. The difference between the two lines indicates the influence of the concrete.

Some notes regarding the construction and interpretation of Figure 5.6 are provided below. Yielding of the structure is illustrated by line C-D. The change in slope in line A-B-C at point B indicates the effect of concrete cracking. If this plot had represented actual data, an estimate of the tensile strain in concrete at point B would have to be made, and compared with the cracking strain of the concrete, to confirm the presumed cracking.

If the concrete in this idealized structure was such that after cracking all ability to carry load or to affect response stiffness was negligible, the measured response would follow a line from point B to point E and later, with increase in load, from point E to point F. The lower deformations for measured response line B-C compared to the response of steel alone, line E-F, illustrate the residual stiffening effect of concrete on the overall response. With increase in load above cracking, this residual stiffening effect dissipates until the structure begins to yield, at point C. At the yield load the stiffening effect of cracked concrete may yet influence total response, accounting for the difference or noncoincidence of points C and F.

The definition of apparent stiffness before cracking is selected to represent the initial response of the containment structure up to the point where cracking of concrete was sensed by the gages. Because a majority of the strain and displacement gages responding in tension show a distinct change in slope of plotted data at 20 psig or higher pressures it was decided to use the apparent secant stiffness at 20 psig for all gages as the definition of apparent stiffness before cracking. As illustrated in Figure 5.6, the waning influence of cracked concrete on response, between the loads causing cracking and yielding, is lowest just before yielding. Gages that did indicate yielding of reinforcement did so at pressures of approximately 105 psig and greater. The cracked-section apparent stiffness was therefore defined as the apparent stiffness at 115 psig, or at the start of yielding, whichever was less. Data at this pressure represent the response of the structure with the least influence of the stiffening effect of concrete.

5.2.2 Cylinder Wall Membrane Response

Strain and displacement gages located within or on the cylinder wall and away from the junctions of the wall to the dome or to the basemat recorded the response of the wall to essentially in-plane membrane forces. A radial deflection profile of the wall (Fig. 4.3) shows that in the elevation range 7 to 21 ft the shape was uniform. Except for the fact that pressure was contained within the structure, the wall response in this elevation range showed no sign that the wall was restrained above and below by a dome and basemat. A total of 123 strain gages located on reinforcing bars within this wall mid-section are considered representative of membrane response. The 24 radial displacement gages within this elevation range and the five vertical displacement gages (which record average vertical strain) between elevations 7 and 24 ft are also considered representative of membrane response. Apparent stiffness before and after cracking and the ratio of the former to the latter was determined for each gage.

A tabulation of the 152 gages used and the stiffness values determined for each is provided in Appendix A, Table A.1. A histogram of the ratio of the apparent stiffness before cracking to the cracked-section apparent stiffness for membrane response data is shown in the top of Figure 5.7. Data from most gages in the set result in a ratio of three. Roughly equal numbers of gages are shown on the histogram on either side of three.

5.2.3 Cylinder Wall Bending Response

Strain and displacement gages located within the cylinder wall near the junction of the wall and basemat recorded the response of the wall to vertical, bending, and radial shear forces. A profile of the deflected wall shape (Fig. 4.4) at elevations below 5 ft illustrates the restraint provided by the basemat, and the increase in outward radial deflection with increase in elevation. Calculated rotation of the wall at its base was presented in Figure 4.5. A total of 49 strain gages located on reinforcing bars between elevations 1 ft 6 in. and 2 ft 8 in. were selected to represent the effect of flexural cracking at the base of the wall. Stiffness values before and after cracking were determined for each gage.

Flexural response is characterized by a nonuniform strain distribution through the wall. Because the response at the base of the wall is mainly due to flexure and not to simple in-plane tension, a measure of the deformation there is more closely represented by curvature than by vertical strain on a particular layer of reinforcement. For this reason, the stiffness ratio which takes into account bending of the wall was calculated as a ratio of uncracked to cracked flexural stiffness. Flexural stiffness is commonly defined as the bending moment required to produce a unit rotation, M/θ. When the curvature of a structural member is integrated along the member length the result is a rotation. Curvature is therefore linearly related to rotation; hence flexural stiffness can be represented by the ratio of moment to curvature, M/ϕ. Curvature at a section can be written as the difference in strain at two locations divided by the separation distance: $\phi = (\varepsilon_{inside} - \varepsilon_{outside})/d$. The gages on vertical reinforcement on the inside of the wall, layers 2 or 10, were paired with gages on vertical reinforcement at equal azimuths and within three inches of elevation of each other on the outside of the wall, layers 5, 7, 8, or 11. A total of 98 pairings of gages resulted. These pairs of gages were used to calculate the ratios of flexural stiffness before and after cracking presented in the histogram in the middle of Figure 5.7. The stiffness ratio was determined according to the following:*

$$R_{flexural} = \frac{(1/K_{c,inside} - 1/K_{c,outside})}{(1/K_{u,inside} - 1/K_{u,outside})} \qquad (5.5)$$

where, K_u represents the apparent stiffness before cracking at a gage on the inside or outside of the wall and K_c represents the cracked-section stiffness

---

* Equation (5.5) was derived from the expression $(M_u/\phi_u) / (M_c/\phi_c)$. The apparent stiffness for a strain gage is the ratio of pressure to strain, eg. $K_{c,inside} = p_c/\varepsilon_{c,inside}$. Prior to flexural yielding the ratio of bending moment to pressure is assumed to be constant, $M_u/p_u = M_c/p_c$. This is not unrealistic considering the estimated bending moment at the wall base, Figure 6.4.

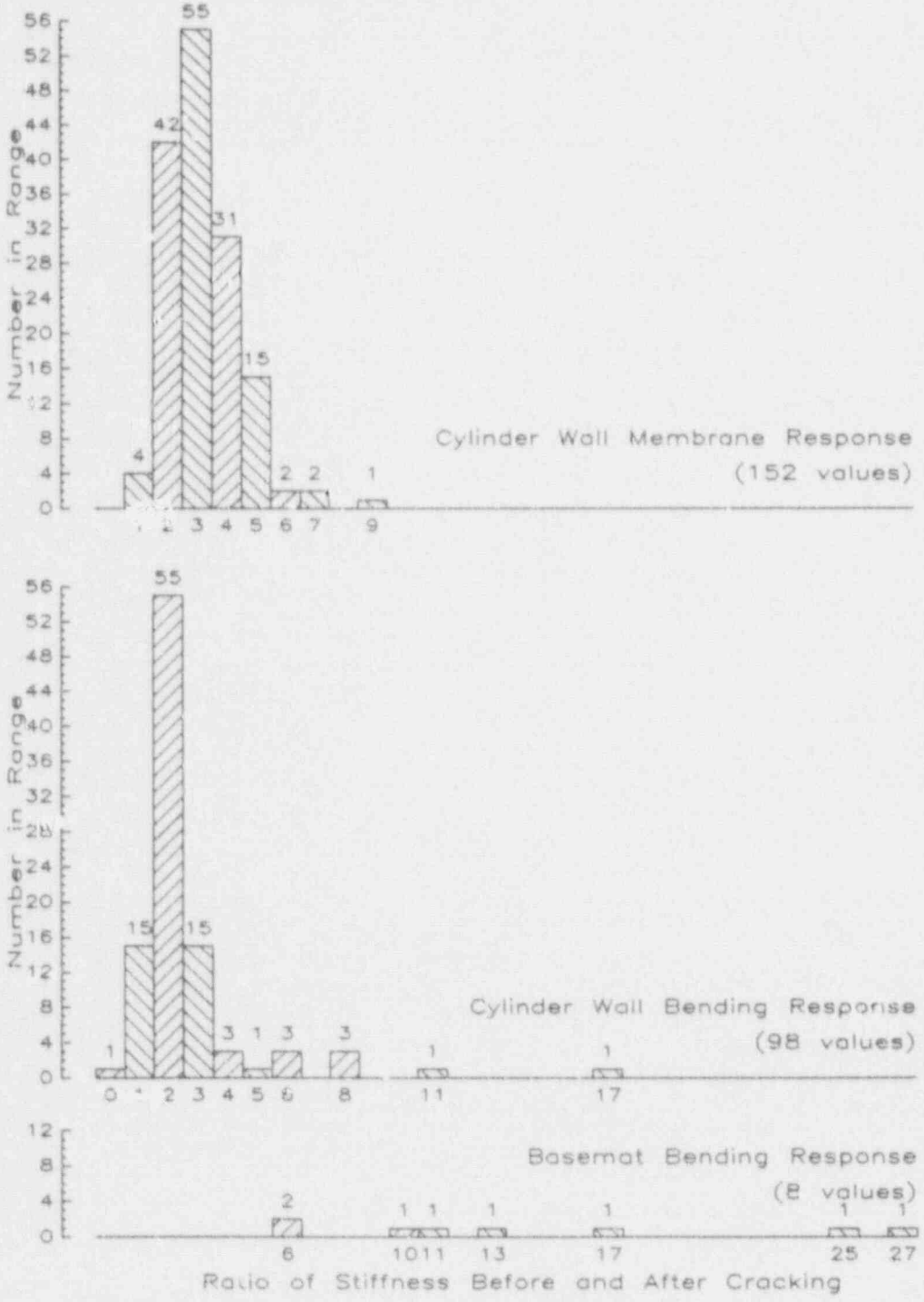

Fig. 5.7 Histograms of a Ratio of Apparent Stiffness Before Concrete Cracking to Apparent Stiffness After Cracking

for these gages. Equation (5.5) assumes that the ratio of bending moment to internal pressure is constant at the two pressure levels selected to determine apparent stiffness before and after cracking. A tabulation of the 98 gage pairs used and stiffness values determined for each is presented in Appendix A, Table A.2. The histogram of the calculated flexural stiffness ratios indicates that data from most of the gage pairs result in a ratio of two and roughly equal numbers of gage pairs result in a ratio that is greater than or less than two (Fig. 5.7).

5.2.4 Basemat Bending Response

Strain gages on radial reinforcement bars within the basemat recorded the response of the basemat to load that produced uplift at the edge and radial extension of the slab. All of the available data to represent the effect of basemat concrete cracking on basemat bending response is provided by data from ten strain gages on basemat radial reinforcement, from two strain gages on basemat circumferential reinforcement, and from two displacement gages that recorded uplift. Apparent stiffness values before and after cracking were determined for each gage. As for characterization of the bending response of the wall, estimates of curvature were used to characterize the bending response of the basemat before and after cracking. Radial strain gages at equal radii at the top and bottom of the basemat were paired and a ratio of flexural apparent stiffness before and after cracking was calculated according to Equation (5.5). Since the uplift of the edge of the basemat was indicated directly by one of either displacement gages, the change in apparent stiffness indicated by each displacement gage is used to illustrate the effect of concrete cracking on basemat bending. Similarly, the circumferential reinforcement gages located near the edge of the basemat indicate slab expansion associated with uplift and bending. The ratio of apparent stiffness before and after cracking for each circumferential strain gage was determined directly, as for the displacement gages that responded to uplift. A histogram of calculated bending stiffness ratios is shown in the bottom of Figure 5.7 and a tabulation of stiffness data used in the calculation is presented in Appendix A, Table A.3.

5.2.5 Summary of the Effects of Cracking on Response

Before this study was begun it was hoped to determine whether the effects of concrete cracking on the measured response of the containment model depended upon the strain distribution within the structure at the locations where cracking occurred. In other words, it was desired to quantify the effects of cracking: to determine if the relative changes in flexibility due to cracking differed if that cracking was initiated by bending or by in-plane tensile forces. Histograms for a ratio of apparent stiffness before and after cracking for each of the three modes of response considered (membrane response of the wall, bending of the wall, and bending of the basemat) were found to be different for each region of the structure. Of course, there is dispersion in the data but the difference between the distribution of the ratio for the wall membrane response compared to the distribution for wall bending response is significant. Based on the histograms, a reasonable estimate of the cracked-section stiffness of the wall in membrane action is one-third the uncracked-section stiffness and an estimate of the cracked-section stiffness of the wall in bending is one-half the uncracked-section bending stiffness. The data for bending of the basemat is sparse (8 values)

compared with response of the wall in bending (98 values) or as a membrane (152 values). No estimate of the cracked-section basemat stiffness can be made based on the data shown in Figure 5.7 other than that the decrease in basemat stiffness due to cracking is greater than the decrease in stiffness of the wall due to cracking. These differences result primarily from the different amounts of reinforcement in the wall and in the basemat (Fig. 2.3).

Simple "bounds" to the change in axial and bending stiffness due to cracking of the wall may be determined by considering the mechanics of reinforced concrete sections. The axial stiffness of a uncracked section may be approximated by $E_c A_g [1 + \rho (n - 1)]$ where E_c is the concrete modulus, A_g is the gross section area, ρ is the ratio of the total area of reinforcement to A_g, and n is the modular ratio of steel to concrete (E_s/E_c). After concrete cracking the contribution of concrete to stiffness may be disregarded. This assumption leads to an estimate of the cracked-section stiffness that results in the greatest deviation from the uncracked-section stiffness. This estimate of cracked-section stiffness eliminates the influence of the stiffening effect of concrete (Section 5.2.1). The cracked-section axial stiffness may then be estimated by $E_c A_g \rho n$ so that a ratio of the change in stiffness due to cracking may be written as $[1 + \rho (n - 1)] / \rho n$. With values for the circumferential reinforcement ratio for the wall ($\rho = 0.03$) and the modular ratio ($n = 8$) a "bound" to the change in membrane stiffness of the wall due to cracking is approximately 5. This is reflected by the data for membrane response of the wall (Fig. 5.7).

A measure of the change in flexural stiffness due to cracking may be obtained from a ratio of the gross-section to cracked-section moment of inertia (I_{gross} / I_{cr}). The gross-section unit moment of inertia for a 9.75-in. wall thickness is approximately 77 in^3. The moment of inertia of the wall after cracking can be estimated from the expression $I_{cr} = M / E_c \phi_{cr}$ where M is a bending moment associated with a curvature, ϕ_{cr}. Both M and ϕ_{cr} may be determined through a moment-curvature calculation (Section 6.1.2). Taking the results of one such calculation (Fig. 6.6) for the wall at an internal pressure of 120 psig ($M = 65$ kips, $\phi_{cr} = 0.00055$/in., $E_c = 3600$ ksi) gives an estimate for I_{cr} of 33 in^3. The ratio obtained for I_{gross} / I_{cr} is roughly 2.3. This reflects, approximately, the mean in the flexural stiffness ratio obtained from the measured data for bending of the wall (Fig. 5.7).

5.3 Analysis of Wall-Basemat Interaction

In this section an analysis model is described that is useful to the interpretation of behavior from response measurements. In contrast to the membrane analysis model above (Section 5.1), the intent of this analysis is to develop an understanding for the behavior of an analytical tool which is meant to simulate the response of the wall-basemat junction of the tested containment. Similarity in calculated and interpreted (from data) behavior allows one to infer the interactions of sections of the analytical model (cracking or yielding of a plate) to the response of the elements of the containment structure (the basemat, for example).

Evaluation of measured response in Sections 4.3 and 4.4 found events in the load history response for radial shear and for hoop moment which could not be explained solely from data observations. When the basemat cracked and began

to deflect upward at its edge at 75 psig the rate of shear transmitted from the wall to the base decreased with increase in pressure while the rate of moment increase remained the same. At 120 psig the wall began to yield in flexure yet the rate of shear increase with pressure increased. A linear-elastic axisymmetric analysis of the wall-basemat junction with appropriate assumptions for material property parameters offers an explanation for these observations. This analysis model is not sufficient, however, to offer a reason for the observed slow-down in strain increase with pressure for the shear reinforcement at 135 psig just as the bars reached their yield strain. It cannot simulate a fully yielded -- no increase with pressure -- moment once the wall yields in flexure.

The analysis model defined below is used to estimate radial shear, moment, and uplift at the edge of the basemat. The analysis proceeds through a series of "stages" and "break points." At each stage a new set of parameters for the elastic moduli for the wall and the basemat are selected. The equations are then solved in terms of shear per unit pressure or moment per unit pressure. A value for shear, moment, or uplift is calculated at the pressure level or "break point" defining the stage and plotted on a graph of test pressure versus calculated response (Fig. 5.9, 5.10). The plotted break points are connected by straight lines so that a rough indication of the change in shear or moment with pressure may be traced. Nonlinear response is included in the analysis. As the pressure level increases the values assumed for elastic modulus of various parts of the structure are reduced at each stage in the analysis from their initial values. Once the model is defined, it will be shown that an important task in the analysis is appropriate selections of the elastic moduli at each stage. The selected modulus values must accurately reflect the nonlinearity of the structure at the pressure level (break point) for each set of values (stage).

5.3.1 Description of Three-Variable-Parameter Analysis Model

An axisymmetric bending theory analysis is used to determine the radial shear force and meridional moment transmitted from the wall to the basemat. In this analysis the wall is assumed to be orthotropic with cylindrical anisotropy [Ref. 5.4] and the basemat is assumed to be isotropic. A schematic illustration of the model and a cut-section at the junction is shown in Figure 5.8. The notation and the sign convention for the internal forces are indicated in the figure. In addition, the figure presents flexibility equations for rotation and for radial displacement at the base of the wall written in terms of internal pressure, and the "sought after" moment and shear forces. The basemat is modeled as a circular plate simply supported at the edge. It is loaded by a uniformly distributed pressure load, an edge moment, and a radially directed in-plane force (wall shear). The influence of the foundation is approximated by neglecting from the flexibility equations the contribution to rotation at the junction, $pR^3/8D_b$ (Fig. 5.8), by the internal pressure. The effect of this approximation is that as pressure increases, the (simply supported) basemat deflects without producing a rotation at its edge. The problem of internal pressure on the plate is curious in that the entire internal pressure load is equilibrated at the edge of the plate because the containment is whole. The weight of the pressurized gas is negligible compared to the weight of the containment. The total dead weight of the structure presents a uniformly distributed load to the foundation of approximately 9 psi. The internal pressure therefore

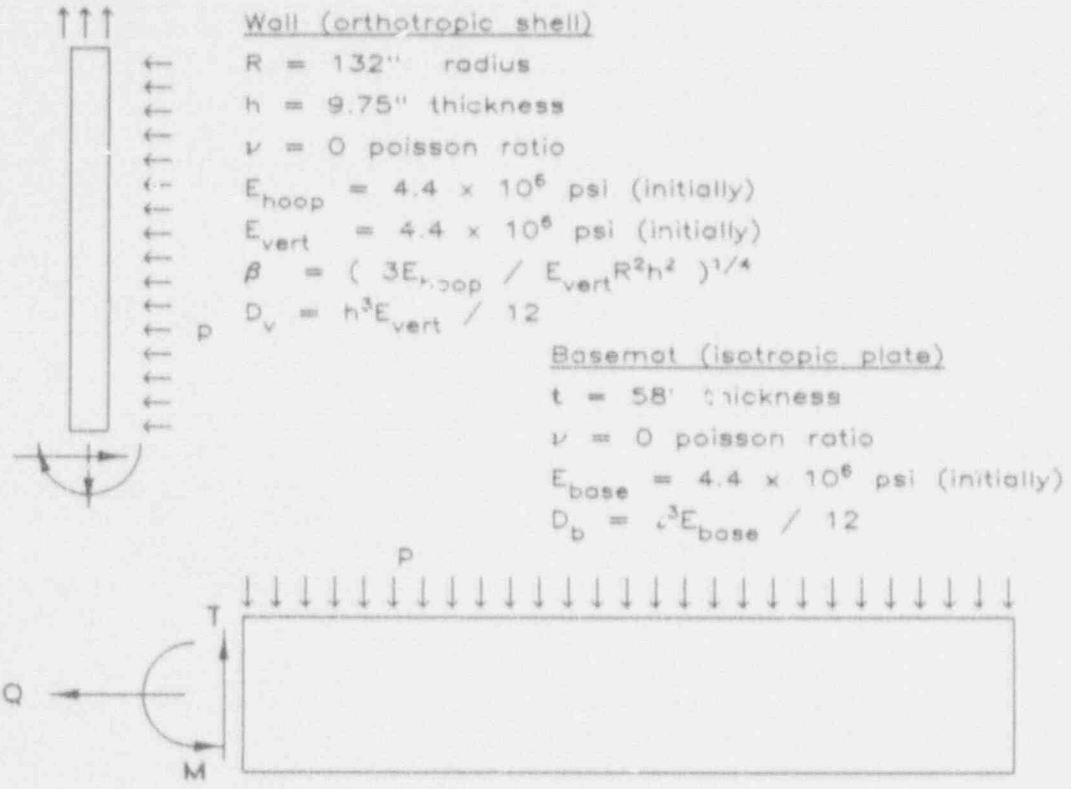

3-Parameter-Model Flexibility Equations:

wall:

$$\Delta = (\beta M - Q)/2\beta^3 D_v + pR^2/E_{hoop}h$$

$$\Theta = (Q - 2\beta M)/2\beta^2 D_v$$

basemat:

$$\Delta = QR/E_{base}t$$

$$\Theta = MR/D_b - pR^3/8D_b$$

$$\Lambda = 5pR^4/64D_b - MR^2/2D_b$$

Δ = Outward radial displacement at base of wall
Θ = Outward rotation at base of wall
Λ = Vertical uplift at edge of basemat

Fig. 5.8 3-Variable-Parameter Analysis Model

deforms the basemat into a concave shape and calculated rotations at the edge are inward. Data from track-mounted displacement gages indicated that the basemat rotation at the base of the wall was outward (Fig. 4.3 - 4.5), meaning that the basemat exhibited reverse curvature from the center to the edge of the slab. Alternate modeling schemes were considered for elastic analysis of the basemat: plate on an elastic foundation, plate supported at its edge to which is given a small deflection above a rigid foundation, circular plate with a hole (annular plate), circular plate with shearing

deformation included, and representations of the circular plate as an equivalent beam, simply supported, on an elastic foundation, etc. Unless a nonlinear analysis of the basemat including nonlinear modeling of the foundation is performed, all linear elastic models considered for the basemat indicated an inward rotation at the edge. For this reason the pressure contribution to edge rotation of the simply supported plate is neglected. The term indicating the contribution of the edge moment to rotation, M/∂_b (Fig. 5.8), is not neglected. The magnitude of edge rotation it adds to the calculation is small (approximately one-eighth) compared to the contribution by internal pressure. An equation for uplift at the edge of the basemat written in terms of internal pressure and edge moment is presented in Figure 5.8.

Variation of parameters for the analysis is treated in two ways. They are either held constant or are varied with each analysis stage. The geometry and Poisson's ratio for the sections of the structure considered are constant, having values listed in Figure 5.8. The values of elastic modulus for the wall in the hoop direction, E_{hoop}, and in the vertical direction, E_{vert}, and the value of elastic modulus for the basemat, E_{base}, vary with successive analysis iterations. The moduli are reduced from their initial values at each of four stages (defined below) as internal pressure increases.

The thickness of the basemat in the analysis is taken as 58 in. This includes the 40-in. reinforced concrete slab (basemat), shown in Figure 2.1, a 3-in. unreinforced concrete leveling course on which the liner was placed, a 3-in. unreinforced concrete protective course, and a 12-in. lightly reinforced fill slab, on top, which was the effective floor of the containment structure. Through a series of finite element analyses [Ref. 5.3] it was found that the combined 18 in. of concrete above the basemat added considerably to stiffness and that calculated basemat uplift compared favorably to measurements only with the total 58-in. slab thickness.

Poisson's ratios for the shell wall and basemat are taken as zero since both portions of the structure are in a state of biaxial tension and cracking occurred in each during application of load. Even though Poisson's ratio for the wall is assumed zero it should be noted that cross-axis stiffness coupling does exist in the real structure through the diagonal reinforcement and the liner. Basemat reinforcement basemat placed on an orthogonal grid also provides some coupling between the hoop and radial directions.

The wall is modeled as an orthogonal shell because there were differences in the change in stiffness due to cracking when cracking was caused by membrane or by bending stresses (Section 5.2) and because the reinforcement ratios in the hoop and vertical directions differed (Fig. 2.3). Excluding the liner, the (membrane) reinforcement ratio in the hoop direction at the wall mid-section was 0.0215 and the vertical (bending) reinforcement ratio at the base of the wall was 0.027. The linear shell analysis model uses parameters based on gross section dimensions. This implies that the stiffness properties in the hoop and vertical directions are identical. To simulate a difference in hoop and vertical stiffness, and to control the variation of the elastic properties in each direction, different values for E_{hoop} and E_{vert} are used. The initial value used for all three moduli (E_{hoop}, E_{vert}, and E_{base}) is 4.4×10^6 psi, from the ACI equation for concrete modulus [Ref. 5.2] at $f'_c = 6000$ psi.

Calculated deformation of the wall due to membrane forces makes use of both E_{hoop} and E_{vert} values whereas the calculated deformations to bending forces, with Poisson's ratio zero, makes use of only E_{vert}. In this analysis the variation of E_{vert} is not influential on the assumptions for the wall membrane response because vertical wall stretch is not calculated and because Poisson's ratio for the wall is assumed zero. Membrane hoop deflection is a part of the flexibility equations in the analysis for radial deflection at the wall base. Even though membrane response is two-dimensional, in the following discussions the variation of E_{hoop} only is associated with membrane response of the wall and E_{vert} is associated with bending response of the wall.

5.3.2 Variable-Stiffness Model

The assumptions for the variation of the elastic modulus parameters are based, in part, on the ratios of apparent stiffness before and after cracking for various regions of the structure (described in Section 5.2). They are based, also, so that target values for measured basemat uplift, and for calculated bending moment, could be estimated at each stage. Use of the model proceeds through the following steps: 1) assume values for the three elastic modulus parameters at a pressure level; 2) solve the flexibility equations for shear and moment; 3) calculate basemat uplift; and 4) compare the calculated values for moment and for uplift with their targets. These steps are repeated for each of four pressure levels (stages). It was found that at each pressure level several iterations of this procedure are necessary to achieve the desired target values (based on data, defined below) and to imitate the ratios of the changes in apparent stiffness due to cracking for appropriate portions of the structure. Since there are three elastic moduli that are varied, and the analysis equations are solved for two unknowns, there could be more than one set of parameters which fit a given set of target values. But by considering also the relative changes in apparent stiffness of the containment, the selection of the elastic moduli is constrained to reflect the observed trends.

The calculation is performed at four pressure levels (break points) corresponding to pressures initiating cracking and yielding within the wall or basemat. These break points are summarized in the following:

20 psig — Initial response (uncracked).

75 psig — Response of the wall after cracking; initial (uncracked) response of the basemat. Values of E_{vert} and E_{hoop} for the wall are reduced from their initial values and E_{base} remains at its initial value.

120 psig — Wall at the onset of flexural yielding; Response of the basemat after cracking. All three parameter values, E_{vert}, E_{hoop}, and E_{base}, are reduced as necessary from their values at the previous step.

145 psig — Yielded response of the wall in flexure and circumferentially over most of the height of the wall; unyielded response of the basemat.

Target values for basemat uplift are based on measured data presented in Figure 4.9. Target values for moment are based on calculations for cracking and yield moment for the wall. Unit cracking moment is determined from $f_t\ h^2/6$ to be 4 kips, with the concrete tensile strength, f_t, equal to 250 psi, based on assumptions for concrete strength described in Section 5.1.2, and the wall thickness, h, of 9.75 in. This moment is assumed to be present in the wall at 20 psig internal pressure, just before flexural cracking. Yield moment at 120 psig is determined from a moment-curvature calculation for the wall (described in Section 6.1.2 with results presented in Figure 6.6) to be 65 kips. A goal in this analysis is to find a realistic set of values for the elastic modulus parameters where the rate of moment increase remains constant between cracking and yielding while at 75 psig the rate of shear increase decreases. The target moment at 75 psig, therefore, lies on a straight line between the cracking and yield moments. At 145 psig the target moment value is assumed unchanged from at 120 psig.

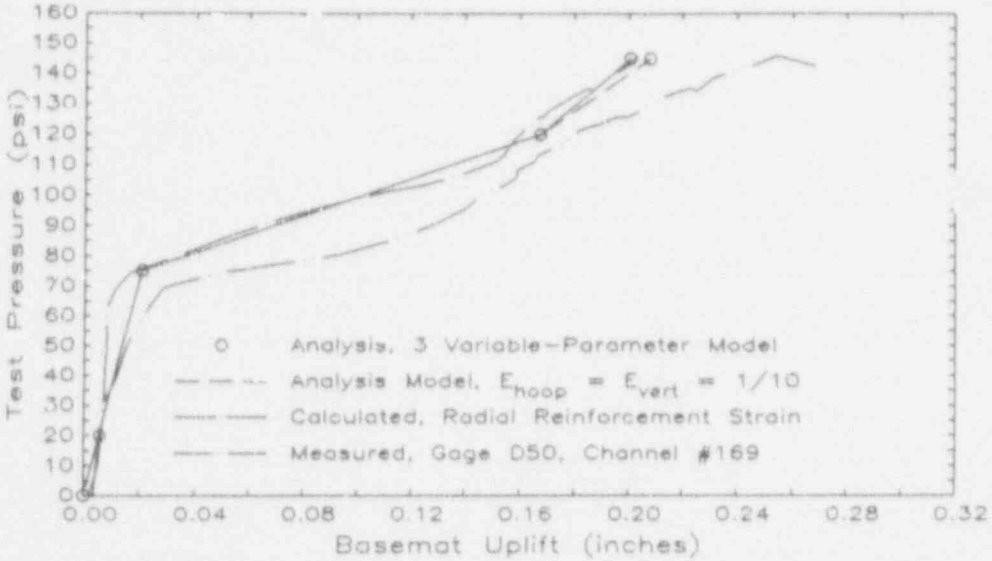

3-Variable-Parameter Model

pressure range (psig)	0~20	0~75	0~120	0~145	0~145
E_{hoop}	1	1/2.7	1/3	1/12	1/10
E_{vert}	1	1/2	1/2	1/8	1/10
E_{base}	1	1	1/5	1/5	1/5

Fig. 5.9 Basemat Uplift Calculated From Analysis Model

The selection of appropriate reductions of the elastic modulus parameters with increase in pressure is made in a somewhat unconventional manner, according to the description which follows. Basemat uplift calculated with the analytical model is compared in Figure 5.9 to measured uplift data. Calculated shear and moment is presented in Figure 5.10.

Using the target values for moment and basemat uplift, it is found that reducing E_{base} by a factor of 5 at 120 psig and 145 psig makes a good match to the data. The median value for the ratio of uncracked to cracked stiffness

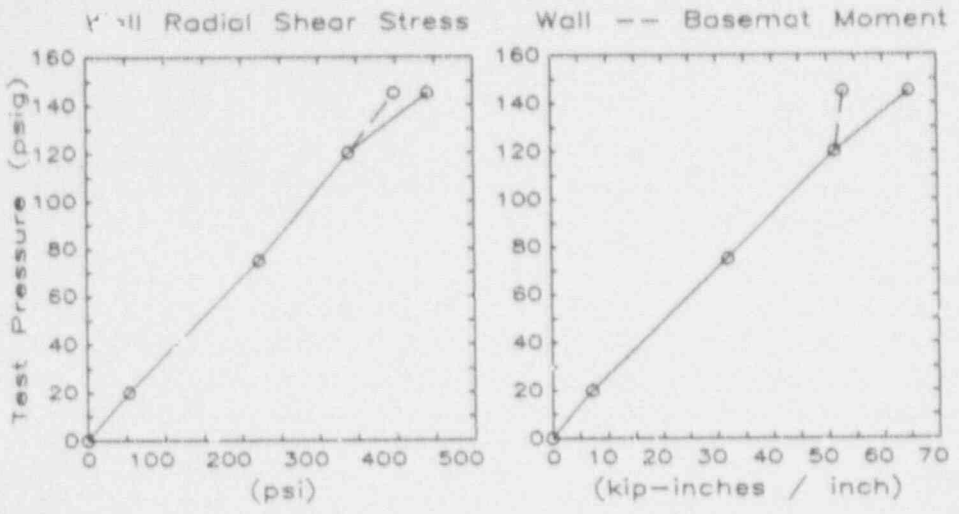

3-Variable-Parameter Model

pressure range (psig)	0~20	0~75	0~120	0~145	0~145
E_{hoop}	1	1/2.7	1/3	1/12	1/10
E_{vert}	1	1/2	1/2	1/8	1/10
E_{base}	1	1	1/5	1/5	1/5
				(solid line)	(dashed line)

Fig. 5.10 Shear and Moment Calculated from Analysis Model

for the wall responding to in-plane forces is 3 whereas the median ratio for the wall responding to bending forces is 2 (Fig. 5.7). These ratios are used as factors for reducing the E_{hoop} and E_{vert} values at 120 psig from their initial value. Values of these two parameters at 75 psig are determined so that moment increases along a straight line from 20 to 120 psig. After several analysis iterations it is found that at 75 psig when E_{hoop} is reduced by a factor of 2.7 and E_{vert} is reduced by a factor of 2, the moment calculated is on a straight line mid-way between the values at 20 and 120 psig (Fig. 5.10).

Two sets of values for E_{hoop} and E_{vert} parameters at 145 psig are shown in Figures 5.9 and 5.10. Assuming that as the wall yields above 120 psig, the relative values of E_{hoop} and E_{vert} retain a ratio of 1/3 to 1/2, the shear, moment, and uplift will increase along the solid lines in the plots. The actual values of E_{hoop} and E_{vert} used in the calculation are 1/12 and 1/8, respectively, of their initial values. Calculated shear and moment are essentially the same for other values of the two moduli as long as the ratio of E_{hoop} to E_{vert} is two to three. Assuming that both parameters are equal, reduced by a factor of, say, ten from their initial value, the calculated quantities increase above 120 psig along the dashed line in the plots.

5.3.3 Behavior Indicated by Analysis

As internal pressure increases from 75 to 120 psig the basemat cracks and starts to lift off its foundation. With other factors unchanged this increase in basemat flexibility is likely to cause a decrease in the rate of

both shear and moment increase with pressure. The analysis suggests that as pressure increases from 75 to 120 psig the stiffness ratio of the wall in the hoop direction decreases from 1/2.7 to 1/3, the basemat stiffness ratio decreases from 1 to 1/5, and the vertical wall stiffness remains unchanged from its value (1/2) at first cracking. These conditions allow the bending moment to be calculated, which continues to increase as pressure increases from 20 psig to 120 psig, giving the illusion that the postulated changes in stiffness do not occur. Shear at the wall-base is sensitive to both the decrease in hoop stiffness of the wall and to the decrease in the stiffness of the basemat. As pressure increases from 75 to 120 psig the rate of shear increase with pressure decreases slightly from its rate in the pressure range 20 to 75 psig. As the stiffness of the basemat decreases at 120 psig the shear at that pressure would correspondingly decrease. As the stiffness of the wall in the hoop direction decreases at 120 psig the shear would increase. The calculated trend (Fig. 5.10) suggests that the shear is influenced more by the decrease in the basemat stiffness than by the decrease in wall hoop stiffness. These trends in shear, from 20 to 120 psig, highlight the influence of the basemat on the response of the wall.

Strains measured on shear reinforcement (Fig. 4.16, 4.17) suggest that above 120 psig the rate of shear increase was greater than in the pressure range just before 120 psig. Strains on vertical reinforcement (Fig. 4.10 to 4.13) suggest that above 120 psig the moment transmitted from the wall to the basemat remains the same or increases slightly from its value at 120 psig. At 145 psig two sets of the three elastic modulus parameters are used and compared. The first set (E_{hoop} = 1/12, E_{vert} = 1/8, E_{base} = 1/5) finds that shear increases above 120 psig at a rate greater than below 120 psig and that moment increases as well. The second set (E_{hoop} = E_{vert} = 1/10, E_{base} = 1/5) finds that moment at 145 psig remains approximately the same as at 120 psig and that shear does not significantly increase from its value at 120 psig. These two parameter sets illustrate the limitation of this analysis model after the wall yields in flexure. The model cannot be used to calculate a moment which does not increase with pressure and be used simultaneously to calculate a shear which increases at a rate greater than it had at a lower pressure level.

An explanation for behavior at the wall-basemat junction above 120 psig is offered. As the vertical reinforcement at the base of the wall yields, the moment there is expected to remain approximately constant. Data from track-mounted displacement gages (Fig. 4.3) show that above 120 psig the mid-section of the wall expands considerably but near the junction to the basemat, at elevations below 4 ft, the wall has not yet yielded in the hoop direction. Results of the "benchmarks" calculation (Section 5.1) found that yielding of circumferential wall reinforcement occurred with a radial displacement of 0.29 in. (Table 5.1). Radial displacements of the wall below 4 ft (Fig. 4.3) were less than this yield displacement. This means that additional increases of internal pressure formerly balanced by hoop stresses in the wall are now carried to the dome and basemat. The rate of shear transmitted to the basemat would correspondingly increase. The overall hoop-direction yielding of the wall at its mid-section and the flexural yielding of the wall at its base occur at approximately the same pressure as a coincidence. The increase in the rate of shear increase with pressure above 120 psig is due to the overall hoop-direction yielding of the wall.

6. INTERNAL FORCES AT THE WALL BASE

In this section estimates are presented of moment and shear at the base of the wall on the basis of the measured strain data. It is concluded that the wall had yielded in flexure at the wall-basemat junction at the end of the test. The maximum unit yield moment is estimated to have been 64 kips at 118 psig internal pressure. Unit shear stress at the base of the wall is estimated to have been 450 psi ($5.7\sqrt{f'_c}$), based on gross sections, at the maximum test pressure of 145 psig. It is also estimated that the rate of increase of this shear would have continued to rise with increases in pressure above 145 psig.

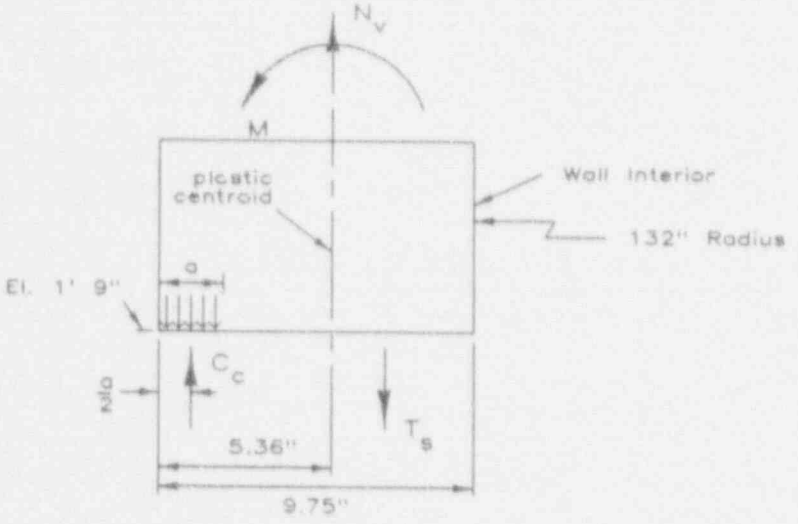

Wall Profile at Elevation 1' 9"

N_v Net unit vertical force, due to internal pressure and dead load
T_s Unit vertical force in reinforcement determined from strain data
C_c Unit vertical force in concrete: $C_c = T_s - N_v$
M Estimated unit moment
a Depth of uniform stress block in concrete: $a = C_c / 0.85\ f'_c$

Fig. 6.1 Illustration of Calculation for Moment at Base of Wall

6.1 Moment at Base of Wall

6.1.1 Procedure for Estimating Moment from Measured Strain

Strains measured on reinforcing bars and the liner are used to estimate meridional moment at the base of the wall. Presented in Figure 6.1 is a free-body diagram of the base of the wall to illustrate the forces in the steel and in the concrete. The tension forces in the steel are determined from strain gage data and the locations of these forces are given by the expected positions of the instrumented bars. Measured strains are converted to stresses according to Young's modulus for steel and the nominal area of each bar. The compressive force in concrete is determined from the difference between the net vertical (statically determined) force due to the pressurization and the force in the steel. This compressive force is located

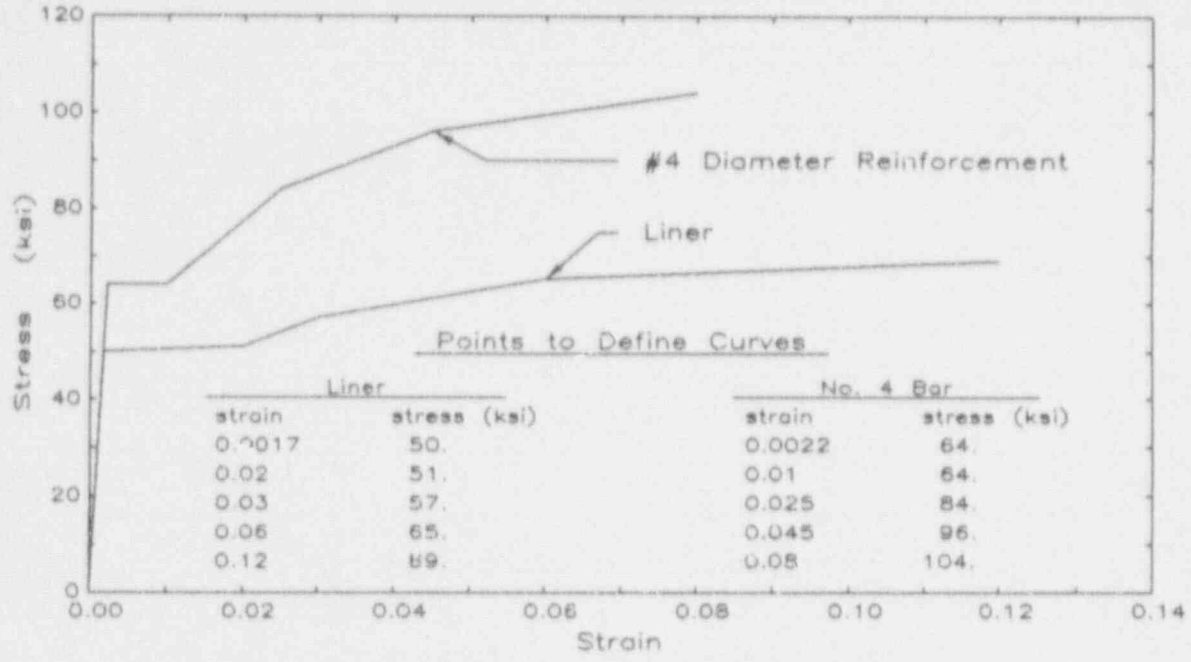

Fig. 6.2 Idealized Stress-Strain Curves for Steel

within the center of a uniform stress block at the exterior of the wall section (Fig. 6.1).

Gages Wr281, Br2, Wr225, Br7, Br1481, Br14, Wr14, and Br23, at the wall-basemat junction at azimuth 90 degrees (Fig. 3.3), represent a complete set of strain data from the reinforcing bars and the liner that transmit moment from the wall to the basemat. Data from these gages are presented in Figures 4.10 to 4.17 (Section 4.3). Measured strains are converted to stress according to the idealized stress-strain curves presented in Figure 6.2. The curves in this figure are based on linear approximations to the strength test data for the liner and No. 4 reinforcement material, as reported in reference 2.3. Since No. 6 reinforcing bars were not tested for strength, it is assumed that the stress-strain curve for the No. 4 bars applies to data from gage Wr225 on a layer 10 reinforcing bar (Fig. 4.12).

The vertical components of force in the steel, T_s, per unit circumference are summed and presented in Figure 6.3. Forces calculated from reinforcement strains which are compressive, at the exterior of the wall, are not included with the total (tensile) steel force. The net vertical unit force (Fig. 5.1) at the wall-base is given by $N_v = (pR^2 - W/\pi)/(2R + t)$, where W is the weight of the cylinder wall and dome (270 kips), R is the inner wall radius, t is its thickness, and p is the internal pressure. The unit force in concrete, C_c, is found from the difference in T_s and N_v and is presented in Figure 6.3. In this calculation, the compressive forces carried by reinforcement layers 5, 7, or 8 (Fig. 4.15 - 4.17) are included with the concrete force. Strains recorded by gages on these bars are small in magnitude compared with strains recorded by gages on layers 2 or 10, or on the liner (Fig. 4.10 - 4.12).

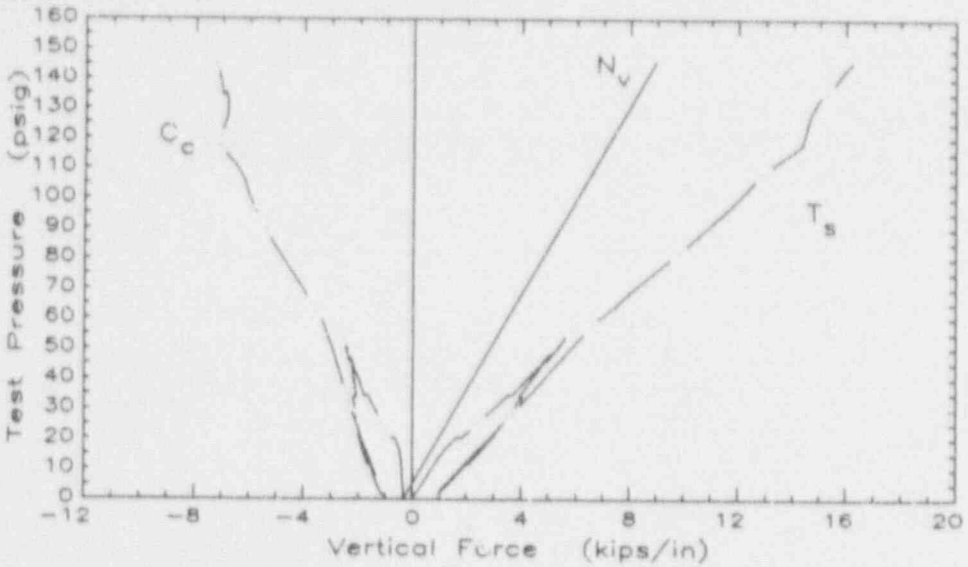

N_v = Statically determined total vertical force

T_s = Sum of tensile forces in reinforcement

C_c = Force attributed to concrete and compression steel

Fig. 6.3 Vertical Unit Forces at Base of Wall

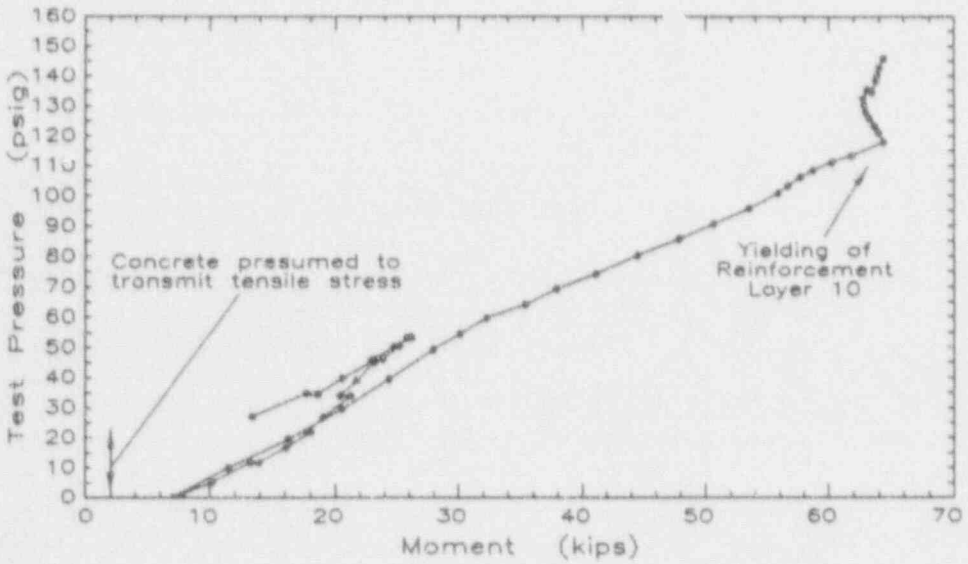

Fig. 6.4 Estimated Moment History at Base of Wall

The location of the concrete force is determined by assuming that the force is transmitted through a uniform stress block having a stress equal to $0.85f'_c$ [Ref. 5.2] for all pressure levels. The plastic centroid for the wall section is 5.36 in. from the exterior wall surface when the wall is compressed uniformly to 0.003 strain. The contributions by the steel and the concrete to meridional bending moment are calculated about this location and presented in Figure 6.4.

The maximum unit moment occurs at 118 psig internal pressure and is estimated to be 64 kips. At this pressure, strains measured on the liner and on reinforcement layer 2 were greater than their yield strain while strain measured on reinforcement layer 10 had just reached its yield strain. Above 118 psig the moment is estimated to be equal to or less than this value. The moment is not plotted in Figure 6.4 at pressures below 25 psig because the wall is uncracked in this range and, since part of the concrete carries tension stresses, the location of the force attributed to concrete is uncertain. It is interesting to note that as flexural yielding occurs at 118 psig, the total tensile force in the steel slows its rate of increase with pressure (Fig. 6.3). The slopes of the curves T_s and N_v in Figure 6.3 are approximately equal above 118 psig and the force attributed to concrete remains constant or decreases slightly in magnitude with further increases in pressure.

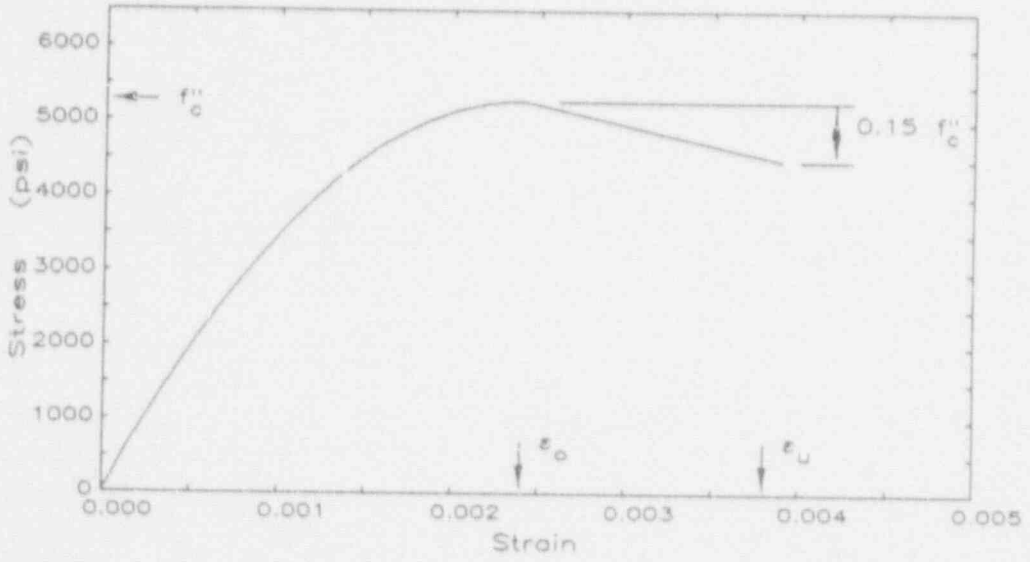

Hognestad curve:

$$f_c = f''_c \left[2(\varepsilon/\varepsilon_o) - (\varepsilon/\varepsilon_o)^2 \right] \qquad \text{for } 0 < \varepsilon \leq \varepsilon_o$$

$$f_c = f''_c \left[1 - 0.15(\varepsilon-\varepsilon_o)/(\varepsilon_u-\varepsilon_o) \right] \qquad \text{for } \varepsilon_o < \varepsilon \leq \varepsilon_u$$

where:

$$\varepsilon_o = 2\, f''_c \,/\, E_c$$

$$f''_c = 0.85\, f'_c$$

$$\varepsilon_u = 0.0038$$

f'_c = compressive strength of sample cylinders

E_c = Young's modulus of concrete

Fig. 6.5 Hognestad Stress-Strain Curve for Concrete

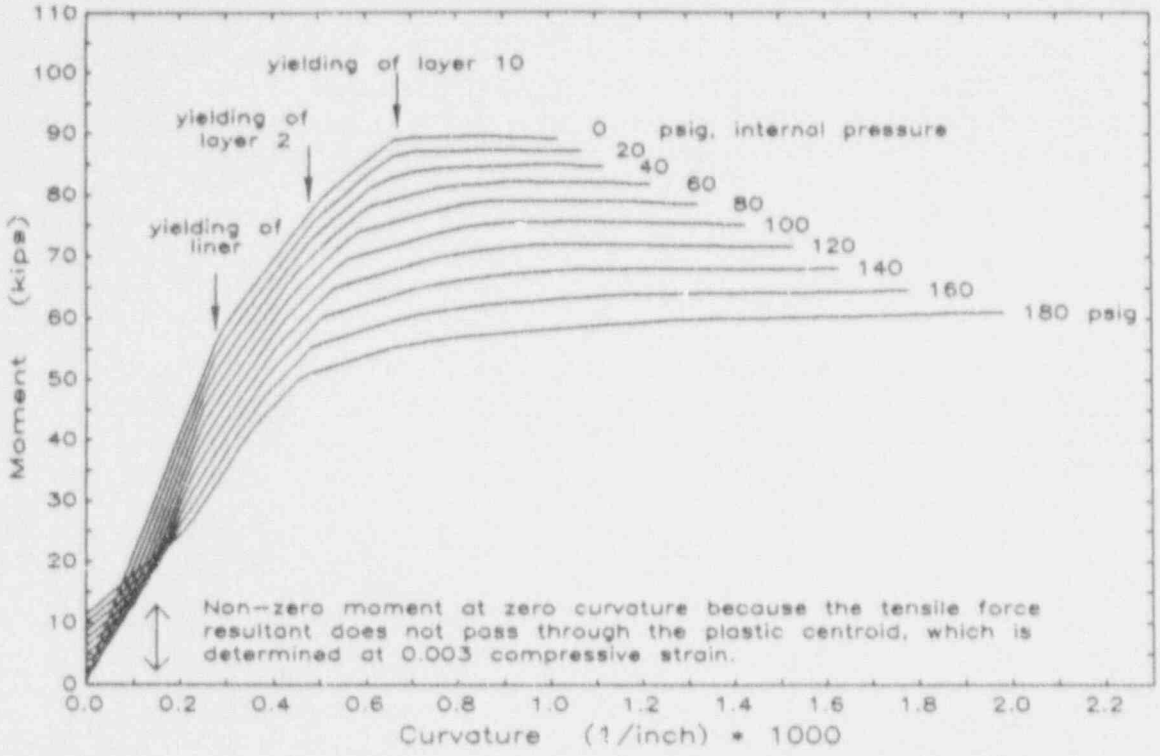

Fig. 6.6 Moment-Curvature Calculation

6.1.2 Moment-Curvature Calculation

A check on the yield moment estimated from strain measurements is possible through a moment-curvature calculation for the wall section. The calculation procedure and its use are described in detail by Pfrang, et al. [Ref. 6.1]. A section of the wall considered is discretized by defining slices at various depths (through the wall thickness). Strain is assumed to have a linear variation with depth. The stress within each slice is determined from the strain at the depth of the slice and from assumptions on the stress-strain curves for the material elements comprising the wall. The calculation proceeds by finding sets of strain distributions for which the net force across the section equals a selected applied load. Moment is calculated at this load for each strain distribution in the set and plotted as a function of curvature.

The stress-strain curves for the reinforcement and the liner shown in Figure 6.2 are used in the calculation. These curves are assumed to be symmetric when converting compressive strains to stress. A stress-strain curve suggested by Hognestad [Ref. 6.2] and shown in Figure 6.5 is used for the concrete. Concrete is assumed to carry only compressive stress.

The resultant moment-curvature curves are presented in Figure 6.6. Each line in the plot represents combinations of moment and curvature given a constant applied force normal to the section. The curves are identified in the figure by the internal pressure load and include the dead load of the containment wall and dome. The unit yield moment at the point where the layer 10 reinforcement yields, at 118 psig internal pressure, is 65 kips.

6.1.3 Uncertainty in Moment Estimate

Five sources of uncertainty in the estimated unit yield moment are considered.

(a) Location of Reinforcing Bars

All estimates of moment from strain measurements are made on the assumption that the reinforcing bars were placed at locations indicated on construction drawings. The containment model was constructed under close supervision [Ref. 2.2] but a shift in depth in the location of a reinforcing bar by approximately a quarter inch is plausible. A shift by this amount for a No. 6 bar could alter the estimated unit yield moment by as much as 1.6 kips or for a No. 4 bar by as much as 0.7 kips.

(b) Stress-Strain Curves for Steel

Twenty No. 4 reinforcing bar samples were tested for strength [Ref. 2.3]. The mean and standard deviation of yield strength are presented in Table 2.1. Yield strength statistics for the samples of liner material are presented in Table 2.2. Making a crude assumption that the coefficient of variation (c.o.v.) of strength for all steel is 0.02, an estimate in the uncertainty (at two standard deviations) in unit moment is 2.6 kips.

(c) Accounting for Initial Vertical Strain Due to Dead Load

Since all strain gages were re-zeroed before the SIT, strains due to dead load could not be measured. An analysis of the effect of initial vertical strain on the estimated yield moment is presented in Appendix B. The analysis finds that assuming a separation distance of the internal force couple of 6.83 in., or approximately seven-tenths the wall thickness, the uncertainty in estimated unit yield moment is approximately 0.4 kips.

(d) Inclusion of Inclined (Shear Reinforcement) Bars in Calculation

The vertical components of force carried by the No. 4 inclined shear reinforcing bar (layer 11) and by the No. 3 stirrup are included in the moment estimate calculation. Since these bars were provided primarily to carry shear and since they cross the wall section near the center of the wall it is debatable whether they should be included with the calculation to estimate moment. If they were to be excluded the estimated unit yield moment would be reduced by approximately 5.5 kips. Excluding these bars does not appreciably change the contribution of steel to the total moment since they are located near the plastic centroid, but they do affect the estimate of the concrete force. The unit concrete force would be reduced by 1.3 kips/in. (from 7.1 to 5.8 kips/in.). Since the concrete force is located near the exterior of the section a large reduction (5.5 kips) in yield moment would result.

(e) Location of the Concrete Force

The concrete force is located according to the size of an equivalent uniform stress block. An alternate method would be to use strain data to determine the neutral axis depth and then apply an assumed stress distribution for

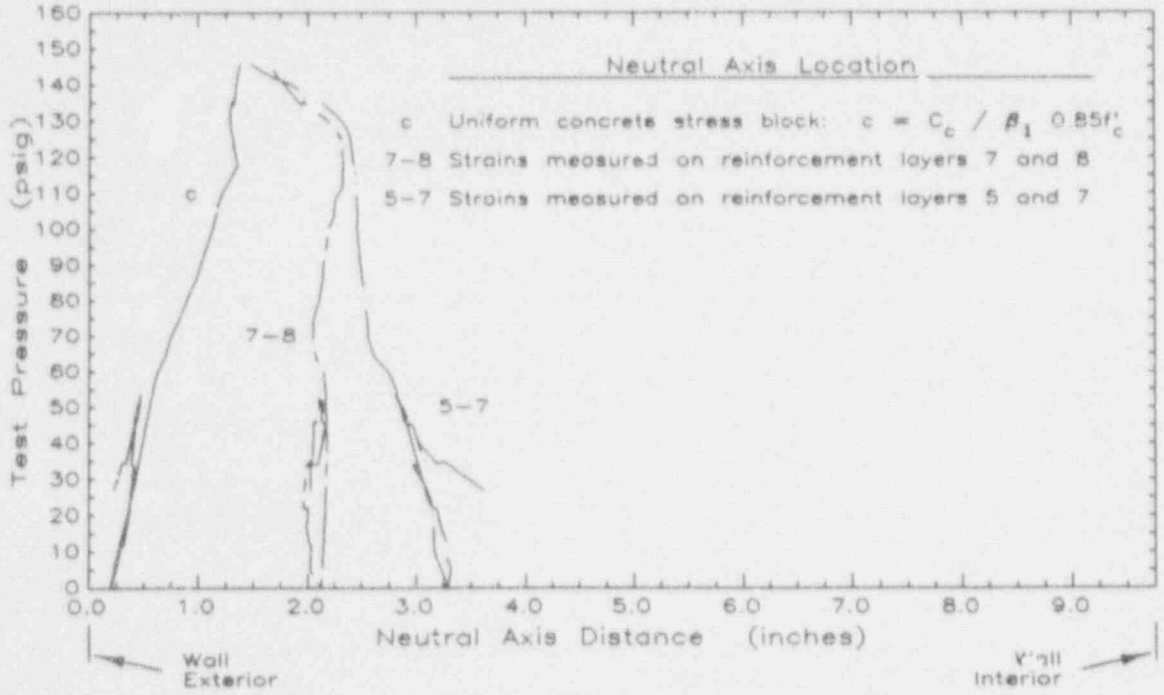

Fig. 6.7 Comparison of Neutral Axis Distance for Alternate Moment Estimates

concrete within the compression region. Strains measured on layers 5, 7, and 8 are nonlinearly distributed through the wall thickness. Location of a neutral axis can be assumed to be given by linear interpolation of data from gages on layers 5 and 7 or of data from gages on layers 7 and 8. The calculations are presented in Figure 6.7. Shown also in the plot is the neutral axis determined from the equivalent uniform stress block method using the expression C_c / $\beta_1 0.85 f'_c$ to locate the neutral axis, where β_1 = 0.75 for f'_c = 6000 psi [Ref. 5.2].

Two stress distributions for concrete may be assumed at each of the two neutral axis locations. The first distribution is triangular, assuming the concrete stress varies linearly, with a centroid at one third the distance to the neutral axis measured from the wall exterior. The second distribution is nonspecific, assuming a nonlinear stress variation, but has a shape similar to the Hognestad stress-strain curve (Fig. 6.5) and a centroid at 0.4 times the neutral axis distance from the exterior.

The unit force attributed to concrete, C_c, is applied to the location of the centroids of the two strain distributions considered for the two different neutral axis depths. The four moment estimates calculated by these alternate procedures are compared with the uniform stress block moment estimate in Figure 6.8. Unit yield moments determined by the alternate procedures are less than the estimated 64 kips moment with a maximum difference of 2.1 kips.

(f) Summary of Uncertainty in Moment Estimate

Each of the five sources of uncertainty in moment estimate identified above indicate the maximum amount by which they can affect the estimated yield

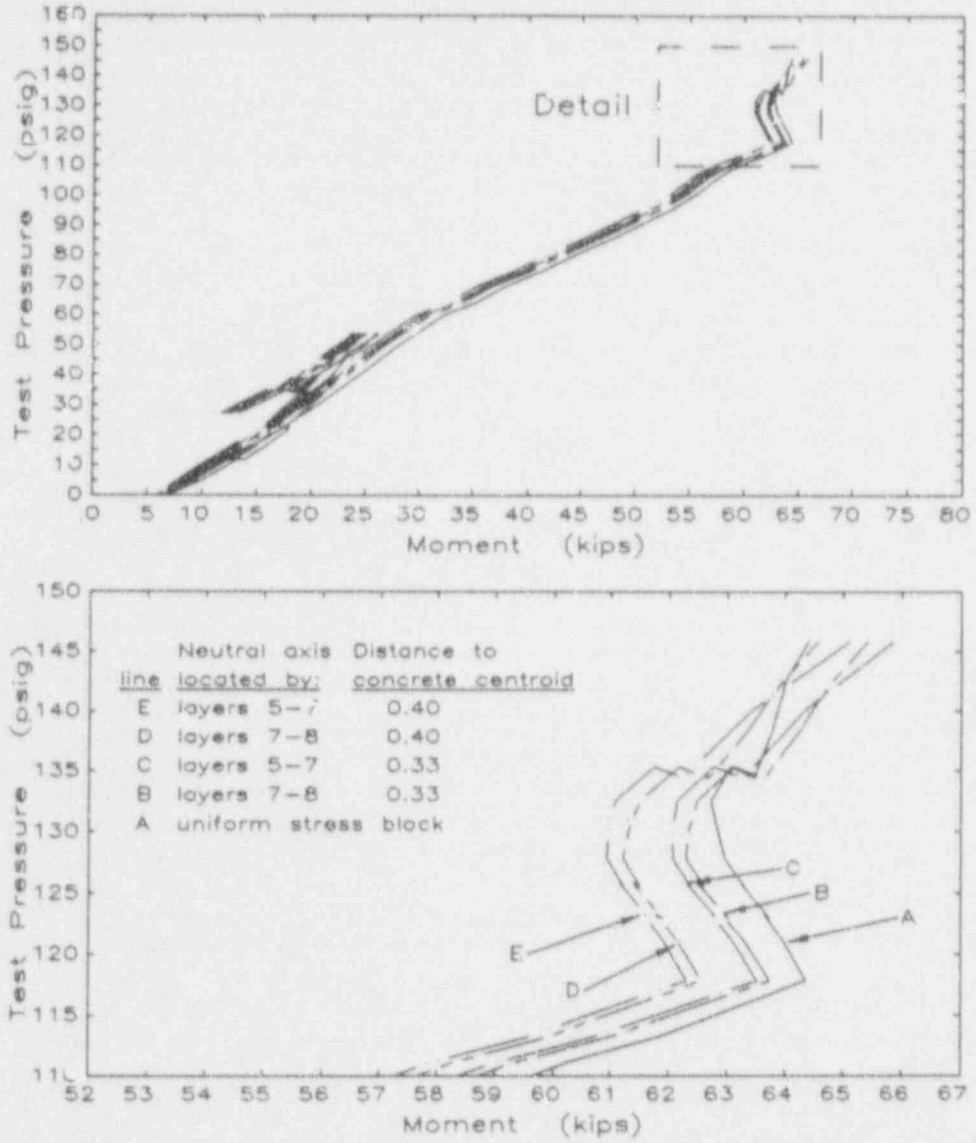

Fig. 6.8 Alternate Estimates of Moment at Base of Wall

moment. Calculation of the combined uncertainty is made, crudely, using a first-order approximation [Ref. 6.3], by taking the square root of the sum of the squares of the coefficient of variation in moment from each source. The c.o.v. of moment for each source is taken as half of the amount by which the unit yield moment would change due to the uncertainty divided by the estimated unit yield moment (64 kips). Data for the calculation are presented in Table 6.1. The total uncertainty in moment expressed as a c.o.v. is 5.2 percent. The maximum likely uncertainty (two standard deviations) in calculated unit yield moment is 6.6 kips.

Table 6.1 Summary of Uncertainty in Unit Yield Moment Estimate

Source of Uncertainty	Deviation in Unit Moment Estimate	c.o.v. of Unit Moment Estimate
Location of reinforcement	1.6 kips	.012
Steel strength	2.6	.020
Initial dead load strain	0.4	.003
Inclusion of shear reinforcement	5.5	.043
Centroid of concrete force	2.1	.016
Combined uncertainty	6.6 kips	.052
Estimated (mean) unit yield moment	64.4 kips	

6.2 Shear at Base of Wall

6.2.1 Shear Estimate from Strain Data

Shear at the base of the wall does not lend itself to determination in a manner similar to that used for moment. The radially directed shear is statically indeterminate, whereas in the moment computation vertical force is determinate. A cut-section at the base of the wall (Fig. 6.9) illustrates the unit shear force carried by the shear reinforcement, V_{sw}, and the unit shear carried by concrete, V_{cw}. The portion of shear carried by reinforcement can be determined from strain data, but the shear in concrete is unknown since the total shear cannot be independently determined. Referring to a cut-section of the basemat at the eleven foot radius (Fig. 6.9) the net tensile force in the basemat is composed of the unit tensile force carried by reinforcement, T_{sb}, and the unit compressive force carried by concrete, C_{cb}. The algebraic sum of these two forces equate to the total unit shear force at the base of the wall. It is assumed that the radial component of force in hoop reinforcement at the 12 ft 4 in. radius, near the exterior of the basemat (Fig. 3.6), carries a negligible fraction of the basemat tension.

Gages Wr14 and Br23 at the 90 degree azimuth (Fig. 6.9) within the base of the wall recorded strains on shear reinforcement that transmit shear across a critical section at the juncture of the wall and basemat. Data from these gages are shown in Figure 6.10. The portion of unit wall shear carried by reinforcement, V_{sw}, is determined from the horizontal component of force in the shear reinforcement. Gages Wr13, Wr11, and Wr5 (Fig. 6.9) recorded strains on radially oriented reinforcement in the basemat at the 11-foot radius. Data from these gages are shown in Figure 6.11. The data are used to determine the portion of unit radial force in the basemat that is carried by reinforcement, T_{sb}. Measured strains on the reinforcement are converted to stress according to the idealized stress-strain curve for a No. 4 bar (Fig. 6.2). It is assumed that the No. 4 bar stress-strain curve applies to No. 3, No. 5, and No. 6 bars.

The calculated unit shear force in the wall carried by reinforcement is presented in Figure 6.12 as curve V_{sw}. The unit radial force in basemat reinforcement at the eleven foot radius is presented in the figure as curve T_{sb}. Both unit forces are converted to a uniform shear stress on the wall by dividing by the 9.75-in. wall thickness. The total unit radial shear in the wall is carried by shear reinforcement, V_{sw}, and concrete, V_{cw}, through

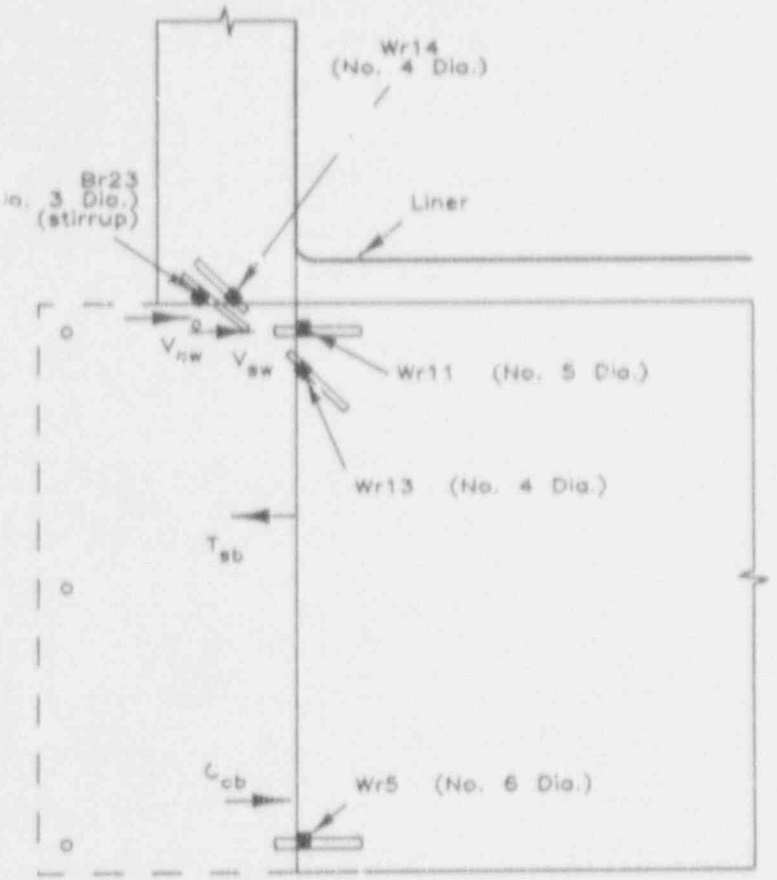

V_{sw} = Radial shear force carried by reinforcement at base of wall
V_{cw} = Radial shear force carried in concrete at base of wall
T_{sb} = Basemat tension force carried by reinforcement
C_{cb} = Basemat compression force carried in concrete

Fig. 6.9 Cut-Section at Wall-Basemat Junction (90° Azimuth)

direct shear or through dowel action. The shear carried by concrete in the wall cannot be determined from strains measured on reinforcement.

The radial force in the basemat is similarly composed of the unit force in reinforcement T_{sb}, and the unit force in concrete, C_{cb}. The force C_{cb} cannot be determined since the total radial force is unknown. Data in Figure 6.11 indicate that throughout most of the test the top of the basemat at the eleven foot radius was in tension and the bottom was in compression. At pressures above 138 psig, however, gage Wr5 on a No. 6 bar at the bottom of the basemat recorded tensile strains. The maximum strain recorded by this gage, at 145 psig internal pressure, is approximately 0.02 percent (Fig. 6.11). Calculated hoop response benchmarks (Section 5.1.2) indicate that the tensile strain that initiates cracking for the concrete in this structure is 0.007 percent (Table 5.1). At the maximum test pressure the entire thickness of the basemat is assumed to be cracked; tensile strain recorded by gage Wr11 on a No. 5 bar at the top of the basemat was approximately 0.10 percent at

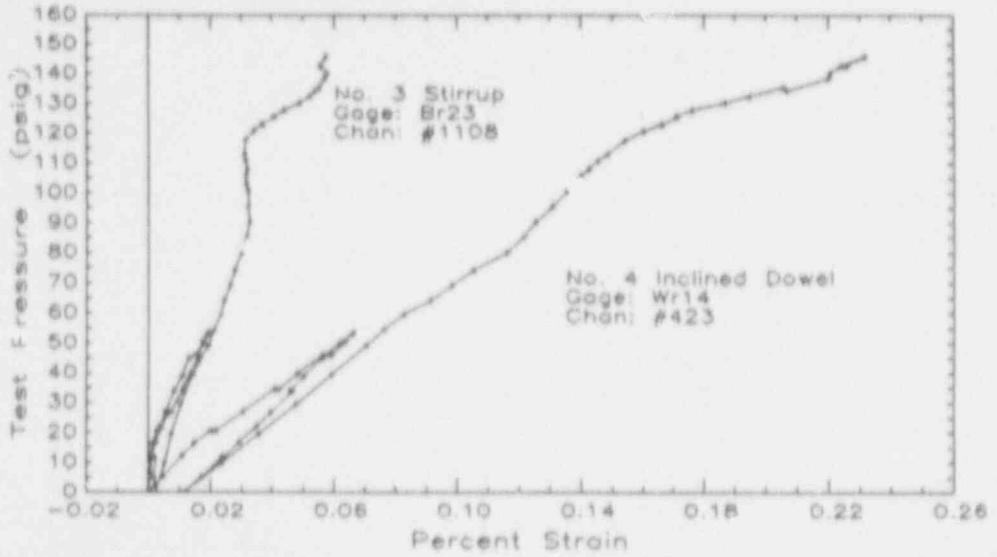

Fig. 6.10 Wall Shear Reinforcement Strain

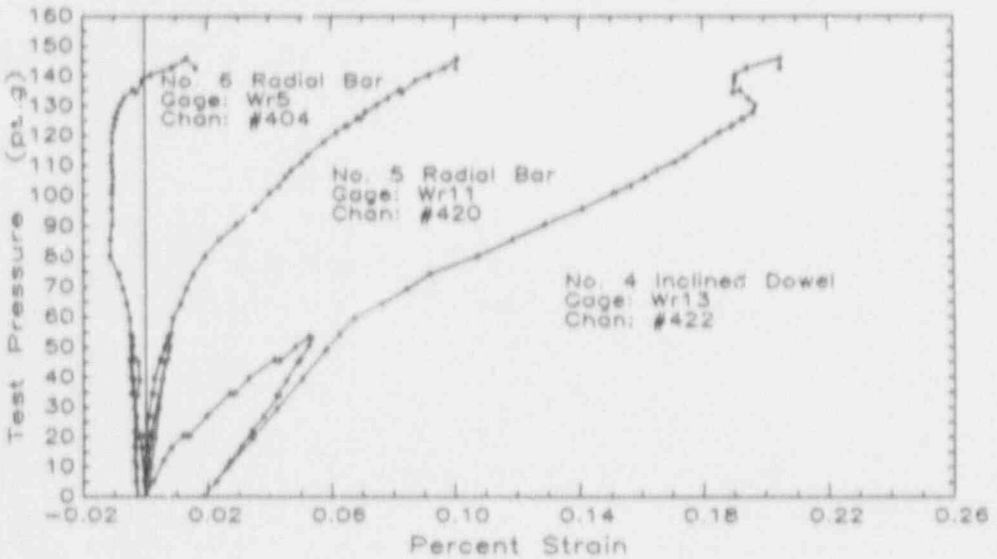

Fig. 6.11 Basemat Radial Reinforcement Strain

this pressure. The radial compressive force in concrete is therefore negligible at the maximum test pressure. This allows an estimate of the total wall shear at pressures greater than 138 psig from force T_{sb} only (Fig. 6.9).

The shear stress in the wall is estimated to be 450 psig or 5.7 $\sqrt{f'_c}$ at the maximum test pressure of 145 psig. This shear exists in combination with a tensile stress across the section of 920 psi (11.7 $\sqrt{f'_c}$). The combination of shear and tensile stresses is well out of the range of experience in experimental tests of comparable wall-basemat connections of models of reinforced concrete containment structures (Section 7.2).

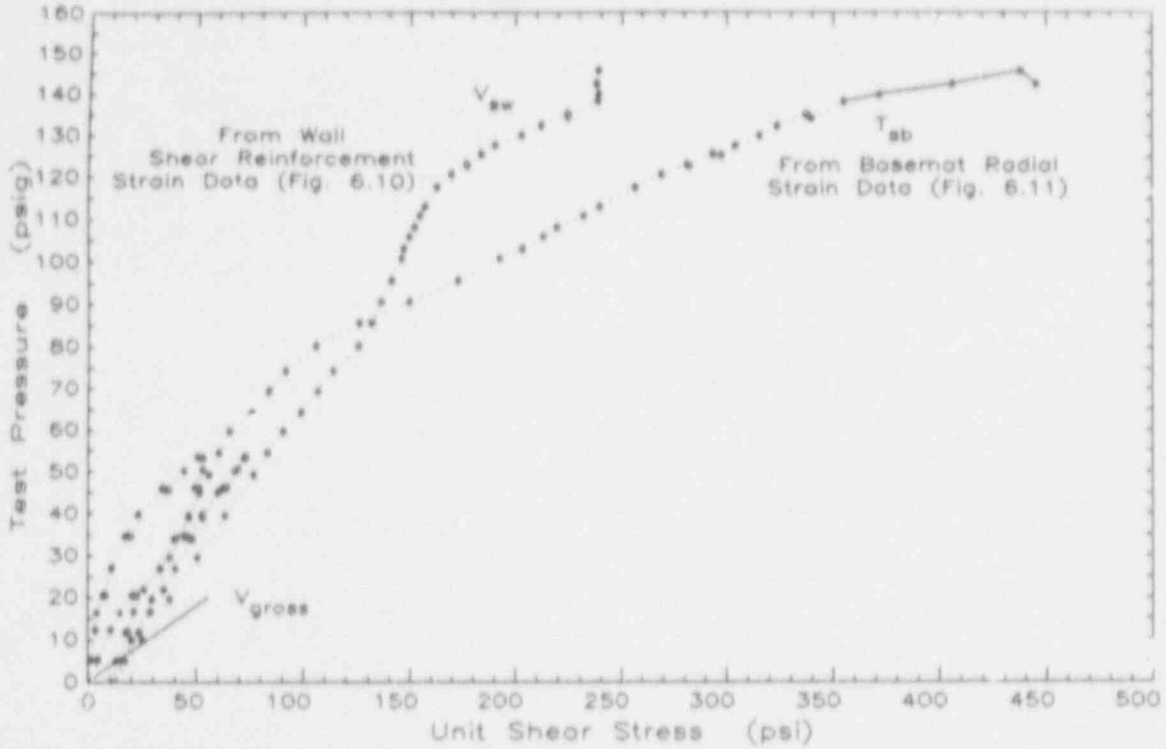

Fig. 6.12 Estimated Radial Shear Stress at Base of Wall

6.2.2 Overview of Shear Stresses in Wall

Before projections about the shear strength of the wall-basemat connection can be suggested it is prudent to first review and identify all known evidence about the internal forces at that location. Unless identified otherwise in the discussion which follows, all forces or stresses mentioned existed at a critical section defined by the junction of the wall and basemat and occurred at the maximum test pressure, 145 psig.

From statics, the unit vertical force was 9.0 kips/in. in tension. The vertical components of unit force carried by reinforcement in the wall summed to 16.2 kips/in. (Fig. 6.3), implying that concrete carried a unit compressive force of 7.2 kips/in. Because the wall was in flexure the concrete force was distributed about an axis near the exterior of the section.

Strain data on reinforcement layers 7 and 8 suggest that the neutral axis was 1.67 in. (Fig. 6.7) from the wall exterior. As internal pressure increased during the tests nonlinear events in behavior caused the neutral axis to shift from near the center of the wall at the beginning of the SIT to the final value at the maximum HPT test pressure (Fig. 4.18, 6.7). As pressure was increased, reduction of the neutral axis depth decreased the area of concrete in compression.

The variation of total shear stress with pressure is not known, however at the maximum test pressure this shear is estimated to have been 450 psi (Fig.

6.12). The portion of this shear transmitted by reinforcement was 240 psi. Strain data used to compute the shear carried by reinforcement (Fig. 6.10) indicate that the No. 4 inclined (layer 11) bar had yielded and that the No. 3 stirrup had stopped developing strain. The stirrup developed a maximum stress of approximately 17 ksi. The portion of total shear carried by concrete either directly or in dowel action was 210 psi or 2.7 $\sqrt{f'_c}$. Based on the strain data, the radial shear carried by shear reinforcement in the wall is not expected to increase with further increases in the total applied shear, if pressure were to be increased above 145 psig.

The stiffness of the basemat relative to the wall influences the variation of the total radial shear with pressure (Sections 4.3 and 5.3). Using a fixed-base assumption and gross section dimensions the initial value of the total shear stress, V_{gross}, is determined from [Ref. 5.3]:

$$V_{gross} = p \sqrt{R/h} \; / \; [3(1 - \nu^2)]^{1/4} \qquad (6.1)$$

where p = internal pressure
R = the wall radius
h = the wall thickness and
ν = Poisson's ratio, which is taken as zero (Fig. 5.8).

This calculated shear is shown as V_{gross} in Figure 6.12 at pressures below 20 psig. Projection of the V_{gross} line to greater pressures indicates that the total wall shear at 145 psig is greater than what would be calculated according to Equation (6.1). At this pressure the estimated shear stress in the wall is greater than calculations using a fixed-based model and gross sections. These assumptions for the fixity of a connection are commonly thought to be conservative.

At the maximum test pressure the wall had yielded in the hoop direction over most of its height (Fig. 4.3). As internal pressure increases, increments of radial force resisted, before yielding, by circumferential reinforcement are carried by seismic and vertical reinforcement to the dome and basemat. The total wall shear is estimated from measured data only at pressures greater than 138 psig. The slope of the total shear (curve T_{sb}) in Figure 6.12 in this pressure range is relatively flat compared to the slope of V_{gross} (Fig. 6.12). This implies that the rate of increase of the total shear for pressures greater than 138 psig was much larger than the rate of increase of total shear initially, for pressures less than 20 psig.

A projection of the total shear due to a hypothetical increase in pressure of 15 psig (to 160 psig) puts the total shear at 590 psi (7.5 $\sqrt{f'_c}$). This shear would exist in combination with a nominal tensile stress of 1010 psi (12.8 $\sqrt{f'_c}$). Since it is believed that the shear reinforcement would not carry additional stresses beyond 145 psig (Section 4.3.2), the portion of the total shear carried by concrete, either directly or in dowel action, would be 350 psi or 4.4 $\sqrt{f'_c}$. Methods for evaluating the shear capacity of this section are presented in Chapter 7.

6.2.3 Uncertainty in Shear Estimate

Three sources of the possible variation in the estimated unit shear stress at the maximum test pressure are considered.

(a) Force Transmitted from the Liner to the Wall

A cut-section of the basemat on an eleven foot radius (Fig. 6.9) shows that force carried by the liner atop the basemat at that section is not included. By excluding this force from the basemat unit tension, T_{ϕ}, the estimate of the calculated shear stress at a critical section of the wall does not change appreciably. A reliable estimate of strain of the liner floor is not available because data from several gages near the junction provide conflicting readings [Ref. 3.1]. This region was subjected to large strain gradients which were difficult to measure reliably.

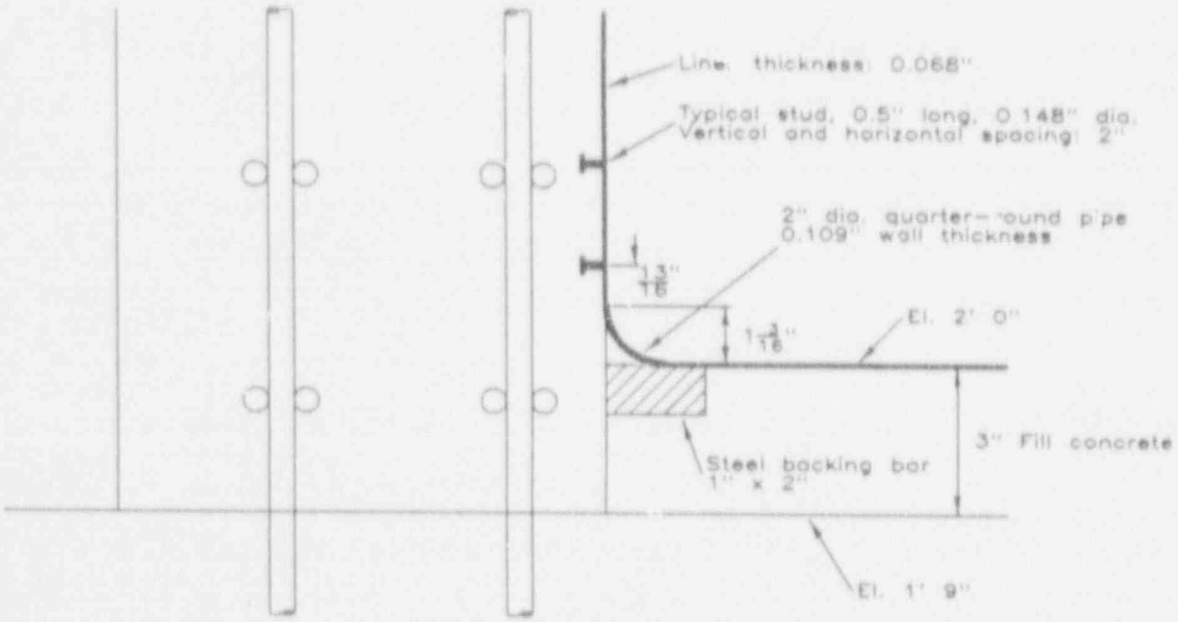

Fig. 6.13 Liner Knuckle Detail

A detail of the wall-basemat connection and liner knuckle is shown in Figure 6.13. The basemat liner rests atop a three-inch fill slab at elevation 2 ft. The liner is attached to the inner wall surface by 0.148-in. diameter studs, 0.5-in. long and spaced at 2 in. A quarter-round section of 2-in. diameter pipe was bent to form the knuckle joint and was welded to the floor and wall liner. A 1 by 2 in. backing bar was placed just below the weld of the knuckle to the basemat liner, within the fill slab, to support these structures during construction.

As indicated by a detailed profile of the connection (Fig. 6.13), radial shear in the wall may be transmitted to the basemat liner primarily through the studs anchoring the wall liner to concrete. Adhesion stresses of wall concrete and the steel liner are expected to be small. The first row of studs begins at approximately 2 in. above the basemat liner or 13/16 in. above the juncture of the wall liner and knuckle. The maximum unit force that may be transmitted from this row of studs to the basemat liner is

limited by the flexural capacity of the lower portion of wall liner. An upper bound to this (unit) force is determined through a limit analysis presented in Appendix C to be 153 lb/in. This equates to a wall shear stress (gross section) of 16 psi. The row of studs considered is approximately 5 in. above the section at which the 450 psi wall shear stress is estimated. Within this distance hoop reinforcement (Fig. 6.13) and the concrete relieve some of the shear force. The additional 16 psi shear stress at the level of the first row of studs is not likely to produce a shear stress there greater than at the section defined by the wall-basemat juncture.

A post-HPT inspection of the interior of the containment structure found that the basemat liner had deformed plastically at the outer 6 in. of the floor. Stresses carried by the liner at the knuckle junction were probably at least equal to the yield stress of the liner material.

(b) Force in Basemat Hoop Reinforcement

Figure 3.6 illustrates all reinforcement visible in a profile of the basemat at azimuth 90 degrees. Four No. 6 hoop reinforcement bars are located at radii greater than eleven feet. Three are at a radius of 12 ft 4 in. and one is at 11 ft 7 in. The radial component of force in these bars is not taken into account when the unit radial force in the basemat at 11 ft is equated to the unit wall shear force. The basemat was found to produce a radial extension at the maximum test pressure which is estimated to be 0.02 in. at the top and 0.14 in. at the bottom of the slab (Fig. 4.8). These extensions are used to estimate the strain in the four exterior circumferential reinforcing bars. The unit radial component of force is calculated to be 153 lb/in. If this unit radial force in the hoop bars was subtracted from the estimated tensile force in the basemat, T_{sb}, (Fig. 6.12) the estimated wall shear stress would decrease by approximately 16 psi.

(c) Stress-Strain Curves for Steel

The wall shear stress estimate is based on strain data from three gages attached to a No. 4, No. 5, and No. 6 bar. Twenty samples of No. 4 bar and four samples of No. 5 bar were tested for strength. Strength statistics for the tested bars are presented in Table 2.1. Using an approximate coefficient of variation of the strength for all reinforcement of 2 percent, the uncertainty in the estimate of the maximum shear stress in the wall (at two standard deviations) is 18 psi.

(d) Summary of Uncertainty in Shear Estimate

Of the three sources of uncertainty in shear estimate identified above only the latter two affect the estimated wall shear stress. The radial shear force transmitted from the wall to the basemat, discussed in point (a) above, can be ignored because this force is comparatively small and because it is transmitted 5 in. above the wall-basemat juncture. The exclusion of force carried by exterior hoop reinforcement reduces the estimated shear stress but uncertainties associated with reinforcement strength could shift the estimate higher or lower. These uncertainties are combined algebraically to give bounds to the estimated wall shear stress equal to 415 and 450 psi at the maximum internal test pressure of 145 psig.

7. EVALUATION OF RADIAL SHEAR STRENGTH

The region near the base of the wall of the containment model is one of the critical locations about the structure from the viewpoint of structural resistance. At the maximum test pressure the unit shear stress estimate there is 450 psi ($5.7\sqrt{f'_c}$). This occurs with a large normal tensile stress of 920 psi ($11.7\sqrt{f'_c}$). The stress combination is greater than the expected shear capacity, based on methods in design codes for estimating shear strength of reinforced concrete sections [Ref. 2.4, 5.2]. For this reason an alternative method for evaluating shear strength was sought and is presented below.

In this chapter methods are presented by which the radial shear strength at the base of the wall may be estimated. Estimates of the strength of reinforced concrete members in shear are based strictly on structural experiments. The word "methods" above should not be misconstrued to indicate all is known about the strength in shear of reinforced concrete sections. Experiments have shown that shear strength, unlike flexural-yield capacity, cannot be determined from the principles of mechanics with consideration of the strengths of the individual components (concrete and steel) at a section. Test data on beams that have failed because of the effects of shear are subject to a great deal of scatter. For example, the range in the ultimate capacity of four identical beams (no web reinforcement, span to depth ratio of 3) tested by Taylor, [Ref. 7.6] which failed due to shear, was 20 percent of the mean of the four strength values. Projection of the results of tests on structures for shear strength to other structural forms or shapes must be qualified by the range in the relevant parameters of the specimens that provide the basis for the projection. Due consideration of the uncertainty in a shear strength estimate must be included with the projection because of the commonly observed scatter.

A calculation procedure is described for evaluating shear strength at the wall-base from the internal compressive force resulting from flexure. This procedure is applied to the 1/6-scale containment structure tested at Sandia [Ref. 2.2] and to a set of 1/12-scale reinforced concrete models of an eighth of a shell wall (45 degree sector) and base foundation connection tested by Aoyagi, et al. [Ref. 7.1]. Based on the wall-basemat connection experiments by Aoyagi, the procedure estimates a radial shear capacity in terms of internal pressure of between 59 and 73 percent of the ultimate pressure required to cause a shear compression failure in the tested specimens. The strength of one of the 1/12-scale wall-basemat connections is then compared to the Sandia 1/6-scale containment via the described calculation to estimate an internal pressure at which the stress conditions in the Sandia containment would resemble those at failure of the 1/12-scale connection. Calculations suggest that at an internal pressure of 185 psig there is an extreme possibility for a radial-shear failure of the containment model.

Section 7.1 begins with a survey of code equations for estimating the shear strength, as found in the reinforced concrete provisions of the ASME Pressure Vessel Code [Ref. 2.4] and the ACI Building Code [Ref. 5.2]. In Section 7.2 a review of experiments of structural members subjected to shear, axial tension, and flexure at a critical section is presented. The relevance and applicability of each in guiding an estimate of the radial shear strength at the wall-basemat connection is noted. Because the shear strength of

connections in full-size reinforced concrete containments is of primary interest, Section 7.3 contains information on modelling considerations that affect the projection of shear strength of structures determined from tests of scale models. The proposed method for evaluating shear strength plus an analysis of potential modes of shear failure at the wall base is described in Section 7.4. The calculation procedure is applied to the 1/6-scale containment model and to the 1/12-scale wall-basemat connection specimens in Section 7.5.

7.1 Survey of Code Equations for Estimating Shear Strength

The ASME Boiler and Pressure Vessel Code [Ref. 2.4] contains provisions for determining the allowable radial shear strength at ultimate load conditions. The provisions allow the contributions of concrete and shear reinforcement in resisting radial shear to be considered separately according to:

$$v_u = v_c + v_s \tag{7.1}$$

where v_u = total nominal shear strength
v_c = nominal shear strength of concrete and
v_s = nominal shear strength of reinforcement.

The contribution of reinforcement to shear strength is determined by taking the radial component of force in each bar that crosses a presumed failure plane with the stresses in the bars equal to the steel yield strength. Assuming that failure could occur along the horizontal construction joint between the basemat and the base of the wall, one No. 4 bar at 45° inclination and one No. 3 stirrup at approximately 40° inclination, both at 4.5-in. spacing, would comprise the total shear reinforcement. The unit radial shear capacity of these bars is determined to be 3.2 kip/in. or 330 psi unit shear strength based on the 9.75-in. wall thickness.

The contribution of concrete to shear strength is influenced by the axial tension and meridional bending at the base of the wall. The net force in the wall will be tensile as the ultimate load is approached. In this case the Code [Ref. 2.4] specifies that the nominal shear strength of concrete shall be determined from:

$$v_c = 2.0 \sqrt{f'_c}\ [1 + 0.002\ N_u/A_g] \tag{7.2}$$

where f'_c = the compressive strength of concrete in psi
N_u = the force (tension negative) acting on section A_g and
A_g = the gross section area.

This equation suggests that concrete strength decreases linearly as the normal tensile stress across the section (N_u/A_g) increases. When the net normal tensile stress exceeds 500 psi, Equation (7.2) assigns zero strength to the concrete.

At the maximum test pressure achieved during the HPT (145 psig) the net tensile stress at the base of the wall is 920 psi. The total shear strength at that section, determined according to Equation (7.1), is 330 psi, which results from the strength of the shear reinforcement only. The total radial

shear stress that is estimated to have existed at that section is 450 psi. Clearly, since there were no visible signs of distress at the toe of the wall, an obvious question is how much is the actual shear strength underestimated by Equations (7.1) and (7.2).

An alternate method to estimate shear strength is by the shear-friction provisions of the ACI Building Code [Ref. 5.2]. The strength of a section to transmit shear across a potential crack surface is determined from the net yield force of all reinforcing bars transverse to the crack and from the construction procedures used in casting the concrete. Shear strength by the shear-friction method is calculated from:

$$v_u = \mu (\rho f_y - \sigma_n) \qquad (7.3)$$

where v_u = nominal shear strength
ρ = reinforcement ratio perpendicular to the section
f_y = yield strength of reinforcement and
σ_n = net tensile stress normal to section (σ_n = 0 if compression).

The Code [Ref. 5.2] specifies μ = 1.0 for conditions such as found at the wall-basemat juncture: the section is a roughened construction joint. Furthermore, there is an upper limit on v_u of 800 psi (for f'_c = 6200 psi) [Ref. 5.2]. The net vertical reinforcement ratio, excluding the liner, at the section considered is 0.027. The reinforcement yield strength is 64,000 psi and σ_n is 920 psi at the maximum test pressure. By Equation (7.3) a shear strength of 810 psi is calculated suggesting that, on the basis of shear-friction, the section has adequate reserve capacity to carry the 450 psi shear stress that is estimated from measured strains.

Equations (7.1) and (7.2) normally apply for proportioning a wall-basemat connection to resist radial shear. But they underestimate strength, as they should for design, and are not particularly useful in this study. It is desired to estimate the actual radial shear strength as closely as is practicable to make a projection of the limiting pressure the containment model could have withstood if the primary mode of failure was due to radial shear at the wall base. The shear-friction method of checking shear capacity is not allowed by the ASME Code for reinforced concrete containment structures. Moreover, experiments on push-off specimens that support the basis for Equation (7.3) did not load the specimens with tension normal to the failed section higher than a unit stress of 400 psi [Ref. 7.22]. It is uncertain whether the 810 psi shear strength estimated by Equation (7.3) is realistic. For this reason a survey of structural experiments was conducted to find alternate means for improving on shear strength estimates from code equations.

7.2 Survey of Experimental Research

A literature survey was conducted to find information on tests of structures in which the critical section at failure was subjected to stresses similar to those in the 1/6-scale containment model at the maximum HPT pressure. The search yielded information on three series of tests of other wall-basemat connections, a series of tests on T-beams subjected to combinations of axial tension plus shear and moment at failure, and two series of tests on push-off

specimens subjected to shear plus moment or shear plus axial tension across the failure plane. In the following sections, the experimental investigations are described and the applicability of their results to evaluation of shear strength at the wall-basemat connection is discussed.

7.2.1 Tests of Wall-Basemat Connections

7.2.1.1 Aoyagi 1/12-scale 45° sectors

Six 1/12-scale specimens representing a 45° sector of a shell wall and basemat connection of a reinforced concrete containment structure were tested by Aoyagi, et al. [Ref. 7.1]. Each specimen consisted of a 500-mm (197-in.) thick basemat, anchored to a floor and a 15-cm (5.9-in.) thick shell wall which extended 150 cm (59 in.) above the base (Fig. 7.1). The walls were provided with 10-mm (0.39-in.) dia. vertical and circumferential reinforcement; one of the six specimens had 6-mm (0.24-in.) dia. shear stirrups. The specimens were loaded by applying tension to vertical reinforcement at the top of the wall while simultaneously applying pressure radially, through a confined pressure bag, to the inner wall surface. During the test, forces in all circumferential reinforcing bars were monitored so that shear forces and hoop moments at the wall base could be determined.

The Aoyagi specimens simulated the loading and configuration at a wall-basemat connection of a 3-dimensional containment structure.* All specimens failed in shear-compression at the wall base: crack patterns showed the failure surface was created by horizontal flexure cracks, formed at the inner wall surface, which propagated along a curved line, radially outward and downward, toward the wall toe (Fig. 7.1). These specimens have potential for guiding strength estimates of the Sandia 1/6-scale model containment or of similar containments. To extrapolate results of these tests to the Sandia model or to other containments consideration of the following design details must be made: the specimens did not include seismic reinforcement, inclined shear reinforcement anchored within the basemat, or a liner, and only one specimen had stirrups.

7.2.1.2 Construction Technology Laboratories

A nearly full-size model of a wall-basemat connection with a skirt, a sloping transition or haunch between wall and basemat, of a typical prestressed concrete containment structure was tested at the Construction Technology Laboratories (CTL) [Ref. 7.15 - 7.17]. The specimen (Fig. 7.2) was planar, not curved as a true shell, with the following dimensions: overall width 84 in., wall height 162 in., wall thickness 32 in., skirt thickness at basemat junction 44 in., and basemat thickness 60 in. Vertical (meridional) wall reinforcement, shear stirrups in the wall, an orthogonal grid (cage) or reinforcement in the basemat, and vertical prestressing tendon ducts were provided. A 1/4-in. liner plate was attached by structural angles to the

---

* The Aoyagi specimens were anchored to a floor and thus could not exhibit basemat uplift, as was observed for the 1/6-scale containment model. However, in Section 7.3.3, speculating on the effects of basemat uplift on radial shear strength of the wall, it is suggested that the basemat of a full-size containment would present to the wall a highly fixed anchorage.

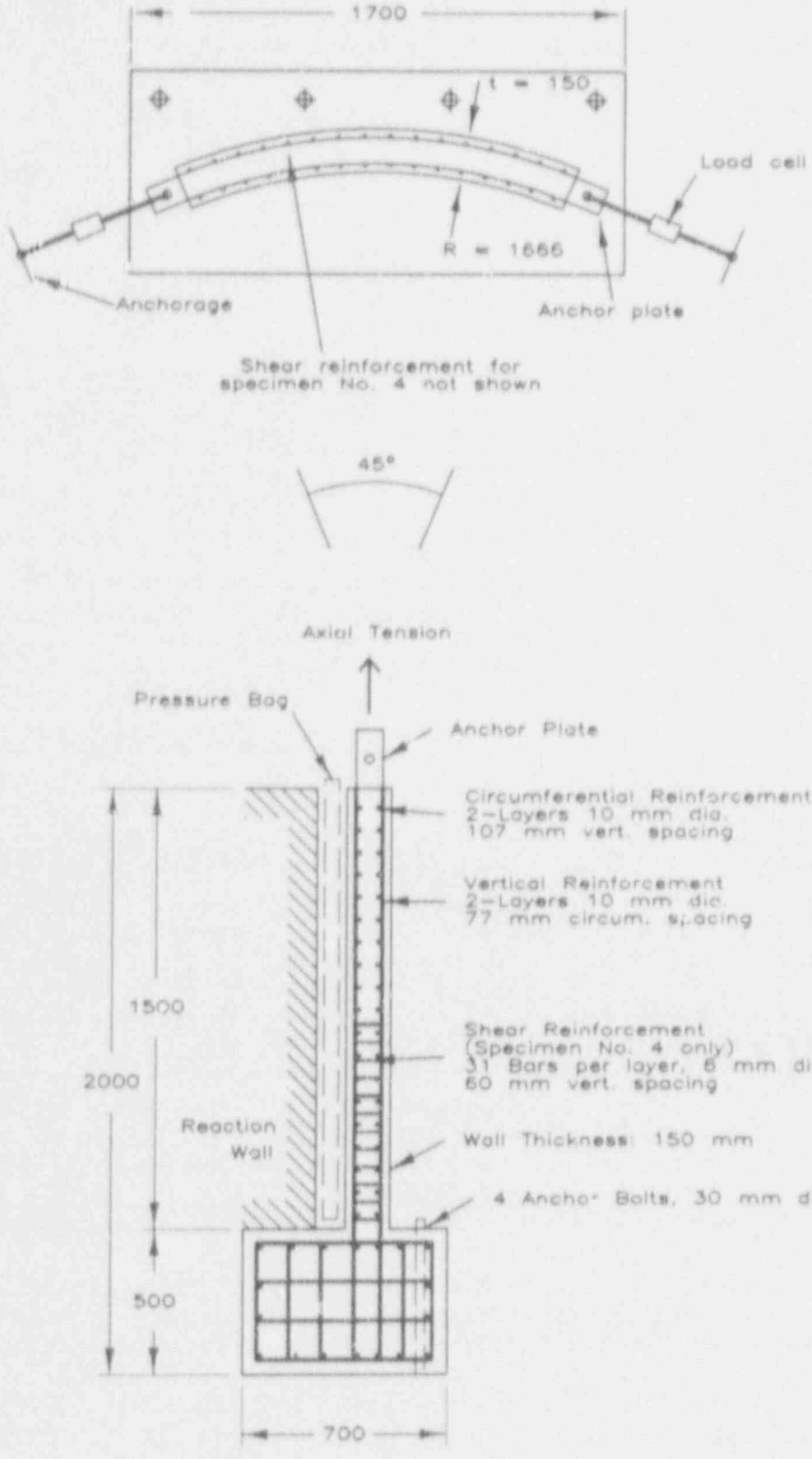

Fig. 7.1 1/12-Scale Wall-Basemat Connection Model Tested by Aoyagi

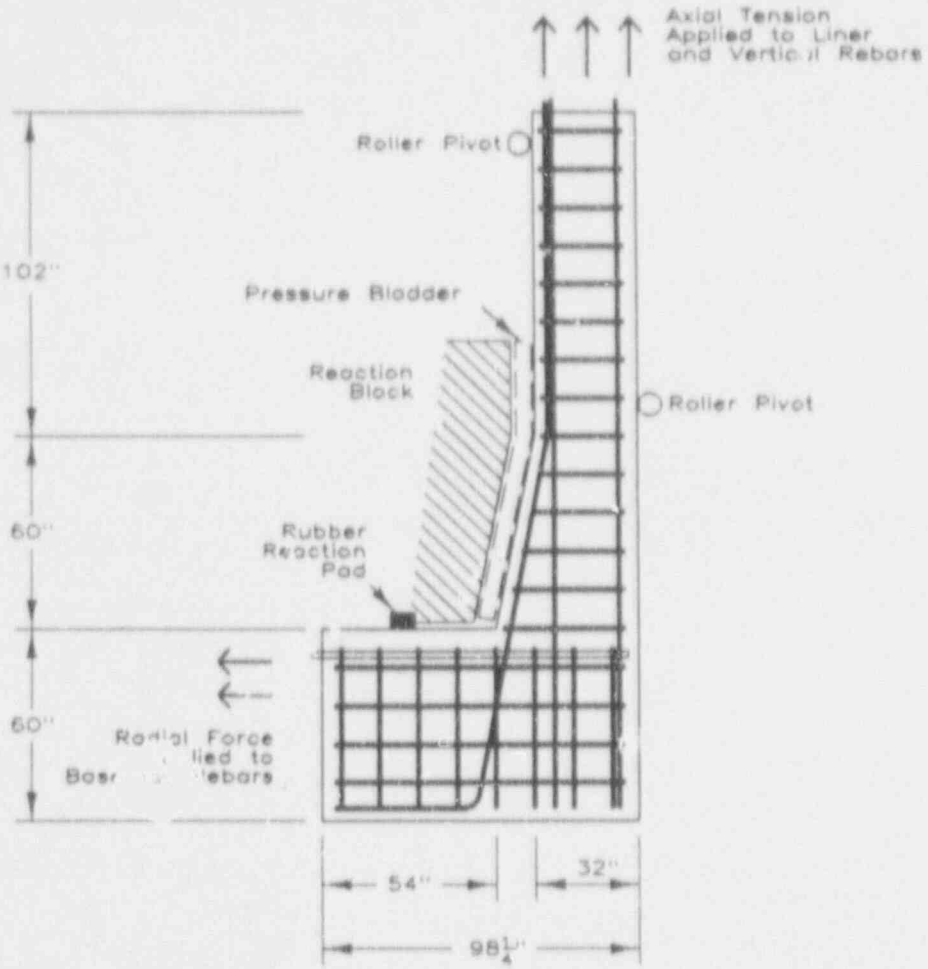

Fig. 7.2 Specimen Tested by Construction Technology Laboratories

inside wall and basemat surfaces. The specimen was loaded by applying tension to the vertical reinforcement and liner at the top of the wall, by applying radial tension to basemat reinforcement at the heel and the toe of the basemat section modeled, and by applying internal pressure to a confined rubber bladder in contact with the liner at the wall-skirt-basemat region. The basemat was restrained vertically by a bearing pad located approximately 20 in. from the inner skirt-basemat corner. The loads produced significant shear forces and hoop moments at the wall-skirt and skirt-basemat junctions.

The internal force conditions for hoop moment and radial shear were similar to those of a full-size containment subjected to high internal pressures. The test produced a severe distress along a horizontal plane, across the 44-in. thick wall at the skirt-basemat intersection. This failure was accompanied by 1.25-in. wide flexural cracks at the inner portions of the wall, which did not propagate to the wall exterior. The test also produced tears in the liner at the wall-skirt and skirt-basemat discontinuities. The tears were attributed to the loss of liner anchorage because of the severe concrete cracking. The mode of failure exhibited in this test occurred at a wall-basemat connection, however, because the contribution of circumferential reinforcement to carry radial shear was ignored (these bars were not loaded)

it is difficult to compare this specimen to an actual containment exhibiting 3-dimensional behavior. In this specimen the entire radial load on the wall was transmitted to the basemat as a radial shear at the wall base. In the specimen tested by Aoyagi (Fig 7.1) or in an actual containment most of the radial load on the wall is carried by circumferential reinforcement. Moreover, seismic reinforcement and inclined shear reinforcement anchored in the basemat were not provided.

7.2.1.3 Stone and Webster Engineering Co.

Two full-scale sections of a reinforced concrete containment wall were tested by Stone and Webster Engineering Co. (S&WE) [Ref. 7.9, 7.12, 7.18, 7.19]. The tests were performed to determine the overall performance, cracking and splitting behavior of the concrete, and the load transfer to the reinforcement at loads resembling the design internal pressure for a containment. The thickness, height, and width of the first specimen was 4 ft 6 in., 4 ft, and 10 in., respectively, and dimensions of the second specimen were 4 ft 6 in., 5 ft ½ in., and 6 in. (Fig. 7.3) [Ref. 7.12]. The specimens were each provided with three No. 18 vertical reinforcing bars, two at the interior and one at the exterior wall surface, and with 3/8-in. liner plate attached to the inside wall surface by studs. Shear reinforcement was provided in the form of steel plates (4 x 3/4 in. for specimen one and 4 x 1 in. for specimen two), inclined at 45°, arc welded to the exterior vertical No. 18 bar and to one interior bar. The specimens were loaded by applying, at the top and bottom of the wall, vertical forces which were offset to induce (radial) shear, axial tension, and (meridional) bending stresses across a section through the wall thickness. Neither specimen was tested to failure. The specimens were loaded so that the highest stressed reinforcing bar was at 90% of its yield strength. The induced unit radial shear stress at the end of the test was equal to 285 psi on a horizontal wall section with a unit normal stress of 1100 psi.

The S&WE specimens were patterned on designs of full-size containment walls. With the exception of the magnitude and method of loading, their performance may be considered to be closely representative of containments subjected to overpressurization. The tests demonstrated the capacity of the walls to carry the high loads at the design pressure without significant cracking of the concrete. The angle of the cracks was approximately 20° from horizontal. The second of the two specimens was instrumented with strain gages on the reinforcing bars and the shear-resisting steel bars. The data indicated that the inclined steel bars were stressed to approximately 9 ksi at the end of the test and that only 38% of the total radial shear was resisted by these bars, with the remainder assigned to concrete and to dowel effects. The tests did not provide a complete indication of wall strength as the circumferential reinforcement was not modeled nor was their ability to carry a part of the radial load. The vertical forces were applied by a steel yoke assembly which most likely added considerably to the overall shear strength and helped to confine the concrete.

7.2.2 Tests of T-Beams

A series of sixty T-beam specimens were tested by Haddadin, et al. [Ref. 7.20, 7.21] at the University of Washington to study the effectiveness of web reinforcement in members subjected to tensile or compressive axial forces.

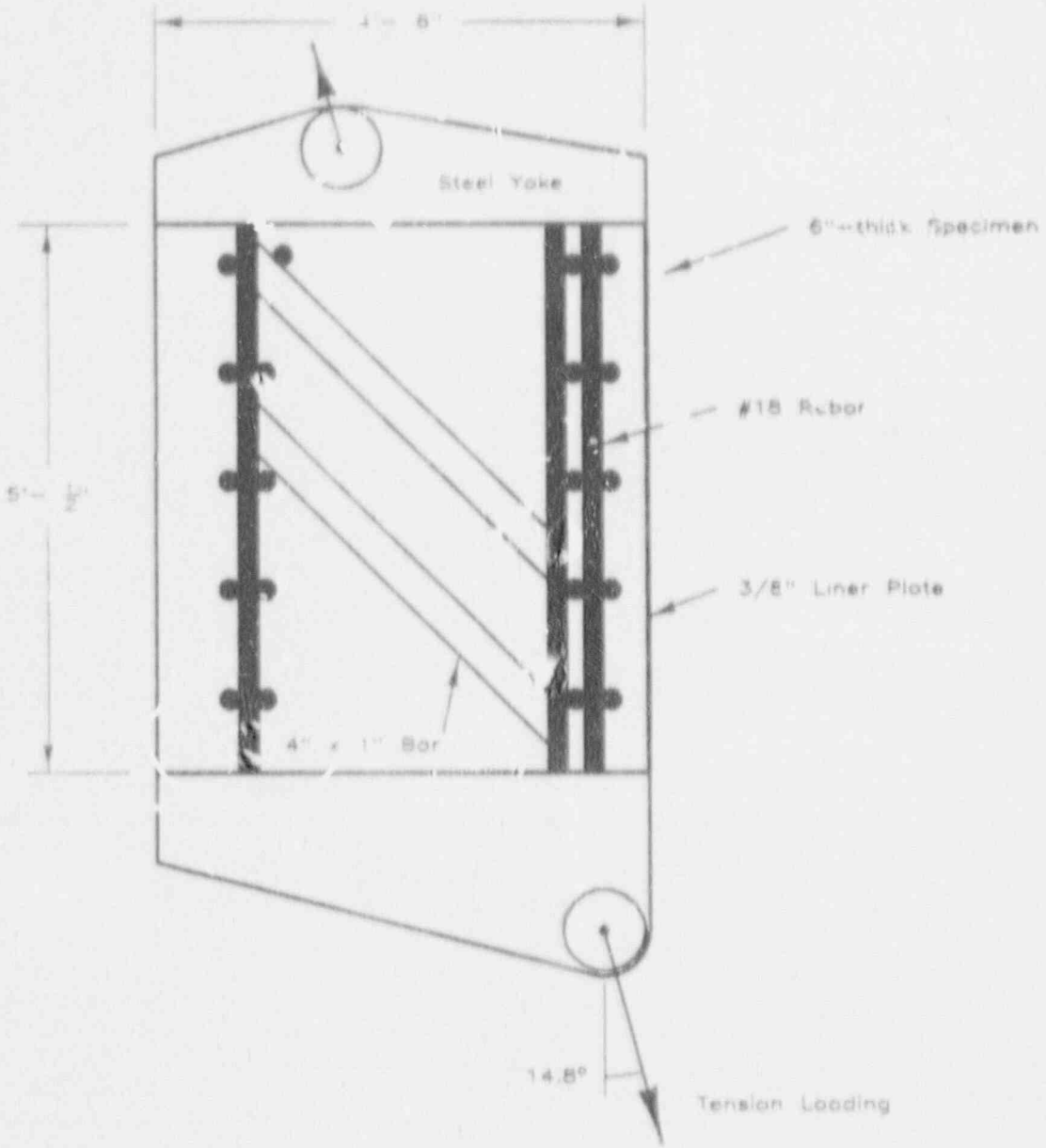

Fig. 7.3 Full-size Model of a Containment Wall Segment Tested by Stone and Webster Engineering Co.

Twenty-one specimens were loaded to approximately 250 psi axial tension before being loaded laterally and then failing in shear. All specimens had the same cross-sectional dimensions; overall depth 18.5 in., effective depth 15 in., web thickness 7 in., flange width 24 in., flange thickness 4 in. (Fig. 7.4). Fifty-five specimens were tested as simply-supported beams with lateral force applied at the center of the span. Span length was different among specimens with a range in shear span ratio (a/d or M/vd) of 2.5 to 6.0. The sizes and spacing of stirrups was also varied with the range in the parameter $\rho_v f_{vy}$ of 99 to 900 psi (ρ_v = shear reinforcement ratio, f_{vy} = yield strength of stirrups). Some specimens had no stirrups.

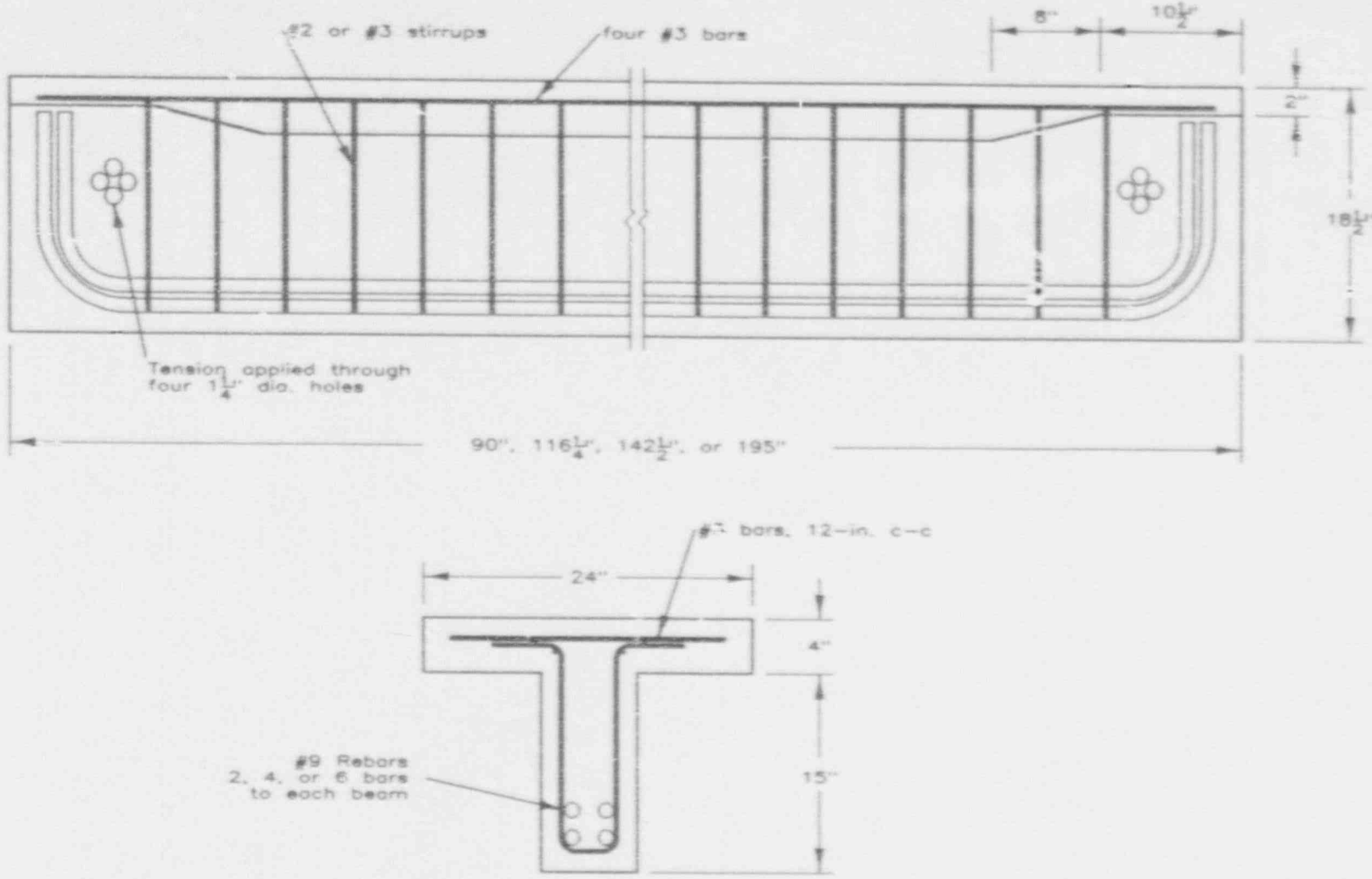

Fig. 7.4 Details of T-Beams Tested in Tension

It was found in these tests that two types of shear failures occurred and they appeared to be dependent on the amount of web reinforcement (stirrups). In beams with a small amount of web reinforcement, failure was by diagonal tension cracking which caused the stirrups to yield as a crack propagated up into the flange, toward the load point at the top face of the beam. In beams with larger amounts of web reinforcement failure was by shear compression of the flange and then yielding of the stirrups. All beams produced yielding of stirrups across a crack at failure. The effectiveness of stirrups in resisting shear was found to be unaffected by the presence of axial tension or compression and stirrups were more effective in increasing shear capacity in the beams failing in diagonal tension than in beams failing in shear compression of the flange. These tests of T-beams suggest that the presence of axial tension in the wall of a containment structure would not reduce the effectiveness of shear reinforcement at the wall base. Quantitative strength results from the tests cannot be applied to a containment structure for several reasons, but chiefly because of the dissimilar cross-section and because of the two-dimensional nature of the T-beams.

7.2.3 Tests of Push-off Specimens

7.2.3.1 Interface Shear of Reinforced Concrete

Two groups of tests by Mattock, et al. [Ref. 7.22] of 21 "push-off" specimens were conducted to study the interface-shear transfer strength of reinforced concrete with moment or tension acting across the shear plane (Fig. 7.5). The first group of twelve specimens were corbel-type tests: a shear force was applied parallel to the failure plane and at an eccentricity that varied with each specimen. These specimens had a 10-in. long by 6-in. wide failure plane interspersed by reinforcement perpendicular to the section. The remaining 9 specimens were shear-tension tests: a shear force was applied on either side of and parallel to the failure plane while tensile forces were applied to the two adjacent portions inducing normal tensile stresses across the critical section. These specimens had a 12-in. long by 7-in. wide failure plane that was also interspersed by transverse reinforcement.

The tests by Mattock, et al. provided fundamental insight into the capability of reinforced concrete to transmit shear across a potential failure plane while simultaneously resisting normal tensile stress, or in the case of corbel-type specimens, a varying distribution of stress normal to the section due to the moment. The tests demonstrated that the frictional strength of concrete to resist unit shear stress may exceed 800 psi, depending on the amount of reinforcement across the section. The results of the first group of push-off specimens, with moment across the shear plane, indicated that moments less than or equal to the flexural ultimate moment for the section do not reduce the shear transfer strength. In the second group of specimens net tensile stresses across the shear transfer plane reduced by an amount equal to the normal tensile stress acting on the section the reinforcement parameter, ρf_y, which is believed to be proportional to the shear transfer strength. Although these tests suggest that the radial shear strength at a containment wall-basemat connection may be quite high, it is doubtful that they provide an adequate representation of the internal force conditions present in a pressurized containment. A comparison of these specimens to a containment can be made roughly only on the basis of similarity of unit stresses. The loading conditions of a containment and of the push-off

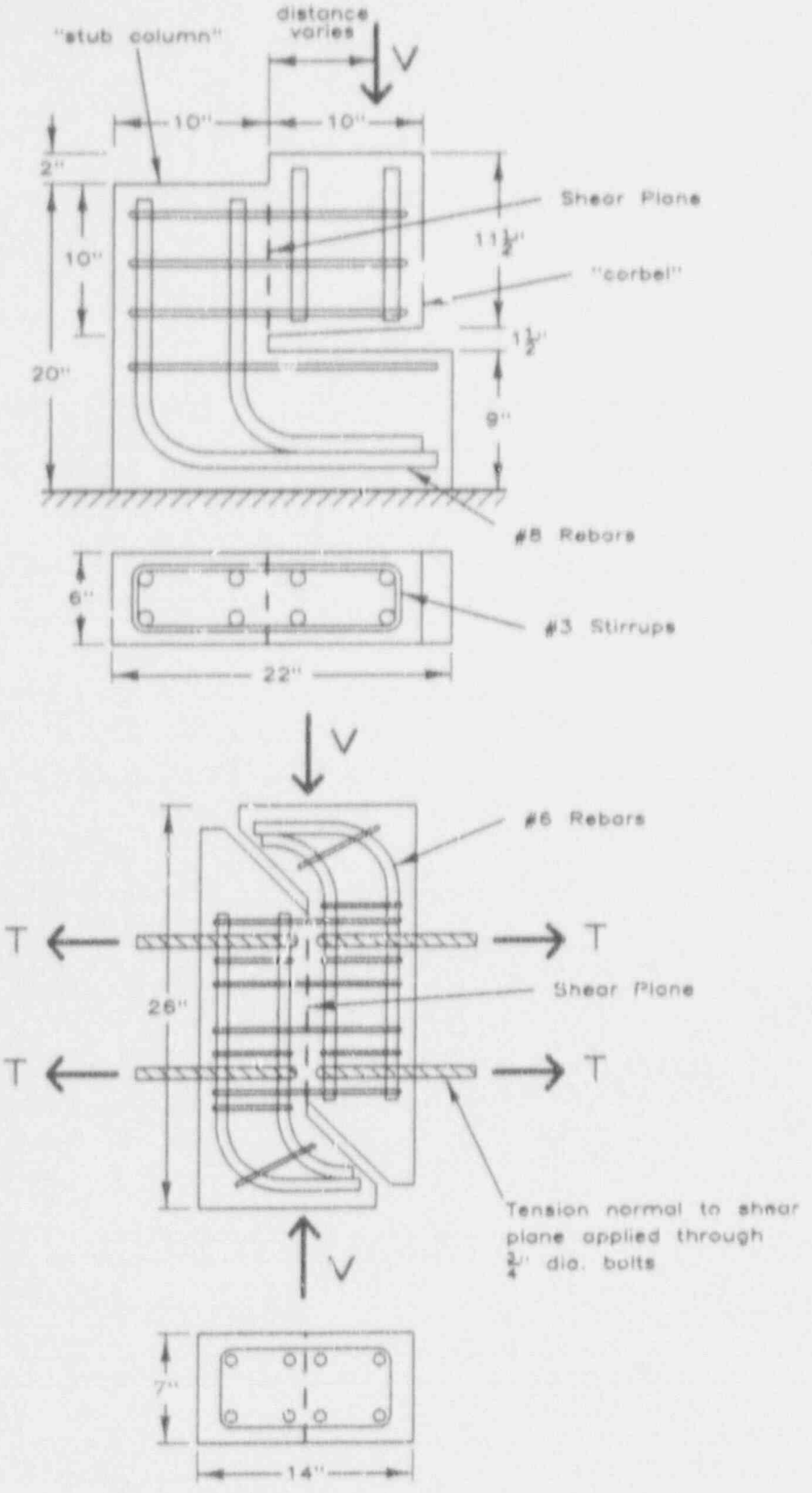

Fig. 7.5 Push-off Specimens Tested by Mattock
(Top: shear & moment, Bottom: shear & tension)

specimens are different. Furthermore, these specimens cannot account for the distribution of reinforcement, including reinforcing bars inclined from a potential shear plane, which was not studied in these tests, or account for the three-dimensional nature of the problem when circumferential stresses in a containment are considered.

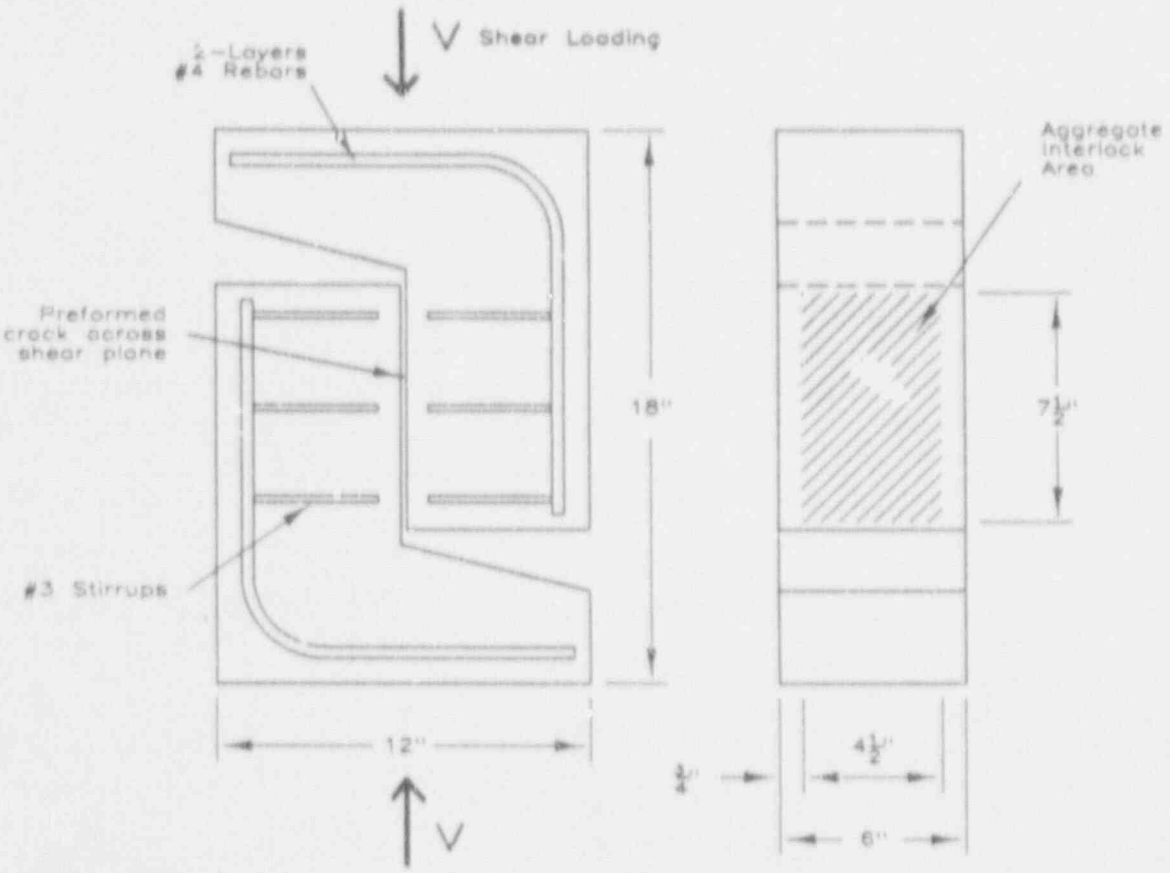

Fig. 7.6 Aggregate Interlock Specimen Tested by Paulay and Loeber

7.2.3.2 Aggregate Interlock Strength of Cracked Concrete

A total of 44 "push-off" specimens were tested by Paulay and Loeber [Ref. 7.23] to study the nature of shear transfer across prepared cracks by the aggregate interlock mechanism. The plane on which shear stresses were transmitted was 7.5 in. long and 4.5 in. wide (Fig. 7.6). No reinforcement was provided across the shear plane. External restraint was provided transverse to the failure surface to maintain crack widths to a constant width. Load was applied on either side of and parallel to the failure plane so that shear stresses could be transmitted across the shear plane only through aggregate interlock.

The Paulay-and-Loeber tests demonstrated the potential shear force that may be transmitted by aggregate interlock. It was found that aggregate sizes and shapes had no noticeable affect on the shear transfer mechanism. The relationship between shear stress and restraining force was approximately

linear up to a shear stress of approximately 1000 psi. The mean ratio of shear force to restraining force was 1.7. These tests are useful in guiding an estimate of radial shear strength of a containment structure only to demonstrate that it is physically possible to transmit high shear stresses across cracks, given an appropriate degree of restraint. In the 1/6-scale containment model the vertical uplift force at the base of the wall due to internal pressure equals the dead load of the wall and dome at approximately 6 psig. A full-size containment would have proportionately a much greater dead load, which could provide the restraint required to develop, to some degree, aggregate interlock shear capacity.

7.2.4 Summary of Experimental Data

Of the several experimental tests described above, the wall-basemat connection experiments by Aoyagi, et al. [Ref. 7.1] have the greatest potential to guide an estimate of the radial shear strength of the Sandia 1/6-scale containment model. Data from the Aoyagi specimens are used in Section 7.5 to illustrate a calculation procedure for shear strength due to the compression force in flexure.

The CTL test of a wall-basemat connection and the S&WE tests of full-size containment walls do not include the effects of the circumferential reinforcement. Aoyagi [Ref. 7.1] states that the failure mode of the six specimens he tested was ductile and not brittle or sudden, even though they did fail in shear compression at the toe of the wall. Aoyagi notes that this ductile behavior observed with shear failure of the wall is due to the presence and influence of circumferential reinforcement.

The T-beams tested in tension at the Univ. of Washington and the push-off specimens tested in tension by Mattock were not subjected to axial tension stresses higher than 400 psi. This is less than half of the net tensile stress present at the wall base of the 1/6-scale containment model at the maximum test pressure. Additional push-off tests with axial tension across the section closer to the 920 psi axial tension observed in the 1/6-scale containment would provide a greater confidence in applying the results of push-off tests to the conditions at the containment wall-base junction.

7.3 Modeling Considerations

The effects of size must be considered in applying the results of tests on reduced scale reinforced concrete specimens to the full-size. Evaluation of shear strength data obtained from tests on simply supported beams of various sizes [Ref. 7.4 to 7.6] lead to somewhat contradictory conclusions on whether reduced scale members provide acceptable indicators of the strength of full-size structures. The literature pertaining to scale effects [Ref. 7.3 to 7.7] of reinforced concrete members indicates that with proper scaling of all significant parameters, including the sizes of aggregates in the concrete mix, the shear strength of full-size beams may typically be equal to or less than the strength of reduced scale models. It is generally found that shear strength decreases as the specimen size increases [Ref. 7.6].

Several factors, all apparently interrelated, affect the extrapolation of shear strength of scale models to the full-size. Principal among these are

the overall dimensions of the model, the distribution, spacing, and cover of reinforcement, the size of aggregates, and the size of samples of material specimens (concrete cylinders, rebar coupons) used to determine the strengths of the materials [Ref. 7.8]. Data indicate that factors related to the properties of concrete have a greater overall influence on size effect than do other factors. At least two effects at the wall-basemat junction in the 1/6-scale containment were not scaled exactly from typical full-size containments: maximum aggregate size and anchorage of stirrups. These two effects plus other factors to consider in relating the performance of the model wall-base connection to a full-size concrete containment are discussed in the following paragraphs.

7.3.1 Maximum Size of Aggregates

The containment model was constructed of normal weight aggregates having a maximum size of 3/8 in., whereas, its prototype would have a maximum aggregate size of 3/4 in. [Ref. 2.1]. Aggregate size influences, among other factors, the tensile strength of concrete which affects the shear capacity of a reinforced concrete member.

A series of tests by Taylor [Ref. 7.6] on "true to scale model beams" without web reinforcement found that reductions in the shear strength of larger beams occurred, compared to the strength of the small beams, when aggregate size is not scaled correctly. He states that, from a designer's point of view, it is necessary to realize that the strength of a meter (39.4 in.) deep beam is likely to be 80 to 90 percent the strength of a similar beam 250 mm (9.8 in.) deep. But when the maximum aggregate size is scaled proportionately Taylor concludes that the loss of strength of a large beam is less significant. The strength of a meter deep beam is then approximately 90 percent of the strength of a 250 mm (9.8 in.) deep beam. Similar findings were presented by Swamy and Qureshi [Ref. 7.4], based on tests of T-beams with and without stirrups. Swamy and Qureshi argue the need to scale aggregate size appropriately because models with different sized aggregates are likely to show primary and secondary modes of failure quite different from those of the prototype. In a somewhat different view Alami and Ferguson [Ref. 7.3] conclude that while scaling the maximum size of aggregates does improve the accuracy of models, aggregates with a maximum size as close as possible to the required size may be used without influencing the results to a great extent. They found that the strength of larger beams was approximately 5 percent less than the strength of smaller beams.

Maximum aggregate size also influences concrete tensile strength and the shear strength at diagonal cracking, v_c. Bazant and Sun [Ref. 7.7] believe that nonlinear fracture mechanics theory may explain the effects of the specimen effective depth and maximum aggregate size on diagonal cracking strength. Their proposed equation suggests that v_c for a full-size containment would be approximately 30 percent less than the diagonal cracking strength for the Sandia model, based on the given maximum aggregate sizes and the thicknesses of the containment walls.

The evidence presented is conflicting. A quantitative assessment of the effect on the shear strength of using a maximum aggregate size in the containment model (3/8 in.) larger than what would be scaled correctly from a prototype (1/8 in.) must be prefaced by the degree of uncertainty in the

strength observed in experiments. The carefully conducted experiments by Taylor [Ref. 7.6] suggest that a full-size containment would exhibit a shear strength of approximately 90% of the strength of the 1/6-scale model. Other researchers [Ref. 7.4, 7.5] suggest that the strength would not be greatly influenced by aggregate size, but the shear strength of all larger specimens tested was less than the strength of scaled models.

7.3.2 Anchorage of Stirrups

The model containment was provided with No. 3 inclined stirrups that were hooked by 135 degree bends to the inner and outer layer vertical reinforcement (layers 2 and 5). This is in accordance with code provisions [Ref. 2.4] but shear reinforcement in some full-size containments have been designed with stirrups welded to the vertical bars. A containment designed by Stone and Webster Engineering Co. [Ref. 7.9] has 3/4 by 4 in. rectangular bars at 45° inclination arcwelded to No. 18 vertical reinforcement at the base of the wall. Welding the stirrups to longitudinal reinforcement ensures overall continuity. It would preclude, in a full-size containment, the postulated stirrup slippage, made in Section 4.3.2 about one of the No. 3 stirrups in the model (Fig. 4.17), that appears to occur above 135 psig internal pressure.

Strain data and a suggestion by Zsutty [Ref. 7.10] on the effectiveness of stirrups for small shear span ratios indicate that the anchorage of the No. 3 stirrups is adequate. A total of seven stirrups located within the lower 12 in. of the wall at various azimuths were instrumented with strain gages. With the exception of one bar (data from an apparently faulty gage) the readings were close. The maximum strain recorded was approximately 0.0007, less than one-third of the yield strain for the bars. In reference to the effectiveness of stirrups in deep beams with shear span ratios less than 1.5, approximately similar to the conditions of the model containment at maximum test pressure, Zsutty points out that stirrups do not appear to develop their full yield capacity prior to a crushing or splitting failure of concrete in a tied-arch mechanism (Section 7.4.1).

Although the stirrups did not develop their full capacity in the tests, as did the adjacent inclined (layer 11) dowels, which extend into the basemat (Section 4.3.2), this cannot be ascribed entirely to slippage of the bar. In Section 7.5.2, shear strength evaluation of the wall-basemat connection uses a discounted capacity of stirrups to resist radial shear by assigning a reduced stress level to them, indicated by strain data, of approximately one-third their yield strength. This should not be interpreted as implying that less stirrups are required. They are necessary to ensure integrity of the wall at regions where bending is expected.

7.3.3 Influence of Basemat

Except for the basemat thickness, the dimensions of the containment model were scaled by a factor 1/6 from typical full-size concrete containments. The 40-in. thick basemat is approximately twice the thickness (scaled by a factor 1/3) [Ref. 7.9] of what would be scaled linearly to account for the (reduced) dead weight of the model [Ref. 2.1]. Forces in scale models decrease according to the scale factor squared. Because gravitational forces decrease (volumetrically) according to the scale factor cubed, the effects of

the pressurization would have resulted in uplift at the slab edge and hoop moment at the wall base that would be much higher than if gravitational forces had scaled by the scale factor squared. The thicker basemat was selected on the basis of pre-test analyses so that calculated moments at the wall-basemat intersection would be scaled, approximately, correctly from a full-size containment [Ref. 2.1].

Evaluation of the load history for moment at the base of the wall (Section 6.1) suggests little influence of the basemat as it cracks at approximately 75 psig and begins to lift off its foundation at the edge. The behavior of the radial shear force (Fig 6.12), indicated by shear reinforcement strains, does show a decrease in the rate of increase with pressure, attributed to basemat cracking and uplift. From an analyst's view of the phenomena, the analytical model of the wall base is simply transforming from a fixed-end condition to an end condition that is less fixed. A speculation, below, about the behavior of flexure cracks in the wall, perpendicular to the inner wall surface, as the basemat begins to uplift may explain the behavior.

A scenario that fits the observed reduction (see Sections 4.4 and 5.3.3) in the rate of radial shear increase with pressure, while the rate of moment increase remains the same, is that flexure cracks in the wall open slightly as the basemat cracks and lifts reducing the shear transmitted across the cracked interface. The crack opening speculated here is principally due to the geometry of the edge uplift and thickness of the wall. Extending the explanation to a full-size containment is perilous even if it could be proved true for the model. Data on crack widths and lengths in concrete structures is usually accompanied by a great deal of scatter. If a similarly loaded full-size containment cracks near the edge of its basemat at approximately 75 psi, the resultant uplift will be approximately 3 times the uplift observed in the model. Since the full-size containment wall thickness is approximately 6 times the model the average crack-opening rotation across the base of the wall will be only about half of what might have been measured on the model. This suggests that the postulated opening of flexure cracks will be less in a full-size containment resulting in a decreased effect on the radial shear transmitted by the cracks. It may be that the full-size containment would not exhibit the observed slow-down in the rate of increase with pressure of strain on shear reinforcement just as the basemat cracks and uplifts.

To clarify the reasoning in this argument it is necessary to point out that behavior similar to what has been described could not be found in a column and girder connection. The base of the cylindrical shell wall has not yet yielded at an internal pressure of 75 psig and it provides a high rotational stiffness. The postulated opening of flexural cracks occur just at the base of the wall.

The previous scenarios suggest that the portion of radial shear transmitted by concrete across cracks at the wall base is greater in a full-size structure than in the model. The full-size basemat would have less influence on the change in wall fixity with pressure so that a greater portion of radial shear would be carried by concrete across flexure cracks. The relative rotation of the basemat (at the wall-basemat junction) of a full-size containment would be less and therefore would present to the wall a stiffer anchorage. The total shear before the circumferential reinforcement

yields would not likely be greater than a calculation based on an elastic fixed-base model for the wall.

At ultimate failure conditions the shear carried across concrete cracks at the base of the wall is not a major contributor to the total shear resistance. Force transmitted across cracks in tests of "push-off" specimens has been found to be approximately linearly related to restraining force. At the wall base there is a large net tensile force and most of the vertical reinforcement is at yield (Section 4.3.1) at the maximum test pressure. The implied crack width effect due to the basemat uplift is not present in the Aoyagi specimens [Ref. 7.1] as the shell wall was attached to a base anchored to the floor.

7.3.4 Summary of Modelling Considerations

Information on the effect of scale on the shear strength of reinforced concrete members lead to the conclusion that the radial shear strength of a full-size containment wall would be less than the strength of the 1/6-scale model. A quantitative estimate of the reduction of approximately 10% is offered on the basis of scaling the maximum sizes of aggregates. It must be observed, however, that the experimental data providing this estimate is from tests of beams by Taylor [Ref. 7.6] and the data of identical beams in the experiment showed a scatter range of 20% of their mean strength. The actual strength of the 1/6-scale model is uncertain as liner tearing did not allow the test to continue to a structural failure. Three main factors to consider in projecting the strength of a full-size containment from the performance of the 1/6-scale model are:

1. Aggregate size in a full-size containment would be proportionately smaller than what was used in the model. This would generally indicate a shear capacity lower by approximately 10%.

2. Stirrups welded to longitudinal reinforcement in a full-size containment would suggest that they could develop their full yield strength in resisting radial shear. The performance of stirrups in the model indicates that a reduced strength of stirrups, to approximately one-third their yield capacity, should be considered in estimates of the contribution of stirrups to strength.

3. The ability of concrete to carry shear stresses across cracks in the tension zone near the wall base may be greater in a full-size containment, because a full-size basemat would be more "inert" than the model. At the ultimate shear failure load, however, the portion of the total shear transmitted in this manner is small.

Other factors, which have not been detailed in the proceeding paragraphs, also should be considered in extrapolating the performance of the 1/6-scale model to the full size. The amount of cover on reinforcement and the area of confined concrete must be considered. It is known that the presence of strain gradients adds to confinement and increases the maximum compressive strain that may be reached in bending prior to failure [Ref. 7.11]. Small scale test specimens fail at a higher shear strength than their prototype partly due to a larger strain gradient (increased confinement) at failure.

7.4 Procedure for Evaluating Shear Strength from the Compression Force in Flexure

7.4.1 Shear Failure Modes

Two likely mechanisms and other less likely mechanisms leading to a severe distortion and a decrease in the ability of the wall base to transmit radial shear are described [see Ref. 7.2]. Shear compression failures were observed in the tests by Aoyagi [Ref. 7.1]. This mode is considered to be the most likely failure mode for the wall base of the 1/6-scale containment, assuming that the structure could be loaded by additional internal pressure and that the containment does indeed fail in shear at this location. In the following descriptions, the shear-span ratio is defined as the ratio of moment to shear at the failure load, at a critical section, divided by the effective depth of the section, M/Vd. At the maximum test pressure the shear-span ratio at the base of the wall is estimated to be approximately 1.5.

7.4.1.1 Shear Compression Failure

At a relatively low internal pressure level cracks due to flexural stresses occur initially across a horizontal plane at the inside of the wall, perpendicular to the vertical axis. With increases in load flexure cracks may propagate and additional cracks may form so that, eventually, there exist cracks that are inclined to the vertical axis. These cracks are commonly referred to as flexure-shear cracks and they are the most common type of crack found near mid-depth of reinforced concrete beams. The rate at which the flexure cracks propagate or the load level at which flexure-shear cracks occur are not well defined in terms of the critical parameters. The trajectory and rate of development of flexure-shear cracks are influenced by many factors, including the internal stress distribution in the concrete, the shear-span ratio, the amount and distribution of longitudinal and shear reinforcement, and the characteristics of the concrete, such as aggregate size and tensile strength.

As internal pressure increases, the inclined cracks may propagate toward the compression region and the area of concrete in compression is reduced. Failure may occur due to concrete crushing as a result of the combined normal compressive stresses and shearing stresses acting across the failure plane. Shear compression failures have been observed in beams having shear span ratios in the range of 1 to 2.5 [Ref. 7.2].

7.4.1.2 Interface Shear Sliding Failure

The connection of the wall and basemat is a construction joint. Because of the confinement provided by vertically oriented reinforcement and by shear reinforcement, radial shear stresses can be transmitted by the concrete across the joint through the irregular interface (roughened concrete). As the two surfaces of a construction joint attempt to slide relative to one another, irregularities on the surfaces cause the joint to open and induce forces in transverse reinforcement. The tensile forces in reinforcement in turn create a clamping force, arresting the imminent slip. Slip due to shear force is a possible mode for failure at the wall base if the available clamping force of steel, multiplied by a coefficient of friction for the surface, is less than the acting shear load. Design for a failure by this

mode employs a friction coefficient value higher than what is appropriate for concrete sliding on concrete, to allow for the dowel effect contribution to the shear resistance.

7.4.1.3 Crushing or Splitting Failure of Concrete

After the appearance of inclined shear-flexure cracks the internal mechanisms by which the applied loads are carried may change so that with further increases in load the inclined cracks do not propagate and additional inclined cracks do not form. For example, shear stresses in a deep beam without web reinforcement are initially distributed over the intact concrete. After the appearance of inclined cracks in the web the load carrying mechanism transforms so that the load is carried as a tied arch that can fail in a number of ways. If the unit compressive force in concrete in the containment model continues to increase after inclined cracks appear, the compressive stress may initiate crushing or splitting of the wall at its exterior surface. Deep beams having shear span ratios of 1 or less have failed in flexure in this manner [Ref. 7.2]. The "crown" of the concrete arch, in these tied arch beams, crushes prior to yielding of the tensile reinforcement.

7.4.1.4 Diagonal Tension Failure

After the appearance of inclined shear-flexure cracks in the middle section of the wall, the transformed internal load carrying mechanism resulting from the cracks may stop or slow the rate of further crack propagation. With increases in load, however, one of the inclined cracks may become unstable and propagate through the wall depth. This sudden event is called "diagonal tension failure" and occurs generally in slender beams, for example, having a shear span ratio greater than 3.

7.4.1.5 Evaluation of a Plausible Failure Mode

Examination of the model containment structure after internal pressure testing did not reveal an area of crushed concrete at the wall exterior, at the juncture with the basemat, implying that a failure had not yet occurred. If the liner had not torn and the containment was pressurized beyond 145 psig, it is of great interest whether the wall base could have withstood a greater radial shear.

The four mechanisms described above have been observed mainly in tests of beams and various other structural elements. A shear compression failure or a shear interface failure, or a failure mode resembling a combination of the two, are plausible ways by which the wall base may fail because of an increased radial shear. Crushing or splitting failure of concrete, a failure mode not directly linked to the level of shear stress at the section, is unlikely because the tension reinforcement at the inner surface of the wall had yielded. With further increases in pressure the unit compressive force in concrete is expected to decrease (Section 6.1.1). A diagonal tension failure is even less likely because of the amount and distribution of reinforcement through the section.

The internal compressive force in the wall, due to flexure, acts near the exterior wall surface. The effect of this force is similar to the clamping

action of transverse reinforcement in push-off tests in preventing a sliding shear failure along a potential crack plane. The clamping force of reinforcement in push-off tests is activated only after the occurrence of a relative slip. The clamping force due to flexure in the wall is developed somewhat differently, however, because its presence is controlled by the bending moment. The clamping force is present regardless of the relative slip along a failure plane. It is reasonable to assume that a portion of the radial shear strength at the wall base is due solely to the compressive force in flexure. The effects of internal friction allow for compressive force to be converted to shear strength. The reasoning is further justified by the confining effect of strain conditions at the wall base which approach those of "plane strain." Maximum circumferential strains there were approximately 0.00015 (Fig. 4.8), less than 7 percent of reinforcement yield strain.

The Coulomb-Mohr/internal-friction theory [Ref. 7.24] states that, at failure, shear stress is related to internal friction, a function of the normal stress acting on the shear plane. In this theory internal friction at a critical section is defined as the sum of a constant "cohesion" value plus a coefficient of friction, related to the "angle of internal friction," multiplied by the normal stress. Conversion of unit vertical compressive force to unit radial shear at the base of the wall via a coefficient of friction of 1.0 is suggested because the wall-basemat junction was intact at the end of pressure testing. Shear sliding had not occurred and there is no evidence of crack propagation toward the external wall surface. The proposed conversion of normal force to shear strength assumes an angle of internal friction of 45° and no cohesion: shear strength is negligible when the compressive force is zero. Tests on unreinforced concrete panels have demonstrated the ability of concrete to carry pure shear stress [Ref. 7.25]. In fact, a Mohr diagram with the compressive strength and a non-zero tensile strength of concrete as principal stresses would indicate a strength in pure shear, at zero compressive stress. The assumption of zero "cohesion" is made for simplicity.

A calculation procedure for evaluating the radial shear strength at the wall-basemat junction is based on the clamping effect of flexure. It is denoted herein as the C-model to reflect the process whereby the clamping or compressive stress is converted to a potential shear resistance via the Coulomb-Mohr theory. A similar rationale for evaluating radial shear strength of reinforced concrete containments is mentioned in references 7.12 and 7.13. The C-model enables a projection of the shear strength of the wall from estimates of the compressive force due to flexure, assumptions for the strain distribution through the wall, and the stress-strain curves of concrete and steel.

7.4.2 Description of the C-model

The paragraphs below describe and define a calculation for shear strength based on the clamping stress in flexure. For simplicity, it is called the C-model. A specific shear failure mode is not evaluated by the calculation procedure. The C-model attempts only a supply and demand assessment of the problem wherein the potential flexure clamping force plus the added contribution to strength by shear reinforcement is compared with the applied radial shear. The compressive force in flexure for various internal pressure levels is determined in a manner equivalent to a moment-curvature calculation

(Section 6.1.2). This force is converted to shear force by a coefficient of friction of unity. To this is added the shear capacity of shear reinforcement at yield which is independent of pressure. The radial shear force acting at the wall base is determined from elastic fixed-based assumptions and from consideration of yielding of circumferential reinforcement over the height of the wall.

7.4.2.1 Compressive Force Due to Flexure

The unit yield moment estimated from strain data (Fig. 6.4) at the internal pressure level initiating flexural yielding is found to compare rather well to the unit yield moment determined at the same internal pressure level by a moment-curvature calculation (Section 6.1.2). After the wall yields in flexure at its base, strain data indicate that as internal pressure increases, the unit compressive force does not increase with further increases in pressure (Fig. 6.3). Results of the moment-curvature calculation (Fig. 6.6) show that as internal pressure increases the unit bending moment required to initiate flexural yielding decreases. Likewise, the sum of the compressive forces in concrete and in steel at flexural yielding decrease as pressure increases. The compressive force due to flexure is a maximum, for a given internal pressure level, at the point of yielding of the vertical reinforcement on the inner surface of the wall. Determination of values of the maximum compressive force and internal

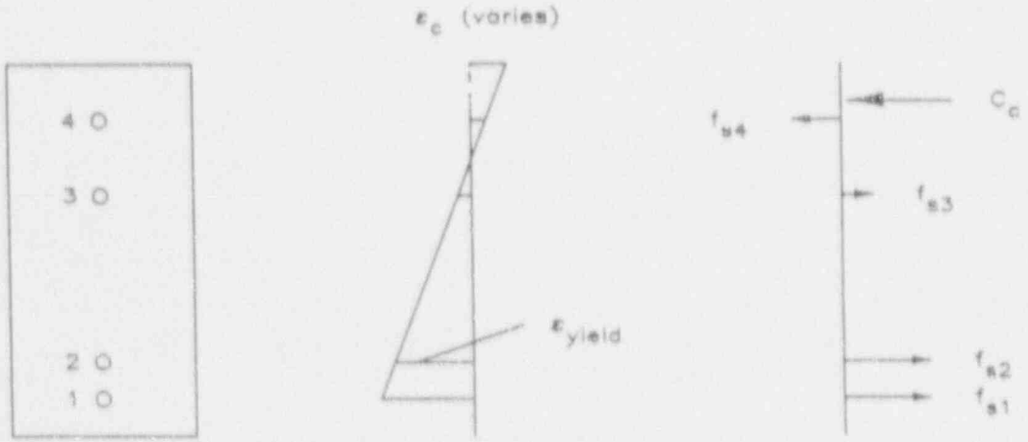

C_f = Force in concrete plus compression steel, $C_f = C_c + f_{s4}$

v_s = Strength of shear reinforcement.

$V_{total} = C_f + v_s$

$N_v = C_f - (f_{s1} + f_{s2} + f_{s3})$

$N_v = (p R^2 - W/\pi) / (2R + t)$

Fig. 7.7 C-Model Calculation for the Compressive Force in Flexure

pressure level may, therefore, be made only at strain distributions that allow the inner vertical reinforcement to yield.

Figure 7.7 illustrates a typical wall section in flexure with the strain distribution assumed and the unit forces in the concrete and steel. The notation used in this calculation is shown in the figure. A linear strain distribution across the section is defined by the reinforcement yield strain, ε_y, at the location of the inner vertical reinforcement and by trial values of the maximum strain in concrete, ε_c, at the wall exterior. At each trial value of ε_c, the forces in steel and concrete are determined according to assumed stress-strain curves and to the areas for the materials. An elastic-perfectly plastic curve for steel and the Hognestad curve [Ref. 6.2] for concrete is used for the calculation. The algebraic sum of the forces determines the unit vertical force, N_v (Section 5.1.1), from which equilibrating internal pressure is found. The compressive force in concrete and the compressive forces in steel located above the neutral axis (Fig. 7.7) are summed together to determine the total compressive force due to flexure, C_f. The calculation is repeated for other values of ε_c to obtain pairs of values of pressure and C_f. All trial values selected for ε_c are less than 0.003, a commonly used crushing strain of concrete.

7.4.2 Strength of Shear Reinforcement

The capacity of shear reinforcement to transmit radial shear is determined by the sum of the horizontal projection of force in all bars, stressed to their yield strength, which cross an assumed shear crack. The unit shear is obtained for each layer of reinforcing bars (stirrups and inclined dowels) by:

$$v_s = nA_v f_{vy} \sin \alpha / h \qquad (7.4)$$

where n = the number of effective bars crossing the crack
A_v = the area of one bar
f_{vy} = its yield strength
α = the inclination of the reinforcement from vertical and
h = the wall thickness.

The number of effective bars crossing the crack surface is determined by:

$$n = h (\cot\alpha + \cot\theta) / s \qquad (7.5)$$

where θ = the inclination of the crack from vertical and
s = the reinforcement spacing measured diagonally along the vertical wall axis [Ref. 7.14].

If the shear reinforcement is not horizontal, a conservative assumption for the crack inclination is to take $\theta = 90°$. The unit radial shear strength of reinforcement, v_s, determined according to Equation (7.4), is added to μC_f (where $\mu = 1.0$) to obtain the variation of the total unit shear strength, V_{total}, with pressure:

$$V_{total} = v_s + \mu C_f \qquad (7.6)$$

The compressive force, C_f, is given by $C_f = C_c + f_{ss}$ (Fig. 7.7).

7.4.2.3 Applied Radial Shear Force

The unit shear stress estimated from strain data (Fig. 6.12) is found to be indicated rather well near the end of the test, at pressures of 140 - 145 psig, by a calculation based on an elastic fixed-base model for the wall (Section 6.2.2). Above the maximum pressure, the applied unit shear force is expected to increase at a rate greater than given by the fixed-base calculation because the circumferential reinforcement in the wall had yielded. A simple means to compute the unit radial shear, Q, is to use the fixed-base calculation up to the pressure required to yield the circumferential reinforcement, p_y, and at greater pressures add half the additional unit radial force due to the pressure acting on the cylindrical wall. That is:

$$Q = p\sqrt{R/h} \,/\, [3(1 - \nu^2)]^{1/4} \qquad \text{for } p \le p_y \qquad (7.7)$$

$$Q = Q(p_y) + \tfrac{1}{2}(p - p_y)\, H/h \qquad \text{for } p > p_y \qquad (7.8)$$

where R = the cylinder radius
h = the wall thickness
H = the total cylinder wall height
ν = Poisson's ratio for the concrete and
$Q(p_y)$ = the radial shear calculated with Equation (7.7) at pressure p_y.

The pressure required to yield circumferential reinforcement is determined from:

$$p_y = \rho_h f_y H/R \qquad (7.9)$$

where ρ_h = the net circumferential reinforcement ratio and
f_y = its yield strength.

The calculation for Q at pressures greater than p_y assumes that the dome and basemat resist equal increments of radial shear after the circumferential reinforcement has yielded. This assumption is justified on the basis of the wall profile measurements: the radial-displaced shape (Fig. 4.3) is fairly symmetric about the mid-height. At the maximum test pressure the radial displacement over most of the wall height exceeds the calculated displacement (Table 5.1) at yielding of the liner, hoop, and diagonal reinforcement.

4.2 C-model Limiting Pressure

Once the variation with pressure of the total unit shear strength, V_{total}, and the applied unit radial shear, Q, are known (Equations 7.6 - 7.9), they are plotted versus pressure on a graph to locate their intercept (Fig. 7.10, 7.11). This procedure is based on the premise that radial shear may be resisted by the sum of the strength of the shear reinforcement and static friction force provided by the compressive force in flexure. The intercept of V_{total} and Q marks the pressure at which radial shear may be resisted at a coefficient of friction equal to 1.0. Pressures sustained that are greater than the calculated limit imply that the effective coefficient of friction at the wall-base is less than 1.0.

7.5 Application of Shear Strength Evaluation Procedure

Because the 1/6-scale model did not fail by radial shear, it is difficult to assess the accuracy of a radial-shear strength calculation for this containment other than assuming that any predicted failure pressure should be greater than 145 psig. An upper-bound to the failure pressure predicted could be found by a limit-analysis with a kinematically admissible mechanism. One limit for the 1/6-scale containment is at approximately 180 psig with all reinforcement in the wall yielded. The wall-basemat connection experiments by Aoyagi [Ref. 7.1] are evaluated for radial shear strength by the C-model first, to illustrate the accuracy and limitations of the calculation. Following this, the procedure is applied to the 1/6-scale containment model.

7.5.1 Aoyagi 1/12-Scale Specimens

Aoyagi [Ref. 7.1] tested six 1/12-scale models of a wall-basemat connection to failure. The specimens were scaled from the design of a typical BWR MARK III reinforced concrete containment vessel, as shown in Figure 7.1. Radial pressure was applied to the wall surface by a pressurized bag. Vertical load was applied by tensile forces on the vertical reinforcing bars at the top of the wall. Forces in circumferential reinforcement were monitored by load cells. The experimental setup allowed the applied radial shear to be determined at all pressure levels from the difference between the total unit radial force due to the lateral pressure and the sum total radial components of force measured by the load cells

Basic data for the Aoyagi specimens are presented in Table 7.1 and selected experimental results, including maximum pressure sustained, are presented in Table 7.2. Of the six specimens tested four were loaded to simulate internal pressurization conditions: vertical unit load was proportional to radial pressure given by pR/2. Specimen No. 4 was provided with 1.2% stirrups and specimen No. 6 with 2% by weight steel fibers.

Table 7.1 Aoyagi Specimen Design Data

Design pressure, p_d	1.05 kg/cm^2
Inner radius, R	166.6 cm
Wall thickness, h	15 cm
Wall height, (H/2)	150 cm
Wall reinforcement	
Yield strength	3973 kg/cm^2
Ultimate strength	5900 kg/cm^2
Circumferential ratio (10 mm dia. bars)	0.0088
Vertical ratio (10 mm dia. bars)	0.0111
Shear reinforcement[1]	
Yield strength	3400 kg/cm^2
Ultimate strength	5380 kg/cm^2
Horizontal ratio (6mm dia. bars)	0.0115

(1) Only specimen No. 4 was provided with shear reinforcing bars. Specimen No. 6 was provided with 2% by weight steel fibers.

Table 7.2 Summary of Experimental Results for Aoyagi Specimen [Ref. 7.1]

Specimen number	1	2	3	4	5	6
	Concrete Properties (kg/cm^2)					
compressive strength	218	218	365	366	184	224
tensile strength	17.4	17.4	31.1	31.1	15.8	20.5
Young's modulus	203,000	203,000	251,000	251,000	171,000	171,000
Vertical load[1]	$\frac{1}{2}pR$	$\frac{1}{2}p_dR$[2]	0[3]	$\frac{1}{2}pR$	$\frac{1}{2}pR$	$\frac{1}{2}pR$
	Pressure at Observed Events (kg/cm^2)					
Yield of vert bars	2.52	-	3.11	2.53	2.46	2.64
Yield of hoop bars	3.30	3.15	3.30	3.30	3.09	3.37
Ultimate pressure	4.95	5.80	5.40	6.30	5.58	6.55
Final vertical stress	29.4	5.6	0	37.8	32.9	39.0
Final radial shear	16.0	16.0	19.9	25.0	18.6	21.8

(1) Vertical unit load was proportional to pressure for specimens indicated.

(2) Load for specimen 2 was constant, equal to the vertical load at the design pressure, p_d.

(3) Specimen 3 was not loaded vertically.

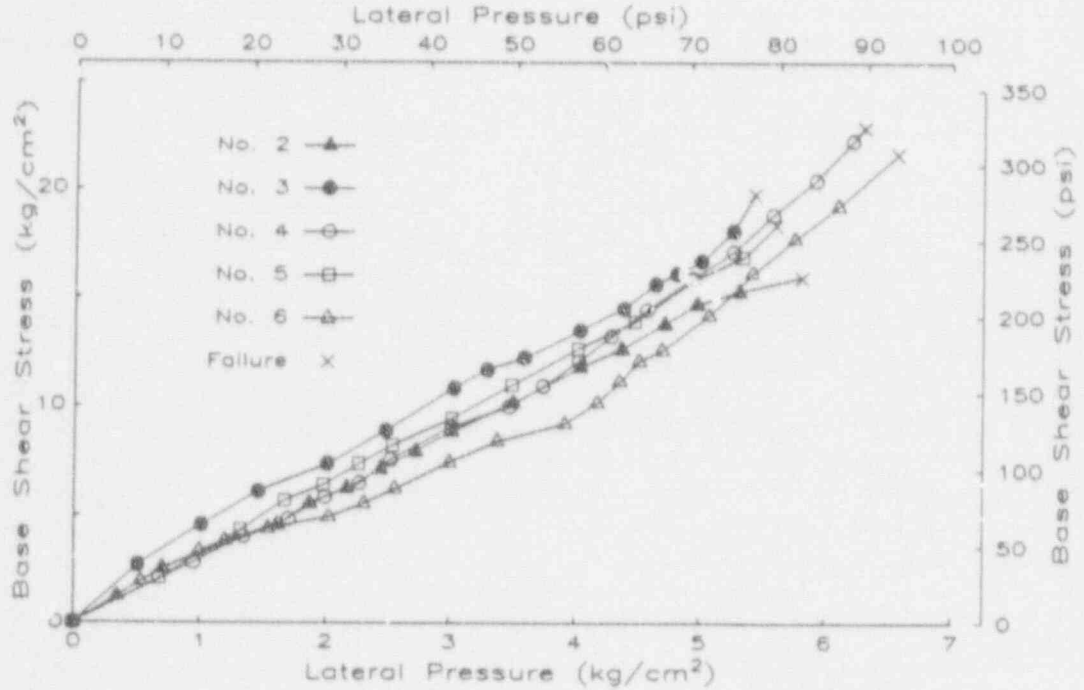

Fig. 7.8 Base Shear Stress vs. Pressure for Aoyagi Specimens

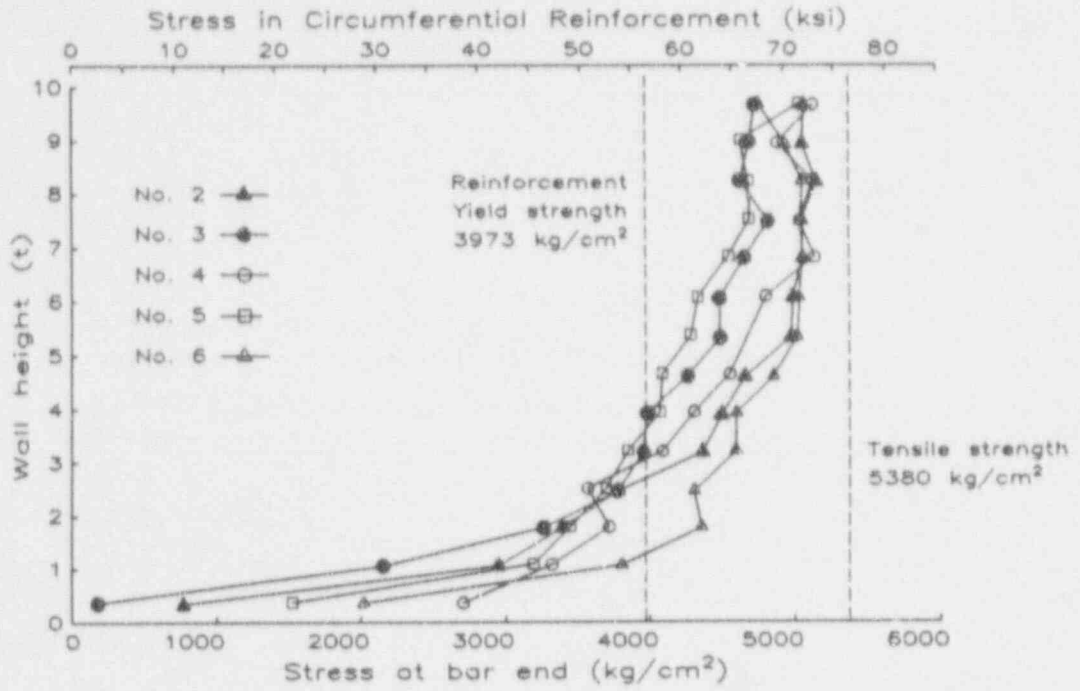

Fig. 7.9 Stress in Circumferential Reinforcement at 98% of Ultimate Pressure

Observed variations of unit base shear stress versus pressure are presented in Figure 7.8. In Figure 7.9 the variation with height of the measured stress in circumferential reinforcement is shown at a pressure equal to 98% of the ultimate pressure sustained by each specimen. The abscissae units on the plot are multiples of wall thickness. It is interesting to note that the circumferential reinforcement within the lower three wall thickness distance was stressed to less than yield strength at 98% of the ultimate internal pressure for all specimens but one. Also, the circumferential reinforcement exhibited a significant amount of strain hardening near the end of the test (Fig. 7.9).

With the specimen dimensions and data on materials strengths (Table 7.1, 7.2), the C-model limit pressure, p_C (Section 7.4.2) was determined for specimens No. 1, No. 4, No. 5, and No. 6. Specimens No. 2 and No. 3 excluded because the applied vertical load was not proportional to internal pressure, as in an actual containment pressurization (Table 7.2). The resulting C-model limit pressure is presented in Table 7.3. A plot illustrating the calculation for specimen No. 4 is presented in Figure 7.10.

The C-model calculation underestimates the ultimate failure pressure by as much as 50 percent for specimen No. 6. The low pressure estimates are partly accounted for by the stress-strain curve for reinforcement. The procedure does not allow for strain hardening of reinforcement (Fig. 7.9), which would increase the estimated unit compressive force due to flexure, C_f, and correspondingly the estimated failure pressure. The effects of strain hardening of circumferential reinforcement decrease the applied radial shear stress at the wall base and result in an increase in the estimated failure pressure. The value of p_C (Table 7.3) for specimen No. 6 does not include the shear capacity of the steel fibers added to the concrete mix.

Table 7.3 Results of Shear Strength Evaluation Procedure

Specimen	P_{ult}	$P_{C(1)}$	$\frac{P_C}{P_{ult}}$	$\frac{P_C}{P_{design}}$	$\frac{P_{ult}}{P_{design}}$
Aoyagi No. 1	4.95 kg/cm^2	3.2 kg/cm^2	0.65	3.0	4.7
Aoyagi No. 4	6.30 kg/cm^2	4.6 kg/cm^2	0.73	4.4	6.0
Aoyagi No. 5	5.58 kg/cm^2	3.3 kg/cm^2	0.59	3.1	5.3
Aoyagi No. 6	6.55 kg/cm^2	3.3 kg/cm^2 (2)	0.50	3.1	6.2
Sandia 1/6 scale	-	160 psig	-	3.5	-

(1) p_C denotes the C-model limit pressure determined according to procedures described in section 7.4.2.

(2) The C-model limit pressure for specimen No. 6 does not take into account the 2% by weight steel fibers present in the concrete mix.

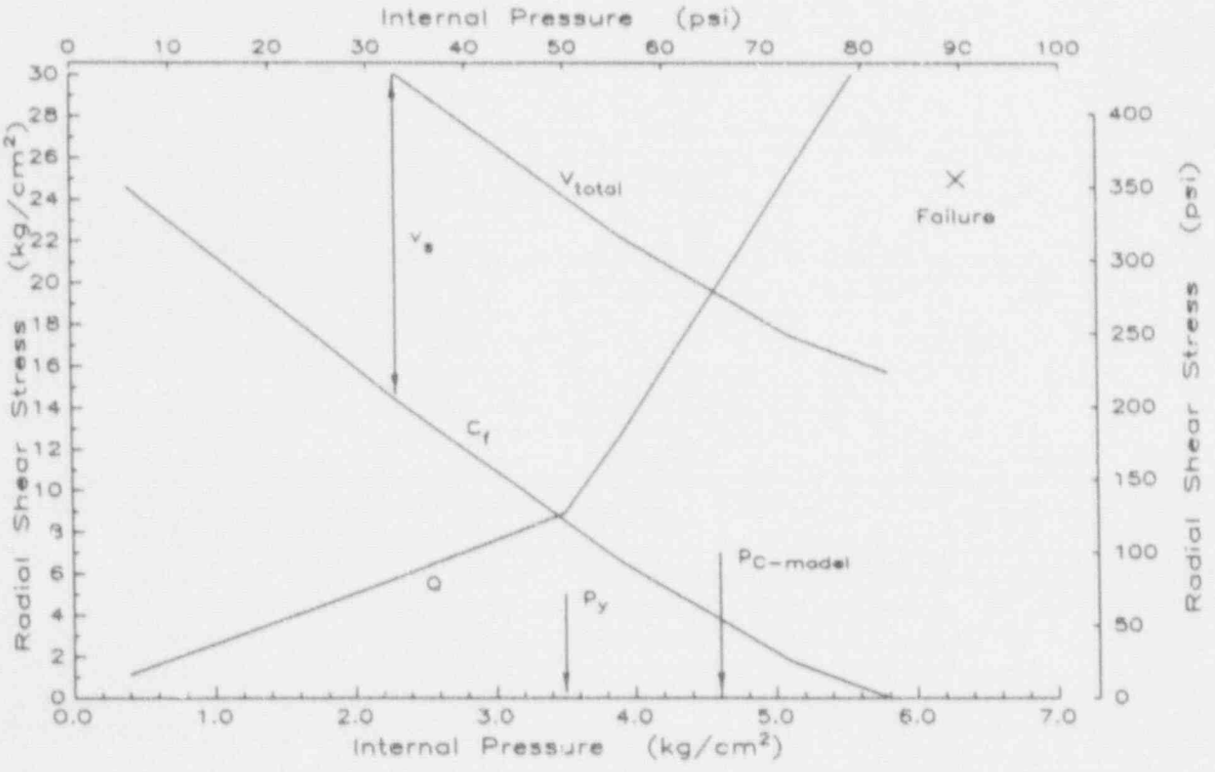

Fig. 7.10 C-Model Shear Strength Evaluation for Aoyagi Specimen No. 4

7.5.2 Sandia 1/6-Scale Containment

The results of the C-model applied to the 1/6-scale containment model are shown in Figure 7.11. Stress-strain curves used for reinforcement, the liner, and concrete are shown in Figures 6.2 and 6.5. The strength of stirrups are reduced to one-third their yield strength, as explained in Section 7.3.2. Using the equations outlined in Section 7.4.2.2, the

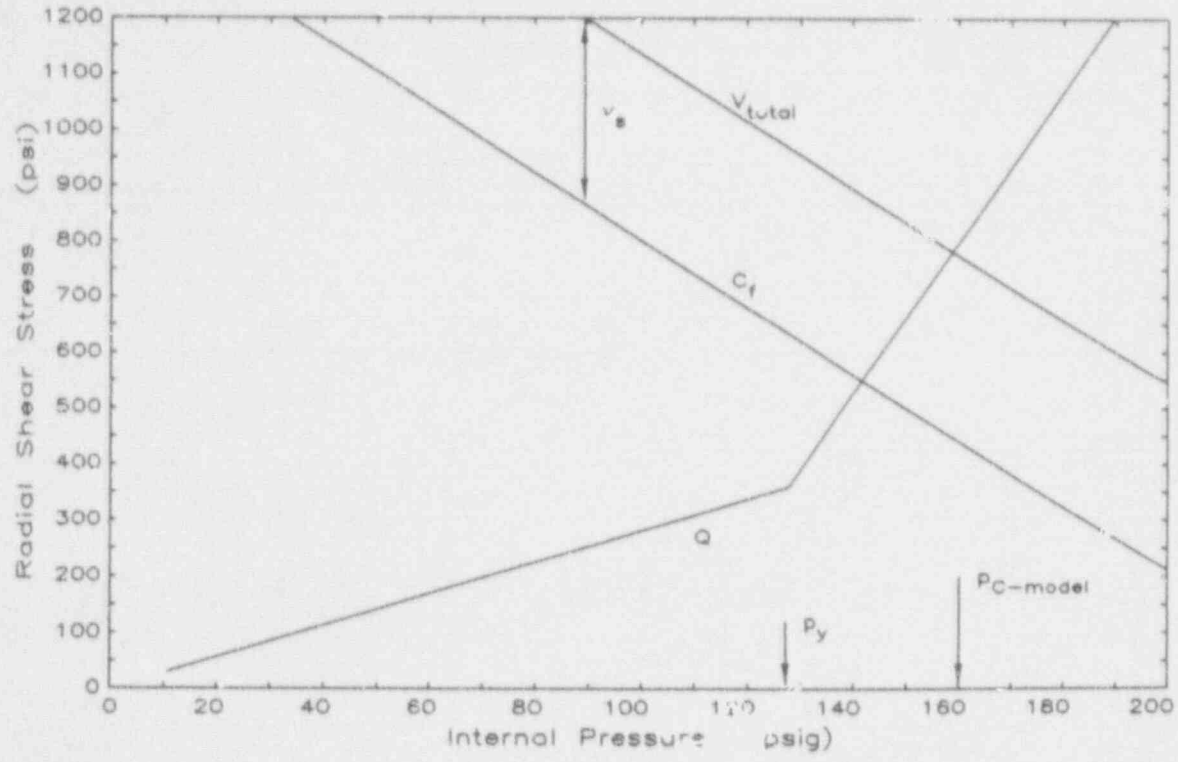

Fig. 7.11 C-Model Shear Strength Evaluation for Sandia 1/6-Scale Containment

contribution to shear strength by the inclined No. 4 bar is 206 psi, based on gross sections. The contribution by the stirrups is 128 psi giving a total v_s of 334 psi. The calculated curves for C_f, the shear capacity due to the flexure clamping force, the total shear capacity, $V_{total} = C_f + v_s$, and the applied radial shear stress, Q, are presented in Figure 7.11. The estimated pressure at which the applied shear exceeds the available resistance is 160 psig.

7.5.3 Strength Comparison of Aoyagi Specimen No. 4 and Sandia Model

The C-model calculation provides a basis on which the radial shear strengths of the Aoyagi specimen No. 4 (Fig. 7.10) and the Sandia containment model (Fig. 7.11) may be compared. In the following paragraphs, information is presented on the relative sizes and material strengths of the two specimens. The results of the C-model calculation for each specimen are then compared on a plot (Fig. 7.13) with normalized values for the shear stress and the internal pressure.

In Table 7.4 pertinent data are presented for Aoyagi specimen No. 4 and the Sandia containment model on the sizes, material strengths, and reinforcement ratios of the two wall-base connections. All quantities are in pound and inch units. Also listed in the table are pressures observed during testing at which flexural yielding and circumferential yielding occurred, as well as the final sustained pressure. The scale factor of the Aoyagi specimen compared with that of the Sandia containment suggests that the Aoyagi specimen would be approximately one-half the size of the Sandia model.

Table 7.4 Size Comparison of Aoyagi Specimen No. 4 and Sandia Containmer

	Aoyagi No. 4	Sandia Containment
Scale Factor	1/12	1/6
Design pressure	15 psig	46 psig
Inner radius	65.5 in.	132 in.
Wall thickness	5.9 in.	9.75 in.
Concrete strength, f_c'	5200 psi	6200 psi
	Wall Reirforcement	
Diameter	0.39 in.	0.5 in.
Strength, f_y	56.5 in.	64 ksi
Circumferential ratio	0.0097	0.0285
Vertical ratio	0.0123	0.0194
	Shear Reinforcement	
Diameter	0.24 in.	0.375, 0.5 in.
Strength, f_y	48.4 ksi	64. ksi
Shear ratio	0.0115	0.0052
	Internal Pressure at Events	
Flexural yielding at Wall Base	36 psig	118 psig
Yielding of Hoop Reinforcement	50 psig	127 psig
Final Pressure	90 psig	145 psig
C-model limit pressure	65 psig	160 psig
Final Radial Shear Stress	355 psi ($4.9\sqrt{f_c'}$)	450 psi ($5.7\sqrt{f_c'}$)

However, the design pressure of the Aoyagi specimen was app oximately one-third that of the Sandia containment model. This is reflected in the design of each by the difference between the circumferential reinforcement ratios (Table 7.4) for the two walls. The Aoyagi specimen was provided with approximately 1% circumferential reinforcement and the Sandia containment was provided with 2.85%. The internal pressure that initiated yielding of circumferential reinforcement of the Aoyagi specimen was 36 psig whereas yielding of circumferential reinforcement of the Sandia model was observed to occur in the range 110 to 130 psig (Section 4.1.1). One last point to note related to the sizes of the two specimens is the radial shear stress at the final pressure sustained in the experiments. Aoyagi specimen No. 4 failed at a shear stress of 355 psi ($4.9\sqrt{f_c'}$, $f_c' = 5200$ psi) whereas the shear stress estimated to have occurred at the maximum pressure sustained in the Sandia containment is 450 psi ($5.7\sqrt{f_c'}$, $f_c' = 6200$ psi).

Table 7.4 presents quantitative information indicating that the Aoyagi specimen was not as strong as the Sandia containment. This is illustrated graphically in Figure 7.12 by a comparison of the C-model calculation for both specimens. The smaller size and lower strength of the Aoyagi specimen do not allow for a direct comparison of the results of the C-model.

A plot of normalized values for radial shear stress and internal pressure is presented in Figure 7.13. The horizontal axis is the ratio of internal pressure to p_y, the pressure at which yielding of circumferential

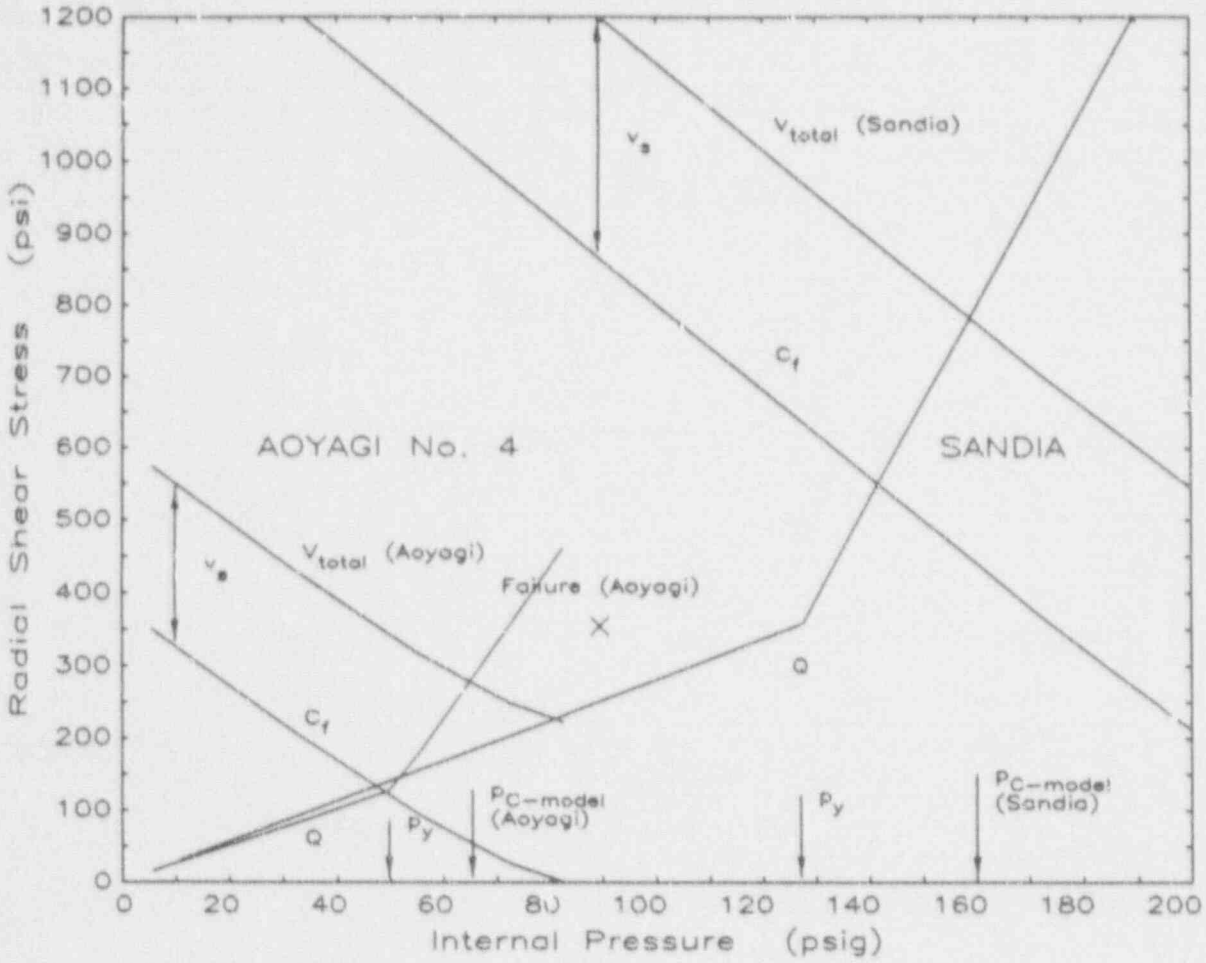

Fig. 7.12 Direct Comparison of Aoyagi Specimen No. 4 and Sandia Containment

reinforcement is initiated. The vertical axis in the plot is the ratio of shear stress to the shear stress calculated at p_y.

The C-model assumptions for applied shear stress employ a linear elastic fixed-base model for the calculation of shear stress before yielding of circumferential reinforcement. The circumferential reinforcement yield pressure for each specimen is shown in Figures 7.10 - 7.12 as p_y. Above this pressure the radial shear stress is calculated on the assumption that the circumferential bars carry no stresses above yield and that the additional radial pressure loads are transmitted equally to the dome and basemat.

The circumferential reinforcement yield pressure, p_y, and the radial shear stress at this pressure, $Q(p_y)$, are used to scale the results of the C-model calculations for the Aoyagi and Sandia connections (Fig. 7.13). Shown in the figure is the estimated radial shear stress, Q, for each specimen. The difference in these lines above a pressure ratio (p/p_y) of 1.0 is due to differences in the wall height of each specimen. The lines indicating the total resistance, V_{total}, are nearly identical on the normalized plot. Furthermore, the p/p_y ratio at the C-model limit pressure is 1.3 for the Aoyagi specimen and 1.25 for the Sandia model.

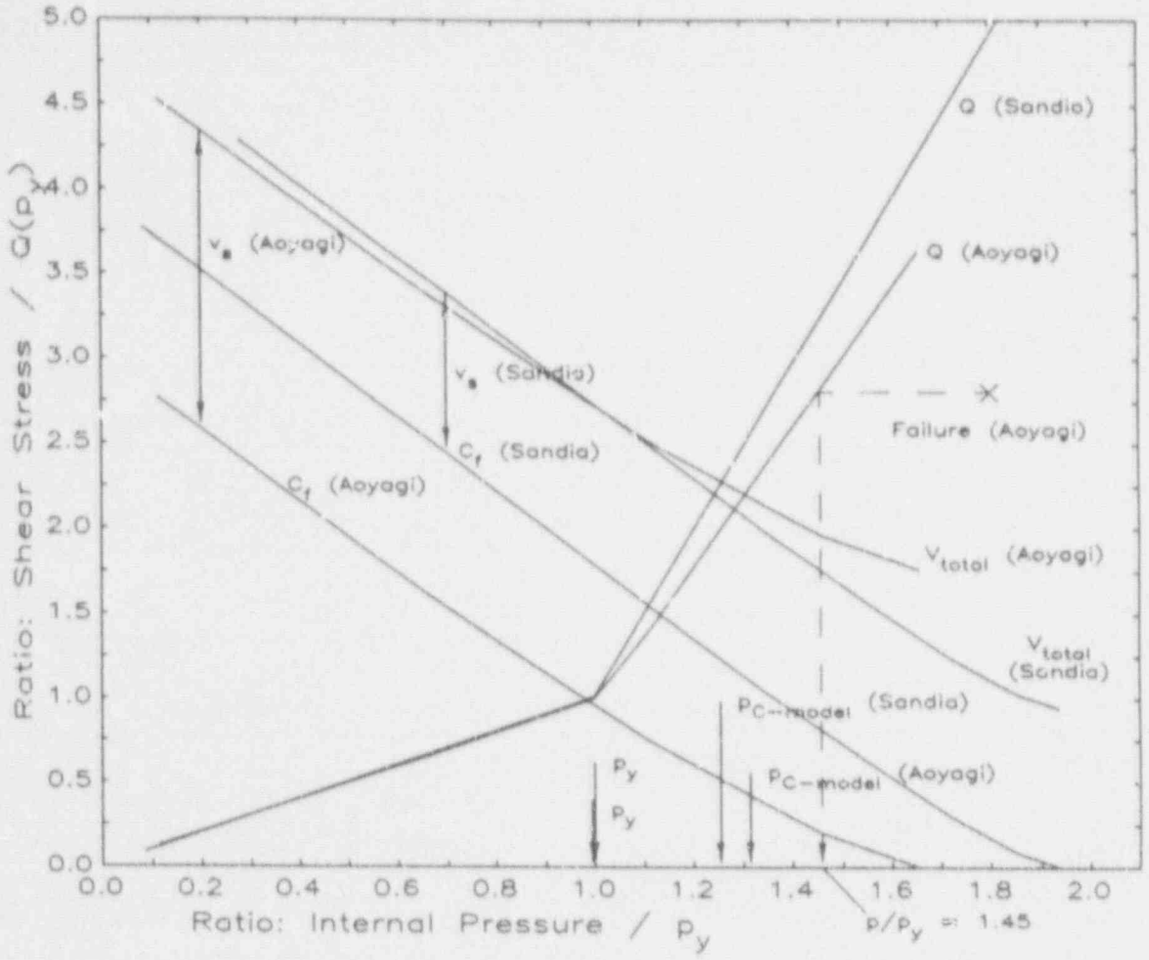

Fig. 7.13 Normalized Comparison of C-Model for Aoyagi Specimen No. 4 and Sandia Containment

The failure of the Aoyagi specimen is located on Figure 7.13. As discussed previously (Section 7.5.1), the radial shear stress at the final pressure for the Aoyagi specimen is underestimated by the C-model. The actual shear stress of the Aoyagi specimen at failure is what is relevant, not the internal pressure at which it occurred. Aoyagi specimen No. 4 failed at a shear stress of 355 psi. This represents a normalized shear stress of 2.8 for $Q(p_y)$ of 127 psi. The calculated internal pressure ratio at which the shear stress ratio equals 2.8 for the Aoyagi specimen is 1.45. This 1.45 pressure ratio is then multiplied by the p_y pressure for the Sandia containment to obtain a internal pressure of 185 psig. The conditions at failure of Aoyagi specimen No. 4, as idealized by the C-model, are equivalent to the conditions for the Sandia containment at an internal pressure of 185 psig. Based on the limited amount of information on wall-basemat connections, the 185 psig pressure cannot be stated with a high confidence as the shear-failure pressure of the Sandia containment. Since it is known that the containment model had not failed at 145 psig, an estimate in the uncertainty in the shear-failure pressure is within 40 psig of the extrapolated 185 psig value.

8. CONCLUDING REMARKS

In this report an interpretation was presented of the behavior of the 1/6-scale reinforced concrete containment structure (Fig. 1.1) tested by internal pressure at Sandia. A potential mode of failure by radial shear was evaluated at the wall-basemat connection. Response data from the containment structure was analyzed for its credibility by comparison to results of calculations by simple analytical models. The history of the internal forces at the wall-base was estimated from strain gage data. A comparison was made of the performance of the containment structure with the results of similarly loaded reinforced concrete test specimens. At the maximum pressure sustained, the stresses estimated to have occurred at the containment model wall-base are out of the range of parameters of available tests for sections that have yielded in flexure and have been loaded simultaneously in shear and axial tension. For this reason a calculation procedure was developed for evaluating radial shear strength in relation to the compressive force generated by flexure.

The following paragraphs summarize the important items learned during the course of study. In addition, in Section 8.3 an assessment of the state of knowledge on the strength of wall-basemat connections of reinforced concrete containments is presented. Conclusions of this study are offered in Section 8.4.

8.1 Behavior Interpretation

8.1.1 Free-field Response

Response in the "free-field" of a shell refers to the response due to statically determined forces that act within the plane of the shell in areas unaffected by discontinuities such as at points of attachment or abrupt changes in shape. These areas are characterized by having minimal bending stresses and small out-of-plane shear stresses. The free-field radial expansion of the cylindrical containment wall was shown to be influenced by concrete cracking and by yielding of the various layers of reinforcement. At the maximum pressure achieved in the tests an overall unrestricted yielding was observed in the circumferential direction but not in the vertical direction. An axisymmetric ring model representing a segment of the cylinder has shown that radial expansion data compared favorably with what may be calculated by analysis for hoop-stress cracking of concrete and for yielding of the liner, circumferential reinforcement, and diagonal reinforcement. The effect of concrete cracking on measured data is represented by changes in apparent response stiffness. These changes were shown to be within "bounds" of what might be expected for the change in stiffness due to cracking for reinforced concrete sections subjected to axial tension or to flexure.

8.1.2 Response at Wall-Basemat Junction

Strain data from reinforcement in the wall and the basemat (Fig. 4.6-4.17) were shown to enable qualitative and quantitative assessments of the shear and moment transmitted at the wall-basemat junction. The rate at which shear force and meridional bending moment increased with pressure, as indicated by strain data, were initially believed to be anomalous. In the pressure range

beginning just after the onset of cracking of the basemat and ending when the wall begins to yield in flexure at its base, the rate of increase in shear decreased. The rate of increase of moment remained the same. A linear elastic analysis model was described and was found to offer an explanation of the observed behavior. The model also has shown that the basemat participated in the response and affected the history of internal forces at the wall-basemat connection.

8.2 Evaluation of Radial Shear Strength

8.2.1 Estimation of Internal Forces

Strain data from gages on reinforcement in the wall (Fig. 4.10-4.17), at the wall-basemat junction, were used to estimate a history of the bending moment. Radial shear force at the base of the wall was estimated at the maximum test pressure from basemat reinforcement strain data (Fig. 4.6, 4.7). It was shown that the wall at this location had yielded in flexure as pressure increased to 118 psig. Because the wall had also yielded circumferentially over most of its height (Fig. 4.3) by the end of the test, if additional units of internal pressure were introduced to the containment, the radial shear at the wall-base would have increased at a rate greater than what would be predicted from an elastic fixed-base analysis model based on gross sections. The unit forces at the maximum test pressure (145 psig), expressed as stress on the gross wall section, were estimated to have been 920 psi ($11.7\sqrt{f'_c}$) axial tension and 450 psi ($5.7\sqrt{f'_c}$) radial shear.

8.2.2 Shear Strength Estimate

Current design procedures for estimating the shear strength of reinforced concrete sections [Ref. 2.4, 5.2] were found either to underestimate strength or to be inapplicable to the conditions at the wall-basemat connection. A survey of literature on experiments of reinforced concrete members subjected to similar stress conditions at failure found no experimental test data that could be used directly to guide an estimate of the shear strength of the 1/6-scale containment. The relationship between shear strength and the geometrical and material properties of reinforced concrete structures is not well understood. All generalizations and calculation methods are limited essentially to the range of critical parameters covered in the tests leading to the particular method. Because of the special stress combinations at the wall-basemat connection, the strength observed in the test of the 1/6-scale containment model stands virtually alone. By itself, it does not support confident projection to similar cases with different stress combinations or reinforcement arrangements. To provide an intelligible connection between the data from the containment test and data from tests of simulated wall-basemat connections, a procedure for estimating the radial shear capacity from the compression force in flexure was defined. This procedure was applied to the 1/6-scale containment and to other 1/12-scale wall-basemat connection experiments [Ref. 7.1]. Applied to the 1/6-scale model, this procedure would indicate a limiting internal pressure of 160 psig which is credible because no such failure was observed in the containment before the test was terminated at 145 psig. This calculation is found to underestimate the shear capacity of the 1/12-scale specimens. Ratios of calculated to observed pressure at failure ranged from 59 to 73 percent. Because the wall-

basemat connection did not fail, a true capacity of the wall base to resist shear is not known. Using the described procedure, at a pressure of 185 psig the stress conditions in the Sandia 1/6-scale containment would be similar to the stress conditions at failure of one of the 1/12-scale connection specimens. The implied 185 psig radial-shear failure pressure of the Sandia containment has an uncertainty of 40 psig because of the limited amount of data. An evaluation of the observed effects of size in other experiments has suggested that the shear strength of the wall of its prototype, full-size containment, would be approximately 10 percent lower.

8.3 Assessment of the State of Knowledge on Strength of the Wall-Basemat Connection

This study has found that the state of knowledge on the strength of connections, such as between the wall and basemat of reinforced concrete containment structures, is not at an equal level with the current state of understanding of the capacities of other reinforced concrete members (beams, columns, walls). The high level of shear stress in combination with axial tension at a section which has yielded in flexure is beyond the range of parameters of available experimental investigations of similar reinforced concrete sections. An immediate conclusion is that if a reliable and close estimate of the shear strength of the wall-basemat connection is desired, additional tests of specimen models of wall-base connections should be conducted. In fact, the evaluation of behavior and strength of the 1/6-scale containment model has shown that the results of this test could not be used to make reliable estimates of radial shear strength with any degree of confidence greater than before the test. The interpretation of the test data herein has shown that the radial shear capacity across a section in tension and flexure is greater than what could be justified by experimental data. The stated purpose [Ref. 2.1] of the containment model test was to generate data that can be used evaluate analytical methods for predicting the response and mode of failure of reinforced concrete containments. A wealth of response data was recorded during the pressurization tests that, no doubt, will be useful in calibrating analyses. However, the response data cannot be used to validate an analytical method that would predict a shear failure at the wall base since no such failure was observed during the test.

The two sections below contain lists of items pertinent to the strength and performance evaluation of this 1/6-scale containment connection which could not be or which could be calculated with a high degree of confidence.

8.3.1 Items Which Could not be Calculated with a High Degree of Confidence

- Shear strength at the base of the wall.
- The effectiveness of stirrups (welded or tied), inclined reinforcement anchored in the basemat, or vertical (moment-resisting) dowels at the connection in resisting shear at failure.
- The effects of scale on extending an estimate of shear strength of a 1/6-scale model containment to the full-size. Present data on the effects of size on shear strength are principally from tests of beams. Projection of the results of these tests to a containment is made cautiously.
- Tensile strength of in-place concrete. Split-cylinder tests on concrete cylinder samples from the containment indicated that tensile strength was 450 psi (5.7 $\sqrt{f'_c}$). Direct-tension tests on concrete samples were inconclusive. The apparent tensile strength estimated from response data was 250 psi (3.2 $\sqrt{f'_c}$).

8.3.2 Items Which Could be Calculated With a High Degree of Confidence

- Estimates of the free-field strength and overall free-field deformations of the containment wall.
- Estimate of the internal pressure which would initiate flexural yielding at the base of the wall.
- Influence of cracking of concrete on the relative changes in flexural and membrane stiffness of the containment.

8.4 Conclusions

The following conclusions are offered:

- A review of the literature on structural tests of reinforced concrete sections indicated that the database of experience for guiding an estimate of shear capacity at the wall-basemat connection is insufficient.
- In applying the experience of tests on reinforced concrete beams to evaluate the effect of size on the shear strength of the wall-basemat connection, it was indicated that a full-size containment would be approximately 10% less strong in shear than the 1/6-scale containment, mainly due to scaling of sizes of aggregates.
- A calculation procedure for evaluating shear strength, based on the compression force in flexure, was described and was shown to be conservative when applied to tests of 1/12-scale 45° sectors of wall-base connections.

APPENDIX A. APPARENT STIFFNESS DATA FOR CALCULATIONS DESCRIBED IN SECTION 5.2

Table A.1 Apparent Stiffness Data for Membrane Response of the Wall

GAGE ID	CHANNEL	ELEVATION Ft	ELEVATION In	RADIUS Ft	RADIUS In	AZIMUTH Deg	DESCRIPTION	(1) STIFFNESS Ku	(1) STIFFNESS Kc	RATIO Ku/Kc
D114	233	7	1.5	11	0.	243.9	WALL RADIAL DISPL	312.	72.	4.3
Wr22	441	7	2.0	11	1.3	90.0	REBAR LAYER 1	84.	63.	1.3
Wr262	1040	7	4.0	11	6.5	45.5	REBAR LAYER 5	185.	72.	2.6
Wr151	689	7	11.0	11	8.0	90.0	REBAR LAYER 7	190.	50.	3.8
D97	216	8	6.6	11	0.	228.4	WALL RADIAL DISPL	712.	248.	2.9
Wr124	642	8	11.0	11	7.3	90.0	REBAR LAYER 6	211.	54.	3.9
Wr266	1044	9	1.3	11	1.3	0.	REBAR LAYER 1	120.	44.	2.7
Wr144	682	9	6.5	11	7.3	46.0	REBAR LAYER 6	228.	63.	3.7
Wr139	667	9	11.0	11	7.3	0.5	REBAR LAYER 6	340.	72.	4.8
Wr23	442	9	11.0	11	1.3	90.0	REBAR LAYER 1	171.	46.	3.7
Wr36	465	9	11.0	11	1.3	270.5	REBAR LAYER 1	112.	67.	1.7
Wr133	661	10	0.3	11	7.3	269.5	REBAR LAYER 6	182.	47.	3.9
Wr129	647	10	0.5	11	7.3	179.0	REBAR LAYER 6	301.	64.	4.7
Wr140	668	10	8.5	11	7.3	0.5	REBAR LAYER 6	160.	68.	2.4
Wr277	1065	10	8.5	11	9.3	45.5	REBAR LAYER 8	176.	50.	3.5
Wr130	648	10	9.5	11	7.3	179.0	REBAR LAYER 6	202.	65.	3.1
Wr24	443	10	9.5	11	1.3	89.5	REBAR LAYER 1	140.	40.	3.5
Wr37	456	10	10.0	11	1.3	270.0	REBAR LAYER 1	140.	33.	4.2
Wr141	669	10	10.3	11	7.3	0.5	REBAR LAYER 6	144.	77.	1.9
Wr84	563	10	10.5	11	1.5	45.5	REBAR LAYER 2	196.	69.	2.8
Wr131	649	10	10.8	11	7.3	179.0	REBAR LAYER 6	225.	81.	2.8
Wr195	783	10	11.0	11	8.8	45.5	REBAR LAYER 8	108.	51.	2.1
Wr237	865	10	11.4	11	7.3	0.5	REBAR LAYER 6	116.	54.	2.1
Wr238	866	10	11.5	11	7.3	179.0	REBAR LAYER 6	169.	52.	3.2
D55	174	11	0.	11	0.	356.9	WALL VERTICAL DISPL	2166.	785.	2.8
D99	218	11	2.4	11	0.	228.6	WALL RADIAL DISPL	669.	267.	2.5
Wr162	720	11	2.5	11	8.0	352.0	REBAR LAYER 7	205.	70.	2.9
Wr155	703	11	3.5	11	8.0	171.5	REBAR LAYER 7	241.	62.	3.9
Wr125	643	11	6.5	11	7.3	89.5	REBAR LAYER 6	260.	102.	2.6
Wr38	467	11	6.5	11	1.3	270.5	REBAR LAYER 1	174.	56.	3.1
Wr25	444	11	6.8	11	1.3	89.5	REBAR LAYER 1	154.	64.	2.4
Wr134	662	11	7.0	11	7.3	269.5	REBAR LAYER 6	229.	92.	2.5
Wr156	704	11	7.5	11	8.0	171.5	REBAR LAYER 7	245.	75.	3.3
Wr163	721	11	7.8	11	8.0	352.0	REBAR LAYER 7	316.	107.	2.9
Wr273	1061	11	7.8	11	8.3	171.5	REBAR LAYER 7	174	64.	2.7
D89	208	11	8.0	11	0.	179.2	WALL VERTICAL DISPL	752.	444.	1.7
Wr271	1049	11	8.0	11	8.3	352.0	REBAR LAYER 7	193.	85.	2.3
Wr26	445	11	9.3	11	1.3	89.5	REBAR LAYER 1	141.	48.	2.9
Wr39	468	11	9.5	11	1.3	270.5	REBAR LAYER 1	135.	74.	1.8
Wr126	644	11	10.0	11	7.3	89.5	REBAR LAYER 6	176.	95.	1.8
Wr152	700	11	10.5	11	8.0	84.5	REBAR LAYER 7	228.	64.	3.5
Wr135	663	11	11.0	11	7.3	269.5	REBAR LAYER 6	450.	156.	2.9
Wr153	701	12	2.0	11	8.0	85.0	REBAR LAYER 7	195.	47.	4.1
Wr160	708	12	2.0	11	8.0	264.0	REBAR LAYER 7	253.	88.	2.9
Wr161	709	12	4.0	11	8.0	264.5	REBAR LAYER 7	170.	56.	3.0
Wr60	509	12	9.0	11	1.5	158.5	REBAR LAYER 2	139.	49.	2.8
Br22	1107	12	9.8	11	7.5	135.0	REBAR LAYER 6	95.	47.	2.0
Br20	1105	12	11.8	11	1.5	134.0	REBAR LAYER 2	441.	95.	4.6
D100	219	13	0.	11	0.	228.6	WALL RADIAL DISPL	951.	261.	3.7
D109	228	13	0.	11	0.	315.0	WALL RADIAL DISPL	1246.	418.	3.0
D87	206	13	0.	11	0.	134.1	WALL RADIAL DISPL	712.	290.	2.5
Wr121	629	13	0.	11	6.3	348.5	REBAR LAYER 5	339.	159.	2.1
Wr233	861	13	0.	11	1.8	348.5	REBAR LAYER 2	154.	96.	1.6
Wr235	863	13	0.	11	6.3	349.0	REBAR LAYER 5	290.	148.	2.0
Wr66	525	13	0.	11	1.5	263.0	REBAR LAYER 2	304.	99.	3.1
Wr67	526	13	0.	11	1.5	262.0	REBAR LAYER 2	114.	45.	2.5
Wr79	548	13	0.	11	1.5	348.0	REBAR LAYER 2	245.	178.	1.4
Wr80	549	13	0.	11	1.5	348.0	REBAR LAYER 2	174.	104.	1.7
Wr81	560	13	0.	11	1.5	342.5	REBAR LAYER 2	304.	72.	4.2

(1) Note: Stiffness units are psi/inch for displacement gages and ksi for strain gages.

Table A.1 (cont.)

GAGE)	CHANNEL	ELEVATION Ft	In	RADIUS Ft	In	AZIMUTH Deg	DESCRIPTION	(1) STIFFNESS Ku	Kc	RATIO Ku/Kc
Wr82	561	13	0.	11	1.5	339.0	REBAR LAYER 2	369.	93.	4.0
Wr103	601	13	0.3	11	6.3	167.0	REBAR LAYER 5	351.	132.	2.7
Wr105	603	13	0.3	11	6.3	156.0	REBAR LAYER 5	238.	89.	2.7
Wr234	862	13	0.3	11	1.8	168.5	REBAR LAYER 2	290.	108.	2.7
Wr236	864	13	0.5	11	6.3	169.0	REBAR LAYER 5	387.	84.	4.6
Wr57	506	13	0.3	11	1.5	168.0	REBAR LAYER 2	313.	124.	2.5
Wr58	507	13	0.3	11	1.5	167.5	REBAR LAYER 2	349.	97.	3.6
D1	120	13	0.4	11	0.	0.	WALL RADIAL DISPL	1317.	412.	3.2
Br21	1106	13	0.5	11	6.3	134.5	REBAR LAYER 5	489.	102.	4.8
Wr122	640	13	0.5	11	6.3	348.0	REBAR LAYER 5	261.	133.	2.0
Wr68	527	13	0.5	11	1.5	258.0	REBAR LAYER 2	216.	57.	3.8
Wr104	602	13	1.0	11	6.3	168.0	REBAR LAYER 5	299.	77.	3.9
Wr110	608	13	1.0	11	6.3	254.0	REBAR LAYER 5	245.	78.	3.2
Wr112	620	13	1.0	11	6.3	305.5	REBAR LAYER 5	129.	74.	1.7
Wr123	641	13	1.0	11	6.3	336.0	REBAR LAYER 5	180.	95.	1.9
Wr59	508	13	1.0	11	1.5	162.5	REBAR LAYER 2	235.	57.	4.1
Wr70	529	13	1.0	11	1.5	305.5	REBAR LAYER 2	186.	103.	1.8
D22	141	13	1.2	11	0.	180.0	WALL RADIAL DISPL	1430.	248.	5.8
Wr108	606	13	1.5	11	6.3	263.0	REBAR LAYER 5	283.	181.	1.6
Wr109	607	13	1.5	11	6.3	262.0	REBAR LAYER 5	268.	110.	2.4
Wr48	487	13	1.5	11	1.5	83.0	REBAR LAYER 2	124.	89.	1.4
Wr49	488	13	1.5	11	1.5	82.0	REBAR LAYER 2	301.	70.	4.3
Wr50	489	13	1.5	11	1.5	78.0	REBAR LAYER 2	162.	54.	3.0
Wr94	582	13	1.5	11	6.3	83.0	REBAR LAYER 5	309.	132.	2.3
Wr95	583	13	1.5	11	6.3	82.0	REBAR LAYER 5	246.	90.	2.7
Wr96	584	13	1.5	11	6.3	74.0	REBAR LAYER 5	658.	93.	7.1
Br19	1104	13	4.5	11	1.3	135.0	REBAR LAYER 1	114.	47.	2.4
Wr263	2041	13	5.0	11	6.5	45.5	REBAR LAYER 5	280.	92.	3.1
Br24	1109	13	9.0	11	8.0	46.5	REBAR LAYER 6	143.	52.	2.7
D15	134	13	10.6	11	0.	90.0	WALL RADIAL DISPL	1716.	448.	3.8
Wr171	729	14	0.	11	8.8	85.0	REBAR LAYER 8	340.	74.	4.6
Wr275	1063	14	0.5	11	9.3	85.0	REBAR LAYER 8	369.	171.	2.2
Wr172	740	14	2.0	11	8.8	83.5	REBAR LAYER 8	456.	129.	3.5
Wr183	761	14	2.5	11	8.8	265.5	REBAR LAYER 8	226.	83.	2.7
Wr276	1064	14	3.5	11	9.3	265.5	REBAR LAYER 8	313.	171.	1.8
Wr184	762	14	5.5	11	8.8	265.0	REBAR LAYER 8	326.	69.	4.7
Wr174	747	14	7.0	11	8.6	171.5	REBAR LAYER 8	270.	65.	4.1
Wr138	766	14	7.0	11	8.8	352.5	REBAR LAYER 8	241	104.	2.3
Wr139	767	14	7.0	11	8.8	351.0	REBAR LAYER 8	326.	69.	4.7
Wr274	1062	14	7.0	11	8.3	187.5	REBAR LAYER 7	340.	62.	5.5
Wr157	705	14	8.0	11	8.0	187.5	REBAR LAYER 7	320.	77.	4.1
Wr164	722	14	8.0	11	8.0	7.0	REBAR LAYER 7	270.	100.	2.7
Wr176	744	14	8.0	11	8.8	171.5	REBAR LAYER 8	320.	104.	3.1
Wr272	1060	14	8.0	11	8.3	7.0	REBAR LAYER 7	243.	88.	2.8
D2	121	14	8.4	11	0.	0.	WALL RADIAL DISPL	1427.	436.	3.3
Wr175	743	14	9.0	11	8.8	171.0	REBAR LAYER 8	316.	58.	5.5
Wr190	768	14	9.0	11	8.8	352.5	REBAR LAYER 8	257.	83.	3.1
D23	142	14	9.2	11	0.	180.0	WALL RADIAL DISPL	1317.	412.	3.2
D56	175	14	9.6	11	0.	0.	WALL RADIAL DISPL	1715.	462.	3.7
Wr158	706	14	10.0	11	8.0	187.5	REBAR LAYER 7	282.	65.	4.3
Wr165	723	14	11.0	11	8.0	6.0	REBAR LAYER 7	244.	85.	2.9
Wr191	769	15	2.5	11	8.8	348.0	REBAR LAYER 8	279.	59.	4.7
Wr177	745	15	3.0	11	8.8	168.5	REBAR LAYER 8	270.	62.	4.4
Wr166	724	15	3.8	11	8.0	8.5	REBAR LAYER 7	456.	91.	5.0
Wr159	707	15	4.0	11	8.0	189.0	REBAR LAYER 7	534.	86.	6.2
D101	220	15	4.9	11	0.	228.5	WALL RADIAL DISPL	631.	290.	2.2
Wr192	780	15	6.5	11	8.8	346.5	REBAR LAYER 8	285.	69.	4.1
Wr178	746	15	7.5	11	8.8	165.5	REBAR LAYER 8	182.	79.	2.3
D96	217	15	11.7	11	0.	227.6	WALL VERTICAL DISPL	1648.	826.	2.0
D115	234	16	2.6	11	0.	225.6	WALL RADIAL DISPL	382.	113.	3.4
Br25	1120	16	3.0	11	8.0	45.5	REBAR LAYER 6	245.	49.	5.0
Wr179	747	16	7.0	11	8.3	163.0	REBAR LAYER 8	190.	58.	3.3
Wr85	564	16	8.5	11	2.0	46.0	REBAR LAYER 2	570.	78.	7.3

(1) Note: Stiffness units are psi/inch for displacement gages and ksi for strain gages.

Table A.1 (cont.)

GAGE ID	CHANNEL	ELEVATION Ft	ELEVATION In	RADIUS Ft	RADIUS In	AZIMUTH Deg	DESCRIPTION	(1) STIFFNESS Ku	STIFFNESS Kc	RATIO Ku/Kc
Wr193	781	16	9.5	11	8.8	350.0	REBAR LAYER 8	415.	86.	4.8
Wr27	446	16	11.5	11	1.5	91.0	REBAR LAYER 1	81.	45.	1.8
D110	229	17	10.3	11	0.	315.0	WALL RADIAL DISPL	851.	412.	2.1
D102	221	17	11.1	11	0.	228.3	WALL RADIAL DISPL	681.	313.	2.2
D104	223	17	11.6	11	0.	223.0	WALL VERTICAL DISPL	782.	333.	2.3
D57	176	17	11.6	11	0.	358.1	WALL VERTICAL DISPL	528.	355.	1.5
D58	177	18	0.	11	0.	359.8	WALL RADIAL DISPL	1372.	393.	3.5
D90	209	18	0.1	11	0.	180.0	WALL RADIAL DISPL	1220.	528.	2.3
Wr268	1046	19	0.3	11	7.3	0.	REBAR LAYER 6	208.	50.	4.2
Wr269	1047	19	0.5	11	7.3	180.0	REBAR LAYER 6	140.	42.	3.3
Wr270	1048	19	0.5	11	7.3	242.0	REBAR LAYER 6	114.	40.	2.8
Wr264	1042	19	1.5	11	6.5	47.0	REBAR LAYER 5	340.	80.	4.3
Wr261	1029	19	2.5	11	7.3	46.0	REBAR LAYER 6	108.	45.	2.4
Wr33	462	19	9.0	11	1.3	135.0	REBAR LAYER 1	166.	82.	2.0
Wr115	623	19	9.4	11	6.3	313.0	REBAR LAYER 5	327.	90.	3.6
D59	178	19	11.7	11	0.	359.7	WALL RADIAL DISPL	1715.	381.	4.5
D92	211	20	0.	11	0.	180.0	WALL RADIAL DISPL	1302.	528.	2.5
Wr113	621	20	0.	11	6.3	312.0	REBAR LAYER 5	309.	92.	3.4
Wr71	540	20	0.5	11	1.5	305.0	REBAR LAYER 2	231.	120.	1.9
Wr72	541	20	0.5	11	1.5	312.0	REBAR LAYER 2	746.	230.	3.2
Wr73	542	20	0.5	11	1.5	313.0	REBAR LAYER 2	697.	200.	3.5
D103	222	20	0.8	11	0.	227.9	WALL RADIAL DISPL	1222.	362.	3.4
Wr114	622	20	1.0	11	6.3	331.5	REBAR LAYER 5	816.	92.	8.9
D106	225	20	1.1	11	0.	289.4	WALL RADIAL DISPL	681.	369.	1.8
D107	226	20	1.4	11	0.	304.5	WALL RADIAL DISPL	1220.	435.	2.8
D108	227	20	1.5	11	0.	312.0	WALL RADIAL DISPL	772.	391.	2.0
Wr136	664	20	6.5	11	7.5	314.0	REBAR LAYER 6	160.	62.	2.6
Wr40	469	20	6.5	11	1.3	314.0	REBAR LAYER 1	190.	65.	2.9
Wr137	665	20	7.5	11	7.5	314.5	REBAR LAYER 6	160.	54.	3.0
Wr34	463	20	9.0	11	1.3	135.0	REBAR LAYER 1	299.	80.	3.7

(1) Note: Stiffness units are psi/inch for displacement gages and ksi for strain gages.

Table A.2 Apparent Stiffness Data for Bending Response of the Wall

GAGE ID	CHANNEL	ELEVATION Ft	ELEVATION In	RADIUS Ft	RADIUS In	AZIMUTH Deg	DESCRIPTION	(1) STIFFNESS Ku	(1) STIFFNESS Kc	RATIO Ku/Kc
Wr76	545	2	4.8	11	1.8	33[illegible].8	REBAR LAYER 2	305.	51.	
Wr182	760	2	8.8	11	8.3	326.5	REBAR LAYER 7	581.	429.	11.0
Wr76	545	2	4.8	11	1.8	332.8	REBAR LAYER 2	305.	51.	
Wr187	765	2	7.8	11	9.3	332.1	REBAR LAYER 8	896.	343.	7.6
Wr76	545	2	4.8	11	1.8	332.8	REBAR LAYER 2	305.	51.	
Wr181	749	2	1.8	11	8.3	328.9	REBAR LAYER 7	-616.	3816.	3.9
Wr76	545	2	4.8	11	1.8	332.8	REBAR LAYER 2	305.	51.	
Wr186	764	2	1.5	11	9.3	330.0	REBAR LAYER 8	2341.	930.	6.4
Wr75	544	2	0.3	11	1.5	332.8	REBAR LAYER 2	132.	49.	
Wr182	760	2	8.8	11	8.3	326.5	REBAR LAYER 7	581.	429.	3.1
Wr75	544	2	0.3	11	1.5	332.8	REBAR LAYER 2	132.	49.	
Wr187	765	2	7.8	11	9.3	332.1	REBAR LAYER 8	896.	343.	2.7
Wr75	544	2	0.3	11	1.5	332.8	REBAR LAYER 2	132.	49.	
Wr181	749	2	1.8	11	8.3	328.9	REBAR LAYER 7	-616.	3816.	2.2
Wr75	544	2	0.3	11	1.5	332.8	REBAR LAYER 2	132.	49.	
Wr186	764	2	1.5	11	9.3	330.0	REBAR LAYER 8	2341.	930.	2.7
Wr75	544	2	0.3	11	1.5	332.8	REBAR LAYER 2	132.	49.	
Pr10	1103	1	11.0	11	8.5	328.8	REBAR LAYER 8	-615.	2443.	2.2
Wr75	544	2	0.3	11	1.5	332.8	REBAR LAYER 2	132.	49.	
Br1811	1124	1	11.5	11	8.3	329.9	REBAR LAYER 7	-585.	-3485.	2.2
Wr75	544	2	0.3	11	1.5	332.8	REBAR LAYER 2	132.	49.	
Wr18	427	1	10.0	11	4.8	332.3	REBAR LAYER 11	196.	80.	3.1
Wr75	544	2	0.3	11	1.5	332.8	REBAR LAYER 2	132.	49.	
Br12	1087	1	10.5	11	6.0	332.8	REBAR LAYER 5	-1142.	221.	1.9
Br5	1080	1	7.8	11	1.5	332.8	REBAR LAYER 2	122.	45.	
Br18	1103	1	11.0	11	8.5	328.8	REBAR LAYER 8	-615.	2443.	2.2
Br5	1080	1	7.8	11	1.5	332.8	REBAR LAYER 2	122.	45.	
Br1811	1124	1	11.5	11	8.3	329.9	REBAR LAYER 7	-585.	-3485.	2.3
Br5	1080	1	7.8	11	1.5	332.8	REBAR LAYER 2	122.	45.	
Wr18	427	1	10.0	11	4.8	332.3	REBAR LAYER 11	196.	80.	3.2
Br5	1080	1	7.8	11	1.5	332.8	REBAR LAYER 2	122.	45.	
Br12	1087	1	10.5	11	6.0	332.8	REBAR LAYER 5	-1142.	221.	2.0
Br5	1080	1	7.8	11	1.5	332.8	REBAR LAYER 2	122.	45.	
Br11	1086	1	8.0	11	6.0	332.8	REBAR LAYER 5	-854.	178.	1.8
Br5	1080	1	7.8	11	1.5	332.8	REBAR LAYER 2	122.	45.	
Wr17	426	1	7.5	11	1.5	332.3	REBAR LAYER 11	261.	67.	1.7
Br5	1080	1	7.8	11	1.5	332.8	REBAR LAYER 2	122.	45.	
Br17	1102	1	9.0	11	8.5	327.9	REBAR LAYER 8	-523.	872.	2.1
Br5	1080	1	7.8	11	1.5	332.8	REBAR LAYER 2	122.	45.	
Wr180	748	1	6.0	11	8.3	331.6	REBAR LAYER 7	-659.	1129.	2.2
Br5	1080	1	7.8	11	1.5	332.8	REBAR LAYER 2	122.	45.	
Wr185	763	1	5.5	11	9.3	326.7	REBAR LAYER 8	-320.	941.	1.9

(1) Note: Stiffness units are k.i for strain gages.

Table A.2 (cont.)

GAGE ID	CHANNEL	ELEVATION Ft	ELEVATION In	RADIUS Ft	RADIUS In	AZIMUTH Deg	DESCRIPTION	(1) STIFFNESS Ku	(1) STIFFNESS Kc	RATIO Ku/Kc
Wr74	543	1	5.8	11	2.0	332.8	REBAR LAYER 2	197.	67.	
Br11	1086	1	8.0	11	6.0	332.8	REBAR LAYER 5	-654	178.	1.5
Wr74	543	1	5.8	11	2.0	332.8	REBAR LAYER 2	197.	67.	
Wr17	426	1	7.0	11	1.5	332.3	REBAR LAYER 11	261.	67.	0.2
Wr74	543	1	5.8	11	2.0	332.8	REBAR LAYER 2	197.	67.	
Br17	1102	1	9.0	11	8.5	327.9	REBAR LAYER 8	-523.	872.	2.0
Wr74	543	1	5.8	11	2.0	332.8	REBAR LAYER 2	197.	67.	
Wr180	748	1	6.0	11	8.3	331.6	REBAR LAYER 7	-659.	1129.	2.1
Wr74	543	1	5.8	11	2.0	332.8	REBAR LAYER 2	197.	67.	
Wr185	763	1	5.5	11	9.3	326.7	REBAR LAYER 8	-320.	941.	1.7
Wr69	528	1	11.0	11	2.3	305.5	REBAR LAYER 2	227.	72.	
Wr111	609	1	11.3	11	6.4	305.8	REBAR LAYER 5	816.	120.	1.7
Wr63	522	2	5.5	11	2.3	210.0	REBAR LAYER 2	386.	63.	
Br16	1101	1	11.0	11	9.3	210.4	REBAR LAYER 8	-380.	9162.	3.0
Wr63	522	2	5.5	11	2.3	210.0	REBAR LAYER 2	386.	63.	
Br10	1085	1	10.5	11	6.3	210.0	REBAR LAYER 5	-371.	143.	1.7
Wr62	521	2	1.0	11	2.0	210.0	REBAR LAYER 2	229	52.	
Br16	1101	1	11.0	11	9.3	210.4	REBAR LAYER 8	-380	9162.	2.7
Wr62	521	2	1.0	11	2.0	210.0	REBAR LAYER 2	229.	52.	
Br10	1085	1	10.5	11	6.3	210.0	REBAR LAYER 5	-371.	143.	1.7
Wr62	521	2	1.0	11	2.0	210.0	REBAR LAYER 2	229.	52.	
Br15	1100	1	8.3	11	9.3	209.5	REBAR LAYER 8	-286.	995.	2.3
Wr62	521	2	1.0	11	2.0	210.0	REBAR LAYER 2	229.	52.	
Br9	1084	1	8.0	11	5.3	210.0	REBAR LAYER 5	-610.	137.	2.0
Br4	1069	1	11.0	11	2.3	210.0	REBAR LAYER 2	114.	42.	
Br16	1101	1	11.0	11	9.3	210.4	REBAR LAYER 8	-380.	9162.	2.1
Br4	1069	1	11.0	11	2.3	210.0	REBAR LAYER 2	114.	42.	
Br10	1085	1	10.5	11	6.3	210.0	REBAR LAYER 5	-371.	143.	1.5
Br4	1069	1	11.0	11	2.3	210.0	REBAR LAYER 2	114.	42.	
Br15	1100	1	8.3	11	9.3	209.5	REBAR LAYER 8	-286.	995.	1.9
Br4	1069	1	11.0	11	2.3	210.0	REBAR LAYER 2	114.	42.	
Br9	1084	1	8.0	11	6.3	210.0	REBAR LAYER 5	-610.	137	1.6
Wr61	520	1	6.5	11	2.5	210.0	REBAR LAYER 2	108.	44.	
Br16	1101	1	11.0	11	9.3	210.4	REBAR LAYER 8	-380.	9162.	1.9
Wr61	520	1	6.5	11	2.5	210.0	REBAR LAYER 2	108.	44.	
Br10	1085	1	10.5	11	6.3	210.0	REBAR LAYER 5	-371.	143.	1.3
Wr61	520	1	6.5	11	2.5	210.0	REBAR LAYER 2	108.	44.	
Br15	1100	1	8.3	11	9.3	209.5	REBAR LAYER 8	-286.	995.	1.7
Wr61	520	1	6.5	11	2.5	210.0	REBAR LAYER 2	108.	44.	
Br9	1084	1	8.0	11	6.3	210.0	REBAR LAYER 5	-610.	137.	.4
Wr226	844	2	1.0	11	3.4	90.7	REBAR LAYER 10	327.	90.	
Wr149	687	2	4.0	11	8.0	85.6	REBAR LAYER 7	3429.	1013.	3.7

(1) Note: Stiffness units are ksi for strain gages.

Table A.2 (cont.)

GAGE ID	CHANNEL	ELEVATION Ft	ELEVATION In	RADIUS Ft	RADIUS In	AZIMUTH Deg	DESCRIPTION	(1) STIFFNESS Ku	(1) STIFFNESS Kc	RATIO Ku/Kc
Wr226	844	2	5.3	11	3.4	90.7	REBAR LAYER 10	327.	90.	
Wr170	728	2	7.0	11	8.3	97.3	REBAR LAYER 8	-1856.	2. .	3.0
Wr226	844	2	5.3	11	3.4	90.7	REBAR LAYER 10	327.	90.	
Wr93	581	2	5.0	11	6.4	93.0	REBAR LAYER 5	1716.	257.	2.9
Wr226	844	2	5.3	11	3.4	90.7	REBAR LAYER 10	327.	90.	
Wr92	580	2	0.5	11	6.4	93.0	REBAR LAYER 5	-560	322.	1.7
Wr226	844	2	5.3	11	3.4	90.7	REBAR LAYER 10	327.	90.	
Wr148	686	2	0.5	11	7.8	88.3	REBAR LAYER 7	-381.	1613.	1.8
Wr47	486	2	5.3	11	2.3	89.2	REBAR LAYER 2	427.	57.	
Wr149	687	2	7.5	11	8.0	85.6	REBAR LAYER 7	3429.	1013.	8.1
Wr47	486	2	5.3	11	2.3	89.2	REBAR LAYER 2	427.	57.	
Wr170	728	2	7.0	11	8.3	97.3	REBAR LAYER 8	-1856.	2205.	5.9
Wr47	486	2	5.3	11	2.3	89.2	REBAR LAYER 2	427.	57.	
Wr93	581	2	5.0	11	6.4	93.0	REBAR LAYER 5	1716.	257.	7.8
Wr47	486	2	5.3	11	2.3	89.2	REBAR LAYER 2	427.	57.	
Wr92	580	2	0.5	11	6.4	93.0	REBAR LAYER 5	-560.	322.	3.5
Wr47	486	2	5.3	11	2.3	89.2	REBAR LAYER 2	427.	57.	
Wr148	686	2	0.5	11	7.8	88.3	REBAR LAYER 7	-381.	1613.	3.4
Wr46	485	2	0.8	11	2.3	89.1	REBAR LAYER 2	93.	50.	
Wr93	581	2	5.0	11	6.4	93.0	REBAR LAYER 5	1716.	257.	1.6
Wr46	485	2	0.8	11	2.3	89.1	REBAR LAYER 2	93.	50.	
Wr92	580	2	0.5	11	6.4	93.0	REBAR LAYER 5	-560.	322.	1.3
Wr46	485	2	0.8	11	2.3	89.1	REBAR LAYER 2	93.	50.	
Wr148	686	2	0.5	11	7.8	88.3	REBAR LAYER 7	-381.	1613.	1.4
Wr46	485	2	0.8	11	2.3	89.1	REBAR LAYER 2	93.	50	
Br1481	1122	1	10.8	11	8.0	89.0	REBAR LAYER 7	-288.	-1299.	1.4
Wr46	485	2	0.8	11	2.3	89.1	REBAR LAYER 2	93.	50.	
Br14	1089	1	10.3	11	8.3	90.1	REBAR LAYER 8	-109.	-322.	1.2
Wr46	485	2	0.8	11	2.3	89.1	REBAR LAYER 2	93.	50.	
Wr14	423	1	10.5	11	4.3	91.9	REBAR LAYER 11	137.	77.	2.0
Br2	1067	1	10.3	11	2.3	88.7	REBAR LAYER 2	105.	39.	
Wr93	581	2	5.0	11	6.4	93.0	REBAR LAYER 5	1716.	257.	2.4
Br2	1067	1	10.3	11	2.3	88.7	REBAR LAYER 2	105.	39.	
Wr92	580	2	0.5	11	6.4	93.0	REBAR LAYER 5	-560.	322.	2.0
Br2	1067	1	10.3	11	2.3	88.7	REBAR LAYER 2	105.	39.	
Wr148	686	2	0.5	11	7.8	88.3	REBAR LAYER 7	-381.	1613.	2.1
Br2	1067	1	10.3	11	2.3	88.7	REBAR LAYER 2	105.	39.	
Br1481	1122	1	10.8	11	8.0	89.0	REBAR LAYER 7	-288.	-1299.	2.0
Br2	1067	1	10.3	11	2.3	88.7	REBAR LAYER 2	105.	39.	
Br14	1089	1	10.3	11	8.3	90.1	REBAR LAYER 8	-109.	-322.	1.5
Br2	1067	1	10.3	11	2.3	88.7	REBAR LAYER 2	105.	39.	
Wr14	423	1	10.5	11	4.3	91.9	REBAR LAYER 11	137.	77.	5.7

(1) Note: Stiffness units are ksi for strain gages.

Table A.2 (cont.)

GAGE ID	CHANNEL	ELEVATION Ft	In	RADIUS Ft	In	AZIMUTH Deg	DESCRIPTION	(1) STIFFNESS Ku	Kc	RATIO Ku/Kc
Wr225	843	1	10.8	11	3.4	90.7	REBAR LAYER 10	122.	56.	
Wr93	581	2	5.0	11	6.4	93.0	REBAR LAYER 5	1716.	257.	1.8
Wr225	843	1	10.8	11	3.4	90.7	REBAR LAYER 10	122.	56.	
Wr92	580	2	0.5	11	6.4	93.0	REBAR LAYER 5	-560.	322.	1.5
Wr225	843	1	10.8	11	3.4	90.7	REBAR LAYER 10	122.	56.	
Wr148	686	2	0.5	11	7.8	88.3	REBAR LAYER 7	-381.	1613.	1.6
Wr225	843	1	10.8	11	3.4	90.7	REBAR LAYER 10	122.	56.	
Br1481	1122	1	10.8	11	8.0	89.0	REBAR LAYER 7	-288.	-1299.	1.6
Wr225	843	1	10.8	11	3.4	90.7	REBAR LAYER 10	122.	56.	
Br14	1089	1	10.3	11	8.3	90.1	REBAR LAYER 8	-109.	-322.	1.2
Wr225	843	1	10.8	11	3.4	90.7	REBAR LAYER 10	122.	56.	
Wr14	423	1	10.5	11	4.3	91.9	REBAR LAYER 11	137	77.	5.4
Br2	1067	1	10.3	11	2.3	88.7	REBAR LAYER 2	105.	39.	
Br1471	1121	1	8.0	11	8.0	90.0	REBAR LAYER 7	-1058.	-745.	2.6
Br2	1067	1	10.3	11	2.3	88.7	REBAR LAYER 2	105.	39.	
Br7	1082	1	8.0	11	6.4	93.0	REBAR LAYER 5	-435.	280.	1.9
Br2	1067	1	10.3	11	2.3	88.7	REBAR LAYER 2	105.	39.	
Wr13	422	1	8.0	11	1.0	91.9	REBAR LAYER 11	225.	78.	2.5
Br2	1067	1	10.3	11	2.3	88.7	REBAR LAYER 2	105.	39.	
Br13	1088	1	7.3	11	8.3	89.2	REBAR LAYER 8	-156.	-444.	1.7
Wr225	843	1	10.8	11	3.4	90.7	REBAR LAYER 10	122.	56.	
Br1471	1121	1	8.0	11	8.0	90.0	REBAR LAYER 7	-1058.	-745.	2.1
Wr225	843	1	10.8	11	3.4	90.7	REBAR LAYER 10	122.	56.	
Br7	1082	1	8.0	11	6.4	93.0	REBAR LAYER 5	-435.	280.	1.4
Wr225	843	1	10.8	11	3.4	90.7	REBAR LAYER 10	122.	56.	
Wr13	422	1	8.0	11	1.0	91.9	REBAR LAYER 11	225.	78.	1.3
Wr225	843	1	10.8	11	3.4	90.7	REBAR LAYER 10	122.	56.	
Br13	1088	1	7.3	11	8.3	89.2	REBAR LAYER 8	-156.	-444.	1.4
Br1	1066	1	8.3	11	2.0	88.7	REBAR LAYER 2	97.	45.	
Br1481	1122	1	10.8	11	8.0	89.0	REBAR LAYER 7	-288.	-1299.	1.7
Br1	1066	1	8.3	11	2.0	88.7	REBAR LAYER 2	97.	45.	
Br14	1089	1	10.3	11	8.3	90.1	REBAR LAYER 8	-109.	-322.	1.3
Br1	1066	1	8.3	11	2.0	88.7	REBAR LAYER 2	97.	45.	
Wr14	423	1	10.5	11	4.3	91.9	REBAR LAYER 11	137.	77.	3.1
Br1	1066	1	8.3	11	2.0	88.7	REBAR LAYER 2	97.	45.	
Br1471	1121	1	8.0	11	8.0	90.0	REBAR LAYER 7	-1058.	-745.	2.1
Br1	1066	1	8.3	11	2.0	88.7	REBAR LAYER 2	97.	45.	
Br7	1082	1	8.0	11	6.4	93.0	REBAR LAYER 5	-435.	280.	1.5
Br1	1066	1	8.3	11	2.0	88.7	REBAR LAYER 2	97.	45.	
Wr13	422	1	8.0	11	1.0	91.9	REBAR LAYER 11	225.	78.	1.6
Br1	1066	1	8.3	11	2.0	88.7	REBAR LAYER 2	97.	45.	
Br13	1088	1	7.3	11	8.3	89.2	REBAR LAYER 8	-156.	-444.	1.5

(1) Note: Stiffness units are ksi for strain gages.

Table A.2 (cont.)

GAGE ID	CHANNEL	ELEVATION Ft	ELEVATION In	RADIUS Ft	RADIUS In	AZIMUTH Deg	DESCRIPTION	(1) STIFFNESS Ku	(1) STIFFNESS Kc	RATIO Ku/Kc
Br1	1066	1	8.3	11	2.0	88.7	REBAR LAYER 2	97.	45.	
Wr147	685	1	5.8	11	7.8	90.8	REBAR LAYER 7	-370.	1082.	1.7
Br1	1066	1	8.3	11	2.0	88.7	REBAR LAYER 2	97.	[illegible]	
Wr90	569	1	6.0	11	6.1	93.0	REBAR LAYER 5	-491.	2[illegible].	1.5
Wr45	484	1	6.3	11	2.5	88.9	REBAR LAYER 2	142.	52.	
Br1471	1121	1	8.0	11	8.0	90.0	REBAR LAYER 7	-1058.	-745.	2.6
Wr45	484	1	6.3	11	2.5	88.9	REBAR LAYER 2	142.	52.	
Br7	1082	1	8.0	11	6.4	93.0	REBAR LAYER 5	-435.	280.	1.7
Wr45	484	1	6.3	11	2.5	88.9	REBAR LAYER 2	142.	52.	
Wr13	422	1	8.0	11	1.0	91.9	REBAR LAYER 11	225.	78.	2.5
Wr45	484	1	6.3	11	2.5	88.9	REBAR LAYER 2	142.	52.	
Br13	1088	1	7.3	11	8.3	89.2	REBAR LAYER 8	-156.	-444.	1.6
Wr45	484	1	6.3	11	2.5	88.9	REBAR LAYER 2	142.	52.	
Wr147	685	1	5.8	11	7.8	90.8	REBAR LAYER 7	-370.	1082.	1.9
Wr45	484	1	6.3	11	2.5	88.9	REBAR LAYER 2	142.	52.	
Wr90	569	1	6.0	11	6.1	93.0	REBAR LAYER 5	-491.	271.	1.7
Wr224	842	1	6.3	11	3.4	90.7	REBAR LAYER 10	217.	64.	
Br1471	1121	1	8.0	11	8.0	90.0	REBAR LAYER 7	-1058.	-745.	3.1
Wr224	842	1	6.3	11	3.4	90.7	REBAR LAYER 10	217.	64.	
Br7	1082	1	8.0	11	6.4	93.0	REBAR LAYER 5	-435.	280.	1.7
Wr224	842	1	6.3	11	3.4	90.7	REBAR LAYER 10	217.	64.	
Wr13	422	1	8.0	11	1.0	91.9	REBAR LAYER 11	225.	78.	17.1
Wr224	842	1	6.3	11	3.4	90.7	REBAR LAYER 10	217.	64.	
Br13	1088	1	7.3	11	8.3	89.2	REBAR LAYER 8	-156.	-444.	1.6
Wr224	842	1	6.3	11	3.4	90.7	REBAR LAYER 10	217.	64.	
Wr147	685	1	5.8	11	7.8	90.8	REBAR LAYER 7	370.	1082.	2.0
Wr224	842	1	6.3	11	3.4	90.7	REBAR LAYER 10	217.	64.	
Wr90	569	1	6.0	11	6.1	93.0	REBAR LAYER 5	-491.	271.	1.8

(1) Note: Stiffness units are kai for strain gages.

Table A.3 Apparent Stiffness Data for Bending Response of the Basemat

GAGE ID	CHANNEL	ELEVATION Ft	ELEVATION In	RADIUS Ft	RADIUS In	AZIMUTH Deg	DESCRIPTION	(1) STIFFNESS Ku	(1) STIFFNESS Kc	RATIO Ku/Kc
Wr1	400	-1	5.9	3	10.0	93.8	MERIDIONAL #6 REBAR	111.	4.	
Wr6	405	1	6.8	3	10.0	89.4	MERIDIONAL #5 REBAR	-1908.	-760.	26.9
Wr2	401	-1	5.9	6	9.0	93.2	MERIDIONAL #6 REBAR	3816.	137.	
Wr7	406	1	7.0	6	9.0	91.6	MERIDIONAL #5 REBAR	-2753.	-1563.	12.7
Wr3	402	-1	5.9	8	0.0	92.8	MERIDIONAL #6 REBAR	3273.	108.	
Wr8	407	1	7.0	8	0.0	91.9	MERIDIONAL #5 REBAR	-12994.	-4798.	25.2
Wr4	403	-1	5.9	10	0.0	92.3	MERIDIONAL #6 REBAR	-2452.	259.	
Wr9	408	1	7.0	10	0.0	92.1	MERIDIONAL #5 REBAR	-3919.	463.	-11.1 (2)
Wr5	404	-1	5.9	11	0.0	91.8	MERIDIONAL #6 REBAR	-1430.	-1088.	
Wr11	420	1	7.0	11	0.0	92.2	MERIDIONAL #5 REBAR	3616.	214.	5.8
Wr10	409	1	6.8	10	9.0	88.7	CIRCUMFERNTIAL #6 REBAR	4911.	486.	10.1
Wr12	421	1	6.8	11	5.5	88.8	CIRCUMFERNTIAL #6 REBAR	3271.	187.	17.5
D50	169	4	8.5	11	0.	83.7	MAT VERTICAL UPLIFT	7150.	664.	10.8
D117	231	-1	-7.0	11	0.	90.0	MAT VERTICAL UPLIFT	28601.	4950.	5.8

Notes:
(1) Stiffness units are psi/inch for displacement gages and ksi for strain gages.
(2) Ratio determined from gages Wr4 and Wr9 are not included in Figure 5.7

(1) Note: Stiffness units are ksi for strain gages.

APPENDIX B. EFFECT OF INITIAL DEAD LOAD STRAIN ON ESTIMATED MOMENT

Since strain gage readings were set to zero before internal pressure loading, gages that recorded strain on vertically oriented bars did not measure a dead load strain. The uncertainty induced in estimates of moment at the base of the wall may be determined through an elastic analysis for the initial vertical strain and through an idealization of the internal force couple at that location.

Shown in Figure B.1 is a representative plot of internal pressure versus measured strain for a gage located on a vertical reinforcing bar. It is assumed that the weight of the structure above this gage produces an initial compressive strain, ε_o, and that the actual strain, ε_a, in the bar is determined by subtracting the dead load strain at all pressure levels from strains that were measured, ε_m. An estimate of the initial strain is found through an elastic analysis of a transformed section to be given by $\varepsilon_o = Wn\rho / A_s E_s(1 + n\rho - \rho)$, where W is the dead load per unit circumference, A_s is the area of steel in a unit section, ρ is the ratio of steel area to gross section area, E_s is Young's modulus of steel, and n is the ratio of Young's modulus of steel to that of concrete.

Shown in Figure B.2 is an idealization of the internal forces at the base of the wall. Before yielding the force in the steel, which is estimated from measured strain, is given by $T_m = E_s A_s \varepsilon_m$, whereas the actual force in the steel is given by $T_a = E_s A_s(\varepsilon_m$). The unit force in concrete estimated from measured reinforcement st. .ns is given by $C_m = T_m - N_v$ where N_v represents the net vertical force in the wall, determined from statics, and includes dead load. The actual unit force in concrete is similarly given by $C_a = T_a - N_v$. The difference in actual and measured unit concrete force is given by $C_a - C_m = -E_s A_s \varepsilon_o$.

The unit hoop moment about the plastic centroid, based on measured strain data, is given by $M_m = T_m(d - p) + C_m(p - k)$. A similar expression gives the unit moment based on actual strains. The difference in moment based on actual strains or on measured strains is given by $M_a - M_m = -E_s A_s(d - k)\varepsilon_o$, which may be further simplified to $-Wn\rho(d - k)/(1 + n\rho - \rho)$. At the pressure initiating flexural yielding (118 psig) the calculation for moment presented in section 6.1.1 found values for d and k equal to 7.51 and 0.68 in., respectively. With given values for the remaining parameters (W = 0.31 kips/in., n = 8, ρ = 0.03), the difference in the actual unit moment from the unit moment estimated from measured vertical strain gages is 0.4 kips.

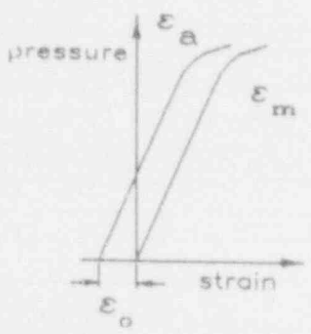

Fig. B.1 Sample Data

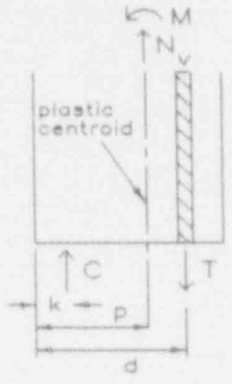

Fig. B.2 Internal Forces

APPENDIX C. LIMIT ON RADIAL SHEAR TRANSMITTED FROM THE WALL TO BASEMAT LINER

Studs welded to the wall liner and embedded in concrete transmit a portion of radial shear stress from the wall to the basemat liner. The geometry and proportions of the connection (Fig. 6.13) suggest that the ability to transfer shear along the indicated path is governed by the flexural capacity of the lower portion of liner on the wall. A limit analysis of the wall liner is performed to determine an upper bound to the unit shear force that may be transferred from studs in the wall to the basemat liner.

A free-body diagram of the bottom of the wall liner is presented in Figure C.1. The liner connects at point A with the knuckle joint and is continuous with liner material above this section at point B. The unit force in the studs is represented by F. At this location 1/2-in. long studs, 0.145 in. in diameter, were spaced at 2 in. on center.

A kinematically admissible deformation for this section is assumed in which hinges form along circumferential lines at points A and B and the section rotates outward, producing a radial deflection, δ, at point B. The unit moments, m_o, induced along circumferential lines A and B are taken equal to the unit plastic moment capacity $\sigma_o h^2/4$ for the liner, where σ_o denotes the liner yield stress. Circumferential strains due to the deflection are assumed to produce a constant unit hoop force, n_o, over the deflected region shown, equal to the unit yield capacity that may be carried in the plane of the wall, $\sigma_o h$. The unit force in studs, F, is determined from setting the external virtual work due to the deflection, δ, equal to the sum of internal virtual work for m_o and n_o due to the deformation. The resultant unit force in studs is given by $F = \frac{\sigma_o h}{2}\left(\frac{h}{s} + \frac{s}{R}\right)$. With given values for the dimensions (h = 0.068 in., R = 132 in., s = 13/16 in.), and the yield strength of the liner given by σ_o = 50.2 ksi, the unit force in studs is 153 lb/in.

The contribution of internal pressure to the external virtual work is not included chiefly because including it would reduce the estimate for F and because part, if not most, of the internal pressure in the containment is transmitted to the concrete wall by contact.

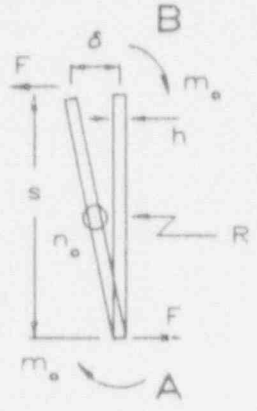

Fig. C.1 Wall Liner

List of References

1.1 von Riesemann, W. A., et al., "U. S. NRC Containment Integrity Programs," Proc. 8th International Conference on Structural Mechanics in Reactor Technology, Paper J1/2, International Association for Structural Mechanics in Reactor Technology, Brussels, Belgium, August 19-23, 1985.

1.2 Clauss, D. B., "Round-Robin Pretest Analyses of a 1:6-Scale Reinforced Concrete Containment Structure Subject to Static Internal Pressurization," NUREG/CR-4913, SAND87-0891, Sandia National Laboratories, Albuquerque, New Mexico, May 1987.

2.1 Horschel, D. S., "Construction of a 1/6 Scale Concrete Containment Model," Nuclear Engineering and Design, Vol. 104, November 1987, p. 341-347.

2.2 Horschel, D. S., "Design, Construction, and Instrumentation of a 1/6 Scale Reinforced Concrete Containment Building," NUREG/CR-5083, SAND88-0050, Sandia National Laboratories, Albuquerque, New Mexico, August 1988.

2.3 Knorovsky, G. A., P. W. Hatch, and M. R. Gutierrez, "Evaluation of Materials of Construction for the Reinforced Concrete Reactor Containment Model," NUREG/CR-5099, SAND88-0052, Sandia National Laboratories, Albuquerque, New Mexico, September 1988.

2.4 ASME Boiler and Pressure Vessel Code, Section III: Nuclear Power Plant Components, division 2: Concrete reactor vessels and containments, American Society of Mechanical Engineers, 1989.

2.5 Klieger, Paul, "Effect of Mixing and Curing Temperature on Concrete Strength," Journal of the American Concrete Institute, Vol. 29, No. 12, American Concrete Institute, June 1958, p. 1063-81.

2.6 Price, Walter H., "Factors Influencing Concrete Strength," Journal of the American Concrete Institute, Vol. 22, No. 6, American Concrete Institute, February 1951, p. 417-432.

2.7 Richart, Frank E., and Rex L. Brown, "An Investigation of Reinforced Concrete Columns," Bulletin, No. 267, University of Illinois Engineering Experiment Station, Urbana, Illinois, June 1934, p. 91.

2.8 Russell, H. G., and W. G. Corley, "Time-Dependent Behavior of Columns in Water Tower Place," Douglas McHenry International Symposium on Concrete and Concrete Structures, ACI Special Publication 55, American Concrete Institute, 1978, p. 347-373.

3.1 Horschel, D. S., "Experimental Results from Pressure Testing a 1:6-Scale Nuclear Power Plant Containment," NUREG/CR-5121, SAND88-0906, Sandia National Laboratories, Albuquerque, New Mexico, September 1991.

5.1 Mindess, Sidney, and J. F. Young, Concrete, Prentice-Hall, Englewood Cliffs, New Jersey, 198?, p. 427.

5.2 Building Code Requirements for Reinforced Concrete and Commentary, ACI 318-89 and 318R-89, American Concrete Institute, 1989.

5.3 Boresi, Arthur P., et al. Advanced Mechanics of Materials, 3rd Edition, John Wiley & Sons, New York, 1978, p. 96.

5.4 Lekhnitskii, S. G., Anisotropic Plates, translated from Russian by S. W. Tsai and T. Cheron, Gordon and Breach, New York, 1968, p. 11.

5.5 Clauss, D. B., "Round-Robin Analysis of the Behavior of a 1:6-Scale Reinforced Concrete Containment Model Pressurized to Failure: Posttest Evaluations," NUREG/CR-5341, SAND89-0349, Sandia National Laboratories, Albuquerque, New Mexico, October 1989.

6.1 Pfrang, E. O., C. P. Siess, and M. A. Sozen, "Load-Moment-Curvature Characteristics of Reinforced Concrete Cross Sections," ACI Journal Proceedings, Vol. 61, No. 7, American Concrete Institute, July 1964, p. 763-778.

6.2 Hognestad, E., "A Study of Combined Bending and Axial Load in Reinforced Concrete Members," Bulletin No. 399, University of Illinois Engineering Experiment Station, Urbana, Illinois, 1951.

6.3 Ang, Alfredo H-S., Wilson H. Tang, Probability Concepts in Engineering Planning and Design, Volume II, John Wiley & Sons, New York, 1984, p. 390-392.

7.1 Aoyagi, Y., O. Isobat, and N. Tanaka, "Design Method of Shell Wall End of Reinforced Concrete Containment Vessel (RCCV) Against Radial Shear," Fifth International Conference on Structural Mechanics in Reactor Technology, Paper J 4/6, International Association for Structural Mechanics in Reactor Technology, August 1979.

7.2 ASCE-ACI Task Committee 426, "The Shear Strength of Reinforced Concrete Members," Journal of the Structural Division, Vol. 99, No. ST6, American Society of Civil Engineers, June 1973, p. 1091-1149.

7.3 Alami, Z. Y., and P. M. Ferguson, "Accuracy of Models Used in Research on Reinforced Concrete," Journal of the American Concrete Institute, Vol. 60, No. 11, American Concrete Institute, November 1963, p. 1643-1661.

7.4 Swamy, R. N., and S. A. Qureshi, "Strength, Cracking and Deformation Similitude in Reinforced T-Beams Under Bending and Shear," Journal of the American Concrete Institute Proceedings, Vol. 68, No. 3, American Concrete Institute, March 1971, p. 187-195.

7.5 Kani, G. N. J., "How Safe are Our Large Reinforced Concrete Beams?," Journal of the American Concrete Institute, Vol. 64, No. 3, American Concrete Institute, March 1967, p. 128-141.

7.6 Taylor, Howard P. J., "Shear Strength of Large Beams," Journal of the Structural Division, Vol. 98, No. ST11, American Society of Civil Engineers, November 1972, p. 2473-2490.

7.7 Bazant, A. P., and H. Sun, "Size Effect in Diagonal Shear Failure: Influence of Aggregate Size and Stirrups," ACI Materials Journal, Vol. 84, No. 4, American Concrete Institute, July - August 1987, p. 259-272.

7.8 Shioya, T., and H. Kawasaki, "Size Effect on Shear Strength of Reinforced Concrete Beam," Finite Element Analysis of Reinforced Concrete Structures, American Society of Civil Engineers, 1986, p. 255-264.

7.9 Rettig, R. A., K. A. Condon, Z. D. Jankov, and C. F. Reeves, "Design of Conventionally Reinforced Concrete Containment Structures for Nuclear Power Plants," Experience in the Design, Construction, and Operation of Prestressed Concrete Pressure Vessels and Containments for Nuclear Reactors Conference Proceedings, York, England, September 8-12, 1975, p. 25-32.

7.10 Zsutty, Theodore, "Shear Strength Prediction for Separate Categories of Simple Beam Tests," American Concrete Institute Journal, Vol. 68, No. 2, American Concrete Institute, February 1971 p. 138-143.

7.11 Clark, L. E., K. H. Gerstle, and L. G. Tulin, "Effect of Strain Gradient on the Stress-strain Curve of Morter and Concrete," American Concrete Institute Journal Proceedings, Vol. 64, No. 9, American Concrete Institute, September 1967, p. 580-586.

7.12 Sarne, Y., and C. F. Reeves, "Design and Analysis of Reinforced Concrete Containment Structures for the Base Shear Force," Experience in the Design, Construction, and Operation of Prestressed Concrete Pressure Vessels and Containments for Nuclear Reactors Conference Proceedings, York, England, September 8-12, 1975, p. 63-68.

7.13 Shunmugavel, P., and O. Gurbuz, "An Evaluation of Structural Failure Modes for Prestressed Concrete Containments," Nuclear Engineering and Design, Vol. 104, November 1987, p. 349-355.

7.14 Nilson, A. H., and G. Winter, Design of Concrete Structures, Tenth Edition, McGraw-Hill Book Company, New York, 1986, p. 118-123.

7.15 Hanson, N. W., D. M. Schultz, J. J. Roller, A. Azizinamini, and H. T. Tang, "Testing of Large-Scale Concrete Containment Structural Elements," Nuclear Engineering and Design, Vol. 100, 1987, p. 129-149.

7.16 Dameron, R. A., R. S. Dunham, and Y. R. Rashid, "Methods for Ultimate Load Analysis of Concrete Containments: Second Phase," Interim Report EPRI NP-4869M, Electric Power Research Institute, March 1987.

7.17 Hanson, N. W., J. J. Roller, D. M. Schultz, J. T. Julien, and T. L. Weinmann, "Concrete Containment Tests, Phase 2 Structural Elements With Liner Plates," Interim Report EPRI NP-4867M, Electric Power Research Institute, August 1987.

7.18 "Report on Reactor Concrete Wall Test for Maine Yankee Atomic Power Station," Stone and Webster Engineering Co., Boston, MA, April 1969.

7.19 "Report on Shear Assembly Tests for Reactor Containment Wall: Beaver Valley Power Station-Unit No. 1, Duquesne Light Company," Stone and Webster Engineering Co., Boston, MA, December 1969.

7.20 Haddadin, M. J., S. T. Hong, and A. H. Mattock, "A Study of the Effectiveness of Web Reinforcement in Reinforced Concrete Beams Subject to Axial Loads," Structures and Mechanics Report, SM69-2, University of Washington, Seattle, WA, September 1969.

7.21 Haddadin, M. J., S. T. Hong, and A. H. Mattock, "Stirrup Effectiveness in Reinforced Concrete Beams with Axial Force," Journal of the Structural Division, Vol. 97, No. ST9, American Society of Civil Engineers, September 1971, p. 2277-2297.

7.22 Mattock, A. H., L. Johal, and H. C. Chow, "Shear Transfer in Reinforced Concrete With Moment or Tension Acting Across the Shear Plane," PCI Journal, Vol. 20, No. 4., July/August 1975, p. 77-93.

7.23 Paulay, T., and P. J. Loeber, "Shear Transfer by Aggregate Interlock," Shear in Reinforced Concrete, Special Publication No. 42, American Concrete Institute, 1974, p. 1-15.

7.24 Ugural, A. C., and S. K. Fenster, Advanced Strength and Applied Elasticity, Elsevier, New York, 1975, p. 111.

7.25 Kupfer, H., H. K. Hilsdorf, and H. Rusch, "Behavior of Concrete Under Biaxial Stresses," ACI Journal, Vol. 66, No. 8, American Concrete Institute, August 1969, p. 656-666.

Distribution:

J. F. Costello (20 Copies)
Structural & Seismic Engr. Branch
Mail Stop NL/S-217A
USNRC/RES
Washington, D. C. 20555

H. L. Graves, III
Structural & Seismic Engr. Branch
Mail Stop NL/S-217A
USNRC/RES
Washington, D.C. 20555

US Department of Energy
Office of Nuclear Energy
Attn: D. Giessing
W. Pasedag (2 copies)
Mail Stop B-107
NE-540
Washington, D.C. 20545

ABB Impell Corporation
Attn: Tim Lu
27401 Los Altos, Suite 480
Mission Viejo, CA 92691

ANATECH Research Corp.
Attn: Y. R. Rashid
P. O. Box 9165
LaJolla, CA 92038

Argonne National Laboratory
Attn: R. F. Kulak,
R. W. Seidensticker (2 copies)
9700 South Cass Avenue
Argonne, IL 60439

Babcock & Wilcox Co.
Attn: James R. Farr
20 S. van Buren Ave.
Barberton, OH 44203

Wilfred Baker Engineering
8700 Crownhill, Suite 310
San Antonio, TX 78209-1128

Battelle Columbus Laboratories
Attn: Richard Denning
Peter Cybulskis (2 copies)
505 King Avenue
Columbus, OH 43201

Bechtel Power Corporation
Attn. Asadour H. Hadjian
Bertold W. Pfeifer (2 copies)
12440 E. Imperial Highway
Norwalk, CA 90650

Bechtel Power Corp.
Attn: Subir Sen
K. Y. Lee (2 copies)
15740 Shady Grove Rd.
Gaithersburg, MD 20877

Bechtel Savannah River, Inc.
Attn: T. E. Johnson
802 E. Martintown Road
North Augusta, SC 29841

Brookhaven National Laboratory
Attn: C. Hofmayer, T. Pratt,
M. Reich (3 copies)
Building 130
Upton, NY 11973

Brookhaven National Laboratory
Attn: Ted Ginsberg
Building 820M
Upton, NY 11973

CBI NaCon, Inc.
Attn: Thomas J. Ahl
800 Jorie Boulevard
Oak Brook, IL 60521

City College of New York
Dept. of Civil Engineering
Attn: C. Costantino
140 Street and Convent Ave.
New York, NY 10031

Cornell University
Attn: Professor Richard N. White
School of Civil & Environ. Engr.
Hollister Hall
Ithaca, NY 14853

EBASCO Services, Inc.
Attn: Robert C. Iotti
Two World Trade Center
New York, NY 10048

EG&G Idaho
Attn: B. Barnes, T. L. Bridges
(2 copies)
Willow Creek Bldg. W-3
PO Box 1625
Idaho Falls, ID 83415

Electrical Power Research Institute
Attn: H. T. Tang, Y. K. Tang (4 copies)
Raf Sehgal, J. J. Taylor
3412 Hillview Avenue
PO Box 10412
Palo Alto, CA 94304

EQE Inc.
Attn: M. K. Ravindra
3300 Irvine Avenue
Suite 345
Newport Beach, CA 92660

General Electric Company
Attn: E. O. Swain, D. K. Henrie,
R. Gou, H. Townsend (4 copies)
175 Curtner Ave.
San Jose, CA 95125

Iowa State University
Department of Civil Engineering
Attn: L. Greimann
420 Town Engineering Bldg.
Ames, IA 50011

Los Alamos National Laboratories
Attn: C. Anderson
PO Box 1663
Mail Stop N576
Los Alamos, NM 87545

Northern Illinois University
Mechanical Engineering Dept.
Attn: A. Marchertas
DeKalb, IL 60115

NUTEC[illegible] gineers, Inc.
Attn [illegible]hn Clauss
1111 [illegible]quinelli Drive, Suite 100
Westmont, IL 60559

Oak Ridge National Laboratory
Attn: Steve Hodge
PO Box Y
[illegible]ak Ridge, TN 37830

Quadrex Corporation
Attn: Quazi A. Hossain
1700 Dell Ave.
Campbell, CA 95008

Sargent & Lundy Engineers
Attn: B. A. Erler
P. K. Agrawal (2 copies)
55 E Monroe St.
Chicago, IL 60603

Stevenson & Associates
Attn: John D. Stevenson
9217 Midwest Ave.
Cleveland, OH [illegible]4125

Tennessee Valley Authority
Attn: Nathaniel Foster
400 Summit Hill Rd.
W9D24C-K
Knoxville, TN 37902

TVA
Attn: D. Danton, W9A18
400 Commerce Ave.
Knoxville, TN 37902

United Engineers & Constructors, Inc.
Attn: Joseph J. Ucciferro
30 S. 17th St.
Philadelphia, PA 19101

University of California at Santa Barbara
Dept. of Chemical & Nuclear Engineering
Attn: T. G. Theofanous
Santa Barbara, CA 93106

University of Illinois
Attn: C. Siess
Dept. of Civil Engineering
Urbana, IL 61801

University of Illinois
1245 Newmark CE Lab
Attn: Prof. Mete A. Sozen
208 N. Romine
MC-250
Urbana, IL 61801

University of Wisconsin
Nuclear Engineering Dept.
Attn: Prof. Michael Corradini
Madison, WI 53706

Westinghouse Electric Corp.
Attn: Vijay K. Sazawal
Waltz Mill Site
Box 158
Madison, PA 15663

Institut fuer Mechanik
Universitaet Innsbruck
Attn: Prof. G. I. Schueller
Technikerstr. 13
A-6020 Innsbruck
AUSTRIA

Nuclear Studies & Safety Dept.
Ontario Hydro
Attn: W. J. Penn
700 University Avenue
Toronto, Ontario
M5G 1X6
CANADA

University of Alberta
Dept. of Civil Engineering
Attn: Prof. D. W. Murray
Edmonton, Alberta
T6G 2G7
CANADA

Commissariat a l'Energie Atomique
Centre d'Etudes Nucleaires de Saclay
Attn: M. Livolant, P. Jamet (2 copies)
F-91191 Gif-sur-Yvette Cedex
FRANCE

Commissariat a l'Energie Atomique
Institut de Protection et de
Surete Nucleaire
Attn: M. Barbe
F-92660 Fontenay-aux-Roses
FRANCE

OECD Nuclear Energy Agency
Attn: K. Stadie
Deputy Director, Safety & Regulation
38, Boulevard Suchet
F-75016 Paris
FRANCE

Kernforschungszentrum Karlsruhe GmbH
Attn: R. Krieg, P. Gast (2 copies)
Postfach 3640
D-7500 Karlsruhe
GERMANY

Technische Universitaet Muenchen
Lehrstuhl fuer Reakordynamik
und Reaktorsicherheit
Attn: Prof. H. Karwat
D-8046 Garching
GERMANY

Staatliche Materialpruefungsanstalt (MPA)
University of Stuttgart
Attn: Prof. K. F. Kussmaul
Pfaffenwaldring 32
D-7000 Stuttgart 80 (Vaihingen)
GERMANY

Gesellschaft fuer Reaktorsicherheit
Attn: H. Schulz, A. Hoefler,
F. Schleifer (3 copies)
Schwertnergasse 1
D-5000 Koeln 1
GERMANY

Kraftwerk Union AG
Attn: M. Hintergraber
Hammerbacherstr. 12-14
D-8520 Erlangen
GERMANY

ISMES
Attn: A. Peano
Viale Giulio Cesare 29
I-24100 Bergamo
ITALY

ENEA
Attn: Raffaele Di Sapia
Via Le Regina Margherita, 125
I-00198 Roma
ITALY

ENEA
Dipartimento Reattori Innovativi
Attn: Paolo Corticelli
Via Dell'Arcoveggio, 56/22-56/23
I-40129 Bologna
ITALY

ENEA-DISP
Attn: Giuseppe Pino
Gianni Petrangeli (2 copies)
Via Vitaliano Brancati, 48
I-00144 Roma
ITALY

Nuclear Equipment Design Dept.
Hitachi Works, Hitachi, Ltd.
Attn: O. Oyamada
3-1-1 Saiwai-Cho
Hitachi-Shi
Ibaraki-ken
JAPAN

Division of Technical Information
Japan Atomic Energy Research Institute
Attn: Jun-ichi Shimokawa
2-2, Uchisaiwai-cho 2-chome
Chiyoda, Tokyo 100
JAPAN

University of Tokyo
Institute of Industrial Science
Attn: Prof. H. Shibata
22-1, Roppongi 7
Minatu-ku, Tokyo
JAPAN

Civil Engineering Laboratory
Central Research Institute of
Electric Power Industry
Attn: Yukio Aoyagi
1646 Abiko Abiko-Shi Chiba
JAPAN

Kajima Corporation
Attn: T. Sugano, K. Umeda
H. Tsubota (3 copies)
KI Building
5-30, Akasada 6-chome
Minato-ku
Tokyo 107
JAPAN

Mitsubishi Heavy Industries, Ltd.
Attn: Kaoru Nagata
Manager, Nuclear Containment Vessel
Designing Section
Steel Structure Department
Kobe Shipyard & Machinery Works
1-1, Wadasaki-cho, 1-Chome, Hyogo-ku,
Kobe 652
JAPAN

NUPEC
Attn: K. Takumi, A. Nonaka (2 copies)
Equipment and Components Dept.
Shuwa Kamiyacho Building
3-13, 4-Chome
Toranomon, Minato-ku
Tokyo 105
JAPAN

Japan Atomic Energy Research Inst.
Attn: Kunihisa Soda
Toshikuni Isozaki (2 copies)
Tokai-Mura, Ibaraki-Ken 319-11
JAPAN

Obayashi Corporation
Technical Research Institute
Attn: Toshikazu Takeda
Matsutaro Seki
4-640, Shimokiyoto, Kiyose-shi
Tokyo 204
JAPAN

Shimizu Corporation
Attn: T. Kuroda, Y. Takeuchi (2 copies)
Nuclear Power Division
Seavans South, No. 2-3, Shibaura
1-chome, Minato-ku
Tokyo 105-07
JAPAN

Universidad Politecnica
Escuela Tecnica Superior
de Ingenieros Industriales
Attn: Agustin Alonso
Madrid
SPAIN

Unidad Electrica S.A.
Attn: Jose Puga
UNESA
ES-28020 Madrid
SPAIN

Principia Espana, SA
Attn: Joaquin Marti
Orense, 36-2
28020 Madrid
SPAIN

Servicio Licenciamiento
Central Nuclear de Asco
Attn: Sr. D. Joaquin Sanchez Baptista
Tres Torres, 7
ES-08017 Barcelona
SPAIN

Central Nuclear de Almaraz
Attn: Sr. D. Jose Maria Zamarron
Subdirector Tecnico
Claudio Coello, 123
ES-28006 Madrid
SPAIN

Nuclenor, S.A.
Attn: Sr. D. Federico del Pozo Obeso
Director General
Hernan Cortes, 26
ES-39003 Santander
SPAIN

UNESA
Attn: Sr. D. Jose Pu[illegible] Fernandez
Francisco Gervas, 3
ES-28020 Madrid
SPAIN

Studsvik Energiteknik AB
Attn: Kjell O. Johansson
S-611 82 Nykoping
SWEDEN

Swedish State Power Board
Nuclear Reactor Safety
Attn: Hans Cederberg
Per-Eric Ahlstrom
Ralf Espefaelt (3 copies)
S-162 87 Vallingby
SWEDEN

Swiss Federal Institute of Technology
Institute of Structural Engineering
Attn: W. Ammann
ETH-Hoenggerberg, HIL
CH-8093 Zurich
SWITZERLAND

Colenco Ltd.
Attn: K. Gahler, A. Huber
J. Jemielewski
A. Schopfer (4 copies)
Mellingerstrasse 207
CH-5405 Baden
SWITZERLAND

Paul Scherrer Institut
Attn: P. Hosemann
CH-5232 Villigen PSI
SWITZERLAND

Swiss Federal Nuclear Safety Inspectorate
Federal Office of Energy
Attn: S. Chakraborty
CH-5303 Wuerenlingen
SWITZERLAND

Swiss Federal Institute of Technology
for Building Materials
Attn: Prof. F. H. Wittmann
ETH-Honggerberg
CH-8093 Zurich
SWITZERLAND

Elektrowatt Ingenieurunternehmung AG
Attn: John P. Wolf
Bellerivestr. 36
CH-8022 Zurich
SWITZERLAND

Atomic Energy Authority
Safety and Reliability Directorate
Attn: D. W. Phillips
Wigshaw Lane
Culcheth
Warrington WA3 4NE
UNITED KINGDOM

Atomic Energy Establishment
Attn: Peter Barr
Winfrith
Dorchester Dorset
DT2 8DH
UNITED KINGDOM

HM Nuclear Installations Inspectorate
Attn: R. Bye, R. J. Stubbs (2 copies)
St. Peter's House
Balliol Road
Bootle, Mereyside L20 3LZ
UNITED KINGDOM

Nuclear Electric
Attn: J. Irving
Booths Hall
Chelford Road
Knutsford
Cheshire WA 16 8QG
UNITED KINGDOM

Taylor Woodrow Construction Limited
Attn: Carl C. Fleischer
Richard Crowder (2 copies)
345 Ruislip Road
Southall, Middlesex
UB1 2QX
UNITED KINGDOM

3141 S. A. Landenberger (5)
3151 G. C. Claycomb
6400 D. J. McCloskey
6460 J. V. Walker
6470 D. J. McCloskey
6473 W. A. von Riesemann (21)
6473 D. S. Horschel
6473 L. D. Lambert
6473 J. S. Ludwigsen
6473 D. W. Pace
6473 M. B. Parks
6473 B. L. Spelter
6473 J. J. Westmoreland
6473 H. P. Walther
6473 R. A. Watson
8523-2 Central Technical Files

NRC FORM 235 (2-89) NRCM 1102, 3201, 3202

U.S. NUCLEAR REGULATORY COMMISSION

BIBLIOGRAPHIC DATA SHEET

(See instructions on the reverse)

1. REPORT NUMBER (Assigned by NRC, Add Vol., Supp., Rev., and Addendum Numbers, If any.)

NUREG/CR-5674
SAND91-7058

2. TITLE AND SUBTITLE

Evaluation of Behavior and the Radial Shear Strength of a Reinforced Concrete Containment Structure

3. DATE REPORT PUBLISHED

MONTH: January
YEAR: 1992

4. FIN OR GRANT NUMBER

A1401

5. AUTHOR(S)

H.P. Walther

6. TYPE OF REPORT

7. PERIOD COVERED (Inclusive Dates)

8. PERFORMING ORGANIZATION – NAME AND ADDRESS (If NRC, provide Division, Office or Region, U.S. Nuclear Regulatory Commission, and mailing address; if contractor, provide name and mailing address.)

Department of Civil Engineering
University of Illinois
Urbana, IL 61801

Under Contract to:
Sandia National Laboratories
Albuquerque, NM 87185

9. SPONSORING ORGANIZATION – NAME AND ADDRESS (If NRC, type "Same as above"; if contractor, provide NRC Division, Office or Region, U.S. Nuclear Regulatory Commission, and mailing address.)

Division of Engineering
Office of Nuclear Regulatory Research
U.S. Nuclear Regulatory Commission
Washington, D.C. 20555

10. SUPPLEMENTARY NOTES

11. ABSTRACT (200 words or less)

This study is on the behavior and strength of the 1/6-scale reinforced concrete containment model tested at Sandia National Laboratories. The containment model was pressurized to more than three times its design pressure until a tear in the liner terminated the test. Deformation data from the test was used to interpret behavior and to estimate the internal forces at the wall-basemat connection. A possible mode of structural failure of containments subjected to high pressures is by radial shear failure at the wall-basemat connection. Although the containment model showed no sign that such a failure was imminent when the test was stopped, if it had been possible to increase the internal pressure, an abrupt shear failure was possible. A method based on the compressive force due to flexure at the wall-base was developed to evaluate the radial shear strength of the 1/6-scale containment. Using the developed methodology, an estimate is made of the pressure that would initiate a shear failure at the wall-basemat junction of the model. This estimate is based on a projection of the observed strength of similar 1/12-scale wall-basemat connections, which have failed in shear.

12. KEY WORDS/DESCRIPTORS (List words or phrases that will assist researchers in locating the report.)

reinforced concrete models
containment behavior
reinforced concrete shear strength
concrete aging
concrete experiments

13. AVAILABILITY STATEMENT

Unlimited

14. SECURITY CLASSIFICATION

(This Page)
Unclassified

(This Report)
Unclassified

15. NUMBER OF PAGES

16. PRICE

NRC FORM 335 (2-89)

THIS DOCUMENT WAS PRINTED USING RECYCLED PAPER

UNITED STATES
NUCLEAR REGULATORY COMMISSION
WASHINGTON, D.C. 20555